Reactivity and Thermochemistry of First-Row Transition Metal Complexes with Stable Organic Radicals

Thomas R. Porter

A dissertation submitted in partial fulfillment
Of the requirements for the degree of

Doctor of Philosophy

University of Washington

2014

Program Authorized to Offer Degree: Department of Chemistry

University of Washington

Abstract

Reactivity and Thermochemistry of First-Row Transition Metal Complexes with Stable Organic Radicals

Thomas R. Porter

Chair of the Supervisory Committee:
Professor James M Mayer
Department of Chemistry

Reactions involving transition metals and organic free radicals are critically important in a variety of chemical and biological processes. Because of their prevalence, there is a fundamental interest in better understanding these types of reactions to fully realize their potential for new applications.

The work presented in this dissertation describes the free radical reactivity and thermochemistry of several different transition metal systems with stable organic radicals. Chapter 1 provides an introduction to transition metal reactivity involving organic free radicals. Chapter 2 describes the catalytic disproportionation of a hydroxylamine by (TMP)Fe^{III}–OH (TMP = *meso*-tetramesityl porphyrin) and some of the radical reactions that make up the catalytic cycle. Chapter 3 describes the preparation, structural characterization and thermochemistry of a previously unreported stable organic radical, $^{t}Bu_2NPArO^{\bullet}$ (2,6-di-*tert*-butyl-4-(4'-nitrophenyl)phenoxyl). Chapter 4 describes the preparation of several $[Tp^{tBu}Cu^{II}]^{+}$ (Tp^{tBu} = hydro-*tris*(3-*tert*-butyl-pyrazolyl)borate) and $[Tp^{tBuMe}Cu^{II}]^{+}$ ($Tp^{tBu}Me$ = hydro-*tris*(3-*tert*-butyl-5-methyl-pyrazolyl)borate) alkoxide compelxes as models for potential intermediates in copper/radical alcohol oxidation catalysis. Treating these complexes with stable radicals such a $^{t}Bu_3ArO^{\bullet}$ (2,4,6-

tri-*tert*-butyl-phenoxyl) did not result in alkoxide oxidation despite having a large driving force. From these studies, we conclude driving force is not a primary predictor for copper/radical alcohol oxidation. Chapter 5 discusses the coordination chemistry of $[Tp^{tBu}Cu^{II}]^+$ and $[Tp^{tBu}Zn^{II}]^+$ with 4-nitro-phenols. With the bulky 2,6-disubstituted 2,6-di-*tert*-butyl-4-nitro-phenoxide, coordination to either metal occurs through a nitronate resonance form. The 2,6-unsubstituted 4-nitro-phenol binds through the phenoxide resonance form. Chapter 6 highlights the large kinetic barrier for ketone reduction or oxidation by titanocene(III/IV) and the hydrogen atom donor/acceptor, $^{t}Bu_3ArO(–H)$. Finally, Chapter 7 describes the selective and stoichiometric reduction of aromatic and aliphatic nitro groups by photoreduced titanium dioxide nanoparticles in acidic aqueous solutions. From thermochemical analysis, it is likely that these reactions proceed through a rate determining $H^+/e^–$ transfer.

Table of Contents

List of Figures ..... *ii*

List of Tables ..... *v*

Chapter 1: Introduction to Organic Free Radical Chemistry with Transition Metal Complexes 1

Chapter 2: Radical Reactivity of the Fe(III)/(II) Tetramesitylporphyrin Couple:Hydrogen Atom Transfer, Oxyl Dissociation, and Catalytic Disproportionation of a Hydroxylamine 19

Chapter 3: Preparation, Structural Characterization and Thermochemistry of an Isolable 4-Aryl Phenoxyl Radical 52

Chapter 4: Synthesis, Radical Reactivity and Thermochemistry of Monomeric Copper(II) Alkoxide Complexes: Insights into Copper/Radical Catalysis of Alcohol Oxidation 67

Chapter 5: Sterically Directed Nitronate Complexes of 2,6-Di-*tert*-Butyl-4-Nitrophenoxide with Cu(II) and Zn(II) and Their H-Atom Transfer Reactivity 113

Chapter 6: High Kinetic Barrier for Ketone Reduction or Alkoxide Oxidation by Titanocenes and H-Atom Transfer Reagents 140

Chapter 7: Selective Aliphatic and Aromatic Nitro Reductions by Colloidal Photo-Reduced TiO_2 Nanoparticles at Low pH 156

List of Figures

Figure Number Page

1.1. The potential energy surface of a hypothetical H^+/e^- transfer reaction that is thermochemically biased to react through a CPET mechanism. 5

1.2. Standard reduction potentials and pK_a values of TEMPO(H) in acetonitrile. 9

1.3. Standard reduction potentials and pK_a values of ^{t}Bu$_3$ArO(H) in acetonitrile 11

2.1. (A) Spectra of the reaction between 80μM (TMP)Fe^{III}(OH) and 4.0 mM TEMPOH *vs.* time in toluene. (B) Kinetic trace of same the reaction at 525 nm and fit. (C) Pseudo-first order plot of k_{obs} *vs.* [TEMPOH]. 21

2.2. Stacked variable temperature ^{1}H NMR spectra of a toluene-d_8 solution containing 4.0 mM (TMP)Fe^{II} and 4.0 mM TEMPO 24

2.3. ^{1}H NMR spectra of 4.0 mM (TMP)Fe^{II} with 0 to 26.6 mM of TEMPO in toluene-d_8 on a 500 MHz spectrometer at 25 °C 26

2.4. Plots of the observed chemical shift of (TMP)Fe^{II}/(TMP)Fe^{III}(TEMPO) vs. concentration of TEMPO 27

2.5. Plot of [(TMP)Fe^{II}]/[(TMP)Fe^{III}(TEMPO)] vs. [TEMPO] from ^{1}H NMR spectra. 28

2.6. (A) Optical spectra of (TMP)Fe^{II} (80 μM) and one equivalent of TEMPO in toluene at temperatures ranging from 25 °C to –90 °C. (B) van't Hoff plot of ln($K_{-2.4}$) vs. 1/T. 29

2.7. ^{1}H NMR spectra of (TMP)Fe^{III}(^{t}Bu$_3$ArO) in toluene-d_8 and (TMP)Fe^{III}(^{t}Bu$_3$ArO) plus excess degassed H_2O in toluene-d_8. 31

2.8. Selected ^{1}H NMR slices of the disproportionation of TEMPO–H in the presence of a catalytic amount of (TMP)Fe^{II} 33

2.9. Kinetic traces for the disproportionation of TEMPO–H catalysed by (TMP)Fe^{II} in toluene-d_8. 33

2.10. Mass balance plot for the catalytic disproportionation of TEMPO–H 47

3.1. ^{1}H NMR Spectrum of ^{t}Bu$_2$NPArO$^\bullet$ in acetonitrile-d_3 shows the presence of only minor diamagnetic impurities. 53

3.2. ORTEPs of ^{t}Bu$_2$NPArO$^\bullet$ and ^{t}Bu$_2$NPArO–H. 54

3.3. X-band EPR spectrum of 1 mM ^{t}Bu$_2$NPArO$^\bullet$ in toluene recorded at 25 °C and simulation 57

3.4. Spectra of $^{t}Bu_2NPArO^{\bullet}$ at multiple concentrations and corresponding Beer's Law plots in (A) toluene and (B) MeCN. 58

3.5. ^{1}H NMR spectrum of equilibrium studies between $^{t}Bu_2NPArOH$ and $^{t}Bu_3ArO^{\bullet}$ radical in toluene-d_8 59

3.6. 2,6-$^{t}Bu_2$-4-X-ArO-H Bond dissociation free energies (BDFEs) vs. 3,5 hyperfine coupling constant for 2,6-$^{t}Bu_2$-4-X-$ArO^{\bullet}$ radicals. 60

4.1. ORTEPs of $Tp^{tBu}Cu^{II}$-OCH_2CF_3 and $Tp^{tBuMe}Cu^{II}$-OCH_2CF_3 71

4.2. ^{1}H NMR spectrum of $Tp^{tBu}Cu^{II}$-OCH_2CF_3 in DCM-d_2. 72

4.3. X-band EPR spectrum of $Tp^{tBu}Cu^{II}$-OCH_2CF_3 in a toluene glass at 120 K with simulation 74

4.4. The overlayed ENDOR spectra of $Tp^{tBu}Cu^{II}$-$OC\underline{H}_2CF_3$ and its deuterium labeled isotopologue $Tp^{tBu}Cu^{II}$-$OC\underline{D}_2CF_3$ 76

4.5. Cyclic voltammograms of 2.5 mM $Tp^{tBu}Cu^{II}$-OCH_2CF_3, $Tp^{tBuMe}Cu^{II}$-OCH_2CF_3 (dotted blue) and $Tp^{tBu}Cu^{II}$-$OCH(CH_3)CF_3$ in dichloromethane. 77

4.6. Kinetic trace for the TEMPO catalyzed disproportionation of $Tp^{tBuMe}Cu^{II}$-OCH_2CF_3 in DCM-d_2/1% MeCN-d_3 (v/v) 85

4.7. X-Ray Crystal Structure of $Tp^{tBuMe}Cu^{II}$-OCH_2CF_3 depicting a space-filling model. 92

4.8. ^{1}H and ^{1}H $\{^{19}F\}$ NMR spectra of $^{t}Bu_3CHD$-TFE expanded to show the chemically inequivalent trifluoroethylene signals 100

4.9. (A) Selected optical spectra of the reaction between $Tp^{tBu}Cu^{II}$-OCH_2CF_3 (0.5 mM) with $^{t}Bu_3ArO$ (26.5 mM). (B) Kinetic trace of the same reaction monitored at 440 nm with fit (C) The *pseudo*-first order plot of the reaction between $Tp^{tBu}Cu^{II}$-OCH_2CF_3 and $^{t}Bu_3ArO^{\bullet}$ collected with three different solvent batches under similar conditions 101

4.9. Kinetic Trace for the Reactions of 15.3 mM $Tp^{tBu}Cu^{II}$-OCH_2CF_3 or $Tp^{tBu}Cu^{II}$-OCD_2CF_3 with 1 eq $^{t}Bu_3ArO^{\bullet}$ in DCM-d_2/1% MeCN-d_3 (v/v) 102

4.10. ORTEP drawing of $Tp^{tBu}Cu^{II}$-$OCH(CH_3)CF_3$. Hydrogen atoms are omitted for clarity 103

4.11. ^{19}F NMR spectra (282 MHz top; 470 MHz bottom) of the decomposition reaction of 15.3 mM or racemic $Tp^{tBu}Cu^{II}$-$OCH(CH_3)CF_3$ or (R) enriched $Tp^{tBu}Cu^{II}$-$OCH(CH_3)CF_3$ in DCM-d_2/1% MeCN-d_3 (v/v) 104

5.1. ORTEP of $Tp^{tBu}Cu^{II}$-$O_2N^{t}Bu_2C_6H_2O$. 116

5.2. X-Band EPR spectrum of $Tp^{tBu}Cu^{II}$-$O_2N^{t}Bu_2C_6H_2O$ at 120 K in a toluene glass .. 117

5.3. ORTEP of $Tp^{tBu}Zn^{II}$-$O_2N^tBu_2C_6H_2O$ 119

5.4. ORTEP of $Tp^{tBu}Cu^{II}$-$OArNO_2$ 120

5.5. X-Band EPR spectrum of $Tp^{tBu}Cu^{II}$-$OArNO_2$ in a toluene glass at 120 K with simulation 121

5.6. Cyclic Voltammogram of $Tp^{tBu}Cu^{II}$-$O_2N^tBu_2C_6H_2O$ in dichloromethane 123

5.7. Stack of optical traces of the reaction between 2.5 mM $[Tp^{tBu}Cu^{I}]_2$, 5 mM $O_2N^tBu_2C_6H_2O$–H and 5 mM $^tBu_3ArO^\bullet$ in benzene over the course of 1 hour. 124

5.8. The ORTEP of $Tp^{PhMe}Ni^{II}$-O^iPr_2Ar with the space-filling diagram overlay..... 126

5.9. ORTEP of $Tp^{tBu}Zn^{II}$-OTf..... 135

5.10. ORTEP of $Tp^{tBu}Cu^{II}$-κ^2-OAc. 136

6.1. ORTEP of $[Cp_2Ti^{IV}Cl]_2$-μ-O..... 143

6.2. ^{1}H NMR spectrum of $Cp_2Ti^{IV}Cl(OAr^tBu_3)$ in benzene-d_6..... 145

6.3. Variable temperature ^{1}H NMR spectra of $Cp_2Ti^{IV}Cl(OAr^tBu_3)$ in C_6D_6..... 146

6.4. . ^{1}H NMR spectrum of the reaction mixture containing $Cp_2Ti^{IV}Cl(OBn)$ and 2 eq of $^tBu_3ArO^\bullet$ in benzene-d_6 after 24 hours. 148

7.1. Anaerobic bleaching of e^-:TiO_2 observed immediately after photolysis is complete. The spectral decay over 18 hours is shown on the left and the single wavelength trace at 600 nm is shown on the right. 158

A.7.1.^{1}H NMR Spectrum of the completed reaction between e^-:TiO_2/H^+ and 4-MeO-TEMPO in 85% D_2O/15% methanol-d_4 showing the formation of 4-MeO-TEMPO–H. 174

A.7.2. ^{1}H NMR Spectrum of the completed reaction between e^-:TiO_2/H^+ and 4-MeO-TEMPO in 85% D_2O/15% methanol-d_4 showing the formation of 2-aminopropane. 175

List of Tables

Table Number Page

2.1. Spectroscopic features of (TMP)Fe species in toluene 22

2.2. Temperature dependent $K_{2.4}$ values at different temperatures in toluene. 46

3.1. Select bond lengths (Å) and aryl-aryl torsion angles (deg) of $^{t}Bu_2NPArO^{\bullet}$ and $^{t}Bu_2NPArO$-H. 55

3.2. Crystallographic data for $^{t}Bu_2NPArO^{\bullet}$ and $^{t}Bu_2NPArO$–H 64

4.1. τ values and EPR Signals for Various $TpCu^{II}$-X complexes 70

4.2. Select interatomic distances (Å) and angles (deg) of $Tp^{tBu}Cu^{II}$-OCH_2CF_3 and $Tp^{tBuMe}Cu^{II}$-OCH_2CF_3 72

4.3. ^{1}H NMR resonances of related $Tp^{tBu}Cu^{II}$-X and $Tp^{tBuMe}Cu^{II}$-X complexes 73

4.4. Select bond lengths (Å) and angles (deg) of $Tp^{tBu}Cu^{II}$-$OCH(CF_3)CH_3$ 103

4.5. Crystallographic collection and refinement data for $Tp^{tBu}Cu^{II}$-OCH_2CF_3, $Tp^{tBuMe}Cu^{II}$-OCH_2CF_3 and $Tp^{tBu}Cu^{II}$-$OCH(CH_3)CF_3$ 108

5.1. Select bond lengths (Å) and angles (deg) of $Tp^{tBu}Cu^{II}$-$O_2N^{t}Bu_2C_6H_2O$ 116

5.2. Select bond lengths (Å) and angles (deg) of $Tp^{tBu}Zn^{II}$-$O_2N^{t}Bu_2C_6H_2O$ 119

5.3. Select bond lengths (Å) and angles (deg) of $Tp^{tBu}Cu^{II}$-$OArNO_2$ 121

5.4. Crystallographic collection and refinement data for several $[Tp^{tBu}Cu^{II}]^+$ and $[Tp^{tBu}Zn^{II}]^+$ complexes 133

5.5. Select bond lengths (Å) and angles (deg) of $Tp^{tBu}Zn^{II}$-OTf. 135

5.6. Select bond lengths (Å) and angles (deg) of $Tp^{tBu}Cu^{II}$-κ^2-OAc 136

6.1. $Cp_2Ti^{IV}Cl(OR)$ Complexes Prepared via alcoholysis of $Cp_2Ti^{IV}Cl(OAr^{t}Bu_3)$ 147

7.1. Particle Titration Data at Two Different Times After Photolysis 159

7.2. Titration Data for e^-:TiO_2 solutions with pre-charge pH values of 2.4 161

7.3. Organic Reduction Reactions Screened for Reactivity with e^-:TiO_2 162

Acknowledgements

I am incredibly grateful for the guidance and support of my advisor Jim Mayer over the last 5 years. Jim's enthusiasm for science and his ability to tailor his mentoring style to each student is a combination that I think few advisors have. I'm sure I've been more than a handful for Jim during my time in his lab but he has been extremely patient and supportive throughout. In addition to being a great advisor, Jim is a great person and I feel so fortunate to have had the opportunity to have him as a mentor. Joining the Mayer Lab is the best choice I could have made and I am proud to leave UW as a 'Mayer Student'.

The Mayer lab has had quite a string of characters pass through during my time. Graduate school hasn't always been roses and rainbows but having such amazing co-workers and friends has made the rough times less rough—and the good times the best times. I'm especially indebted to Miles Braten, Carolyn Valdez, David Lao, Tristan Tronic, Caroline Saouma, Carlos Rodriguez del Rio(Gato) and Mike Pegis. Without the scientific and emotional support I've received from each of these people, I would have almost certainly not made it through. During the hardest parts of graduate school, these folks were there and I am thankful to have had them as friends. Outside of the lab, I owe the same gratitude to my Seattle friends Mike Larsen, John "J. Meaux" Morrison, Eric "Fish" Fischer, Ryan Sims, Sarah Dean, Hailey Rademacher and Johnny from the Moon Temple.

Finally, I need to thank my family for their unwavering support and love. My little brother and sister, Jimmy and Paige, are the best siblings I could ask for and I love them both dearly. My parents, Tom and Marybeth, have encouraged my interest in science since I was little and continue to be my biggest supporters. Without their patience and love, this thesis would not exist.

Dedication

For my parents, Tom and Marybeth.

Chapter 1:
Introduction to Organic Free Radical Chemistry With Transition Metal Complexes

1.1. Introduction

An organic free radical is any organic compound with an unpaired valence electron. These species are often highly reactive and most often (but not always) short lived due to their propensity to react via radical coupling, disproportionation or by abstracting a hydrogen atom ($H^{\bullet} \equiv H^{+}/e^{-}$) from another molecule.[1] Radicals are powerful and reactive chemical reagents which makes them exceptionally good at accomplishing difficult chemical transformations. However, it is often the case that their highly reactive nature makes selectively harnessing their potential challenging. Using transition metal complexes to mediate organic radicals is an effective way for utilizing their reactivity in a controlled manner.

Despite their often unstable natures, organic radicals and their reactivity are critical and ubiquitous in both chemistry and biology.[2] Chemists have utilized radicals for an extremely broad number of application. These range from the classic sophomore organic chemistry example of anti-Markovnikov hydro-bromination of olefins first reported in 1933[3] to the modern day and highly sophisticated atom transfer radical polymerization (ATRP) pioneered by Matyjaszewski and others.[4] In biology, enzymes utilize radical processes with high efficiency to preform a wide variety of important tasks (i.e. cytochrome P450, photosystem II, galactose oxidase and many more).[5]

While a great deal is known about radicals and radical chemistry,[2] there is still much to be learned. Continuing to build a fundamental understanding – particularly the way organic radicals interact with transition metals – will provide insight into how these unusual and sometimes formidable compounds can be put to use for carrying out and understanding new chemical reactions.

1.2. Thermodynamics of Radical Reactions

As a chemist, knowledge the bond strengths of the bonds being broken and formed in a reaction are extremely useful for predicting whether a radical transfer reaction occurs or does not occur.[1a,6] In a radical transfer reaction, if the bond being

broken is weaker than the bond being formed, the reaction is expected to proceed. This point seems trivial since clearly a reaction *should* only occur if it is exoergic, but this relationship is especially important in radical reactions. Unlike many other chemical transformations, elementary atom and group transfer processes (which are essentially just inner-sphere electron transfers)[7] often have low activation barriers so their reactivity or lack of reactivity is closely linked to the overall thermochemistry of the system.[1a]

In many systems, this thermochemistry-kinetics relationship can be predicted and modeled by the use of linear free energy relationships in which the activation energy scales linearly with the driving force for the reaction.[1a,6] For hydrogen atom transfer (HAT) reactions (or equivalently, concerted proton-electron transfer), this relationship has been shown to be parabolic and follow a Marcus model.[6c,d]

Traditionally, free radical chemists have used enthalpies of reactions ($\Delta H_{rxn}°$) rather than free energies of reactions ($\Delta G_{rxn}°$) to predict reactivity. In many cases this is a reasonable simplification since it is often true that in radical transfer reaction $|\Delta S_{rxn}°| \cong 0$ and so $\Delta G_{rxn}° = \Delta H_{rxn}°$. This is particularly true for HAT reactions between organic molecules since no change in charge occurs in these reactions and the size of the reactants are roughly the same as the products. This approach fails in cases where large structural and vibrational changes are accompanied with radical transfer in which case the entropy can have significant contributions to $\Delta G°$. This is highlighted in the reports by Mader and Mayer regarding iron(II) and cobalt(II) *tris*(*bis*-imidazoline) complexes that have ground state entropy changes of -30 and -40 eu, respectively, upon hydrogen atom transfer to the persistent radical TEMPO (2,2,6,6-tetramethylpiperidinyl)(*vida infra*).[8] These large entropy changes are attributed to vibrational differences between the M^{III} and M^{II} complexes (M = Fe, Co) while changes in spin state also contribute in the case of cobalt.

The contribution of $\Delta S_{rxn}°$ is especially important for radical dissociation/association reactions in which the molecularity of the forward and reverse reactions are different. For example, de Bruin and co-workers reported the reversible bond homolysis of TEMPO from a (porphyrin)rhodium(III) TEMPO complex. The enthalpy of dissociation was found to be $\Delta H°$ = 14.7 kcal mol^{-1} with a non-negligible entropic contribution of $\Delta S°$ = –30.6 e.u. (eq 1.1)[9]

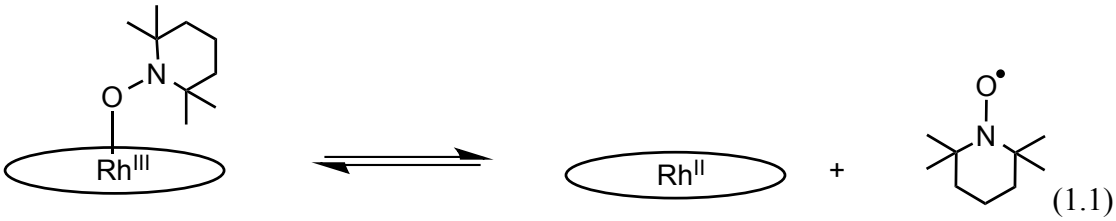

(1.1)

Because of the importance of entropy in many radical reactions, the enthalpy of a reaction alone is not always a good predictor for determining whether a reaction will or will not occur. Consequently, it is preferred to compare bond dissociation free energies (BDFEs) rather than BDEs for assessing reaction thermodynamics. There are a variety of methods available for experimentally accessing these values.

One common methods for determining BDFE values of acidic X–H bonds is by measuring the pK_a of X–H and the reduction potential ($E°$) of $X^{\bullet/-}$ and applying Hess' Law using eq 1.2. The term C_G is a constant that encompasses the free energy of formation of $H^\bullet$ ($\Delta G_f°(H^\bullet)$), the solubility of H ($\Delta G_{solv}°(H^\bullet)$), and the nature of the reference electrode.[10]

$$BDFE_{solv}(X–H) = 1.37pK_a + 23.06E° + C_{G,solv} \quad (1.2)$$

Another method by which X–H bond strengths are measured is via equilibrium studies with a hydrogen atom acceptor (Y) with a known Y-H BDFE (equations (1.3), (1.4)). This method generally gives more precise values since free energy is proportional to ln(K_{eq}) so even large errors in K_{eq} translate to small errors in BDFE. In practice, measuring BDFEs in this way is often limited due to the limited number of well-suited hydrogen atom acceptors available.

$$X–H + Y \rightleftharpoons X + H–Y \quad (1.3)$$

$$BDFE(X–H) = BDFE(Y\text{-}H) – RT\ln(K_{eq}) \quad (1.4)$$

Bond strength values of non-acidic bonds (i.e. C–H, C–C, C–O, etc.) are less convenient to determine and not as routinely measured. A large number of gas phase BDEs have been tabulated[11] and are useful estimates of BDFEs in many cases. However,

these values must be interpreted conservatively because they neglect entropic contributions.

Because of differences in solvation energies of the products and reactants in a radical reaction, BDFE values can vary substantially depending on the particular solvent. For example, the solution BDFE of the O–H bond in $^{t}Bu_3ArO$–H (2,4,6-tri-*tert*-butyl-phenol) is 80.6 kcal mol^{-1} in DMSO and 76.7 kcal mol^{-1} in benzene. A method for converting BDFE values between solvents using empirically determined hydrogen-bonding parameters has been described by Warren and Mayer[12] and has proven quite successful in many cases. To our knowledge, this has only been applied for X–H bond but could in principle be used for converting solution BDFEs any type of bond.

1.3. Thermochemical Bias for Radical Transfer

The net result of a radical transfer reaction is that a bond is broken and a new bond is formed (eq 1.5).

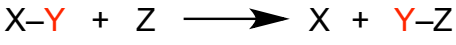

(1.5)

There are several mechanisms by which this reaction could occur. For the sake of clarity, let us first examine the case where the transferred radical (Y) is a hydrogen atom ($H^{\bullet} = H^{+}/e^{-}$). The net transfer of a hydrogen atom could in theory proceed by (*i*) proton transfer (PT) followed by electron transfer (ET) (eq 1.6), (*ii*) electron transfer followed by proton transfer (eq 1.7) or (*iii*) through concerted proton-electron transfer (CPET; ≡ HAT) where both particles are transferred in the same kinetic step (eq 1.8).[6c,d]

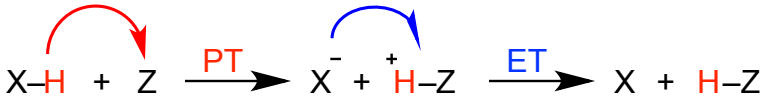

(1.6)

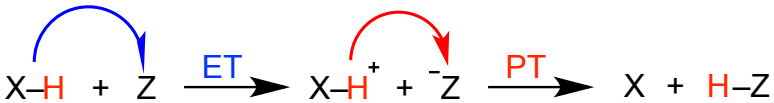

(1.7)

(1.8)

In mechanisms (*i*) and (*ii*), the intermediate, charge separated species can be described thermodynamically from the pK_a or standard reduction potential of X–H. In

mechanism (*iii*), these intermediate charge separated species are bypassed. If the intermediates expected by mechanism (*i*) and (*ii*) are high in free energy but the overall HAT reaction is exoergic, the reaction will likely proceed through mechanism (*iii*) (Figure 1.1).[6c,d]

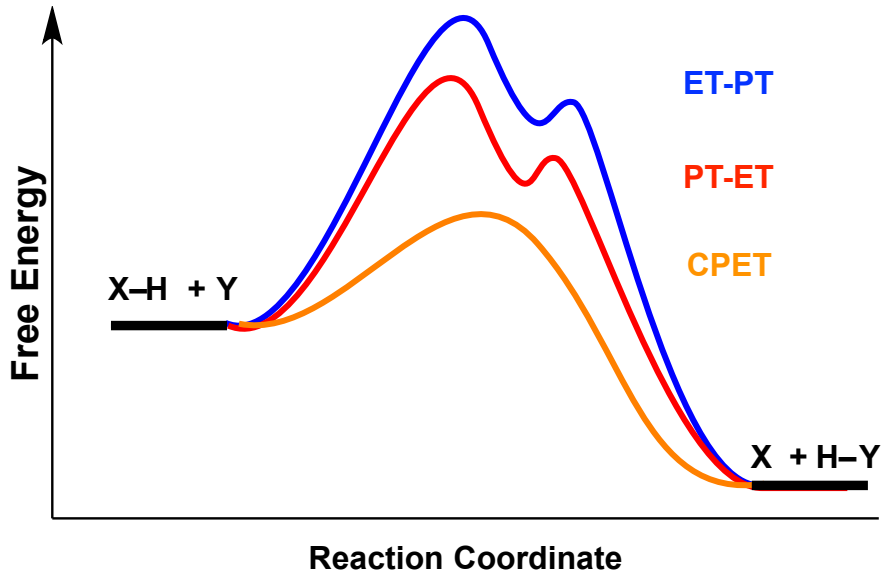

Figure 1.1. The potential energy surface of a hypothetical H^+/e^- transfer reaction that is thermochemically biased to react through a CPET mechanism (mechanism *iii*).

Similar arguments can be made for reactions involving a halide (X) transfer from a metal complex (M^n) (eq 1.9).[7]

$$M^n\text{–}X + Z \longrightarrow M^{n-1} + X\text{–}Z \qquad (1.9)$$

In a halide transfer reaction, one could envision the most plausible reaction mechanisms where (*iv*) an outersphere electron transfer occurs and is followed by the transfer of a formal "X^+" (eq 1.10), (*v*) an X^- ligand transfer occurs from M^n–X to Z and is followed by an electron transfer back to $[M^n]^+$ (eq 1.11) or (*vi*) where a halide atom is transferred in a single kinetic step (eq 1.12).

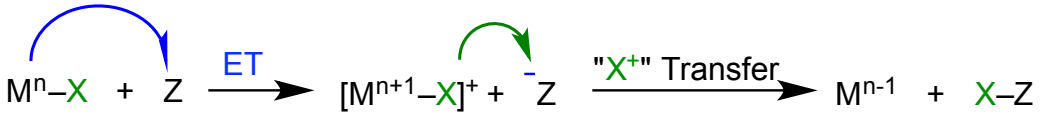

(1.10)

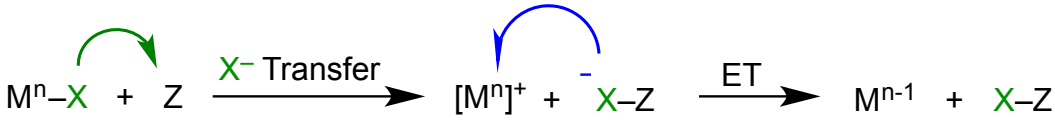

(1.11)

(1.12)

Mechanisms (*iv*) and (*v*) involve charge separated intermediates whereas mechanism (*vi*) bypasses these. In cases where the intermediates expected from mechanism (*iv*) and (*v*) are very high in energy but the overall reaction is exoergic, mechanism (*vi*) is favorable and the halide atom is transferred as a radical in a single kinetic step.[7]

The same mechanistic arguments can be made for group transfer reactions but in many of these systems, a rate determining concerted radical dissociation reaction followed by bond formation is also a possibility (eq 1.13). This can occur if the X–Group bond is very weak.[6e-h,9,13]

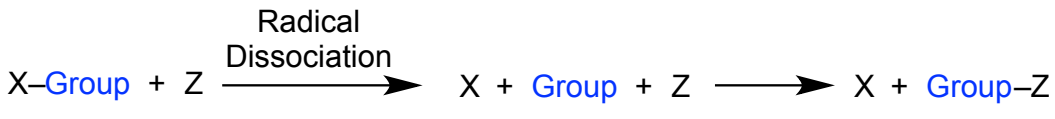

(1.13)

When a reaction is described as a *radical reaction*, a concerted bond cleavage mechanism is implicit. This can be concomitant with the formation of a new bond or simply a dissociative or associative event. These cases will be distinguished explicitly.

1.4. Stable and Persistent Organic Radicals

While most organic radicals are highly reactive and only short lived, some radicals have long lifetimes under the right conditions and in some cases these can even be isolated.[1,14] Ingold has defined[15] the term *persistent radical* to describe any radical that has a sufficiently long lifetime such that it can be handled and studied using conventional spectroscopic techniques. The term *stable radical* is used when it can be purified and isolated as a pure material. These terms have not been universally adopted but for the sake of clarity these definitions will be used here for differentiating between the two cases.

The first description of a persistent organic radical was made in 1900 by Gomberg when he reported the tri-phenyl-methyl radical.[16] In solution this radical was found to reversibly and asymmetrically dimerize forming a bond between the *ispo*-carbon of one radical and the *para*-phenyl carbon of a second radical (eq 1.14). This bond was found to be quite weak with a BDFE of ~17 kcal mol^{-1} at 298 K ($\Delta H°$ = 10.7 kcal mol^{-1}, $\Delta S°$ = 20 eu) so that it was slightly dissociated in dilute solutions.[17]

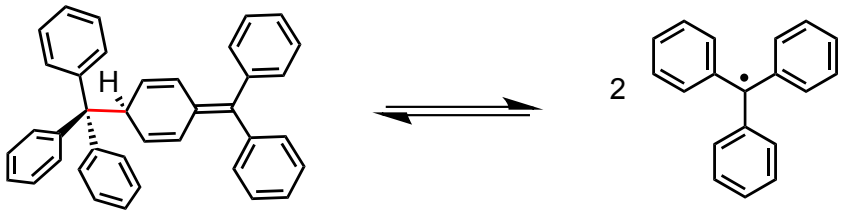

(1.14)

This discovery marked the beginning of free radical chemistry from which a large number of persistent and stable organic and inorganic radicals have been discovered and their properties and reactivities studied. While an exhaustive review is beyond the scope of this introduction, excellent reviews by Hicks[1] and Power[14] are available and expand on the history and breadth of stable and persistent organic and inorganic free radicals, respectively.

In the work described within this thesis, nitroxyl and phenoxyl radicals have been used extensively. These are two types of radicals that have proven extremely useful for a multitude of different functions that are made possible by of their stable nature.

1.4.1 Nitroxyl radicals

Nitroxyl radicals are perhaps the most well recognized and widely used class of stable organic free radicals. Many nitroxyl radicals are stable in the presence of oxygen and moisture making them especially robust as chemical reagents.[1] Several examples include their used as EPR spin labels,[18] as mediators for controlled radical polymerization,[4c] in fundamental CPET (concerted proton electron transfer ≡ HAT here) studies[6c,d] and in aerobic alcohol oxidation catalysis.[19]

The stability of nitroxyl radicals is due to the π-delocalization of the radical over both the nitrogen and oxygen atoms (eq 1.15).[1] This is evident from the room temperature solution EPR spectrum of ^{17}O labeled TEMPO radical which displays strong hyperfine

coupling to both ^{14}N and ^{17}O (a^{14N} = 15.2 G, a^{17O} = 19.0 G in pentane) corresponding to a spin distribution of ~54% on the nitroxyl nitrogen and ~46% on oxygen.[20]

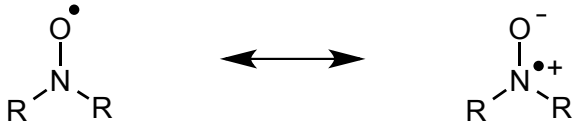

(1.15)

Also contributing to the stability of isolable and persistent nitroxyl radicals of the form $R_2NO^{\bullet}$ is the nature of the R group.[1] When the R group is a tertiary carbon (or in special cases an aryl group)[21] the radical is typically stable or at least persistent. This is not true with nitroxyls with an α-C–H bond. Nitroxyl radicals of this form rapidly disproportionate by transferring a hydrogen atom from the α-C–H position to the oxygen of another radical yielding a hydroxylamine and a nitrone (eq 1.16).

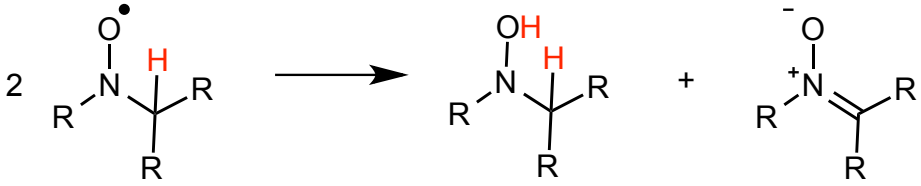

(1.16)

The thermochemistry of nitroxyl radicals has been well studied and their hydrogen atom affinities (hydroxylamine O–H BDFEs) are known in a variety of solvents.[10] These values generally range from 65-68 kcal mol^{-1} in most solvents for the most commonly encountered examples, TEMPO, its 4-substituted derivatives and $^{t}Bu_2NO$ (di-*tert*-butyl nitroxyl radical). These values are quite small making these relatively weak H-atom *acceptors* and their corresponding hydroxylamines relatively strong hydrogen atom *donors*. There are examples of nitroxyls with higher H-atom affinities (i.e. N-hydroxyphthalimide $BDFE_{MeCN}$ = 84.8 kcal mol^{-1})[10,22] but these are not isolable which limits their usefulness in some cases.

In addition to their stability, TEMPO, its 4-substituted derivative and $^{t}Bu_2NO$ are strongly biased thermochemically to react through radical mechanisms. This is especially true for H-atom transfer reactions. Specifically, these nitroxyl radicals are very poor outer sphere oxidants and bases and their corresponding hydroxyalmines are very poor outer-sphere reductants and acids which make stepwise PT or ET mechanisms thermodynamically unfavorable (Figure 1.2).[10]

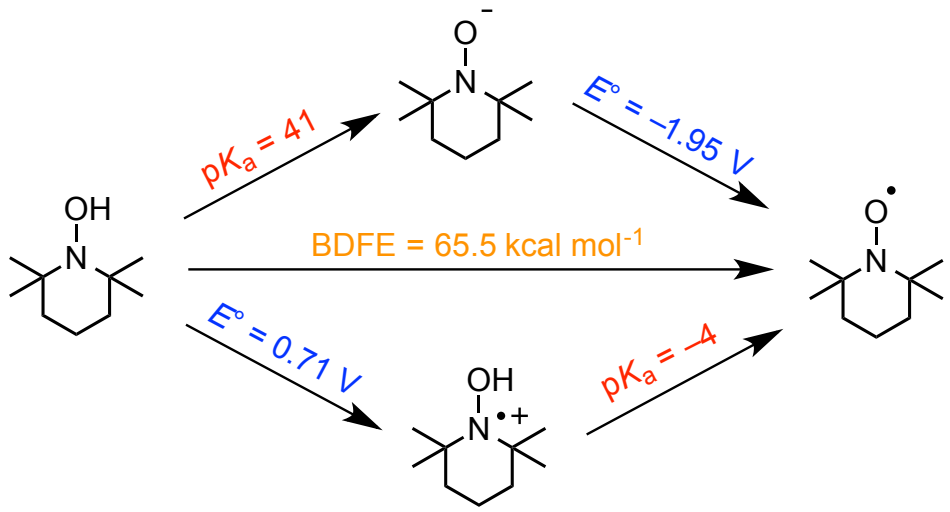

Figure 1.2. Standard reduction potentials (vs. $Fc^{+/0}$) and pK_a values of TEMPO(H) in acetonitrile.[10]

1.4.2. Phenoxyl radicals

Phenoxyl radicals are probably the second most commonly known class of stable or persistent organic free radicals.[23] These have received a great deal of attention because of their relevance to tyrosyl radicals that are commonly encountered in biological electron transfer and enzyme catalysis.[2b,5] They have found a special place in the field of fundamental proton coupled electron transfer (PCET) for which the phenol/phenoxyl transformation is the favored model reaction for many leading research groups.[24] Phenoxyl radical-metal complexes have also been studied quite extensively. In particular, Stack and coworkers have synthesized a library of copper complexes with phenoxide/phenoxyl ligands as functional models for the enzyme galactose oxidase.[25]

Phenoxyl radicals are generally more reactive than nitroxyl radicals and while a large number of persistent phenoxyl radicals have been reported, only a few have been isolated in pure form. The variability in phenoxyl radical stability can be largely rationalized by considering the resonance delocalization of the radical (scheme 1). Solution EPR studies of different ^{13}C and ^{17}O enriched derivatives of 2,4,6-di-*tert*-butyl phenoxyl radical ($^{t}Bu_3ArO^{\bullet}$) at room temperature have shown this resonance delocalization is quite substantial and in fact only ~36% of the total spin is centered on the phenolic oxygen while 4.5%, 12.5%, 5% and 25% is centered at the 1, 2/4, 3/5 and 4

positions of the phenoxyl.[23] As might be predicted, in the absence of substituents at the 2, 4 and 6 positions, radical dimerization occurs rapidly. When bulky substituents such as *tert*-butyl or phenyl are installed at these positions, phenoxyl radical stability is greatly enhanced due to steric protection against dimerization.[23]

Scheme 1. Phenoxyl radical resonance forms

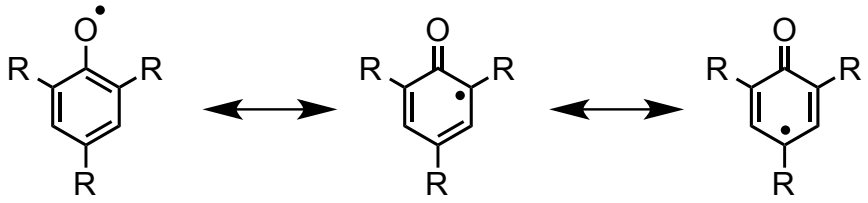

Radical dimerization in phenoxyl radicals is typically irreversible but in special cases it can be reversible. One such case is 2,6-di-*tert*-butyl-4-methoxy-phenoxyl radical (^{t}Bu$_2$-OMe-ArO$^\bullet$) reported by Wittman and Mayer which has an 'intermediately bulky' methoxide substituent at the 4 position.[26] This radical reversibly dimerizes at the 4,4' position with a very weak bond carbon-carbon BDFE of 0 kcal mol^{-1} at 20°C in CCl_4 ($\Delta H° = 6.1 \pm 0.5$ kcal mol^{-1}, $\Delta S° = 21 \pm 1$ eu) (eq 1.17).

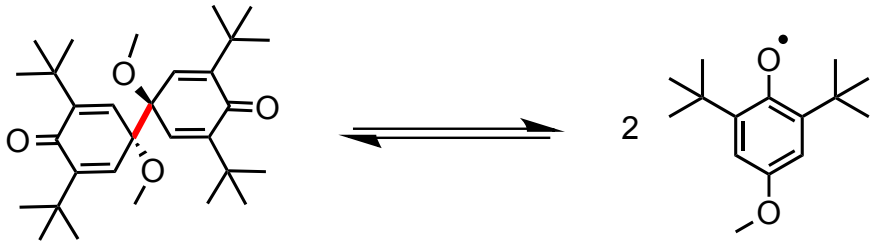

(1.17)

The thermochemistry of phenols/phenoxyls is well established and varies greatly depending on the nature of substituents (i.e. O–H BDFE(4-nitro-phenol) = 93.1 kcal mol^1 and BDFE(2,4,6-tri-*tert*-butyl-phenol) = 80.2 kcal mol^{-1}; both in DMSO).[10] Typically, the relative stability of a phenoxyl radical scales well with its phenolic O–H BDFE so consequently, most isolable radicals have hydrogen affinities that fall on the lower end of this scale. Reported isolable radicals include 2,4,6-tri-*tert*-butyl-phenoxyl (^{t}Bu$_3$ArO$^\bullet$) (O–H BDFE(toluene) = 76.7 kcal mol^{-1}),[9,27] 2,6-di-*tert*-butyl-4-methoxy-phenoxyl (^{t}Bu$_2$-MeO-ArO$^\bullet$) (O–H BDFE(toluene) = 73.8 kcal mol^{-1}),[9,26] and 2,6-di-*tert*-butyl-4-(4'-nitro-phenyl)phenoxyl radical (^{t}Bu$_2$NPArO$^\bullet$) (O–H BDFE(toluene) = 78.5 kcal mol^{-1}).[28] These phenoxyl radicals are stronger hydrogen atom acceptors than the nitroxyl radicals

previously discussed by roughly 10 kcal mol^{-1} and to our knowledge have the highest thermodynamic affinities for H$^{\bullet}$ of any class of isolable organic radical.

Like the nitroxyl radicals previously mentioned, phenoxyl radicals are biased thermochemically for HAT chemistry albeit to a slightly lesser extent. The stable phenoxyl radicals mentioned are all poor bases and poor outer-sphere oxidants and their corresponding phenols are weak acids and poor outer-sphere reductants (Figure 1.3).[10]

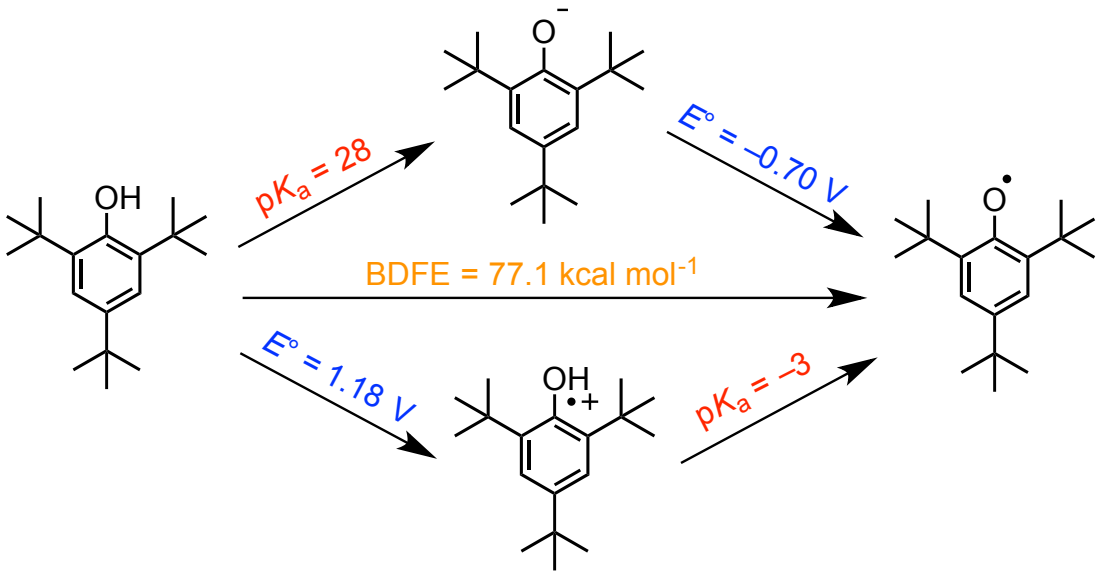

Figure 1.3. Standard reduction potentials (vs. $Fc^{+/0}$) and pK_a values of $^{t}Bu_3ArO(H)$ in acetonitrile.[10]

1.5. Reactivity of Organic Radicals with Transition Metals

Due to their propensity to react through one-electron processes, redox active transition metal (TM) complexes often have reactivities that parallel the reactivities of organic radicals. The term metalloradical has been used to explicitly describe coordinatively unsaturated metals that are strongly reducing or oxidizing.[29] These complexes are often quite reactive and have been used extensively as reagents in organic synthesis.[30,4]

Probably the first well recognized TM-radical reaction was described nearly 150 years ago by Fenton who discovered that aqueous ferrous sulfate reacts with hydrogen peroxide to generate ferric hydroxide and the highly reactive hydroxyl radical (HO–H BDFE = 122.7 kcal mol^{-1} in water) (eq 1.18).[31,10] This reaction (now known as the Fenton

reaction) is an excellent example of the synergistic capabilities of pairing radicals with transition metals and is still relevant today.[32]

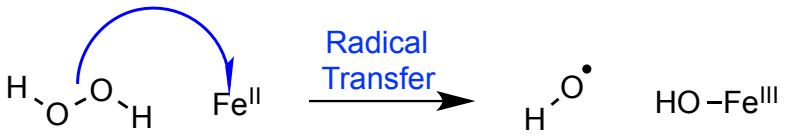

(1.18)

Since the discovery of Fenton chemistry, the field of TM-radical chemistry has grown immeasurably. Pioneered by Kochi,[2a] the use of TM-radical reactivity in organic chemistry has lead to huge advances in the field and is still a highly active area of research for practical synthetic usage. Likewise, critical TM-radical reactions are also now widely recognized and studied in biological systems.[2b,5] Several particularly important and relevant examples will be expanded upon here.

1.6. Important Examples of Transition Metal-Radical Reactivity

Traditional radical polymerization reactions rely on simple radical initiators such as AIBN (azobisisobutyronitrile) or alkyl peroxides to initiate a radical chain reaction with olefin monomers.[4c] In these reactions, the concentration of free radical present at any time is highly variable and difficult to control. Using this polymerization technique often results in poor chain length distributions and self-termination from radical-radical coupling. The introduction of transition metals to radical polymerization through atom transfer radical polymerization (ATRP) helped to improve this process.

ATRP is a good example of a process that harnesses the cooperative nature of transition metals and radicals.[4] ATRP utilizes a transition metal complex (typically containing copper(I)) to reversibly abstract a halide atom from the terminal monomer of a polymer. This generates an organic radical that can propagate with monomers in solution. The feature that makes ATRP so effective is that equilibrium for halide atom abstraction from the polymer by the transition metal complex can be tuned to lie far on the side of the deactivated form with only a small amount of organic radical present at any given time. Because the steady state concentration of free radical in solution is highly controlled by a transition metal and very low, the polymer radicals do not self-terminate and grow with much higher monodispersity (Scheme 2). This equilibrium is highly dependent on the

difference between the bond strength of the alkyl–halide bond being broken and the bond strength of the transition metal-halide bond being formed, which dictate the equilibrium constant for these reactions.[6a,b]

Scheme 2. ATRP Mechanism (adapted from ref. 4b).

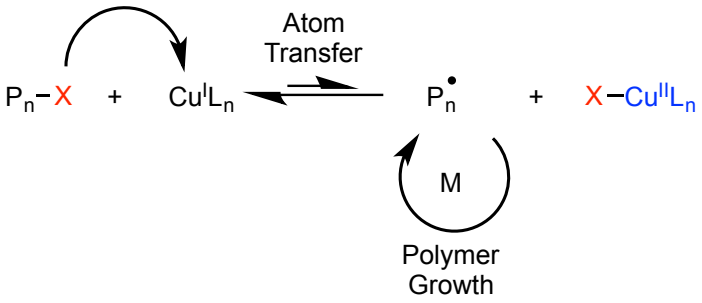

In biology, Cytochrome P450 is a quintessential example of a class of enzymes that relies on radical reactivity to carry out difficult chemical transformations.[33] These enzymes are capable of hydroxylating strong C–H bonds using O_2 as a terminal oxidant and are responsible for metabolizing roughly 75% of all commercially available pharmaceuticals.[33] The mechanism by which these enzymes activate strong C–H bonds has been extensively studied and is known as the rebound mechanism.[34] In the rebound mechanism, a hydrogen atom ($H^{\bullet}$) is abstracted from the substrate (H–R) by an iron(IV)-oxo-ligand radical cation moiety in the active site of the enzyme to generate a transiently lived iron(IV)-hydroxo and a carbon centered radical ($^{\bullet}R$). Radical recombination with $^{\bullet}R$ results in hydroxylation of the organic compound and a return to the ferric resting state (Scheme 3).

Scheme 3. Rebound Mechanism of Cytochrome P450s

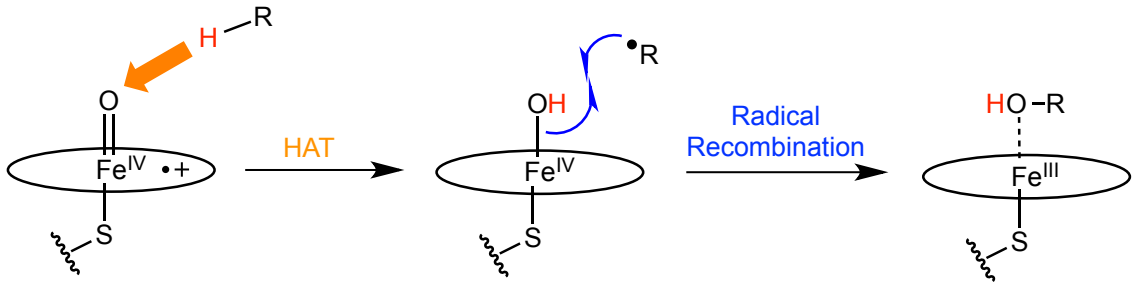

The ability of cytochrome P450 to abstract a hydrogen atom from a strong C–H bond has been attributed to the high basicity of the iron(IV)-oxo intermediate (pK_a of iron(IV)–OH in water is roughly equal to 12)[35] that arises due to the axial cysteinate ligand bound *trans* to the metal-oxo/hydroxo ligand. The high basicity contributes to the overall strength of the O–H bond formed in iron(IV)-hydroxo and provides the driving force necessary for cleaving strong C–H bond. The structurally similar enzyme, myoglobin, contains an axial histidine residue and has a substantially less basic iron(IV)-oxo intermediate with a pK_a of the corresponding hydroxo of $\leq$ 2.7.[36] Myoglobin is not capable of carrying out C–H activations like cytochrome P450 and it has been suggested that this is because of the difference in basicity which affects the overall O–H bonds strengths of the different iron(IV)-O–H complexes.[36]

In both ATRP and in cytochrome P450, the cooperativity between transition metals and organic radicals is of paramount importance for the success of these systems. While these examples serve to highlight just two examples, this motif is critical for a huge number of processes and continuing to develop a fundamental understanding of these types of interactions will be important for designing and predicting new potentially powerful radical reactions.

1.7. Conclusions

Due to the prevalence of radical-transition metal chemistry throughout chemistry and biology, there is a fundamental interest in better understanding these types of reactions to fully realize their potentials (and limitations) for new and existing applications. The Mayer group and others have studied fundamental hydrogen atom transfer reactions (or equivalently CPET) involving organic and inorganic systems. These processes are now generally well understood and a predictive model has been developed.[6c,d] Radical transfer reactions involving other radicals have also been studied but have received less attention from a fundamental standpoint. This is especially true for reactions involving stable radicals and metals that are not traditionally thought of as ‘metalloradicals.’ Developing a better understanding of these reactions and how their thermochemistry and reactivity are related would be valuable as the field of TM-radical chemistry continues to develop.

The work presented in this thesis describes the free radical reactivity and thermochemistry of several different systems involving early, middle and late first row transition metal complexes as well as a brief introduction to radical reactions with colloidal titanium dioxide nanoparticles. The objective of these studies was to add to the fundamental understanding of transition metal-radical chemistry by studying stoichiometric reactions with stable and thermochemically well-defined organic radical reagents. The results of these studies are described and discussed.

Notes for Chapter 1

---

(1) Hicks, R. G. *Org. Biomol. Chem.* **2007**, 5, 1321.

(2) (a) Kochi, J. K. *Free Radicals*; Wiley: New York, 1973. (b) Halliwell, B.; Gutteridge, J. M. C. *Free Radicals in Biology and Medicine*; Oxford University Press: Oxford, U.K., 2007.

(3) Kharasch, M. S.; Mayo, F. R. *J. Am. Chem. Soc.* **1933**, 55, 2468.

(4) (a) Matyjaszewski, K. *Macromolecules*, **2012**, 45, 4015. (b) Matyjaszewski, K.; Xia, J. *Chem. Rev.* **2001**, 101, 2921. (c) Matyjaszewski, K.; Davis, T. P. *Handbook of Radical Polymerization*; Wiley: New York, 2002.

(5) (a) Styring, S.; Sjöholm, J.; Mamedor, F. *Biochim. Biophys. Acta* **2012**, 1817, 76. (b) Reece, S. Y.; Nocera, D. G. *Ann. Rev. Biochem.* **2009**, 78, 673. (c) McEvoy, J. P.; Brudvig, G. W. *Chem. Rev.* **2006**, 106, 4455. (d) Whittaker, J. W. *Chem. Rev.* **2003**, 103, 2347.

(6) (a) Lin, C. Y.; Coote, M. L.; Gennaro, A.; Matyjaszewski, K. *J. Am. Chem. Soc.* **2008**, 130, 12762. (b) Lin, C. Y.; Marque, S. R. A.; Matyjaszewski, K.; Coote, M. L. *Macromolecules*, **2011**, 44, 7568. (c) Mayer, J. M. *Ann. Rev. Phys. Chem.* **2004**, 55, 363. (d) Mayer, J. M. *J. Phys. Chem. Lett.* **2011**, 2, 1481. (e) Marque, S.; Mercier, C. L.; Tordo, P.; Fischer, H. *Macromolecules*, **2000**, 33, 4403. (f) Moad, G.; Rizzardo, E. *Macromolecules*, **1995**, 28, 8727. (g) Hodgson, J. L.; Lin, C. Y.; Coote, M. L.; Marque, S. R. A.; Matyjaszewski, K. *Macromolecules*, **2010**, 43, 3728. (h) Skene, W. G.; Belt, S. T.; Connolly, T. J.; Hahn, P.; Scaiano, J. C. *Macromolecules*, **1998**, 31, 9103.

(7) Zhang, N.; Samanta, S. R.; Rosen, B. M.; Percec, V. *Chem. Rev.* **2014**, 114, 5848.

(8) (a) Mader, E. A.; Davidson, E. R.; Mayer J. M. *J. Am. Chem. Soc.* **2007**, 129, 5153. (b) Mader, E. A.; Manner, V. W.; Markle, T. F.; Wu, A.; Franz, J. A.; Mayer, J. M. *J. Am. Chem. Soc.* **2009**, 131, 4335.

(9) Chan, K. S.; Li, X. Z.; Dzik, W. I.; de Bruin, B. *J. Am. Chem. Soc.* **2008**, 130, 2051.

(10) Warren, J. J.; Tronic, T. T.; Mayer, J. M. *Chem. Rev.* **2010**, 110, 6961.

(11) Luo, Y.-R. *Comprehensive Handbook of Chemical Bond Energies*; CRC Press: Boca Raton, Fl, 2007.

(12) Warren, J. J.; Mayer, J. M. *Proc. Natl. Acad. Sci.* **2010**, 107, 5282.

(13) (a) Huang, K. –W.; Waymouth, R. M. *J. Am. Chem. Soc.* **2002**, 124, 8200. (b) Mahanthappa, M. K.; Huang, K.–W.; Cole, A. P.; Waymouth, R. M. *Chem. Commun.* **2002**, 502. (c) Huang, K. –W.; Han, J. H.; Cole, A. P.; Musgrove, C. B.; Waymouth, R. M. *J. Am. Chem. Soc.* **2005**, 127, 3807. (d) Smith, J. M.; Mayberry, D. E.; Margarit, C. G.; Sutter, J.; Wang, H.; Meyer, K.; Bontchev, R. P. *J. Am. Chem. Soc.* **2012**, 134, 6516.

(14) Power, P. P. *Chem. Rev.* **2003**, 103, 789.

(15) Griller, D.; Ingold, K. W. *Acc. Chem. Res.* **1976**, 9, 13.

(16) Gomberg, M. *J. Am. Chem. Soc.* **1900**, 22, 757.

(17) Neumann, W. P.; Uzick, W.; Zarkadis, A. K. *J. Am. Chem. Soc.* **1986**, 108, 3762.

(18) Berliner, L. J. *Spin Labelling: Theory and Applications*; Academic Press: New York, 1979.

(19) For example: (a) Semmelhack, M. F.; Schmid, C. R.; Cortés, D. A.; Chou, C. S. *J. Am. Chem. Soc.* **1984**, 106, 3374. (b) Gamez, P.; Arends, I. W. C. E; Sheldton, R. A.; Reedijk, J. *Adv. Synth. Catal.* **2004**, 346, 805. (c) Kumpulainen, E. T. T.; Koskinen, A. M. P. *Chem. Eur. J.* **2009**, 15, 10901. (d) Hoover, J. M.; Stahl. S. S. *J. Am. Chem. Soc.* **2011**, 133, 16901. (e) Hoover, J. M.; Ryland, B. L.; Stahl, S. S. *J. Am. Chem. Soc.* **2013**, 135, 2357. (f) Ryland, B. L.; McCann, S. D.; Brunold, T. C.; Stahl, S. S. *J. Am. Chem. Soc.* **2014**, 136, 12166.

(20) Aurich, H. G.; Hahn, K.; Stork, K.; Weiss, W. *Tetrahedron*, **1977**, 33, 969.

(21) Osanai, K.; Okazawa, A.; Nogami, T.; Ishida, Y. *J. Am. Chem. Soc.* **2006**, 128, 14008.

(22) Recupo, F.; Punta, C. *Chem. Rev.* **2007**, 107, 3800.

(23) Altwicker, E. R. *Chem. Rev.* **1967**, 475.

(24) For example: (a) Schrauben, J. N.; Cattaneo, M.; Day, T. C.; Tenderholt, A. L.; Mayer, J. M. *J. Am. Chem. Soc.* **2012**, 134, 16635. (b) Markle, T. F.; Rhile, I. J.; Mayer, J. M. *J. Am. Chem. Soc.* **2011**, 133, 17341. (c) Markle, T. F.; Mayer, J. M. *Angew. Chem. Int. Ed. Engl.* **2008**, 47, 738. (d) Rhile, I, J.; Markle, T. F.; Nagao, H.; DiPasquale, A. G.; Lam, O. P.; Lockwood, M. A.; Rotter, K.; Mayer, J. M. *J. Am. Chem. Soc.* **2006**, 128, 6075. (e) Rhile, I. J.; Mayer, J. M. *J. Am. Chem. Soc.* **2004**,

126, 12718. (f) Huynh, M. H. V.; Meyer, T. J. *Chem. Rev.* **2007**, 107, 5004. (g) Costentin, C.; Robert, M.; Savéant, J.–M. *Acc. Chem. Res.* **2010**, 43, 1019. (h) Irebo, T.; Zhang, M.; Markle, T. F.; Scott, A.; Hammarström, L. *J. Am. Chem. Soc.* **2012**, 134, 16247. (i) Zhang, M.; Irebo, T.; Johansson, O.; Hammarström, L. *J. Am. Chem. Soc.* **2011**, 133, 13224. (j) Irebo, T.; Reece, S.; Sjödin, M.; Nocera, D.; Hammarström, L. *J. Am. Chem. Soc.* **2007**, 129, 15462. (k) Sjödin, M.; Irebo, T.; Utas, J.; Lind, I.; Mereny, G.; Åkermark, B.; Hammarström, L. *J. Am. Chem. Soc.* **2006**, 128, 13076. (k) Wenger, O. *Coord. Chem. Rev.* **2014**, ASAP.

(25) Lyons, C. T.; Stack, T. D. P. *Coord. Chem. Rev.* **2013**, 257, 528.

(26) Wittman, J. M.; Hayoun, R.; Kaminsky, W.; Coggins, M. K.; Mayer, J. M. *J. Am. Chem. Soc.* **2013**, 135, 12956.

(27) Manner, V. W.; Markle, T. F.; Freudenthal, J. H.; Roth, J. P.; Mayer, J. M. *Chem. Commun.* **2008**, 256.

(28) Porter, T. R.; Kaminsky, W.; Mayer, J. M. *J. Org. Chem.* Accepted.

(29) (a) Baird, M. C. *Chem. Rev.* **1988**, 88, 1217. (b) Hoff, C. D. *Coord. Chem. Rev.* **2000**, 206, 451.

(30) For example: (a) Ryn, I. *Chem. Soc. Rev.* **2001**, 30, 16. (b) Kobayashi, T.; Ohmiya, H.; Yorimitsu, H.; Oshima, K. *J. Am. Chem. Soc.* **2008**, 130, 11276. (c) Cui, X.; Xu, X.; Lin, H.; Zhu, S.; Wojtas, L.; Zhang X. P. *J. Am. Chem. Soc.* **2011**, 133, 3304. (d) Munabe, T.; Yanagi, S. –i.; Kouichi, O.; Uemura, S. *Organometallics*, **1998**, 17, 2942.

(31) (a) Fenton, H. J. H. *Chem. News* **1876**, 190. (b) Wardman, P.; Candeias, L. P. *Radiat. Res.* **1996**, 145, 523.

(32) Neyens, E.; Baeyens, J. *J. Haz. Mat.* **2003**, 98, 33.

(33) Ortiz de Montellano, P. R. *Cytochrome P450: Structure, Mechanism and Biochemistry*; Springer: New York, 2004.

(34) Groves, J. T.; McClusky, G. A. *J. Am. Chem. Soc.* **1976**, 98, 859.

(35) Yoska, T. H.; Rittle, J.; Krest, C. M.; Onderko, E. L.; Silakov, A.; Calixto, J. C.; Behan, R. K.; Green, M. T. *Science*, **2013**, 342, 825.

(36) Yoska, T. H.; Behan, R. K.; Krest, C. M.; Onderko, E. L.; Langstron, M. C.; Green, M. T. *J. Am. Chem. Soc.* **2014**, 136, 9124

Chapter 2:
Radical Reactivity of the Fe(III)/(II) Tetramesitylporphyrin Couple: Hydrogen Atom Transfer, Oxyl Dissociation, and Catalytic Disproportionation of a Hydroxylamine[1]

2.1 Introduction

Heme proteins are ubiquitous and have a wide range of functions. In recent years, cytochromes P450 and peroxidases have been a focus of research because of their ability to accomplish difficult oxidative reactions by using high-valent ferryl intermediates (compounds I and II).[2] Other heme enzymes, however, accomplish inner-sphere oxidations and reductions using just the $Fe^{III/II}$ couple.[3] One example is the autotrophic bacterial multi-heme enzyme hydroxylamine oxidoreductase (HAO),[4] which catalyses the oxidation of hydroxylamine to nitrite using just ferric and ferrous oxidation states.[5] These low-valent odd-electron transformations tend to be underappreciated relative to their high-valent counterparts.

In many cases, the interconversion between heme oxidation states is coupled to proton transfer. Examples range from proton-pumping in cytochrome c oxidase[6] to aliphatic hydroxylations by cytochromes P450.[2] Reactions involving the transfer of e^- and H^+ ($\equiv H^\bullet$) are broadly referred to as proton-coupled electron transfer (PCET) processes, and are ubiquitous in chemistry as well as in biochemistry.[7] The hydroxylamine-to-nitrite process mentioned above is one example. The transfer of one proton and one electron in a single kinetic step is hydrogen atom transfer (HAT), or more generally concerted proton-electron transfer (CPET).[8] Some enzymes and other catalysts utilize CPET to avoid high energy intermediates, but a variety of pathways are possible for PCET reactions.[9] While PCET and CPET are frequently invoked pathways for high-valent heme reactions, low-valent heme reactions of this type have received substantially less attention.

Herein we describe inner sphere redox chemistry of the ferric hydroxide and ferrous states of *meso*-tetramesitylporphyrinato ligated model complexes. Namely, we address three related topics: PCET reactivity, oxyl radical binding to Fe^{II}, and catalytic disproportionation of the hydroxylamine TEMPO–H. Each is presented and discussed in turn below.

meso-Tetramesitylporphyrinato-iron(III) hydroxide, (TMP)Fe^{III}(OH), and related porphyrin complexes have been extensively used as models for heme enzymes by Groves,[10] Balch[11], LaMar,[11b,c] Valentine,[12] Nam[13] and others. An advantage of this porphyrin ligand is that the steric bulk of the mesityl substituents prevents the formation of μ-oxo dimers, so the ferric hydroxide is readily prepared.[11b] We first observed that (TMP)Fe^{III}(OH) is readily reduced by the hydroxylamine TEMPO–H (2,2,6,6,-tetramethylpiperidin-1-ol) to give the ferrous derivative (TMP)Fe^{II}, when the reactions are performed and monitored at low concentrations. However, the same reaction gives a different product when performed at higher concentrations, because the TEMPO (2,2,6,6-tetramethylpiperdinyl) product reversibly binds to the ferrous heme to form (TMP)Fe^{III}(TEMPO). Reactions with excess TEMPO–H gave yet another set of products, as the iron complexes catalyse the redox disproportionation of TEMPO–H. These results highlight the rich and perhaps underappreciated free-radical chemistry of low-valent heme compounds.

2.2. Results

2.2.1. (TMP)Fe^{III}(OH) as a Net Hydrogen Atom Abstractor

The addition of one equivalent of TEMPO–H to a dark green solution of (TMP)Fe^{III}(OH) (80 μM in toluene) forms a bright red solution over approximately 45 minutes. The UV-visible absorption spectrum of the reaction product displayed a Soret band at 418 nm and Q bands at 445 and 538 nm, in good agreement with the spectrum of the known[11c] 4-coordinate ferrous porphyrin (TMP)Fe^{II} and with an independently prepared sample (Table 2.1).[14] These data indicate a net hydrogen atom transfer from TEMPO–H to (TMP)Fe^{III}(OH), as shown in eq 2.1.

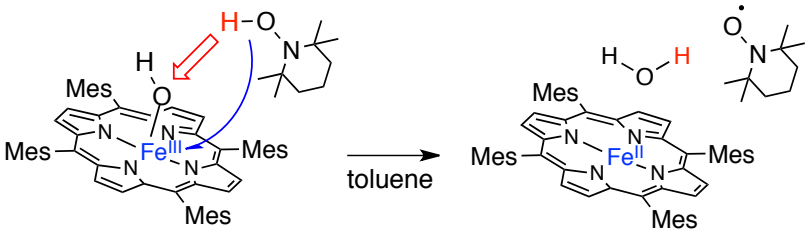

(TMP)Fe^{III}(OH) + TEMPO–H **(TMP)Fe^{II} + H_2O + TEMPO** (2.1)

Reaction 2.1 was monitored by stopped-flow spectrophotometry under *pseudo*-first order conditions ([TEMPO–H] = 3.6-14.4 mM) (Figure 2.1). The kinetics are first order in both (TMP)Fe^{III}(OH) and TEMPO–H, with $k_{2.1}$ = 76 ± 5 M^{-1} s^{-1} at 25° C ($\Delta G^{\ddagger}_{2.1}$(25° C) = 15.0 ± 0.1 kcal mol^{-1}).

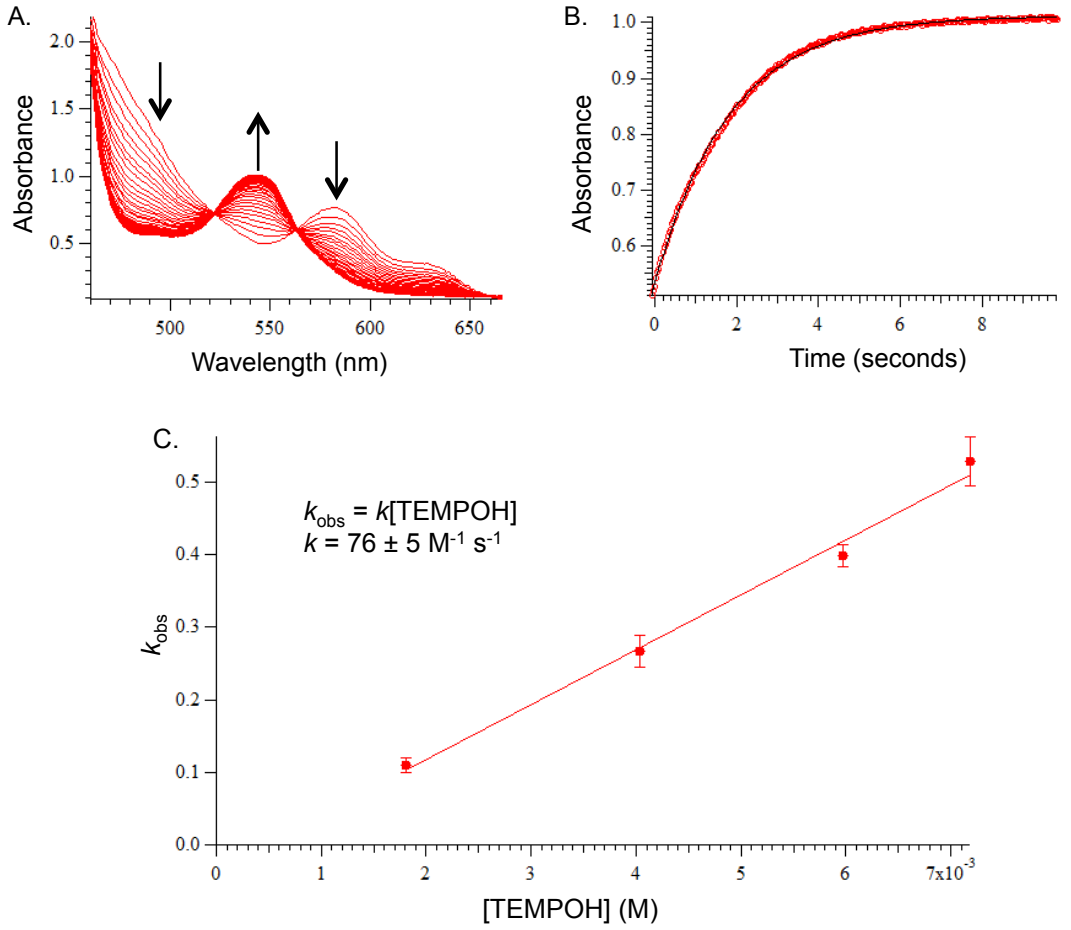

Figure 2.1. A. Spectra of the reaction between 80μM (TMP)Fe^{III}(OH) and 4.0 mM TEMPOH *vs.* time in toluene. **B.** Kinetic trace of same the reaction at 525 nm (red markers) and fit (black line). **C.** Pseudo-first order plot of k_{obs} *vs.* [TEMPOH].

Table 2.1. Spectroscopic features of (TMP)Fe species in toluene.[a]

Compound	^{1}H NMR chemical shifts				Q_1 abs.
	m-H	*o*-CH_3	*p*-CH_3	β-pyr	λ_{max} (ε)
(TMP)Fe^{II}	11.72	5.62	6.04	2.86	538 (11.6)
(TEMP)Fe^{II} at –80 °C[10c]	14.70	7.79	8.39	–1.44	—
(TMP)Fe^{III}(TEMPO)	11.06	n.o.	3.26	81.0	—
(TMP)Fe^{III}(TEMPO) at –80 °C	14.24,13.19	n.o.	3.96	124	565 (8.7)
(TMP)Fe^{III}(^{t}Bu$_3$ArO)	13.76, 12.67	5.35	3.30	89.50	—
(TMP)Fe^{III}(OH)	12.14, 11.18	n.o.	3.29	81.5	580 (7.5)[15]

[a] Values at 25 °C unless otherwise noted. NMR spectra in toluene-d_8, with chemical shifts in ppm; n.o. = not observed. Optical spectra: λ_{max} in nm, ε in cm^{-1} M^{-1} × 10^{-3}.

The reactivity of (TMP)Fe^{III}(OH) with other potential hydrogen atom donors has been examined in toluene-d_8 at 4.0 mM concentrations. TEMPO–H is a strong H-atom donor because its O–H bond dissociation free energy (BDFE) is only 65.2 kcal mol^{-1}.[9] The first N–H bond in 1,2-diphenylhydrazine is similar, BDFE = 64.3 ± 1.5 kcal mol^{-1}.[9] Adding 0.5 equivalents (1 $H^{\bullet}$ equivalent) PhNHNHPh to (TMP)Fe^{III}(OH) resulted in a color change from dark green to deep red and ^{1}H NMR spectroscopy showed (TMP)Fe^{II} and PhN=NPh had been generated (eq 2.2). The same reaction was carried out at a lower concentrations (80 μM (TMP)Fe^{III}(OH), 40 μM PhNHNHPh) in toluene and monitored optically. Over approximately 8 hours, the characteristic absorption features of (TMP)Fe^{III}(OH) were replaced with those of (TMP)Fe^{II}. The weaker H-atom donor $PhNHNH_2$ (BDFE = 67.5 ± 1.5 kcal mol^{-1})[9] also reacted with (TMP)Fe^{III}(OH) but only slowly, requiring approximately 24 hours at RT for 4.0 mM (TMP)Fe^{III}(OH) plus 2.0 mM $PhNHNH_2$ (eq 2.3). 2,4,6-Tri-*tert*-butyl phenol, with a significantly stronger O–H bond (BDFE = 76.6 kcal mol^{-1})[9] did not react with (TMP)Fe^{III}(OH) over 24 hours.

$$(TMP)Fe^{III}(OH) + ½\ PhNHNHPh \rightarrow (TMP)Fe^{II} + ½\ PhN{=}NPh + H_2O \qquad (2.2)$$

$$(TMP)Fe^{III}(OH) + ½\ PhNHNH_2 \rightarrow (TMP)Fe^{II} + ½\ [PhN{=}NH]^{16} + H_2O \qquad (2.3)$$

Surprisingly, the reaction between (TMP)Fe^{III}(OH) and TEMPO–H at higher concentrations, 4.0 mM of each reagent, proceeds to a different set of products. Under these conditions, reaction solutions rapidly turn dark brown, rather than the red solution described above for 80 μM solutions. ^{1}H NMR spectra of this reaction mixture showed the complete consumption of TEMPO–H but some (TMP)Fe^{III}(OH) remained. Peaks were also observed for new organic and Fe^{III} products, which were later assigned to 2,2,6,6-tetramethyl piperidine, TEMP–H, and a (TMP)Fe^{III}-TEMPO complex, as described in the next sections.

2.2.2. Reactions of (TMP)Fe^{II} with Oxyl Radicals

2.2.2.1. Reaction of (TMP)Fe^{II} and TEMPO

Addition of one equivalent of the stable oxyl radical TEMPO to a 80 μM toluene solution of (TMP)Fe^{II} at room temperature showed very little change by UV/Vis absorption spectroscopy. In contrast, carrying out the same reaction at fifty times higher concentrations (4.0 mM in toluene-d_8) showed an instantaneous and dramatic color change from deep red to dark green. The ^{1}H NMR spectrum of this reaction mixture showed the complete disappearance of (TMP)Fe^{II} and the appearance of a new species with a broad downfield resonance characteristic of the β-pyrrolic signal of a high-spin (TMP)Fe^{III}X species.[11a] Typically, such C_{4v}–symmetric (TMP)Fe^{III}X complexes have inequivalent *meta*-aryl protons that are resolvable by ^{1}H NMR spectroscopy, due to hindered rotation about the porphyrin-mesityl bond.[11a] However, in this case only a single peak was observed, indicating a high-spin [(TMP)Fe^{III}]$^+$ complex with effective D_{4h} symmetry on the NMR timescale.

^{1}H NMR spectra of similar reactions with 0.5 or 2 equivalents of TEMPO were surprising because in both cases no (TMP)Fe^{II} was identifiable in solution and each reaction appeared to have cleanly generated a different D_{4h}–symmetric [(TMP)Fe^{III}]$^+$ complex. These results suggested an equilibrium reaction in which (TMP)Fe^{II} and TEMPO are in rapid equilibrium with a C_{4v} symmetric adduct, (TMP)Fe^{III}(TEMPO) (eq 2.4). In the rapid exchange limit, the observed chemical shifts are the weighted average of all the species present, so different shifts are observed with different reagent ratios.[17]

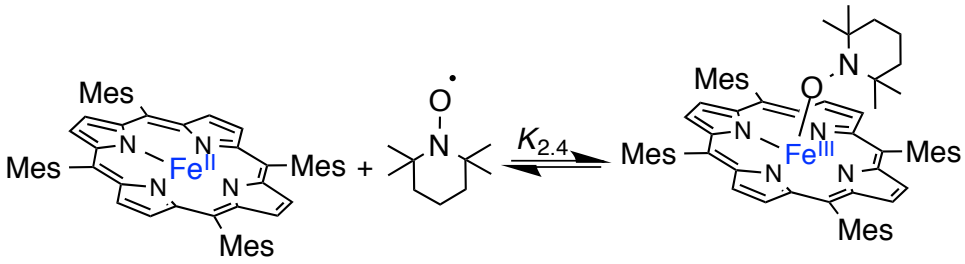

(2.4)

This interpretation was confirmed by ^{1}H NMR spectra of (TMP)Fe^{II} plus sub-stoichiometric TEMPO at –80° C, which displayed distinguishable resonances for (TMP)Fe^{II} and the C_{4v}–symmetric (TMP)Fe^{III}(TEMPO) (Figure 2.2). Thus at ambient temperatures, TEMPO must be rapidly dissociating from (TMP)Fe^{III}(TEMPO) and re-binding to (TMP)Fe^{II}, a process that would give the apparent D_{4h} symmetry observed. The coalescence temperature of ~235 K and the chemical shift difference of ~500 Hz, provide estimates of the dissociation rate constant of $k_{-2.4}$(235 K) = 1100 ± 200 s^{-1} and a barrier $\Delta G^{\ddagger}_{-2.4}$(235 K) = 16.9 ± 0.5 kcal mol^{-1}.

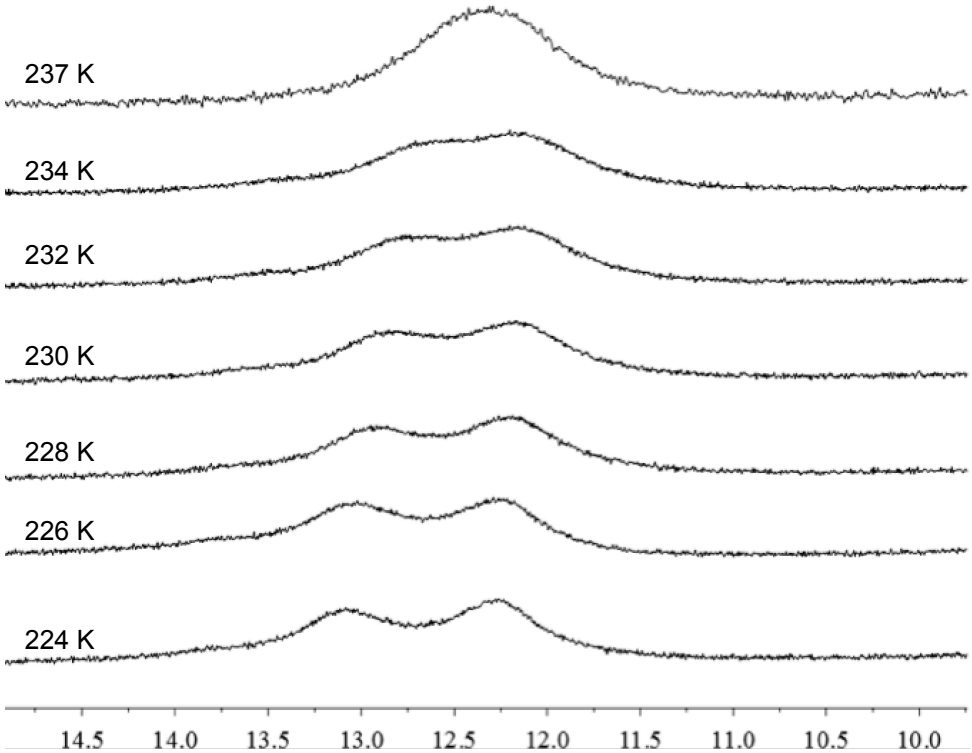

Figure 2.2. Stacked variable temperature ^{1}H NMR spectra of a toluene-d_8 solution containing 4.0 mM (TMP)Fe^{II} and 4.0 mM TEMPO.

An oximato-iron(III) adduct, R=N-O-Fe^{III}(TMP), closely related to (TMP)Fe^{III}(TEMPO), has been similarly prepared from the fluorenone oxime and (TMP)Fe^{III}OH (eq 2.5).[10j] While this product is stable, and was structurally characterized, slow dissociation of the fluorenyl oxyimyl radical was indicated and radical formation was facilitated by the addition of CO.

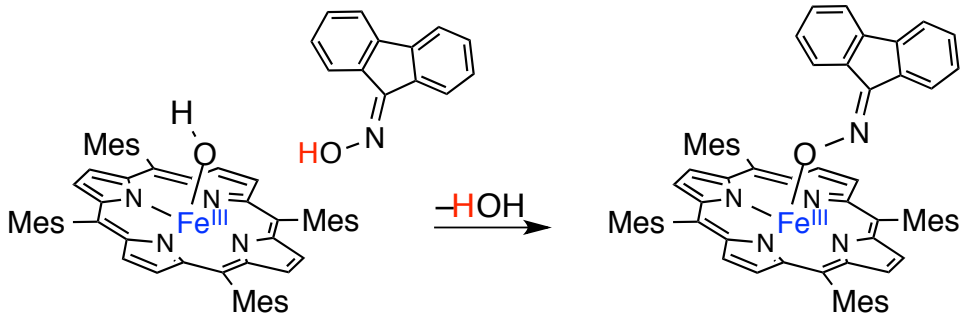

(2.5)

To study the TEMPO dissociation equilibrium (eq 2.4), multiple 4.0 mM samples of (TMP)Fe^{II} in toluene-d_8 were prepared with various concentration of TEMPO. Their ^{1}H NMR spectra at 25 °C showed peaks with positions that changed as a function of TEMPO concentration (Figure 2.3).

Plotting the porphyrin chemical shifts vs. [TEMPO] showed smooth curves that were extrapolated to high [TEMPO] to give the chemical shifts of pure (TMP)Fe^{III}(TEMPO) (Figure 2.4). Reasonable estimates of these chemical shifts could be made for *m*-H, *p*-CH_3, and β-pyrrolic peaks (Table 2.1) but was not possible for the *o*-CH_3 peak because significant broadening of this signal was observed even at low concentrations of TEMPO. Taking the observed chemical shifts of each sample as the weighted average of the shifts of (TMP)Fe^{III}(TEMPO) and (TMP)Fe^{II} in solution and assuming mass balance, a plot of the [(TMP)Fe^{III}(TEMPO)]/[(TMP)Fe^{II}] ratio vs. the concentration of free TEMPO in solution gives the equilibrium constant. $K_{2.4}$ was calculated using the β-pyrrolic, *m*-aryl, and *p*-CH_3 resonances to give a value of 520 ± 25 M^{-1} (Figure 2.5).

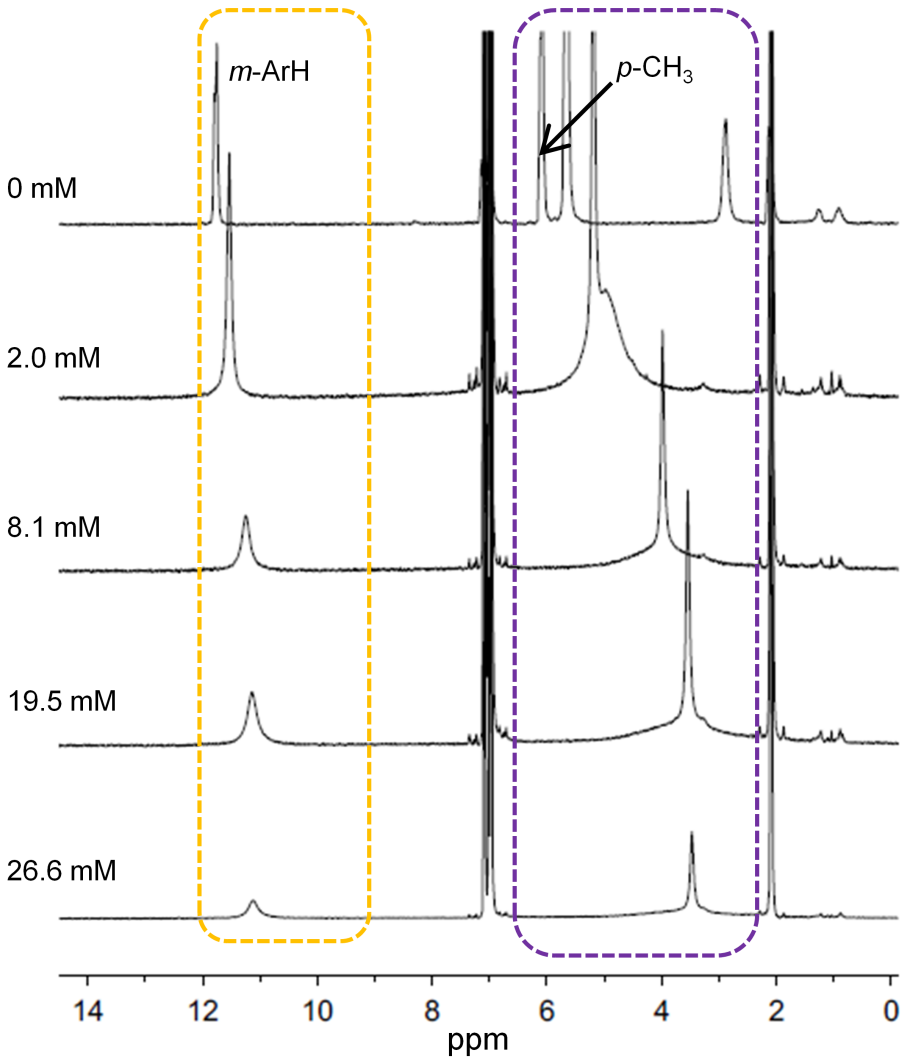

Figure 2.3. ^{1}H NMR spectra of 4.0 mM (TMP)Fe^{II} with 0 to 26.6 mM of TEMPO in toluene-d_8 on a 500 MHz spectrometer at 25 °C. The dotted box at left shows the shift of the *meta*-aryl protons, and the box at the right shows the shift of the *p*-CH3 groups, indicating the equilibrium formation of (TMP)Fe^{III}(TEMPO). The broad, downfield β-pyrrolic peaks are not shown.

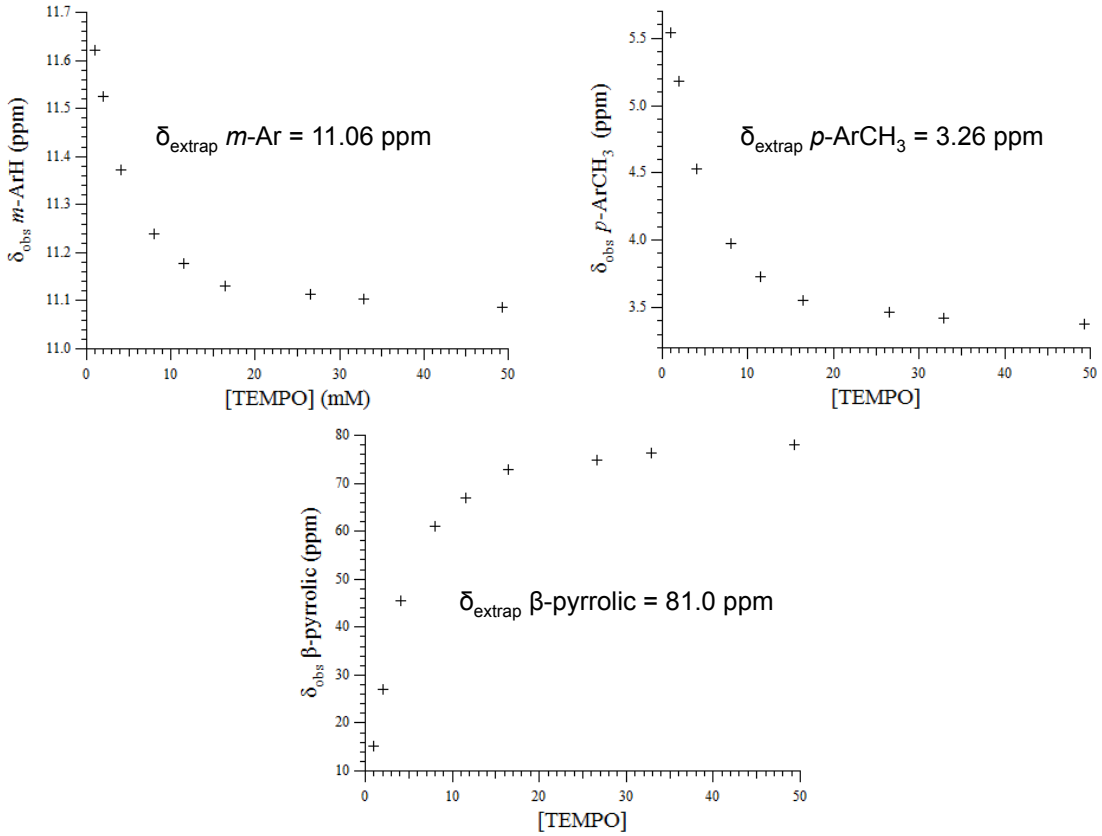

Figure 2.4. Plots of the observed chemical shift of (TMP)Fe^{II} /(TMP)Fe^{III}(TEMPO) vs. concentration of TEMPO. Values of "pure" (TMP)Fe^{III}(TEMPO) are determined by extrapolating to infinite [TEMPO].

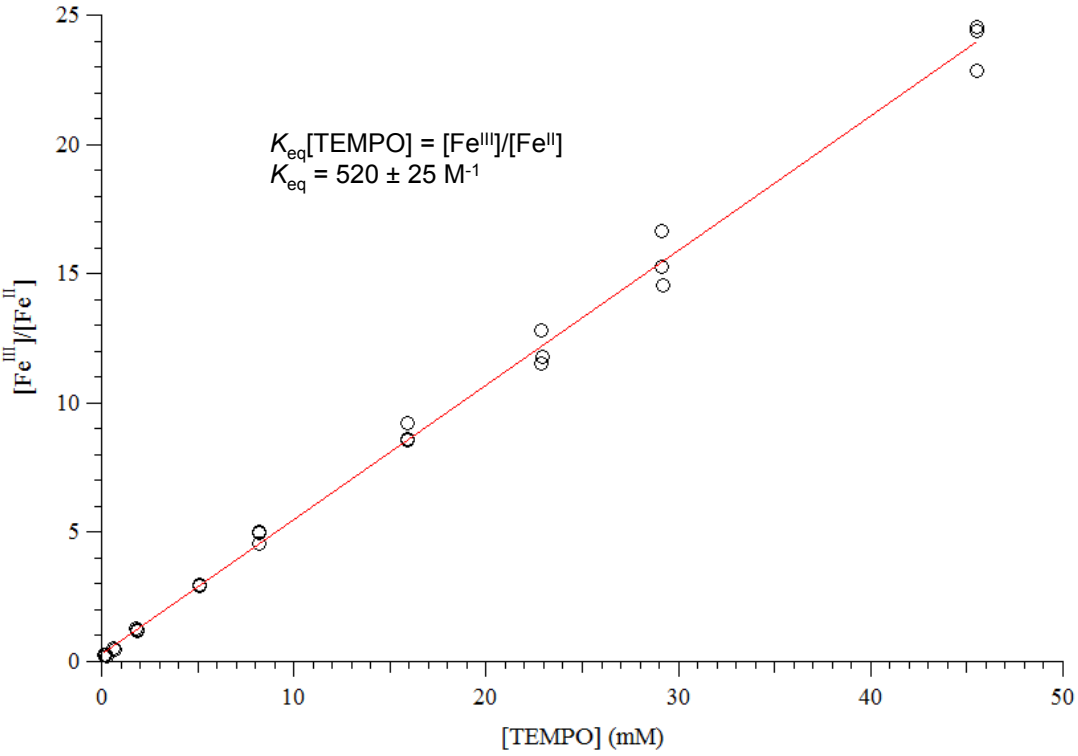

Figure 2.5. Plot of [(TMP)Fe^{II}]/[(TMP)Fe^{III}(TEMPO)] vs. [TEMPO] from ^{1}H NMR spectra. Concentrations of (TMP)Fe^{II}, (TMP)Fe^{III}(TEMPO) (abbreviated Fe^{II} and Fe^{III}), and TEMPO were calculated using the following expressions using mass balance assumptions:

$$[Fe^{II}] = [Fe^{II}_0]\,(\delta_{obs} - \delta_{Fe(III)})/(\delta_{Fe(II)} - \delta_{Fe(III)})$$
$$[Fe^{III}] = [Fe^{II}_0] - [Fe^{II}]$$
$$[TEMPO] = [TEMPO_0] - [Fe^{III}]$$

[Fe^{II}] is the equilibrium concentration of Fe^{II}, [Fe$^{II}_0$] is the initial concentration of Fe^{II}, δ_{obs} is the observed chemical shift, $\delta_{Fe(III)}$ is the extrapolated chemical shift of Fe^{III}, $\delta_{Fe(II)}$ is the chemical shift of Fe^{II}, and [TEMPO$_0$] is the initial concentration of TEMPO. Plotting [Fe^{III}]/ [Fe^{II}] vs. [TEMPO] gives a linear fit that goes through the origin. The slope is the equilibrium constant: $K_{2.4}$ = 520 ± 25 M^{-1}.

The TEMPO binding equilibrium was also studied by optical spectroscopy, using 80 μM (TMP)Fe^{II} and one equivalent of TEMPO in toluene, at temperatures from 25 °C to –90 °C (Figure 2.6.A). As the temperature decreased, the Q band associated with (TMP)Fe^{II} at 538 nm began to disappear and a new Q band assigned to (TMP)Fe^{III}(TEMPO) at 565 nm grew in. Equilibrium constants were obtained at each temperature from the absorbance at three different wavelengths (487, 538, and 565 nm), assuming mass balance for the iron species and that the extinction coefficients in Table 2.1 are independent of temperature (and ignoring the very small absorbance due to free TEMPO).[18] The value obtained at 25 °C, $K_{2.4}(25\ °C)_{optical}$ = 550 ± 25 M^{-1}, is in good agreement with that obtained by NMR measurements, and together those give a consensus value of 535 ± 20 M^{-1}. This $K_{2.4}$ is consistent with the differences observed in the above experiments, that the TEMPO adduct is mostly formed at NMR concentrations but mostly dissociated at the lower concentrations used for optical studies.

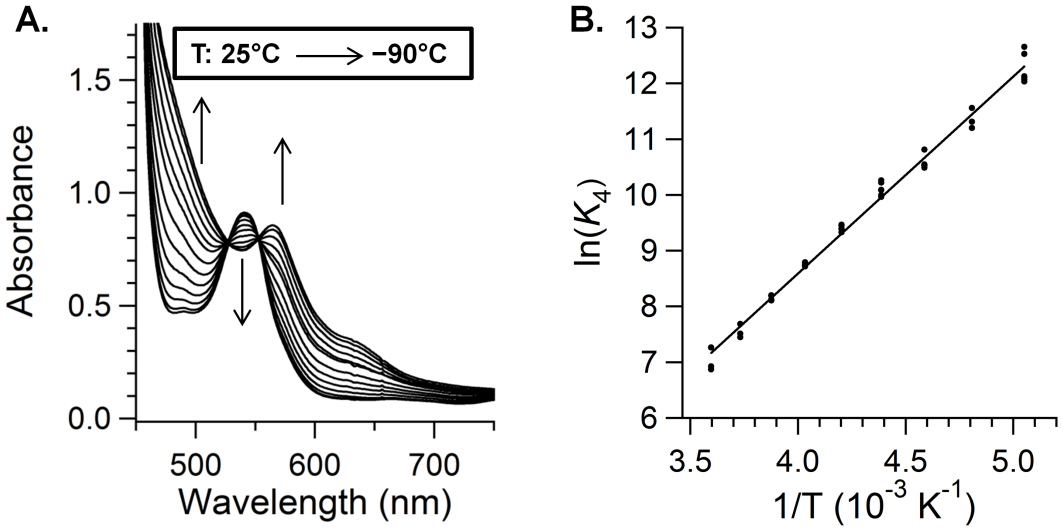

Figure 2.6. A. Optical spectra of (TMP)Fe^{II} (80 μM) and one equivalent of TEMPO in toluene at temperatures ranging from 25 °C to –90 °C. **B.** van't Hoff plot of ln($K_{-2.4}$) vs. 1/T.

A van't Hoff analysis of TEMPO binding gives $\Delta H°_{2.4}$ = –7.0 ± 1.5 kcal mol^{-1} and $\Delta S°_{2.4}$ = –11 ± 5 cal K^{-1} mol^{-1} (Figure 2.6.B). The Fe–O bond in (TMP)Fe^{III}(TEMPO) is remarkably weak, with a bond dissociation enthalpy (BDE) of only 7 kcal mol^{-1} (a BDFE of only 4 kcal mol^{-1}).

Combining $K_{2.4}$(235 K = 1.3 × 10^4 M^{-1} with the dissociation rate constant ($k_{-2.4}$(235 K)) gives the rate constant for TEMPO addition $k_{2.4}$(235 K) = $K_{2.4}k_{-2.4}$ = (1.4 ± 0.5) × 10^7 M^{-1} s^{-1} and $\Delta G^{\ddagger}_{2.4}$(235 K) = 21.3 ± 0.5 kcal mol^{-1}.

2.2.2.2. Reaction of (TMP)Fe^{II} and ^{t}Bu$_3$ArO$^\bullet$

To explore the same type of reactivity with another stable organic radical, (TMP)Fe^{II} was reacted with the 2,4,6-tri-*tert*-butyl phenoxyl radical, ^{t}Bu$_3$ArO$^\bullet$.[19] ^{1}H NMR spectra of 1:1 mixtures of (TMP)Fe^{II} plus ^{t}Bu$_3$ArO$^\bullet$ in toluene-d_8 have a broad downfield β-pyrrolic resonance at 89 ppm (Table 2.1), indicating the oxidation of iron(II) to iron(III).[11a] Interestingly, two resonances are observed for the m-aryl protons, as is typical for (TMP)Fe^{III}X species with C_{4v} symmetry. These data indicate that ^{t}Bu$_3$ArO$^\bullet$ is bound to the iron center: (TMP)Fe^{III}(^{t}Bu$_3$ArO). The pair of *m*-aryl resonances shows that dissociation of the aryloxyl radical is slow on the NMR timescale, so that the two sides of the porphyrin ring are inequivalent. This slow exchange is also indicated by ^{1}H NMR spectra of solutions with (TMP)Fe^{II} with 0.5 equivalents of ^{t}Bu$_3$ArO$^\bullet$, which show separated signals for (TMP)Fe^{III}(^{t}Bu$_3$ArO) and (TMP)Fe^{II} at 25 °C.

(TMP)Fe^{III}(^{t}Bu$_3$ArO) reacts with excess distilled, degassed water to cleanly form (TMP)Fe^{III}(OH) and ^{t}Bu$_3$ArOH, by ^{1}H NMR spectroscopy (eq 2.6; Figure 2.7). This reaction is consistent with the inability of (TMP)Fe^{III}(OH) to abstract a hydrogen atom from ^{t}Bu$_3$ArOH that was mentioned above. This reaction is also essentially the reverse of reactions (2.1 + 2.4) and 2.5.

$$\text{(TMP)Fe}^{\text{III}}(^t\text{Bu}_3\text{ArO}) + \text{H}_2\text{O} \rightarrow \text{(TMP)Fe}^{\text{III}}\text{(OH)} + {}^t\text{Bu}_3\text{ArOH} \qquad (2.6)$$

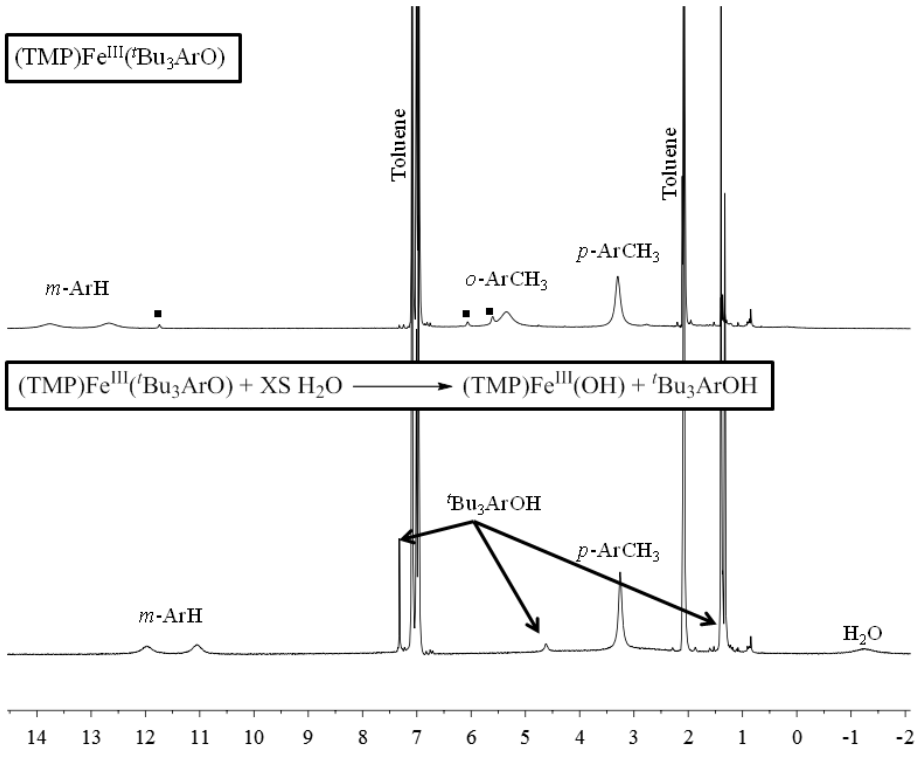

Figure 2.7. ^{1}H NMR spectra of (TMP)Fe^{III}(^{t}Bu$_3$ArO) in toluene-d_8 (top) and (TMP)Fe^{III}(^{t}Bu$_3$ArO) plus excess degassed H_2O in toluene-d_8 (bottom). The broad β-pyrrolic resonances are not shown. In the top spectrum, a small amount of (TMP)Fe^{II} impurity is present (■).

2.2.3. The Catalytic Disproportionation of TEMPO–H by (TMP)Fe^{II}

In a reaction originally formulated as a control experiment, one equivalent of TEMPO–H was added to a 4.0 mM toluene-d_8 solution of (TMP)Fe^{II}. No reaction was expected as both of these reagents typically act as reductants. To our surprise, the solution slowly turned from deep red to green. After 24 hours, the ^{1}H NMR spectrum indicated the presence of (TMP)Fe^{III}(OH), a (TMP)Fe^{II}/(TMP)Fe^{III}(TEMPO) equilibrium mixture, and a set of resonances for 2,2,6,6-tetramethylpiperidine (TEMP–H), in a 1:1:1 ratio (eq 2.7). The piperidine product was identified by GC/MS and by comparison of its ^{1}H NMR signals to an authentic sample. The chemical shifts for (TMP)Fe^{II} + TEMPO/(TMP)Fe^{III}(TEMPO) are sensitive to the position of the equilibrium, so these shifts indicate the concentration of TEMPO. The concentration

of TEMPO was determined to be half of the initial concentration of TEMPO–H, indicating the overall product stoichiometry of 1:1:1:1 as indicated in eq 2.7. When 2 equivalents of TEMPO–H were used, $(TMP)Fe^{II}$ was completely converted to $(TMP)Fe^{III}(OH)$, one equivalent of TEMP–H and presumably one equivalent of NMR silent TEMPO (eq 2.8).

$$(TMP)Fe^{II} + TEMPO–H \rightarrow \tfrac{1}{2}\,(TMP)Fe^{III}(OH) + \tfrac{1}{2}\,(TMP)Fe^{II} + \tfrac{1}{2}\,TEMP–H + \tfrac{1}{2}\,TEMPO \quad (2.7)$$

$$(TMP)Fe^{II} + 2\,TEMPO–H \rightarrow (TMP)Fe^{III}(OH) + TEMP–H + TEMPO \quad (2.8)$$

Since the $(TMP)Fe^{III}(OH)$ product could be reduced by additional TEMPO–H back to $(TMP)Fe^{II}$ (eq 2.1 above), reactions 2.8 and 2.1 indicate that the disproportionation of TEMPO–H should be catalytic in iron, using either $(TMP)Fe^{II}$ or $(TMP)Fe^{III}(OH)$. To test this, 12 equivalents of TEMPO–H were added to a toluene-d_8 solution of $(TMP)Fe^{III}(OH)$. After 24 hours, ^{1}H NMR spectra showed the presence of 4 equivalents of TEMP–H and a broad upfield water resonance, and the $(TMP)Fe^{III}(OH)$ was unchanged, consistent with the expected stoichiometry (eq 2.9).

$$3\,TEMPO–H \xrightarrow{(TMP)Fe^{III}(OH)} TEMP–H + 2\,TEMPO + H_2O \quad (2.9)$$

Over 100 turnovers of TEMPO–H disproportionation was observed in benzene-d_6 over 9 hours with 0.08 mM $(TMP)Fe^{II}$ loading and 33 mM TEMPO–H. The disappearance of TEMPO–H resonances matches the growth of TEMP–H resonances in a 3:1 ratio with nearly quantitative yield (~96% mass balance), determined by ^{1}H NMR with a hexamethylbenzene internal standard (Figure 2.8, 2.9A). The reaction is substantially inhibited by the addition of excess TEMPO (Figure 2.9B), presumably due to the equilibrium reaction of TEMPO with $(TMP)Fe^{II}$ previously described (eq 2.4).

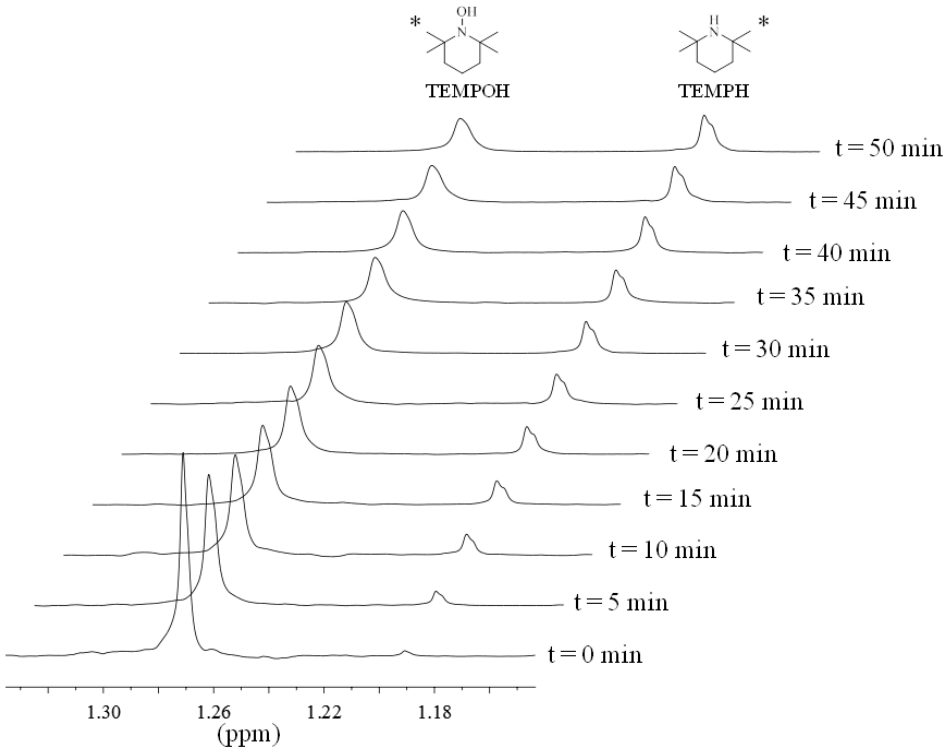

Figure 2.8. Selected ^{1}H NMR slices of the disproportionation of TEMPO–H in the presence of a catalytic amount of (TMP)Fe^{II}.

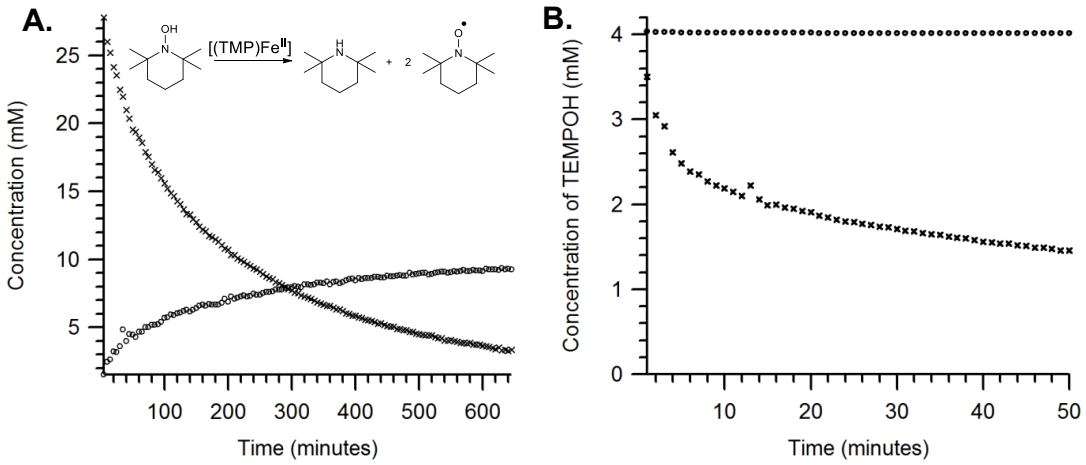

Figure 2.9. Kinetic traces for the disproportionation of TEMPO–H catalysed by (TMP)Fe^{II} in toluene-d_8. Concentrations were determined by ^{1}H NMR using a hexamethylbenzene internal standard. **A.** The disappearance of TEMPO–H (×) (initial concentration = 33 mM) and the appearance of TEMP–H (○) vs. time in the presence of 0.08 mM (TMP)Fe^{II}. **B.** The disappearance of TEMPO–H (initial concentration = 4 mM) vs. time with 0.04 mM (TMP)Fe^{II} in the absence (×) or presence (●) of 20 mM TEMPO added at t = 0.

To probe the mechanism of the catalytic disproportionation, the reactivity of the methoxy-amine TEMPO-CH_3 was explored. No reaction was observed between TEMPO–CH_3 and (TMP)Fe^{II} or (TMP)Fe^{III}(OH), even after heating at 75 °C for 48 h. Since TEMPO–H reduces itself in reaction 2.8, we also tested whether TEMPO-CH_3 could be reduced by TEMPO–H, PhNHNHPh, or $^{t}Bu_3ArOH$ in the presence of (TMP)Fe^{II}. However, no products derived from TEMPO-CH_3 were observed.

2.3. Discussion

2.3.1. Net H-atom transfer to (TMP)Fe^{III}(OH); the "Effective BDFE" of (TMP)Fe^{II} + H_2O

(TMP)Fe^{III}(OH) reacts with TEMPO–H, PhNHNHPh and $PhNHNH_2$ by net hydrogen atom transfer to give (TMP)Fe^{II}, water and the oxidized donor (TEMPO, PhN=NPh or [PhN=NH]). The TEMPO–H reaction (eq 2.1, repeated here) is quantitative and therefore provides thermochemical information (independent of the mechanism of the reaction, which is discussed below).

$$\text{(TMP)Fe}^{\text{III}}\text{(OH)} + \text{TEMPO–H} \rightarrow \text{(TMP)Fe}^{\text{II}} + \text{TEMPO} + \text{H}_2\text{O} \qquad (2.1)$$

Reaction 1 shows that the effective O–H BDFE of the (TMP)Fe^{II} + H_2O combination should be comparable to or greater than the O–H BDFE of TEMPO–H (65.2 kcal mol^{-1}).[9] The effective BDFE is defined in 2.10; the term effective is used because equation 2.10 is not a simple bond homolysis. It encompasses both the (unfavourable) binding of H_2O to (TMP)Fe^{II} and the cleavage of the (TMP)Fe^{II}(HO–H) bond. Because the reduced product, (TMP)Fe^{II} + H_2O, is two molecules, the thermochemical analysis of eq 2.1 is not as simple as a typical H-atom transfer reaction X + HY → XH + Y, for which K_{eq} has no units. The experimental execution of eq 2.1 was done at 80 mM concentrations, and these low concentrations will entropically favor the products (3 species vs. 2), as compared with 1 M standard state. This provides an extra driving force under the reaction conditions, so the effective BDFE of (TMP)Fe^{II} + H_2O could be slightly lower than the BDFE of TEMPO–H and

reaction would still proceed to completion. We conclude that the BDFE of $[(TMP)Fe^{II} + H_2O] \geq 64$ kcal mol^{-1}.

To complement this lower limit, a firm upper limit is provided by the downhill reaction of $(TMP)Fe^{III}(^{t}Bu_3ArO)$ with H_2O to form $(TMP)Fe^{III}(OH)$ + $^{t}Bu_3ArOH$ (eq 2.6). Equations 2.10-2.12 sum to equation 2.6, as shown below. Reaction 2.12, the dissociation of aryloxyl from Fe^{II}, was shown above to be very unfavourable. Therefore, the effective BDFE of $(TMP)Fe^{II} + H_2O$ must be substantially less than the BDFE of 2,4,6-tri-*tert*-butyl phenol, BDFE = 76.6 kcal mol^{-1}.[9]

$$(TMP)Fe^{II} + H_2O \rightarrow (TMP)Fe^{III}(OH) + H^{\bullet} \qquad (2.10)$$

$$\Delta G^{\circ}_{2.9} = \text{effective BDFE}$$

$$H^{\bullet} + {}^{t}Bu_3ArO^{\bullet} \rightarrow {}^{t}Bu_3ArOH \qquad (2.11)$$

$$\Delta G^{\circ}_{2.10} = \text{BDFE}(^{t}Bu_3ArOH)$$

$$(TMP)Fe^{III}(^{t}Bu_3ArO) \rightarrow (TMP)Fe^{II} + {}^{t}Bu_3ArO^{\bullet} \qquad (2.12)$$

$$\Delta G^{\circ}_{2.11} >> 0$$

$$(TMP)Fe^{III}(^{t}Bu_3ArO) + H_2O \rightarrow (TMP)Fe^{III}(OH) + {}^{t}Bu_3ArOH \qquad (2.6)$$

$$\Delta G^{\circ}_{2.6} = \Delta G^{\circ}_{2.10} + \Delta G^{\circ}_{2.11} + \Delta G^{\circ}_{2.12}$$

The conclusion that 64 kcal mol^{-1} $\leq$ BDFE$[(TMP)Fe^{II} + H_2O]$ << 76.6 kcal mol^{-1} is consistent with the reactions of $(TMP)Fe^{III}(OH)$ with hydrazines. 1,2-Diphenylhydrazine, in which the first N–H bond (BDFE = 64.3 ± 1.5 kcal mol^{-1}) is likely even weaker than that in TEMPO–H and phenylhydrazine, in which the first N–H bond is slightly stronger (BDFE = 67.5 ± 1.5 kcal mol^{-1}).[9] There are clearly kinetic as well as thermodynamic effects in play, because PhNHNHPh reacts more slowly than TEMPO–H even though its X–H bond is likely weaker. These data suggest an effective BDFE of 67 ± 3 kcal mol^{-1}.

The mechanism of H^+ and e^- transfer from TEMPO–H to (TMP)Fe^{III}(OH) could occur by (*i*) concerted proton-electron transfer (called CPET or H-atom transfer), (*ii*) initial proton transfer then electron transfer (PT/ET), (*iii*) initial electron transfer then proton transfer (ET/PT), or (*iv*) an initial protolytic ligand-exchange mechanism (see below).

The stepwise ET/PT and PT/ET paths are unlikely based on thermochemical arguments. TEMPO–H is a poor one-electron reductant, E = 0.71 V in MeCN,[9] while (TMP)Fe^{III}(OH) is reported to be quite difficult to reduce, $E_{1/2}$ = –1.23 V in dichloromethane (all potentials vs. $Cp_2Fe^{+/0}$).[15] While the differences in solvent preclude a completely quantitative comparison, the rough estimate is that ET is nearly 2 V or 45 kcal mol^{-1} endoergic. This value is substantially higher than the observed kinetic barrier for reaction 2.1, $\Delta G^{\ddagger}_{2.1}$ = 15.0 ± 0.1 kcal mol^{-1}, even considering the uncertainties involved. Thus it is unlikely the reaction of (TMP)Fe^{III}(OH) with TEMPO–H proceeds through an ET/PT mechanism. In a similar vein, initial PT is unlikely because TEMPO–H is a very weak acid (pK_a in MeCN of 41[9]), and (TMP)Fe^{III}(OH) is not very basic. (TMP)Fe^{III}(OH) is not protonated in CD_2Cl_2 by 20 equivalents of the weak acid *tert*-butylimino-*tris*(pyrolidino)phosphorane hydrofluoroborate, P1-phosphazene$H^+BF_4^-$, which has a pK_a in MeCN of 28.42[20] (See experimental). The ET/PT and PT/ET mechanisms are particularly unlikely in toluene solution because the formation of charged intermediates is even more difficult in this low-polarity solvent. The results are thus consistent with a mechanism of H-atom transfer (concerted H^+ and e^- transfer), which is very common for TEMPO–H.

However, a protolytic ligand-exchange mechanism is also possible. This path would involve TEMPO–H substituting for the OH ligand on (TMP)Fe^{III}(OH) with proton transfer to form water and (TMP)Fe^{III}(TEMPO), which subsequently dissociates TEMPO. Such a protolytic pathway is likely followed by the closely related fluorene oxime reaction[10j] shown in eq 2.5 above. The displacement of ArOH from (TMP)Fe^{III}(OAr) by water (eq 2.6) has to be hydrolytic because the HAT pathway is precluded by the high water O–H BDFE. This mechanism has been studied for exchange of phenolate ligands in (TMP)Fe^{III}(OAr) with carboxylic acids

and alcohols.[21] The alcohol exchange reactions are quite slow, with rate constants ~ 10^{-2} M^{-1} s^{-1} at 60 °C, and are slower for less nucleophilic and more crowded alcohols.

Based on these precedents, we tentatively favor a HAT mechanism for the TEMPO–H reaction rather than a hydrolytic one. TEMPO–H is a crowded molecule, yet it reacts with (TMP)Fe^{III}(OH) many orders of magnitude faster than alcohols react with (TMP)Fe^{III}(OAr). TEMPO–H has a very low acidity (pK_a 31[9] in DMSO, vs. 16.2 for fluorenone oxime[22]) making it less likely to participate in protolytic reactions. Finally, the qualitative rate comparison observed here, k(TEMPOH) > k(PhNHNHPh) >> k($PhNHNH_2$), is more consistent with a hydrogen atom transfer mechanism based on the X–H bond strengths, but clearly do not parallel the pK_a values: TEMPOH, 31 > $PhNHNH_2$, 28.8 > PhNHNHPh, 26.2 (in DMSO[9]). The very weak O–H bond in TEMPO–H (BDE ~70 kcal mol^{-1}) biases its reactivity toward HAT as opposed to the fluorene oxime (BDEs ~70 vs. ~82 kcal mol^{-1} [23]). These mechanistic arguments are, however, suggestive rather than definitive.

2.3.2. Binding of stable oxyl radicals to (TMP)Fe^{II}

The binding of the oxyl radicals TEMPO (2,2,6,6-tetramethylpiperdine-N-oxyl radical) and $^tBu_3ArO^\bullet$ (2,4,6-tri-*tert*-butyl phenoxyl radical) to (TMP)Fe^{II} is reminiscent of the much-studied reversible binding of O_2 to ferrous hemes.[24] The product (TMP)Fe^{III}(OR) complexes are well described as high-spin Fe^{III} species based on their ^{1}H NMR spectra.11a The binding of TEMPO is reversible, with $K_{2.4}$ = 535 ± 20 M^{-1} from both NMR and optical studies. A van't Hoff analysis gives the TEMPO-iron bond dissociation enthalpy as only $-\Delta H°_{2.4}$ = 7.0 ± 1.5 kcal mol^{-1}. This is a very weak bond (the Fe–O homolytic bond dissociation free energy (BDFE) is 3.7 ± 0.1 kcal mol^{-1}). To our knowledge, these are the first measurements of such Fe–O homolytic bond energies, other than for the binding of O_2.

The (1.4 ± 0.5) × 10^7 M^{-1} s^{-1} and 1100 s^{-1} rate constants for TEMPO association and dissociation are near the middle of the ranges of related values for O_2 binding to natural and synthetic hemes. These vary from 10^4 to almost 10^9 M^{-1} s^{-1} for k_{on}, and from 2 to 10^5 s^{-1} for k_{off}.[24]

Related redox coordination chemistry of TEMPO with transition metal complexes has received significant attention, for instance in the area of living radical polymerizations.[25] Waymouth and co-workers have shown that TEMPO reversibly binds Ti(III) sandwich complexes in an η^1 fashion through the TEMPO oxygen.[26] With $Cp_2Ti^{IV}Cl(TEMPO)$, for instance, Ti–O bond homolysis occurs at 60 °C in the presence of CCl_4 to afford $Cp_2Ti^{IV}Cl_2$, TEMPO, and $^{\bullet}CCl_3$. The Ti–O BDE of $Cp_2Ti^{IV}Cl(TEMPO)$ was determined to be approximately 27 kcal mol^{-1}.[26c]

The reaction between $(TMP)Fe^{II}$ and TEMPO bears a particularly close resemblance to the reactivity of $(TMP)Rh^{II}$ with TEMPO reported by de Bruin and co-workers.[27] The Rh complex makes a somewhat stronger bond, $\Delta H°_{Rh\text{-}TEMPO}$ = 14.7 ± 1.4 kcal mol^{-1}. The higher bond energy for Rh^{III}–TEMPO is reasonable considering that second row transition metals typically form stronger bonds than first row metals, and that Rh^{II} is generally a less favorable oxidation state than Fe^{II}.

The entropy for the association of TEMPO to $(TMP)Rh^{II}$ was reported as $\Delta S°$ = –30.6 ± 4.6 cal mol^{-1} K^{-1}, much more negative than the analogous value reported here for $(TMP)Fe^{III}(TEMPO)$, –11 ± 5 cal mol^{-1} K^{-1}. Only a small part of this difference is due to the entropy of the spin multiplicity change. The entropy of the electron spin states is given by S° = Rln(2S+1), where R is the ideal gas constant and S is the spin multiplicity of the system. So in the binding of $(TMP)Rh^{II}$ and TEMPO, both S = ½, to give the diamagnetic, S = 0 $(TMP)Rh^{III}(TEMPO)$ complex, spin accounts for a positive entropy change of ~3 cal mol^{-1} K^{-1}. The reaction of intermediate spin S = 1 $(TMP)Fe^{II}$ [11c] with S = ½ TEMPO results in the formation of a high-spin S = 5/2 $(TMP)Fe^{III}(TEMPO)$ complex has an associated entropy change of only ~ –1 cal mol^{-1} K^{-1}. Thus the differences in the spin entropy of the two systems accounts for only ~4 cal mol^{-1} K^{-1} of the 20 cal mol^{-1} K^{-1} measured difference, suggesting that there must be significant difference in the structural and vibrational change upon TEMPO coordination between the rhodium and iron compounds.

The $^{t}Bu_3ArO^{\bullet}$ radical binds significantly more strongly to $(TMP)Fe^{II}$ than TEMPO. From one perspective this is surprising because of the high degree of steric bulk on both the iron porphyrin as well as the phenoxide. $^{t}Bu_3ArO^{\bullet}$ would seem to be slightly more bulky than TEMPO, having *tert*-butyl groups bound to the carbons β to

the oxyl centre while TEMPO has two methyl groups in those positions. The stronger bond in (TMP)Fe^{III}(^{t}Bu_3ArO) is likely due primarily to ^{t}Bu_3ArO$^\bullet$ being a less stabilized radical than TEMPO, as evidenced by the O–H bond being 11.5 kcal mol^{-1} stronger in ^{t}Bu_3ArO–H vs. TEMPO–H. If the ^{t}Bu_3ArO and TEMPO ligands were rigidly held between the mesityl substituents, the (TMP)Fe^{III}(OR) compounds would have C_{2v} symmetry with inequivalent β-pyrrolic signals, but these resonances are broad and cannot be resolved.

2.3.3. Catalytic disproportionation of TEMPO–H.

(TMP)Fe^{III}(OH) catalyses the disproportionation of TEMPO–H to TEMPO, TEMP–H and water (eq 2.9). Over 100 turnovers have been observed with no sign of catalyst degradation. Catalysis is fast initially, but slows over time. The chemistry reported above suggests that the catalytic cycle likely proceeds in a ping-pong fashion, as depicted in Scheme 1. The substrate oxidation part presumably proceeds by PCET from TEMPO–H to (TMP)Fe^{III}(OH). Then the slowing of the catalysis is due to the reversible binding of the TEMPO product to (TMP)Fe^{II}, removing it from the catalytic cycle.

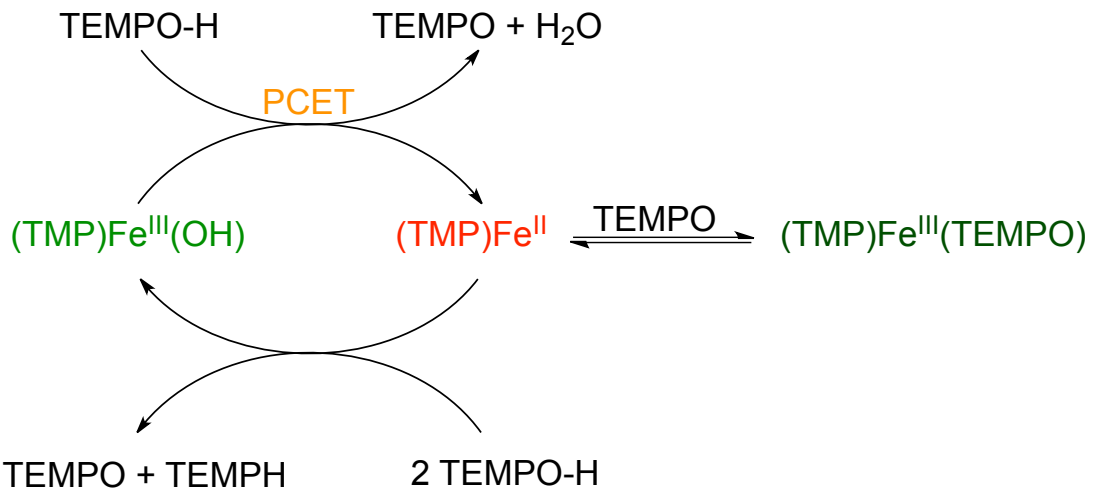

Scheme 1. Proposed reaction cycle for the catalytic disproportionation of TEMPO–H by (TMP)Fe^{III}(OH).

The substrate reduction side, $(TMP)Fe^{II}$ + 2 TEMPO–H → $(TMP)Fe^{III}(OH)$ + TEMPO + TEMP–H, has also been observed in stoichiometric reactions. The mechanism, however, remains obscure, especially how the N–O bond is cleaved. The lack of reactivity between $(TMP)Fe^{II}$ and TEMPO-CH_3 argues against a pathway in which TEMPO–R transfers OR (R = H or CH_3) to $(TMP)Fe^{II}$ to form the tetramethylpiperdinyl radical. The N–O homolytic bond strength of TEMPO–CH_3 should be weaker than that of TEMPO–H (because CH_3 is more electron donating than H), so OR transfer should be more facile for TEMPO–CH_3 than for TEMPO–H. Although sterics could conceivably play a role, the strong binding of the bulky phenoxyl radical $^tBu_3ArO^\bullet$ to $(TMP)Fe^{II}$ suggests that attack of TEMPO–CH_3 should not be precluded. Reduction of TEMPO–H does not occur by outer-sphere electron transfer from $(TMP)Fe^{II}$, because TEMPO–H is unreactive with the much stronger reductant cobaltocene (over 24 h in toluene-d_8).

The disproportionation of TEMPO–H by $(TMP)Fe^{III}(OH)$ is potentially related to the biochemical conversion of hydroxylamine to nitrite by the multi-heme enzyme hydroxylamine oxidoreductase (HAO).[4] This complicated enzyme has inspired a number of different studies into the reactivity of hydroxylamine with both heme[28] and non-heme[29] transition metal complexes. For instance, two equivalents hydroxylamine react with $(TPP)Fe^{III}Cl$ in MeOH/$CHCl_3$ to give NH_4Cl, water, and (TPP)FeNO.[28a,b] Water soluble iron porphyrin complexes catalyse the disproportionation of hydroxylamine to high yields of NH_3 (the reduced product) and a mixture of N_2 and N_2O as the oxidized products.[18c] The mechanism is not well understood in either case, but there is some evidence for a pre-equilibrium formation of $(porphyrin)Fe^{III}(NH_2OH)^{2+}$, and the possibility of radical pathways has been discussed.[28a,b] NH_2OMe is catalytically decomposed to 1/3 NH_3, 1/3 N_2 and MeOH by aquapentacyanoferrate in aqueous buffer.[29] A mechanism of $^\bullet NH_2$ abstraction by iron(II) to yield a $^\bullet OCH_3$ radical was suggested based on studies with the radical trap DMPO, although such an N–O cleavage is not indicated by the chemistry reported here (and spin adducts of DMPO can also be generated via non-radical mechanisms in the presence of ferric ions[30]).

TEMPO–H may be considered a simpler surrogate for hydroxylamine. Its oxidation stops at the stable TEMPO radical, while removal of H$^{\bullet}$ form hydroxylamine starts a cascade to ½ N_2 and H_2O.[31] The bond strength of the NH_2O–H bond in water is only 7.4 kcal mol^{-1} stronger than that of TEMPO–H.[9] So the results reported here indicate that hydrogen atom transfer from NH_2OH to (heme)Fe^{III}(OH) is a reasonable step in the catalytic cycle of HAO and related enzymes.

2.4. Conclusions

Described here are a number of inner-sphere reactions of the (TMP)Fe$^{III/II}$ redox couple (TMP = *meso*-tetramesitylporphyrinato). (TMP)Fe^{III}(OH) reacts with compounds with very weak O–H and N–H bonds, TEMPO–H, PhNHNHPh and $PhNHNH_2$, with transfer of a proton to the hydroxide ligand and an electron to the iron center. This is a convenient way to generate (TMP)Fe^{II}. The data are consistent with either a pathway involving hydrogen atom transfer (concerted $H^+ + e^-$ transfer), or by initial hydrolytic conversion of (TMP)Fe^{III}(OH) + TEMPO–H to (TMP)Fe^{III}-(TEMPO) + H_2O followed by TEMPO dissociation. The thermochemical data rule out pathways involving initial electron or proton transfer. Analysis of the reactivity with different hydrogen atom transfer reagents gives an estimate of 67 ± 3 kcal mol^{-1} for the effective bond dissociation free energy (BDFE) of (TMP)Fe^{II} + H_2O → (TMP)Fe^{III}(OH) + H$^{\bullet}$.

The ferrous porphyrin (TMP)Fe^{II} homolytically binds oxyl radicals to generate (TMP)Fe^{III}–OR complexes. With TEMPO, this reaction is rapid and reversible on the NMR timescale at room temperature but is slower at low temperatures. This is, to our knowledge, the first reported case of a (porphyrin)Fe^{III}–TEMPO complex. Equilibrium studies show that the Fe–O bond is remarkably weak, with a bond dissociation enthalpy of only 7.0 ± 1.5 kcal mol^{-1} (the BDFE is 4 kcal mol^{-1}).

Both (TMP)Fe^{II} and (TMP)Fe^{III}(OH) catalyse the disproportionation of the hydroxylamine TEMPO–H to 2/3 TEMPO + 1/3 TEMP–H (2,2,6,6-tetramethylpiperidine). This type of catalytic disproportionation has been observed with hydroxylamine and metal porphyrins but no radical intermediates have been

directly observed. The results reported here suggest that the previously reported reactions of hydroxylamine with metal porphyrins may involve hydrogen atom transfer.

In discussions of substrate transformations by heme cofactors, the conversation is often dominated by high-valent intermediates, and the chemistry of lower valent heme species can be overlooked. The results reported here serve to highlight both the rich inner-sphere chemistry of the lesser-explored $Fe^{III/II}$ couple as well as the critical role that PCET can play in these systems.

2.5. Experimental

2.5.1. Materials

Unless otherwise noted, all chemicals were purchased from Sigma-Aldrich and used without purification. Toluene-d_8 and dichloromethane-d_2 were purchased from Cambridge Isotope Labs, dried over NaK and CaH_2, respectively, and vacuum distilled. Other solvents were purchased from Fischer and dried using a "Grubbs type" Seca Solvent System installed by GlassContour. TEMPO was purified by sublimation. TEMPO–H,[32] TEMPO–CH_3,[33] ^{t}Bu$_3$ArO$^\bullet$,[19] $TMPH_2$,[34] (TMP)$Fe^{III}Cl$,[35] and P1-phosphazene$H^+BF_4^-$,[36] were prepared using established literature protocols. All glassware was dried in an oven at 150 °C overnight and pumped into a nitrogen filled glovebox while hot. Celite was dried at 100 °C overnight under vacuum.

2.5.2. Instrumentation

All ^{1}H NMR spectra were obtained on Bruker 300 and 500 MHz instruments. Variable temperature spectra were acquired on a Bruker 500 MHz instrument. The chemical shifts reported are referenced to TMS using the residual solvent peak. UV-visible absorption spectra were collected with a Hewlett-Packard 8453 diode array spectrometer equipped with a Unisoku USP-203 cryostat. Kinetic measurements were performed on an OLIS RSM-1000 stopped-flow spectrophotometer.

2.5.3. Syntheses

(*meso*-Tetramesitylporphyrinato) iron(III) hydroxide, (TMP)Fe^{III}(OH). (TMP)Fe^{III}(OH) was prepared from (TMP)Fe^{III}Cl as described in the literature.[11a] The dark green solid product was macerated with a spatula and dried at 60 °C under high vacuum for 24 hours to remove residual water from the product. Disappearance of characteristic upfield water resonance11a at δ –1.2 confirmed that the product was dry. ^{1}H NMR (300 MHz, toluene-d_8) δ: 81.55 (broad, 8H, β-pyrrole), 12.14 (s, 4H, *m*-Ar), 11.18 (s, 4H, *m*-Ar), 3.29 (s, 12H, *p*-CH_3).

(*meso*-tetramesitylporphyrinato) iron(II), (TMP)Fe^{II}. (TMP)Fe^{III}–Cl (217 mg, 0.249 mmol) was treated with equimolar cobaltocene (47.1 mg, 0.249 mmol) in 10 mL of toluene in a nitrogen filled glovebox. The solution was stirred for 30 minutes then filtered through a Celite plug to remove cobaltocenium chloride. The solvent was removed under reduced pressure and a dark red solid was collected (148 mg, 71%). The identity was confirmed by comparison with literature ^{1}H NMR characterization.[11c] ^{1}H NMR (300 MHz, toluene-d_8) δ: 11.72 (s, 8H, *m*-Ar), 6.04 (s, 12H, *p*-CH_3), 5.62 (s, 24H, *o*-CH_3), 2.86 (s, 8H, β-pyrrole).

2.5.4. Representative Reaction Procedure

In a typical NMR-scale reaction, equimolar solutions of (TMP)Fe^{II} and TEMPO were prepared in toluene-d_8 in the glovebox (4.0 mM). Solutions were added to a J. Young NMR tube and the tube sealed. In a typical optical absorption spectroscopy experiment, equimolar solutions of (TMP)Fe^{II} and TEMPO were prepared in toluene in a nitrogen filled glovebox (80 μM). Solutions were added to a 1 cm pathlength quartz cuvette fitted with a Kontes valve and sealed. For both optical and NMR experiments, the sample was inverted several times to ensure that complete mixing had occurred prior to obtaining spectra. ^{1}H NMR data for (TMP)Fe^{III}(TEMPO) and (TMP)Fe^{III}(^{t}Bu$_3$ArO) are given in Table 2.1.

2.5.5. BDFE calculations using Abraham's Model

The interconversion between solution BDFEs ($BDFE_{solv}$) of different hydrogen atom transfer reagents can be achieved by first converting $BDFE_{solv}$ to a gas phase BDFE ($BDFE_g$) by accounting for the free energy of solvation of $H^\bullet$ and the difference in free energy of solvation of XH and $X^\bullet$ (eq 2.13).[1] The reported BDFE values of 1,2-diphenylhydrazine and phenylhydrazine in DMSO are 67.1 and 70.3 kcal mol^{-1}, respectively.[9]

$$BDFE_{solv} = BDFE_g + \Delta G°_{solv}(H^\bullet) + [\Delta G°_{solv}(X^\bullet) - \Delta G°_{solv}(XH)] \qquad (2.13)$$

$\Delta G°_{solv}(H^\bullet)$ can be calculated from the solubility of $H^\bullet$ (assumed to be the same as H_2[1]) at STP in different solvents (eq 2.14). $\Delta G°_{solv}(H^\bullet)$ in toluene is 4.77 kcal mol^{-1} and $\Delta G°_{solv}(H^\bullet)$ in DMSO is 5.61 kcal mol^{-1}.[37,38]

$$(\Delta G°_{solv}(H^\bullet) = -RT\ln(K_{sol}) \qquad (2.14)$$

In aprotic solvents, the $[\Delta G°_{solv}(X^\bullet) - \Delta G°_{solv}(XH)]$ term is taken as the free energy of the XH-solvent hydrogen bond. This can be calculated using empirically determined H-bonding acidity
(α_2^H) and basicity parameters (β_2^H) described by Abraham (eq 2.15).

$$(3)\ \Delta G°_{solv} = -10.02\alpha_2^H\beta_2^H - 1.492 \qquad (2.15)$$

The β_2^H parameter in DMSO is 0.78 and in toluene is 0.14.[39] The α_2^H value of 1,2-diphenyl hydrazine or phenylhydrazine is not reported but an estimate of 0.3 can be made for both by comparison to other reported N-H compounds (diphenylamine α_2^H = 0.324, aniline = 0.264, and 3-chloroaniline = 0.33).[49]

Combining these equations, the BDFE values of 1,2-diphenylhydrazine and phenylhydrazine reported in DMSO can be converted to BDFE values in toluene.

$$BDFE_{tol} = BDFE_{DSMO} - [\Delta G°_{solv}(H^\bullet)_{DMSO} - \Delta G°_{solv}(XH)_{DMSO}] + [\Delta G°_{solv}(H^\bullet)_{tol} - \Delta G°_{solv}(XH)_{tol}] \qquad (2.16)$$

Converting the reported BDFE values for 1,2-diphenylhydrazine and phenylhydrazine in DMSO to BDFE values in toluene using this model give values of 64.3 ± 1.5 and 67.6 ± 1.5 kcal mol^{-1}, respectively.

A more complete description of the use of Abraham's model of interconverting solution BDFE values can be found in reference 39.

2.5.6. Details of the van't Hoff analysis of (TMP)Fe^{II} + TEMPO using variable temperature optical data.

The epsilon values of "pure" (TMP)Fe^{III}(TEMPO) were measured by preparing a sample of 80 μM (TMP)Fe^{II} in toluene with 5 equivalents of TEMPO. Optical spectra were taken as the temperature was lowered. When the temperature was decreased below approximately –50 °C, no additional spectral changes were observed. The absorption spectrum observed in this temperature independent regime was taken to be that of "pure" (TMP)Fe^{III}(TEMPO). The epsilon values of (TMP)Fe^{III}(TEMPO) from three different wavelengths were used to calculate equilibrium concentrations: 487 nm (17600 M^{-1} cm^{-1}), 538 nm (8250 M^{-1} cm^{-1}), and 565 nm (10500 M^{-1} cm^{-1}). The ε values at the same wavelengths for (TMP)Fe^{II} were also used: 487 nm (5720 M^{-1} cm^{-1}), 538 nm (11600 M^{-1} cm^{-1}), and 565 nm (5670 M^{-1} cm^{-1}). Although there was a slight temperature dependence on these values (~5%), it was assumed that they were effectively constant over the temperature range from which they were taken (5°C to -75°C). A larger error is reported to compensate for this simplification. The absorption of free TEMPO was negligible within the error of the measurements [TEMPO λ_{max} (MeCN) = 460 nm (10.3 M^{-1} cm^{-1})[18]].

At each temperature, $K_{2.4}$ was determined from the optical spectrum at the three wavelengths mentioned using the following equations derived from mass balance assumptions (the 1 cm pathlength term is not included):

$$[Fe^{II}] = (A_{obs} - \varepsilon_{Fe(III)}[Fe^{II}_0])/(\varepsilon_{Fe(II)} - \varepsilon_{Fe(III)})$$

$$[Fe^{III}] = [Fe^{II}_0] - [Fe^{II}]$$

$$[TEMPO] = [TEMPO_0] - [Fe^{III}]$$

$$K_4 = [Fe^{III}]/[Fe^{II}][TEMPO]$$

Where $[Fe^{II}]$ is the equilibrium concentration of (TMP) Fe^{II}, A_{obs} is the observed absorbance, $\varepsilon_{Fe(III)}$ is the epsilon value of (TMP)Fe^{III}(TEMPO), $\varepsilon_{Fe(II)}$ is the epsilon value of (TMP)Fe^{II}, $[Fe^{II}_0]$ is the initial concentration of (TMP)Fe^{II}, [TEMPO] is the equilibrium concentration of TEMPO, and $[TEMPO_0]$ is the initial concentration of TEMPO.

Table. 2.2. Temperature dependent $K_{2.4}$ values at different temperatures in toluene.

Temperature (°C)	$K_4 (M^{-1})$
5	1120
–5	1900
–15	3440
–25	6320
–35	12000
–45	24400
–55	41000
–65	85700
–75	210000

Plotting $\ln(K_{2.4})$ vs. 1/T shows a linear relationship. The values of $\Delta H°$ and $\Delta S°$ were determined by applying the van't Hoff equation:

$$\ln(K_{2.4}) = -(\Delta H°/RT) + (\Delta S°/R)$$

2.5.8. Experimental details for the treatment of (TMP)Fe^{III}(OH) with excess P1 phosphazene$H^+BF_4^-$

In a J.Young NMR tube, 20 equivalents of *tert*-butylimino-tris(pyrolidino)phosphorane hydrofluoroborate, P1-phosphazene$H^+BF_4^-$, was added to a 6.6 mM solution of (TMP)Fe^{III}(OH) in dichloromethane-d_2. No reaction was observed by ^{1}H NMR after 1 h.

2.5.7. Details for mass balance calculations for the disproportionation of TEMPO–H in the presence of catalytic (TMP)Fe^{II}.

Using the data shown in Figure 2.9.B., mass balance was calculated using the following equation based on the reaction stoichiometry:

$$F(t) = ([TEMPH]_t + [TEMPO]_t + [TEMPO–H]_t)/[TEMPOH]_0$$

Where t is time, $[TEMPH]_t$ is the concentration of TEMPH at time t, $[TEMPO–H]_t$ is the concentration of TEMPOH at time t, $[TEMPO]_t$ is the concentration of TEMPO at time t (taken to be = 2 × $[TEMPH]_t$) and $[TEMPO–H]_0$ is the concentration of TEMPO–H at t = 0.

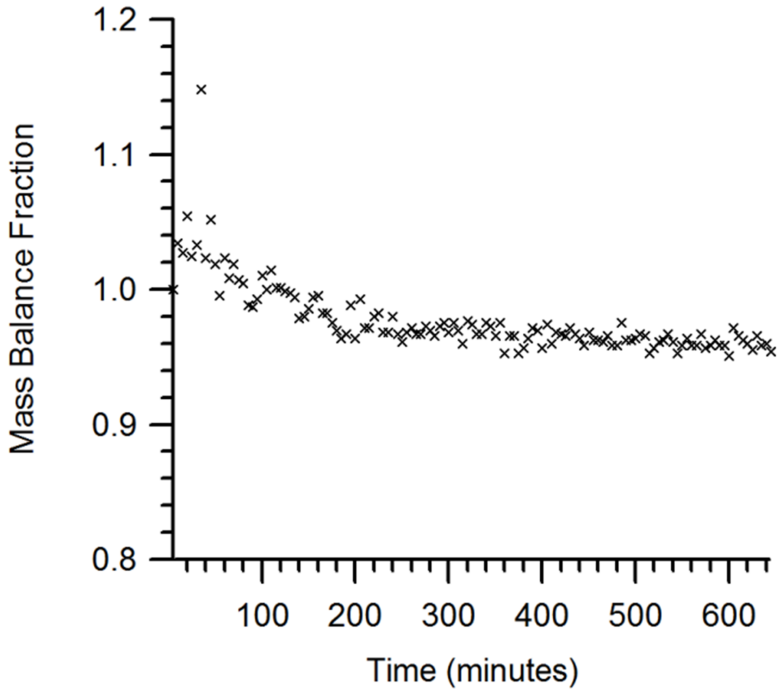

Figure 2.10. Mass balance plot for the catalytic disproportionation of TEMPO–H. Mass balance fraction describes the observed amount of TEMP-H generated in relation to the amount of observed TEMPO–H consumed. A mass balance fraction equal to 1 would describe perfect mass balance in which one TEMP-H was generated for every 3 TEMPO–H consumed.

Notes for Chapter 2

---

(1) Unless noted otherwise, this chapter has been published in: Porter, T. R.; Mayer, J. M. *Chem. Sci.* **2014**, 5, 372.

(2) Meunier, B.; de Visser, S. P.; Shaik, S. *Chem. Rev.* **2004**, 9, 3947.

(3) Guengerich, F. P. *Chem. Res. Toxicol.* **2000**, 14, 611.

(4) Igarashi, N.; Moriyama, H.; Fujiwara, T.; Fukumori, Y.; Tanaka, N. *Nature Struc. Biol.* **1997**, 4, 276.

(5) Fernandez, M. L.; Estrin, D. A.; Bari, S. E. *J. Inorg. Biochem.* **2008**, 102, 1523.

(6) Kaila, V. R. I.; Verkhovsky, M. I.; Wilkstrom, M. *Chem. Rev.* **2010**, 110, 7062.

(7) Mayer, J. M.; *Annu. Rev. Phys. Chem.* **2004**, 55, 363.

(8) Constentin, C.; Evans, D. H.; Robert, M; Savéant, J.–M.; Singh, P. S. *J. Am. Chem. Soc.* **2005**, 127, 12490.

(9) (a) Warren, J. J.; Tronic, T. T.; Mayer, J. M. *Chem. Rev.* **2010**, 110, 6961. (b) BDFE values in toluene are assumed to be the same as those reported in benzene. (c) BDFE values in DMSO were taken from reference 9a and converted to BDFE values in toluene using Abraham's model. See Experimental for more details.

(10) (a) Haushalter, R. C.; Nakamura, M.; Nemo, T. E.; Evans, B. J.; Groves, J. T. *J. Am. Chem. Soc.* **1981**, 103, 2884. (b) Nemo, T. E.; Groves, J. T. *J. Am. Chem. Soc.* **1983**, 105, 5786. (c) Nemo, T. E.; Groves, J. T. *J. Am. Chem. Soc.* **1983**, 105, 6243. (d) Quinn, R.; McMurry, J. T.; Nakamura, M.; Lang, G.; Boso, B.; Groves, J. T. *J. Am. Chem. Soc.* **1985**, 107, 354. (e) Gilbert, J. A.; Groves, J. T. *Inorg. Chem.* **1986**, 25, 123. (f) Watanabe, Y.; Groves, J. T. *J. Am. Chem. Soc.* **1986**, 108, 7834. (g) Watanabe, Y.; Groves, J. T. *J. Am. Chem. Soc.* **1988**, 110, 8443. (h) Gross, Z.; Stern, M. K.; Groves, J. T. *Inorg. Chem.* **1994**, 33, 5065. (i) Groves, J. T.; Han, Y. Z.; Ortiz de Montello, P. R. *Cytochrome P450: Structure, Mechanism, and Biochemistry*; Plenium: New York, 3rd edition, 2004, pp 1-34. (j) Wang, C. C. –Y.; Ho, D. M.; Groves, J. T. *J. Am. Chem. Soc.* **1999**, 121, 12094.

(11) (a) Chen, R.–J.; Latos-Grażyński, L.; Balch, A. L. *Inorg. Chem.* **1982**, 21, 2412. (b) Latos-Grażyński, L.; Chen, R.–J.; La Mar, G. N.; Balch, A. L. *J. Am. Chem.*

Soc. **1982**, 104, 5992. (c) Chan, Y.–W.; Chen, R.–J.; La Mar, G. N.; Latos-Grażyński, L.; Renner, M. W.; Balch, A. L. *J. Am. Chem. Soc.* **1984**, 106, 7779. (d) Latos-Grażyński, L.; Renner, M. W.; Balch, A. L. *J. Am. Chem. Soc.* **1985**, 107, 2983. (e) Arasasingham, R. D.; Cornman, C. R.; Balch, A. L. *J. Am. Chem. Soc.* **1989**, 111, 7800.

(12) (a) Sisemore, M. F.; Selke, M.; Burstyn, J. N.; Valentine, J. S. *Inorg. Chem.* **1997**, 36, 979. (b) Selke, M.; Valentine, J. S. *J. Am. Chem. Soc.* **1998**, 120, 2652. (c) Wertz, D. L; Valentine, J. S. *Struct. Bond.* **2000**, 97, 37. (d) Wertz, D. L.; Sisemore, M. F.; Driscoll, J.; Valentine, J. S. *J. Am. Chem. Soc.* **1998**, 120, 5331.

(13) (a) Lim, M. H.; Oh, S.–Y.; Nam, W. *Inorg. Chem.* **2000**, 39, 5572. (b) Kamachi, T.; Kuono, T.; Nam, W.; Yoshikawa, K. *J. Inorg. Biochem.* **2006**, 100, 751. (c) Han, A.–R.; Jeong, Y. J.; Kang, Y.; Lee, J. Y.; Seo, M. S.; Nam, W. *Chem. Comm.* **2008**, 1076. (d) Kang, Y.; Chen, H.; Jeong, Y. J.; Lai, W.; Bae, E. H.; Shaik, S.; Nam, W. *Chem. Eur. J.* **2009**, 15, 10039. (e) Nam, W. *Acc. Chem. Res.* **2007**, 40 522.

(14) The conclusion that the product is 4-coordinate (TMP)Fe^{II} rather than a 5-coordinate aquo complex is based on ^{1}H NMR spectra. We observe the same spectrum for (TMP)Fe^{II} generated from (TMP)Fe^{III}Cl under rigorously moisture free conditions with cobaltocene and for (TMP)Fe^{II} + H_2O generated from (TMP)Fe^{III}(OH) + 0.5 eq PhNHNHPh (eq 2.2). Furthermore, alcohols, ethers, and H_2O are known to be poor ligands for ferrous porphyrins (i.e. K_{eq} for THF binding to (TPP)Fe^{II} in C_6H_6 = ~5 M^{-1}): Mashiko, T.; Dolphin, D. In *Comprehensive Coordination Chemistry*; Wilkinson, G., 1st edition, Pergamon Press: New York, 1987; Chapter 21, p 813.

(15) (a) Swistak, C.; Mu, X. H.; Kadish, K. M. *Inorg. Chem.* **1987**, 26, 4360. (b) Converted from the reported $E_{1/2}$ = –0.86 V vs SCE in CH_2Cl_2.

(16) PhN=NH is bracketed since it is unstable to decomposition and is not oberved by ^{1}H NMR. See Huang, P.–K.; Kosower, E. M. *J. Am. Chem. Soc.* 1968, 90, 2367.

(17) Sandström, J., *Dynamic NMR Spectroscopy*; Academic Press: New York, 1st edition, 1982.

(18) Wu, A.; Mader, E. A.; Datta, A.; Hrovat, D. A.; Mayer, J. M. *J. Am. Chem. Soc.* **2009**, 131, 11985.

(19) Manner, V. W.; Markle, T. F.; Freudenthal, J. H.; Roth, J. P.; Mayer, J. M. *Chem. Comm.* **2008**, 44, 256.

(20) Kaljurand, I.; Kütt, A.; Sooväli, L.; Rodima, T.; Mäemets, V.; Leito, I.; Koppel, I. A. *J. Org. Chem.* **2005**, 70, 1019.

(21) Nee, M. W.; Smith, J. R. L. *J. Chem. Soc. Dalton Trans.* **1999**, 3373.

(22) Bordwell, F. G. *Acc. Chem. Res.* **1988**, 21, 456.

(23) Luo, Y.–R. *Comprehensive Handbook of Chemical Bond Energies*; CRC Press: Boca Raton, Fl, 2007.

(24) Collman, J. P.; Boulatov, R.; Sunderland, C. J.; Fu, L. *Chem. Rev.* **2004**, 104, 561.

(25) Benoit, D.; Chaplinski, V.; Bradslau, R.; Hawker, C. *J. Am. Chem. Soc.* **1999**, 121, 3904.

(26) (a) Mahanthappa, M. K; Huang, K.; Cole, A. P.; Waymouth, R. M. *Chem. Comm.* **2002**, 502. (b) Huang, K.; Waymouth, R. M. *J. Am. Chem. Soc.* **2002**, 124, 8200. (c) Huang, K.; Han, J. H.; Cole, A. P.; Musgrave, C. B.; Waymouth, R. M. *J. Am. Chem. Soc.* **2005**, 127, 3807.

(27) Chan, K. S.; Li, X. Z.; Dzik, W. I.; de Bruin, B. *J. Am. Chem. Soc.* **2008**, 130, 2051.

(28) (a) Choi, I. K.; Liu, Y.; Wei, Z.; Ryan, M. D. *Inorg. Chem.* **1997**, 36, 3113. (b) Bari, S. E.; Amorebieta, V. T.; Gutiérrez, M. M.; Olabe, J. A.; Doctorovich, F. *J. Inorg. Biochem.* **2010**, 104, 30. (c) Alluisetti, G. E.; Almaraz, E. A.; Amorebieta, V. T.; Doctorovich, F.; Olabe, J. *J. Am. Chem. Soc.* **2004**, 126, 13432.

(29) Gutiérrez, M. M.; Olabe, J. A.; Amorebieta, V. T. *Inorg. Chem.* **2011**, 50, 8817.

(30) (a) Ranguelova, K.; Mason, R. P. *Magn. Reson. Chem.* **2011**, 49, 152. (b) Eberson, L. *J. Chem. Soc. Perkin. Trans. II* **1994**, 171. (c) Makino, K.; Hagiwara, T.; Hagi, A.; Nishi, M.; Murakami, A. *Biochem. Biophys. Res. Commun.* **1990**, 172, 1073. (d) Leinisch, F.; Ranguelova, K.; DeRose, E. F.; Jiang, J.; Mason, R. P. *Chem. Res. Toxicol.* **2011**, 24, 2217.

(31) Lind, J.; Merényi, G. *J. Phys. Chem. A.* **2006**, 110, 192.

(32) Mader, E. A.; Davidson, E. R.; Mayer, J. M. *J. Am. Chem. Soc.* **2007**, 129, 5153.

(33) Whitesides, G. M.; Newirth, T. L. *J. Org. Chem.* **1975**, 40, 3448.

(34) Wagner, R. W.; Lindsey, J. S. *J. Org. Chem.* **1989**, 54, 828.

(35) Jiao, J.; Schmidt, I.; Taniguchi, M.; Lindsey, J. S.; Bocian, D. F. *Langmuir* **2008**, 24, 12047.

(36) Willaredt, J.; Schlemper, H.; Keller, M.; Schmitt, D.; Fritz, H.; Schwesinger, R. *Chem. Ber.* **1994**, 127, 2435.

(37) Brunner, E. J. *J. Chem. Eng. Data* **1985**, 30, 269.

(38) Symons, E A. *Can. J. Chem.* **1971**, 49, 3940.

(39) Warren, J. J.; Mayer, J. M. *Proc. Natl. Acad. Sci.* **2010**, 107, 5282.

(40) Abraham, M. H.; Grellier, P. L.; Prior, D. V.; Duce, P. P. *J. Chem. Soc. Perkin Trans. II* **1989**, 699.

Chapter 3:
Preparation, Structural Characterization and Thermochemistry of an Isolable 4-Aryl Phenoxyl Radical[1]

3.1 Introduction

Stable and transient phenoxyl radical species are important in chemical processes spanning a large range of applications. Examples include tyrosine/tyrosyl radical mediated enzymatic electron transfers and hydrogen atom transfers,[2] in food preservation (such as butylated hydroxytoluene or BHT),[3] and in fundamental studies of proton-coupled electron transfer (PCET)/hydrogen atom transfer (HAT) reactions.[4] While most phenoxyl radicals are transient, sufficiently sterically encumbered phenoxyl radicals can be stable in solution under anaerobic conditions.[5] The 2,6-di-*tert*-butyl-4-phenyl-phenyoxyl radical (^{t}Bu$_2$PhArO$^\bullet$), for instance, was prepared by Müller and co-workers in 1959, and isolated in 78-88% purity.[6] Our laboratory has reported the clean isolation and structural characterization of the 2,4,6-tri-*tert*-butyl-phenoxyl radical (^{t}Bu$_3$ArO$^\bullet$)[7] and the 4,4' coupled dimer of the 2,6-di-*tert*-butyl-4-methoxy-phenoxyl radical (^{t}Bu$_2$MeOArO$^\bullet$).[8] The latter has a very weak C–C bond and is primarily dissociated in solution.

The O-H bond dissociation free energies (BDFEs) of the 2,6-di-*tert*-butyl-6-R-phenols are significantly modulated by the R substituent. The H-atom affinities of the corresponding phenoxyl radicals (described by phenolic O-H BDFEs) range from 73.8 kcal mol^{-1} for the isolable[8] R = OMe species to 80.4 kcal mol^{-1} for the transiently-lived[9] R = NO$_2$ species (BDFEs in toluene), with the R = ^{t}Bu and Ph derivatives being the same within error.[10a] The isolable R = ^{t}Bu and OMe derivatives have proved to be useful hydrogen atom accepting reagents,[11] complimentary due to their different hydrogen atom affinities.[11a,b] With the goal of preparing an isolable phenoxyl radical with a higher H-atom affinity, we report here the preparation, full characterization and thermochemistry of 2,6-di-*tert*-butyl-4-(4'-nitrophenyl)phenoxyl radical, or ^{t}Bu$_2$NPArO$^\bullet$.

3.2. Results and Discussion

3.2.1. Preparation and Crystallographic Characterization

$^{t}Bu_2NPArO^{\bullet}$ was prepared by treating a benzene solution of 2,6-di-*tert*-butyl-4-(4'-nitrophenyl)phenol, $^{t}Bu_2NPArO$-H,[12] with aqueous 1 M sodium hydroxide and potassium ferricyanide under anaerobic conditions. After 30 minutes, removal of the solvent under vacuum, extraction of the dark green material with pentane and crystallization at –30 °C over 24 hours yielded black crystals. These were found to be of high purity from elemental analysis and the ^{1}H NMR spectra showed only minor diamagnetic impurities (<5%) (Figure 3.1).

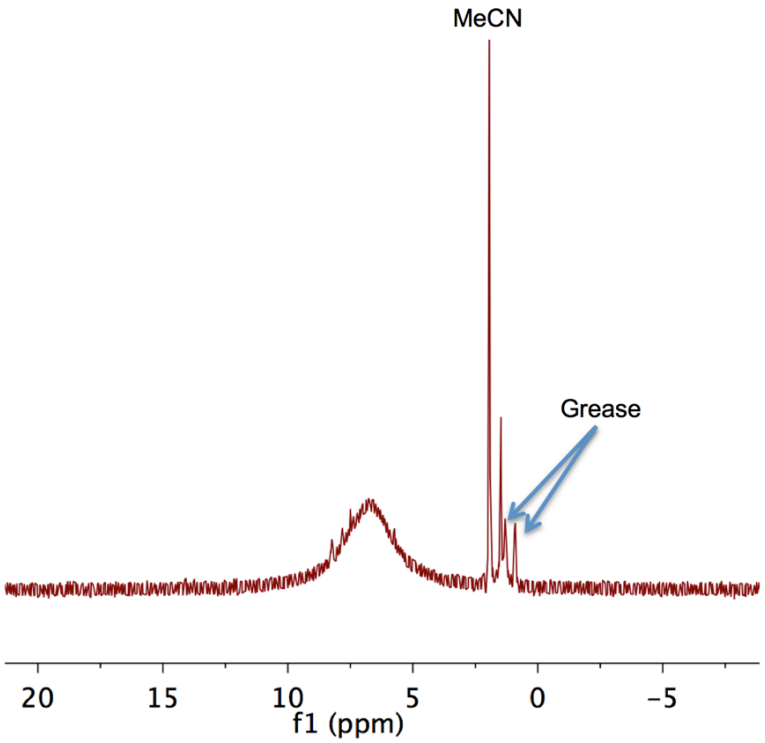

Figure 3.1. ^{1}H NMR Spectrum of $^{t}Bu_2NPArO^{\bullet}$ in acetonitrile-d_3 shows the presence of only minor diamagnetic impurities.

High quality X-ray crystal structures of $^{t}Bu_2NPArO^{\bullet}$ and its parent phenol were collected for structural comparison (Figure 3.2, Table 3.1). This type of direct structural comparison of a phenoxyl radical/phenol has previously not been possible. The parent phenol of the only previously structurally characterized phenoxyl radical, $^{t}Bu_3ArO$-H, was found to be disordered over three positions in its crystals.[7]

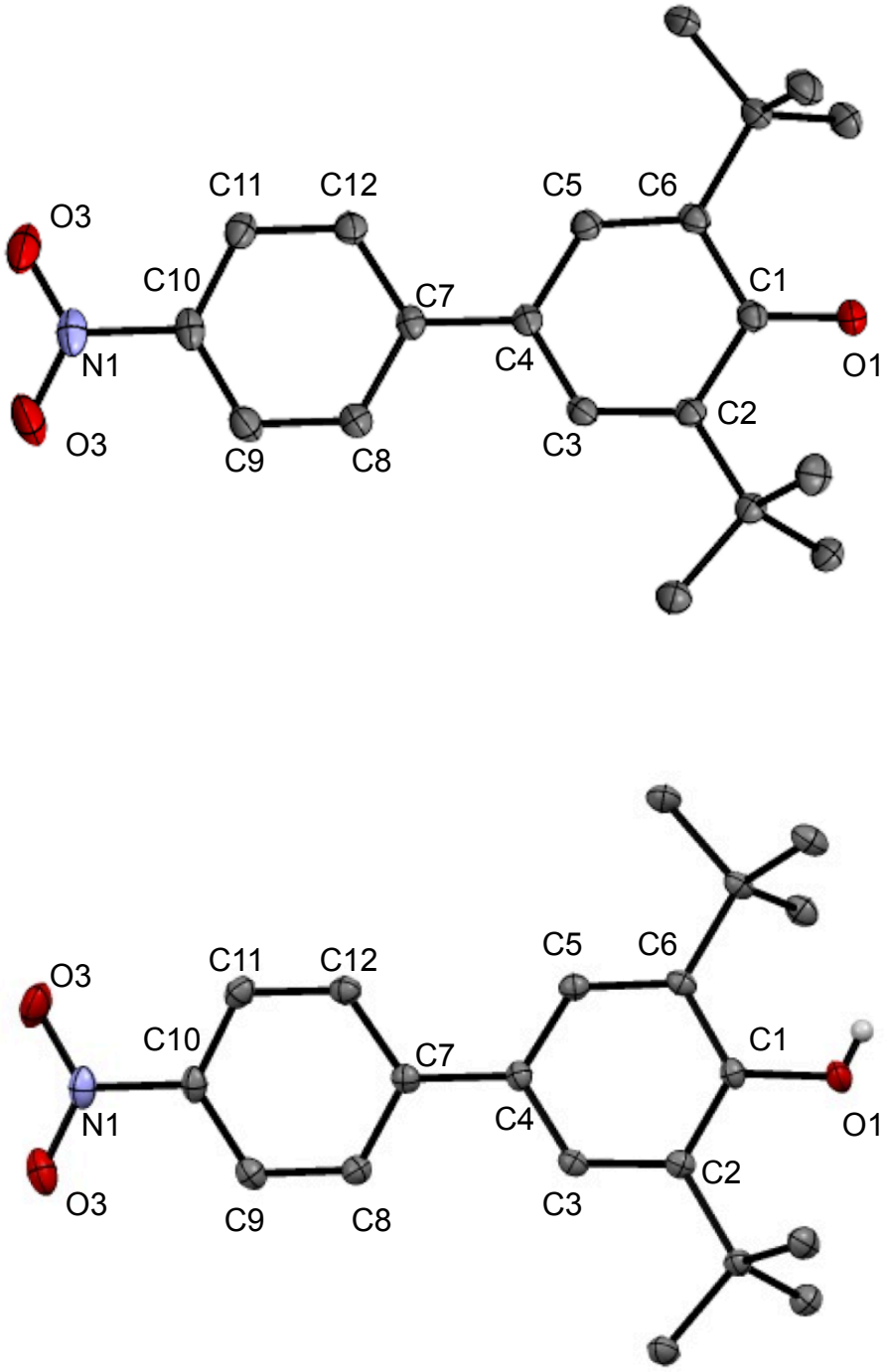

Figure 3.2 ORTEPs of $^{t}Bu_2NPArO^{\bullet}$ (top) and $^{t}Bu_2NPArO$–H (bottom) showing 50% probability thermal ellipsoids and labels for select atoms. All hydrogen atoms except the phenolic hydrogen are omitted for clarity.

The largest difference between the phenoxyl and phenol structures is in the O1-C1 bond distance, 1.251 vs. 1.379 Å. This bond shortening of 0.128 Å is consistent with previous conclusions that phenoxyl radicals have significant ketone character, as suggested by the resonance forms in Scheme 1.[5,7,13] The changes in the phenolic aromatic bond lengths support this model, as the C1-C2 and C1-C6 bond lengthen (avg. 0.062 Å) more than the C3-C4 and C4-C5 bonds (avg. 0.027 Å) while the C2-C3 and C5-C6 bonds shorten (avg. –0.024 Å).

Table 3.1. Select bond lengths (Å) and aryl-aryl torsion angles (deg) of $^{t}Bu_2NPArO^{\bullet}$ and $^{t}Bu_2NPArO$-H.

	$^{t}Bu_2NPArO^{\bullet}$	$^{t}Bu_2NPArO$-H	Difference
O1-C1	1.2509(14)	1.3794(12)	-0.1285(18)
C1-C2	1.4699(17)	1.4100(14)	0.0599(22)
C2-C3	1.3696(16)	1.3944(13)	-0.0248(21)
C3-C4	1.4194(16)	1.3928(13)	0.0266(21)
C4-C5	1.4228(17)	1.3964(13)	0.0264(21)
C5-C6	1.3711(16)	1.3941(14)	-0.0230(21)
C6-C1	1.4751(16)	1.4120(14)	0.0631(21)
C4-C7	1.4754(16)	1.4829(13)	-0.0075(21)
C7-C8	1.4069(17)	1.4008(14)	0.0061(22)
C8-C9	1.3833(17)	1.3861(14)	-0.0028(22)
C9-C10	1.3873(18)	1.3839(15)	0.0034(23)
C10-C11	1.3828(19)	1.3842(15)	-0.0014(24)
C11-C12	1.3842(17)	1.3853(14)	-0.0011(22)
C12-C7	1.4114(16)	1.4023(14)	0.0091(21)
C10-N1	1.4272(16)	1.4672(13)	-0.0400(21)
N1-O2	1.2262(16)	1.2312(13)	-0.0050(21)
N1-O3	1.2289(16)	1.2286(13)	-0.0003(21)
Avg. Ar-Ar torsion angle[b]	17.5(1)	31.9(1)	-14.4(1)

[a] Average aryl-aryl torsion angle refers to the average dihedral angle measured for C5-C4-C7-C2 and C3-C4-C7-C8.

The aryl-aryl linkage is slightly shorter in the radical, by 0.0075(22) Å, suggesting a small quinomethide component (Scheme 1). This is also suggested by the 0.0400(21) shortening of the C10–N1 bond to the nitro group, and the smaller average aryl-aryl torsion angle,[14] of 17.5° in the radical vs. 31.9° observed in the phenol.

Scheme 1. Radical resonance forms of $^{t}Bu_2NPArO^{\bullet}$.

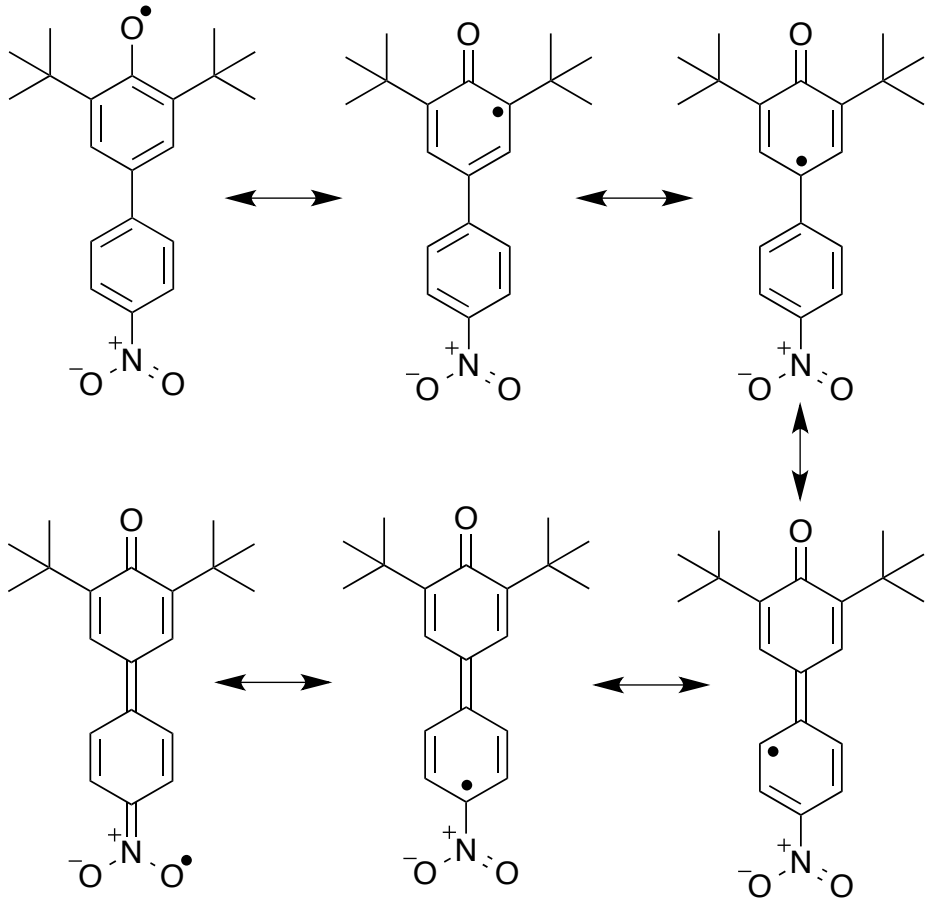

3.2.2. EPR and EPR Simulation of $^{t}Bu_2NPArO^{\bullet}$

The X-band CW EPR spectrum of $^{t}Bu_2NPArO^{\bullet}$ in toluene displays a multi-line pattern centered at g = 2.007(2) that is well modeled by simulation (Figure 3.3). Hyperfine coupling constants were assigned by comparison to previously reported phenoxyl radical data[9] and from the structural changes observed in the crystal structure: $a_{3,5}$(2H) = 1.80 G, $a_{8,12}$(2H) = 1.61 G, $a_{9,11}$(2H) = 0.74 G and a_{NO2}(1N) = 0.50 G.[15] The ^{14}N hyperfine coupling indicates spin density on the nitro group, as depicted in the bottom of Scheme 1. The observed spin density on the nitro group suggests that the thermochemistry of $^{t}Bu_2NPArO^{\bullet}$ should be perturbed from that of the unsubstituted $^{t}Bu_2PhArO^{\bullet}$.

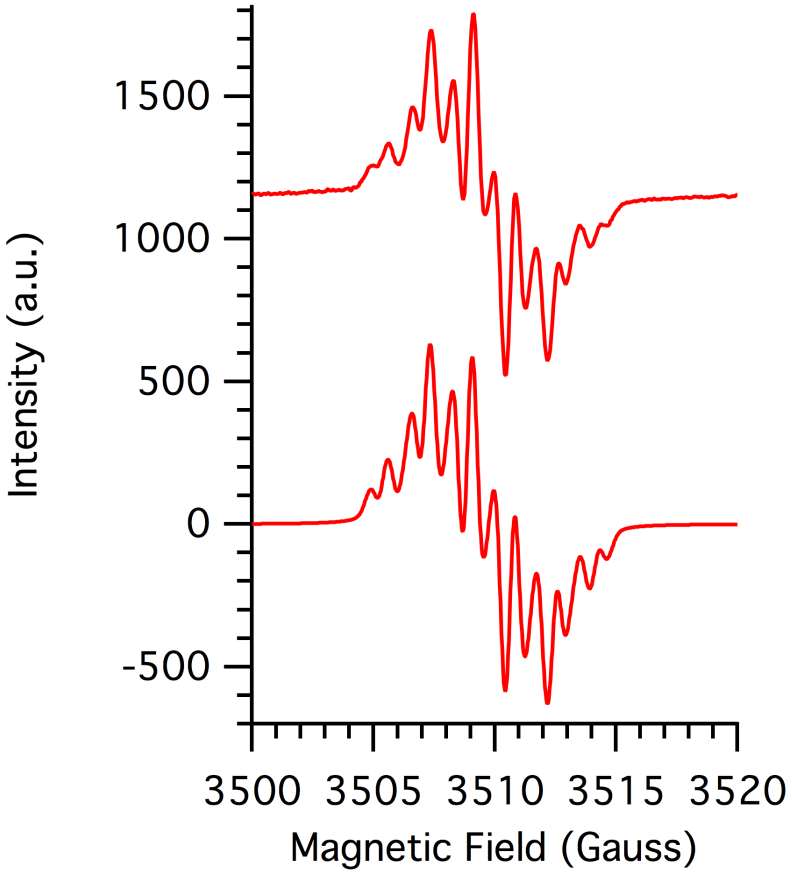

Figure 3.3. X-band EPR spectrum of 1 mM $^{t}Bu_2NPArO^{\bullet}$ in toluene recorded at 25 °C (top) and simulation (bottom).

3.3.3. Determination of the Molar Extinction Coefficient (ε) of $^{t}Bu_2NPArO^{\bullet}$.

The molar extinction coefficient (ε) of $^{t}Bu_2NPArO^{\bullet}$ at 625 and 480 nm was determined in both MeCN and toluene using Beer's law plots with 4 different concentrations of $^{t}Bu_2NPArO^{\bullet}$: ε_{625}(MeCN) = 495 ± 25 M^{-1} cm^{-1}, ε_{480}(MeCN) = 510 ± 25 M^{-1} cm^{-1}; ε_{625}(toluene) = 520 ± 25 M^{-1} cm^{-1}, ε_{480}(MeCN) = 505± 25 M^{-1} cm^{-1}.

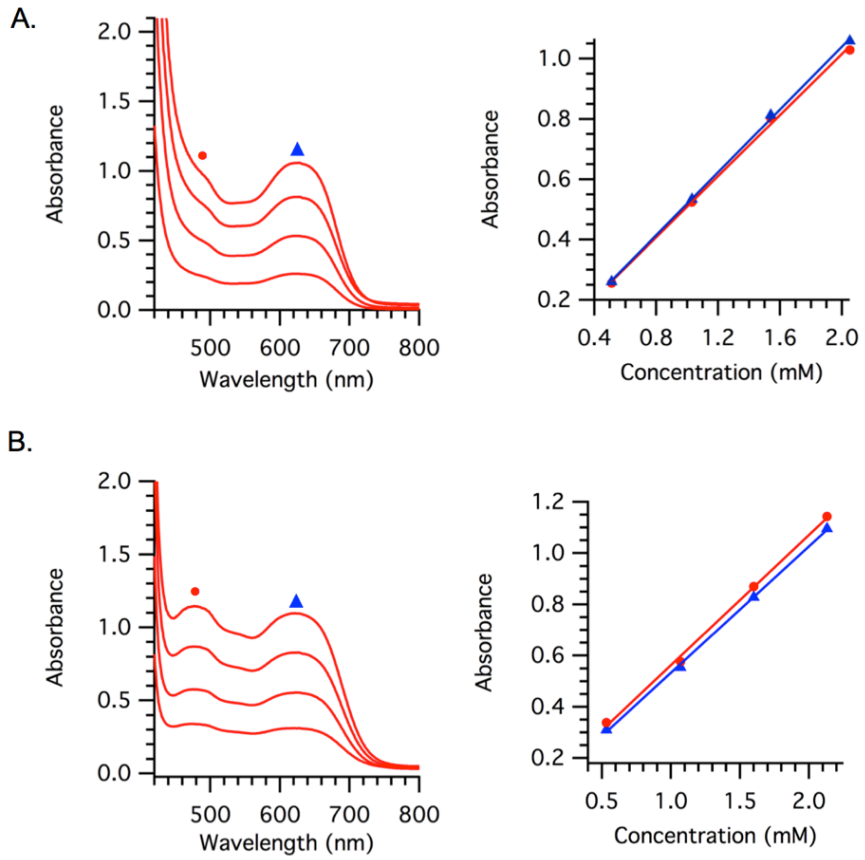

Figure 3.4. Spectra of $^{t}Bu_2NPArO^{\bullet}$ at multiple concentrations and corresponding Beer's Law plots in (A) toluene and (B) MeCN.

While the ε values at both 625 and 480 nm were similar in MeCN and toluene, there is a higher energy absorbance band (*ca*. 400 nm) that displays solvatochromatic behavior. This band is observed at a lower energy in toluene than in MeCN. To confirm this difference in optical spectra was solvent related and not related to decomposition, a cuvette with a 180° Schlenk adapter was filled with $^{t}Bu_2NPArO^{\bullet}$, ~2 mM in toluene and the optical spectrum was collected. The solvent was then removed *in vacuo* and the

residual solid was redissolved in MeCN and the optical spectrum was collected and in agreement with previous MeCN spectra collected. Removal of the MeCN *in vacuo* and redissolution in toluene yielded the same spectrum initially observed.

3.3.4. Thermochemistry of $^{t}Bu_2NPArO(H)$

The O-H BDFE of $^{t}Bu_2NPArO$-H, was determined by equilibration with the thermochemically well-established[4a] $^{t}Bu_3ArO^{\bullet}$ radical. In either acetonitrile-d_3 or toluene-d_8, a known concentration of $^{t}Bu_2NPArO$-H was combined with several different concentrations of $^{t}Bu_3ArO^{\bullet}$ (eq 3.1; Figure 3.5).

$$^{t}Bu_2NPArO\text{-}H + {}^{t}Bu_3ArO^{\bullet} \rightleftharpoons {}^{t}Bu_2NPArO^{\bullet} + {}^{t}Bu_3ArO\text{-}H \qquad (3.1)$$

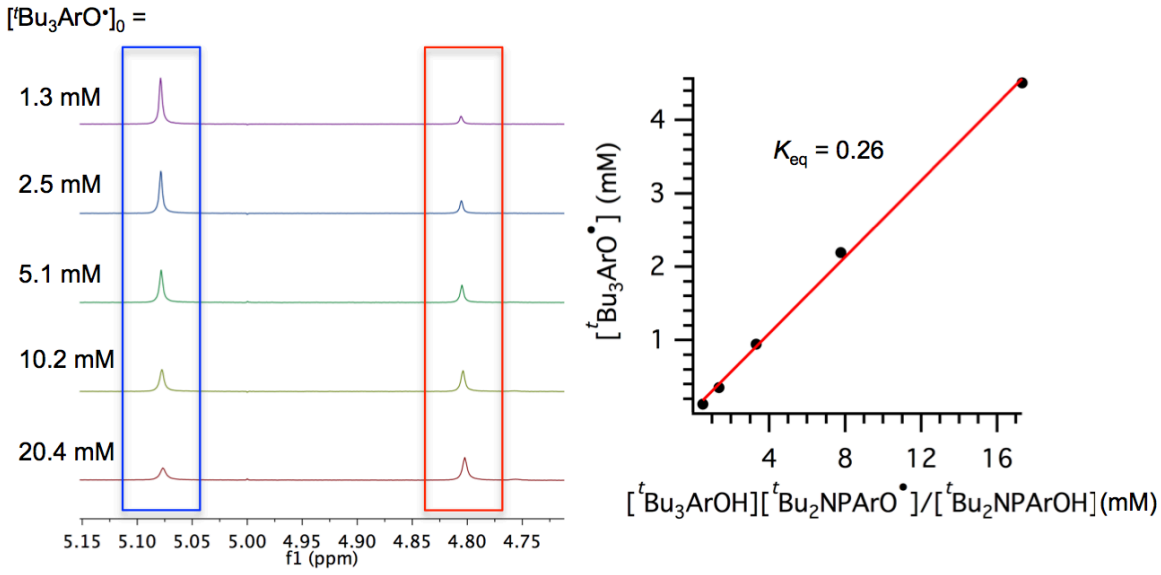

Figure 3.5. ^{1}H NMR spectrum of equilibrium studies between $^{t}Bu_2NPArOH$ and $^{t}Bu_3ArO^{\bullet}$ radical in toluene-d_8. Blue box corresponds to the phenolic O-H signal of $^{t}Bu_2NPArOH$ and the red box corresponds to the phenolic O-H signal of $^{t}Bu_3ArOH$. The plotted equilibrium data is shown in the graph on the right.

Integration of the ^{1}H NMR signals of these solutions gave equilibrium concentrations from which equilibrium constants were determined: K_{eq}(acetonitrile) = 0.25 ± 0.03, K_{eq}(toluene) = 0.26 ± 0.03. Thus the O-H bond in $^{t}Bu_2NPArO$-H is 0.8 ± 0.1 kcal mol^{-1} stronger than that in $^{t}Bu_3ArO$-H in both acetonitrile and toluene. Using the known BDFE values of $^{t}Bu_3ArO$-H[3] and eq 2.2 gives: BDFE($^{t}Bu_2NPArO\text{-}H_{MeCN}$) = 77.8 ±

0.5 kcal mol^{-1} and BDFE(^{t}Bu$_2$NPArO-H$_{tol}$) = 77.5 ± 0.5 kcal mol^{-1}. While this is a small increase, ^{t}Bu$_2$NPArO$^\bullet$ is to our knowledge the thermodynamically strongest isolable, reagent quality organic hydrogen atom abstractor available.

$$\text{BDFE}(^t\text{Bu}_2\text{NPArO-H}) = \text{BDFE}(^t\text{Bu}_3\text{ArO-H}) - \text{RTln}(K_{eq}) \qquad (3.2)$$

Pedulli and co-workers have previously reported an empirical correlation between the O-H bond strengths of 2,6-tbutyl substituted phenols with the EPR hyperfine coupling constants, $a_{3,5}$, of the corresponding phenoxyl radicals.[10a] Figure 3.6 shows a slightly modified version of this correlation using revised BDFE values.[16] The values for ^{t}Bu$_2$NPArO$^\bullet$ follow this correlation very closely.

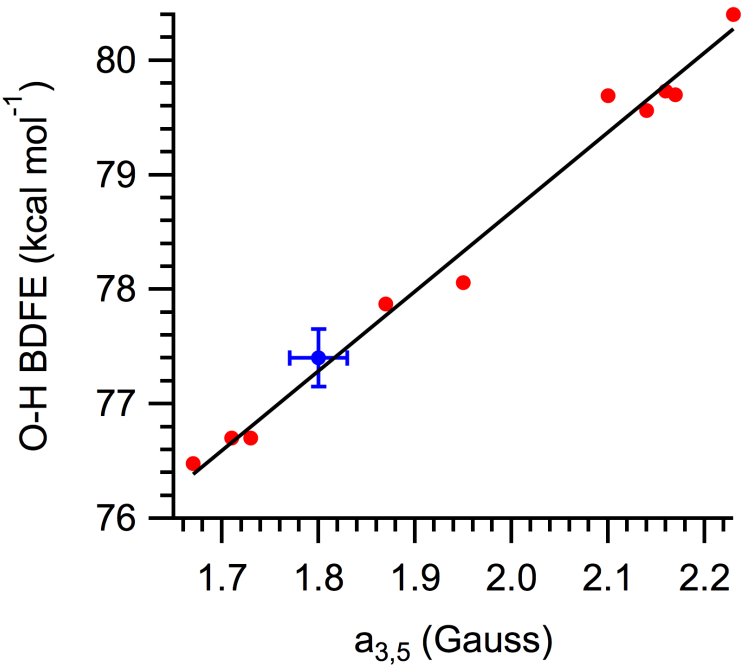

Figure 3.6. 2,6-^{t}Bu$_2$-4-X-ArO-H Bond dissociation free energies (BDFEs) vs. 3,5 hyperfine coupling constant for 2,6-^{t}Bu$_2$-4-X-ArO$^\bullet$ radicals. Data in red are part of the correlation reported in reference 10a (revised to use updated BDFE values[16]); blue data point is ^{t}Bu$_2$NPArO(-H).

Cyclic voltammetry of $^{t}Bu_2NPArO^{\bullet}$ in acetonitrile with 0.1 M $[^{n}Bu_4N]PF_6$ as a supporting electrolyte displayed a reversible couple with $E_{1/2}$ = –0.436 ± 0.010 V vs. $Fc^{+/0}$. This value is 0.26 V more negative than the related $^{t}Bu_3ArO^{0/-}$ potential of –0.70 V vs. $Fc^{+/0}$.[4a] This is much larger than the reported potential difference of only 0.045 V between $^{t}Bu_2PhArO^{\bullet}$ and $^{t}Bu_3ArO^{\bullet}$ in 9:1 $MeCN/H_2O$,[17] illustrating the effect of the nitro substituent on the phenoxyl/phenol thermochemistry.

The cyclic voltammogram of $^{t}Bu_2NPArO$-H displayed an irreversible anodic peak centered at 0.975 ± 0.010 V vs. $Fc^{+/0}$. It is presumably irreversible due to loss of the proton from the highly acidic radical cation.

The reduction potential of $^{t}Bu_2NPArO^{\bullet}$ and the BDFE($^{t}Bu_2NPArO$-H) imply that in acetonitrile the pK_a of $^{t}Bu_2NPArOH$ is 24 ± 0.4 by Hess' Law (eq 3.3). Compared to its parent phenyl-phenol, the nitrophenyl-phenol has a significantly higher acidity[18] and more positive reduction potential. These are both due to the stabilization of the phenoxide anion by the 4-substituted nitrobenzene group. The higher BDFE of $^{t}Bu_2NPArO$-H is due to the shifts in pK_a and $E°$ not exactly offsetting each other, with the nitro group affecting the pK_a less in free energy terms.

$$\text{BDFE} = 1.37\text{p}K_a + 23.06E° + C_G \quad [19] \qquad (3.3)$$

These values can be assembled into a 'square scheme' that describes the PCET thermochemistry of $^{t}Bu_2NPArO$-H (Scheme 2). We have included the irreversible anodic peak potential, $E_{a,p}$, even though it is not a thermochemical value. Using this value to crudely estimate $E°(^{t}Bu_2NPArO\text{-}H^{+/0}) \cong +0.95$ V would imply that the pK_a of the radical cation is about 9 units lower than that of the phenol.

Scheme 2. Thermochemical 'Square Scheme' for $^{t}Bu_2NPArO(-H)$.[a]

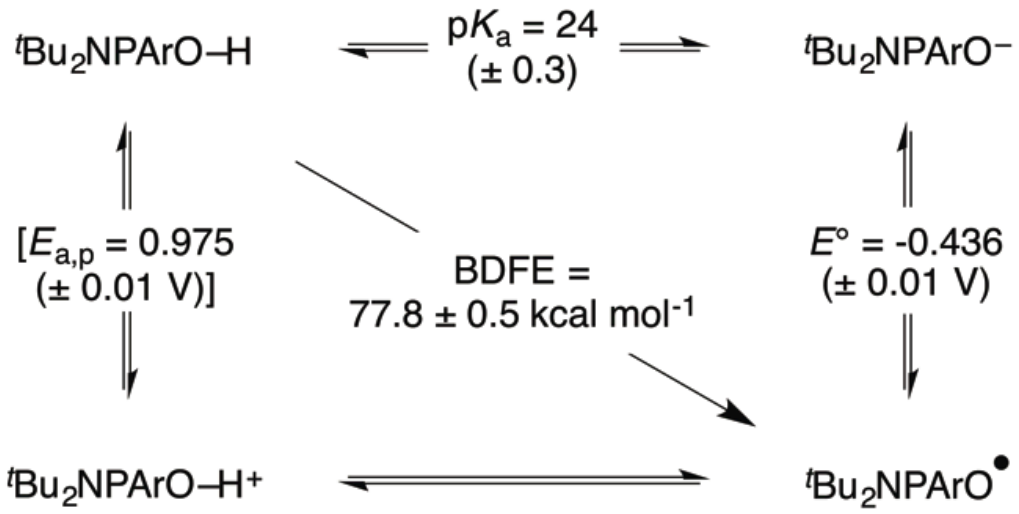

[a] $E_{a,p}$ is bracketed since it refers to an irreversible anodic peak potential and is not a thermochemical value.

In conclusion, the 4-nitrophenyl-phenoxyl radical $^{t}Bu_2NPArO^{\bullet}$ is a previously unreported phenoxyl radical that is easily prepared in high purity and reasonable yield. Equilibrium studies show that the $^{t}Bu_2NPArO$-H BDFE is modestly stronger than that of its unsubstituted isolable relative, $^{t}Bu_2PhArO^{\bullet}$ ($\Delta BDFE_{toluene}$ = 0.8 kcal mol^{-1}). $^{t}Bu_2NPArO$-H has the highest reported BDFE of any isolable organic hydrogen atom acceptor: 77.8 ± 0.5 kcal mol^{-1} in acetonitrile and 77.5 ± 0.5 kcal mol^{-1} in toluene. The combination of easy isolation of the phenoxyl radical in pure form and its relatively high hydrogen atom affinity should make this a useful reagent for studying hydrogen atom transfer reactions.

3.4. Experimental

3.4.1. Materials

Unless otherwise noted all chemicals were purchased from commercial sources and used without purification. Toluene was dried using a "Grubb's type" Seca Solvent System. Acetonitrile was purchased from Burdick & Jackson (low-water brand) and stored in an argon-pressurized glovebox plumbed directly into the glovebox. Toluene-d_8 and acetonitrile-d_3 were, dried over NaK and CaH_2, respectively, and vacuum distilled. $^{t}Bu_3ArO^{\bullet}$[7] and $^{t}Bu_2NPArOH$[20] were prepared following literature methods.

3.4.2. Instrumentation

All NMR spectra were collected on 500 MHz spectrometers and chemical shifts referenced to TMS using residual solvent peaks. The reported EPR spectrum was collected using an X-band spectrometer at room temperature in toluene. Simulation of the spectrum was preformed using the W95EPR program.

3.4.3. Synthesis of $^{t}Bu_2NPArO^{\bullet}$

A 100 ml two neck roundbottom flask was charged with 467 mg (1.43 mmol) of $^{t}Bu_2NPArOH$ dissolved in ~15 mL of benzene, 5 mL of 1 M NaOH and a stir bar. The flask was fitted with a 180° Schlenk adapter on one neck and a solid addition funnel containing 1.20 grams (3.64 mmol) of solid $K_3Fe(CN)_6$ on the other neck. The biphasic mixture was degassed by 3 sequential freeze-pump-thaw cycles. After degassed, the mixture was frozen and the $K_3Fe(CN)_6$ was added. The frozen mixture was allowed to thaw at room temperature and left to stir. After 1 hour of stirring, the solvents were removed in vacuo and extracted with pentane. Crystals were grown from a saturated pentane solution at -30 °C. Yield: 279 mg, 52%. Anal. Calcd. for $C_{20}H_{24}NO_3$: C, 73.59; H, 7.41; N, 4.29. Found: C, 73.88; H, 7.60; N, 4.34.

3.5. Crystallographic Data

Table 3.2 Crystallographic data for $^{t}Bu_2NPArO^{\bullet}$ and $^{t}Bu_2NPArO–H$

	$^{t}Bu_2NPArO^{\bullet}$	$^{t}Bu_2NPArO–H$
Empirical formula	$C_{20}H_{24}NO_3$	$C_{20}H_{25}NO_3$
Formula weight	326.40	327.41
Temperature	100(2) K	100(2) K
Wavelength	0.71073 Å	0.71073 Å
Crystal description	Black piece	Yellow piece
Crystal system	Orthorhombic	Monoclinic
Space group	P b c a	P 2_1/n
Unit cell dimensions		
a (Å)	12.0741(8)	11.2752(4)
b (Å)	13.1671(8)	10.1733(4)
c (Å)	22.1093(14)	15.1181(5)
α (deg)	90	90
β (deg)	90	94.113(2)
γ (deg)	90	90
Volume ($Å^3$)	3515.0(4)	1729.67(11)
Z	8	4
Density (calculated) (Mg/m^3)	1.234	1.257
Absorption coefficient (mm^{-1})	0.082	0.084
F(000)	1400	704
Crystal size (mm^3)	0.40 x 0.10 x 0.01	0.60 x 0.20 x 0.10
θ range for data collection	2.47 to 28.37°.	2.18 to 28.38°.
Index ranges	-16<=h<=16, -17<=k<=17, -29<=l<=29	-15<=h<=15, -13<=k<=13, -20<=l<=20
Reflections collected	116007	59096
Independent reflections	4383	4313
R_{int}	0.0472	0.0297
Completeness to θ = 25.00°	100.0 %	100.0 %
Max/min. transmission	0.9992/0.9678	0.9917/0.9514
Refinement method	Full-matrix least-squares on F^2	
Data / restraints / parameters	4383/0/223	4313/1/227
Goodness-of-fit on F^2	1.008	1.040
Final R	0.0398,	0.0364
R_w	0.1022	0.0970
Largest diff. peak and hole ($e/Å^{-3}$)	0.366/-0.191	0.362/-0.233

Notes for Chapter 3

---

(1) Unless noted otherwise, this chapter has been published in: Porter, T. R.; Kaminsky, W.; Mayer, J. M. *J. Org. Chem.* **2014**, 79, 9451.

(2) (a) Styring, S.; Sjöholm, J.; Mamedov, F. *Biochim. Biophys. Acta* **2012**, 1817, 76. (b) Reece, S. Y.; Nocera, D. G. *Annu. Rev. Biochem.* **2009**, 78, 673. (c) McEvoy, J. P.; Brudvig, G. W. *Chem. Rev.* **2006**, 106, 4455. (d) Whittaker, J. W. *Chem. Rev.* **2003**, 103, 2347.

(3) Babich, H. *Environ. Res.* **1982**, 29, 1.

(4) (a) Warren, J. J.; Tronic, T. T.; Mayer, J. M. *Chem. Rev.* **2010**, 110, 6961. (b) Weinberg, D. R.; Gagliardi, C. J.; Hull, J. F.; Murphy, C. F.; Kent, C. A.; Westlake, B. C.; Paul, A.; Ess, D. H.; McCafferty, D. G.; Meyer, T. J. *Chem. Rev.* **2012**, 112, 4016.

(5) Altwicker, E. R. *Chem. Rev.* **1967**, 67, 475.

(6) (a) Müller, E.; Schick, A.; Scheffler, K. *Chem. Ber.* **1959**, 92, 474. (b) Related 4-tolyl- and 4-anisyl-phenoxyl radicals have been reported but not isolated; See reference 4.

(7) Manner, V. W.; Markle, T. F.; Freudenthal, J. H.; Roth, J. P.; Mayer, J. M. *Chem. Commun.* **2008**, 256.

(8) Wittman, J. M.; Hayoun, R.; Kaminsky, W.; Coggins, M. K.; Mayer, J. M. *J. Am. Chem. Soc.* **2013**, 135, 12956.

(9) Cook, C. D.; Gilmour, N. D. *J. Org. Chem.* **1960**, 25, 1429.

(10) (a) Brigati, G.; Lucarini, M.; Mugnaini, V.; Pedulli, G. F. *J. Org. Chem.* **2002**, 67, 4828. (b) Lucarini, M.; Pedrielli, P.; Pedulli, G. F.; Cabiddu, S.; Fattuoni, C. *J. Org. Chem.* **1996**, 61, 9259. (c) Lucarini, M.; Pedulli, G. F. *Chem. Soc. Rev.* **2010**, 39, 2106. (d) Reiker, A.; Scheffler, K. *Justus Liebigs Ann. Chem.* **1965**, 689, 78.

(11) (a) Waidmann C. R.; Zhou, X.; Tsai, E. A.; Kaminsky, W.; Hrovat, D. A.; Borden, W. T.; Mayer, J. M. *J. Am. Chem. Soc.* **2009**, 131, 4729. (b) Warren, J. J.; Mayer, J. M. *Proc. Natl. Acad. Sci.* **2010**, 107, 5282. (c) Valdez, C. N.; Braten, M. B.; Soria, A.; Gamelin, D. R.; Mayer, J. M. *J. Am. Chem. Soc.* **2013**, 135, 8492. (d) Schrauben, J. N.; Hayoun, R.; Valdez, C. N.; Braten, M. M.; Fridley, L.; Mayer, J. M. *Science*

2012, 336, 1298. (e) Manner, V. W.; Lindsey, A. D.; Mader, E. A.; Harvey, J. N.; Mayer, J. M. *Chem. Sci.* **2012**, 3. 230. (f) Warren, J. J.; Mayer, J. M. *J. Am. Chem. Soc.* **2011**, 133, 8544. (g) Mader, E. A.; Manner, V. W.; Markle, T. F.; Wu, A.; Franz, J. A.; Mayer, J. M. *J. Am. Chem. Soc.* **2009**, 131, 4335.

(12) Chern, Y. T.; Ju, M. H. *Macromolecules* **2009**, 42, 169.

(13) (a) O'Malley, P. J. *J. Phys. Chem. B.* **2002**, 106, 12331. (b) Xie, C.; Lahti, P. M.; George, C. *Org. Lett.* **2000**, 2, 3417.

(14) Average torsion angle refers to the average dihedral angle measured for atoms C3-C4-C7-C8 and C5-C4-C7-C12.

(15) EPR hyperfine coupling constants reported have an assumed error margin of ~ ± 0.05 Gauss.

(16) The correlation in reference 9a used bond dissociation enthalpies (BDEs), which were determined from equilibration experiments. ΔBDE values were obtained from these equilibrium constants, and then converted to BDEs using a gas phase BDE of ^{t}Bu$_3$ArO-H. Here, we take their equilibrium constants to be a ΔBDFEs and scale them to the reported BDFE of ^{t}Bu$_3$ArO-H in benzene; ref 3.

(17) (a) Steuber, F. W.; Dimroth, K. *Chem. Ber.* **1966**, 99, 258. (b) Values reported in (a): $E_{1/2}(^{t}Bu_2PhArO^{\bullet/-}) = -0.014$ V; $E_{1/2}(^{t}Bu_3ArO^{\bullet/-}) = -0.059$ V (both vs Ag/AgCl; in 9:1 MeCN/H_2O; 0.01 *m* [Me_4N^+][OH^-], 0.01 *m* [Me_4N^+][Cl^-]).

(18) The pK_a of ^{t}Bu$_2$PhArO-H is taken to be roughly equal to the pK_a of ^{t}Bu$_3$ArO-H (~28 in MeCN; ref. 3) since their BDFEs and $E°$ are roughly equivalent.

(19) C_G is a constant that contains the free energy of formation of H$^{\bullet}$, free energy of solvation of H$^{\bullet}$, as well as the nature of the electrode. In MeCN, C_G = 54.9 kcal mol^{-1}. A more detailed description can be found in reference 3.

(20) Chern, Y. T.; Ju, M. H. *Macromolecules*, **2009**, 42, 169.

Chapter 4:
Synthesis, Radical Reactivity and Thermochemistry of Monomeric Copper(II) Alkoxide Complexes: Insights into Copper/Radical Catalysis of Alcohol Oxidation[1]

4.1. Introduction

Copper/radical mediated alcohol oxidation has been studied extensively in biological[2] and synthetic organic systems.[3] In these systems, the $2H^+/2e^-$ oxidation of an alcohol to an aldehyde or ketone is achieved using oxidizing equivalents from copper(II) and an oxyl radical. In biology, this reaction is carried out by the fungal contained enzyme, galactose oxidase. Galactose oxidase performs this reaction with copper(II) and an antiferromagnetically coupled tyrosine derived oxyl radical.[2] In synthetic organic applications, alcohol oxidation is typically achieved with the use of an L_nCu^{II} complex and a nitroxyl radical such as TEMPO (2,2,6,6-tetramethylpiperidinyl).[3]

Both galactose oxidase and Cu/nitroxyl systems have been well studied and catalytic schemes have been constructed for both. These have been derived from a combination of kinetic and computational data.[2,3] In both examples, the consensus mechanisms of alcohol oxidation involve the formation of a copper(II) alkoxide intermediate through a protolytic ligand exchange pathway. The subsequent reaction in both cases involves the net transfer of one electron to copper(II) and a hydrogen atom (H^+/e^-) from the α-C–H position of the alkoxide to the radical.

Scheme 4.1.

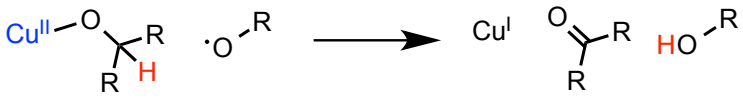

Previous kinetic studies in both systems have shown that deuteration of the α-position of the alcohol substrate results in a large primary KIE, suggesting a hydrogen atom transfer event is involved in the rate determining step.[2i,3d] This is interesting from a thermodynamic standpoint since typically the bond strength of the α-C–H bond in an alcohol is much stronger than the O–H bond formed by the oxyl radical. The α-C–H bond dissociation enthalpies (BDEs) of most primary and secondary aliphatic alcohols are ~95 kcal mol^{-1} while the O–H bond formed in TEMPO or in phenoxyl radical are much weaker with O–H BDEs of ~70 and ~87 kcal mol^{-1}, respectively.[4] This implies that a rate determining hydrogen atom transfer from the α-C–H position to an oxyl radical should be

thermochemically unfavorable and that Cu(II) must be playing a substantial role in modulating the thermochemistry of the alkoxide ligand in these systems.

As such, the mechanism by which the hydrogen atom and electron are transferred from the alkoxide intermediate has attracted considerable attention in both bioinorganic and synthetic organic chemistry. Several mechanisms have been proposed.

In galactose oxidase, the mechanism has not yet fully been resolved but it is generally thought that alkoxide oxidation proceeds either through (*i*) a rate determining HAT from the α-C–H position to the tyrosyl radical, generating a short lived copper(II)-ketyl intermediate or (*ii*) through a concerted mechanism in which both HAT and ET occur in a single kinetic step (Scheme 4.2).[2a,i] Computational studies have suggested mechanism (*ii*) may be operative but that the transition state has mostly HAT character.[2d]

Scheme 4.2. Stepwise vs concerted mechanisms for copper/radical alcohol oxidation

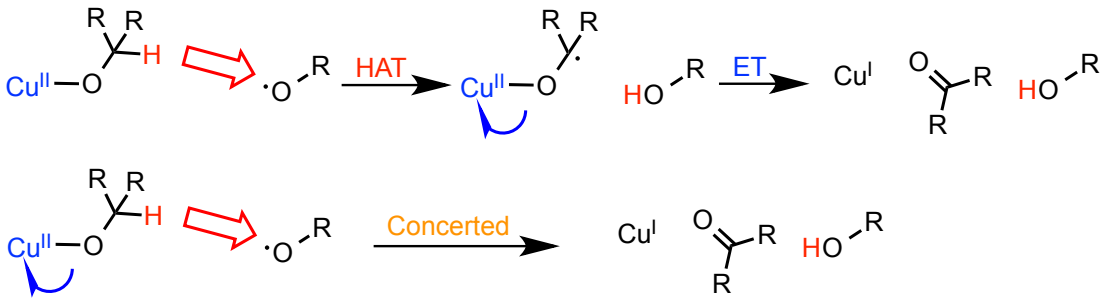

In nitroxyl radical/copper systems, it has previously been suggested that a similar sort of concerted HAT/ET may be involved.[3d] A recent computational study by Stahl and co-workers has suggested that instead, alkoxide oxidation involves the pre-coordination of the nitroxyl radical η^1 to copper(II) which is followed by a concerted $H^+/2e^-$ transfer reaction (Scheme 4.3).[3f]

Scheme 4.3. Copper/Nitroxyl Alkoxide Oxidation Proposed by Stahl

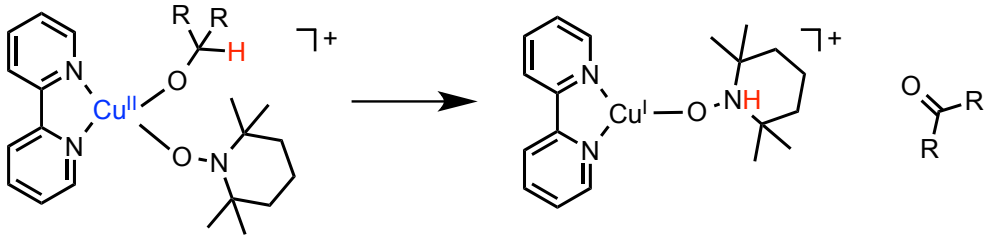

One of the major challenges associated with studying this mechanism – and why theoretical studies have been relied on so heavily – is because of the synthetic challenges

associated with preparing copper(II) alkoxide model complexes for stoichiometric reactivity studies. A literature survey reveals there are very few examples of monomeric copper(II) alkoxide complexes. Nearly all existing examples involve tertiary alkoxides,[5] highly fluorinated hexafluoroisopropoxides,[6] or exotic ancillary ligands.[7] Because of this, mechanistic interpretations of both galactose oxidase and Cu/nitroxyl systems have been limited to what can be extrapolated from kinetic studies of the overall catalytic reaction and from computational methods.

We report here the preparation and characterization of a series of isolable copper(II) alkoxide complexes as models for potential intermediates in galactose oxidase and copper/nitroxyl alcohol oxidation systems. These include $Tp^{\S}Cu^{II}$-OCH_2CF_3 with $Tp^{\S}$ = Tp^{tBu} = hydro-*tris*(3-*tert*-butyl-pyrazol-1-yl)borate **(1)** and $Tp^{\S}$ = Tp^{tBuMe} = hydro-*tris*(3-*tert*-butyl-5-methyl-pyrazol-1-yl)borate **(2)**. We found both **(1)** and **(2)** were competent hydrogen atom *acceptors* capable of cleaving X–H bonds with bond dissociation free energies (BDFEs) up to 76.7 and 70.7 kcal mol^{-1} in toluene, respectively. In toluene, the products of these reactions were ½ $[Tp^{\S}Cu^{I}]_2$, $HOCH_2CF_3$ and $^{\bullet}X$.

Using these reactions as thermodynamic benchmarks, we were able to calculate '*effective* BDFEs' for the α-C–H bonds of the copper(II) bound alkoxide ligands using Hess' Law assumptions. These values, which encompass the α-C–H BDFEs of the alkoxide ligands, ET to Cu(II) and the formation of $[Tp^{\S}Cu^{I}]_2$, were found to be quite weak with high limits of ~43 kcal mol^{-1} for **(1)** and ~49 kcal mol^{-1} for **(2)**. Treatment of **(1)** with the $^{t}Bu_3ArO^{\bullet}$ (2,4,6-tri-*tert*-butylphenoxyl radical; phenolic O–H $BDFE_{toluene}$ = 76.8 kcal mol^{-1}) resulted in the net transfer of $^{\bullet}OCH_2CF_3$ generating an unusual dieneone product and ½ $[Tp^{tBu}Cu^{I}]_2$. Treatment of **(2)** with $^{t}Bu_3ArO^{\bullet}$ resulted in no reaction despite HAT/ET being exoergic by ~25 kcal mol^{-1}. In toluene, **(2)** was also unreactive with TEMPO (TEMPO–H $BDFE_{toluene}$ = 65.2 kcal mol^{-1}).

From these results, we conclude the alkoxide α-C–H bond is not strongly modulated by the oxidizing capability of the Cu(II) metal center. Unlike many other radical reactions, overall thermodynamics are not a primary predictor for reactivity in HAT/ET coupled reaction, if such a reaction exists.

4.2. Results

4.2.1 Preparation and Characterization of Copper(II) Alkoxides:

The addition of one equivalent of DBU (1,8-diazabicycloundec-7-ene) and a slight excess of TFE (2,2,2-trifluoroethanol) to $Tp^{tBu}Cu^{II}$-OTf in dichloromethane yields $Tp^{tBu}Cu^{II}$-OCH_2CF_3 **(1)**. This was evident by the dramatic color change from deep purple to orange as well as the appearance of new paramagnetically shifted pyrazole resonances in the ^1H NMR spectrum. Recrystallization from saturated pentane solutions at –30 °C yields large red-orange crystals. The related complex, $Tp^{tBuMe}Cu^{II}$-OCH_2CF_3 **(2)** was prepared in the same manner by co-worker Dany Capitao.

The X-ray structures of both **(1)** and **(2)** were found to be quite similar. Both exhibit a 4-coordinate copper center and trigonal monopyramidal geometry consisting of 2 short pyrazole N–Cu bonds and a short alkoxide O–Cu bond in the basal plane with the third pyrazole nitrogen binding axially with a notably longer Cu–N bond (Figure 4.1). The degree of geometric distortion from tetrahedral can be described quantitatively with the pyramidalization normalization parameter, τ ($\tau = [\Sigma(L_{basal}\text{-}M\text{-}L_{basal}) - \Sigma(L_{basal}\text{-}M\text{-}L_{axial})]/90$; $\tau = 0$ for a perfect tetrahedral and t = 1 for perfect trigonal monopyramidal).[8] The τ values for **(1)** and **(2)** were both 0.76. This was in contrast to $Tp^{tBu}Cu$-X and $Tp^{tBuMe}Cu^{II}$-X complexes previously reported by Tolman[9] and Parkin[10] which have much more tetrahedral geometries (τ ~0.4) but similar to $Tp^{iPriPr}Cu^{II}$-X complexes reported by Kitajima/Fujisawa (τ ~0.65-0.8)[11] (Table 4.1, Table 4.2).

Table 4.1. τ values and EPR Signals for Various $TpCu^{II}$-X complexes

Complex	τ value	EPR Signal	Reference
$Tp^{tBu}Cu^{II}$-OCH_2CF_3 **(1)**	0.76	Axial	This work
$Tp^{tBuMe}Cu^{II}$-OCH_2CF_3 **(2)**	0.76	Axial	This work
$Tp^{tBuMe}Cu^{II}$-$OCH(CH_3)CF_3$ **(3)**	0.63	Rhombic	This work
$Tp^{tBu}Cu^{II}$-Cl	0.47	Rhombic	10a, 9d
$Tp^{tBu}Cu^{II}$-OTf	0.39	Rhombic	9a
$Tp^{tBuMe}Cu^{II}$-Cl	0.44	NR	10b
$Tp^{iPriPr}Cu^{II}$-OOCm[a,b]	0.75	Axial	11b, 11f
$Tp^{iPriPr}Cu^{II}$-$SArF_5$[a]	0.64	Axial	11a
$Tp^{iPriPr}Cu^{II}$-S^{t}Bu[a]	0.82	Axial	11c

[a]Tp^{iPriPr} = hydro-t*ris*(3,5-di-*iso*-propyl-pyrazolyl)borate. [b]OOCm = cumene peroxide. NR = not reported.

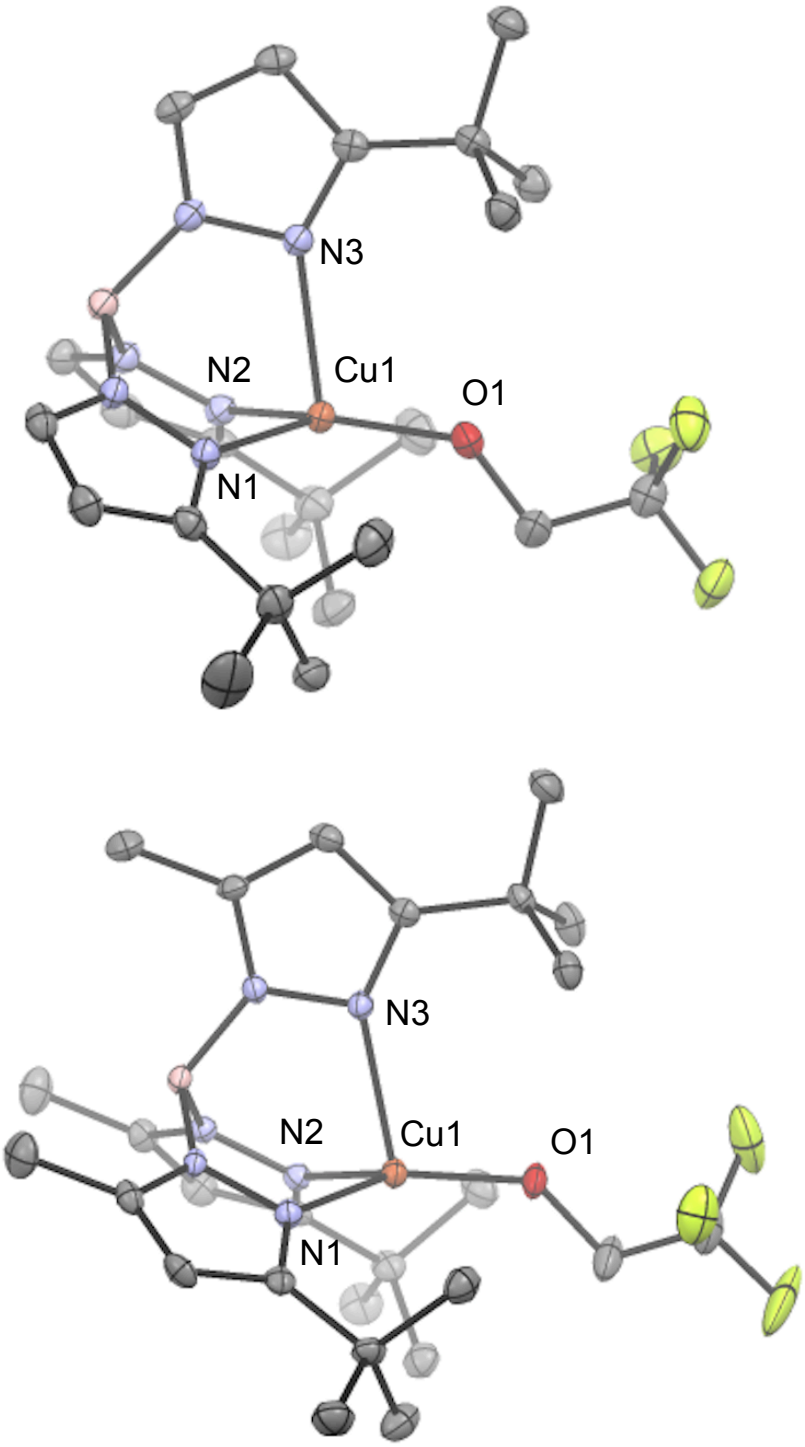

Figure 4.1. ORTEPs of $Tp^{tBu}Cu^{II}$-OCH_2CF_3 **(1)** (top) and $Tp^{tBuMe}Cu^{II}$-OCH_2CF_3 **(2)** (bottom) showing 50% probability thermal ellipsoids and select atom labels. Hydrogen atoms are omitted for clarity.

Table 4.2. Select interatomic distances (Å) and angles (deg) of **(1)** and **(2)**.

Bond	**(1)**	**(2)**
N1-Cu1	1.9717(11)	1.951(2)
N2-Cu1	1.9638(11)	1.964(2)
N3-Cu1	2.2270(11)	2.230(2)
O1-Cu1	1.8324(10)	1.840(2)
Angle		
N1-Cu1-N2	94.21(5)	93.77(10)
N1-Cu1-N3	91.15(4)	91.04(9)
N1-Cu1-O1	127.18(5)	133.35(10)
N2-Cu1-N3	90.92(4)	91.66(9)
N2-Cu1-O1	134.28(5)	128.58(10)
N3-Cu1-O1	104.96(4)	104.44(9)

In solution, these distortions are rapidly fluxional and **(1)** and **(2)** have effectively C_{3v} symmetry as indicated by the equivalent pyrazole signals observed in their ^{1}H NMR spectra (Figure 4.2). This NMR pattern is the same as was seen for related complexes with more tetrahedral solid state structures (Table 4.3). We found these relatively sharp spectral features useful for describing the solution structure of these molecules as well as for monitoring reactions with radical transfer reagents (*vida infra*).

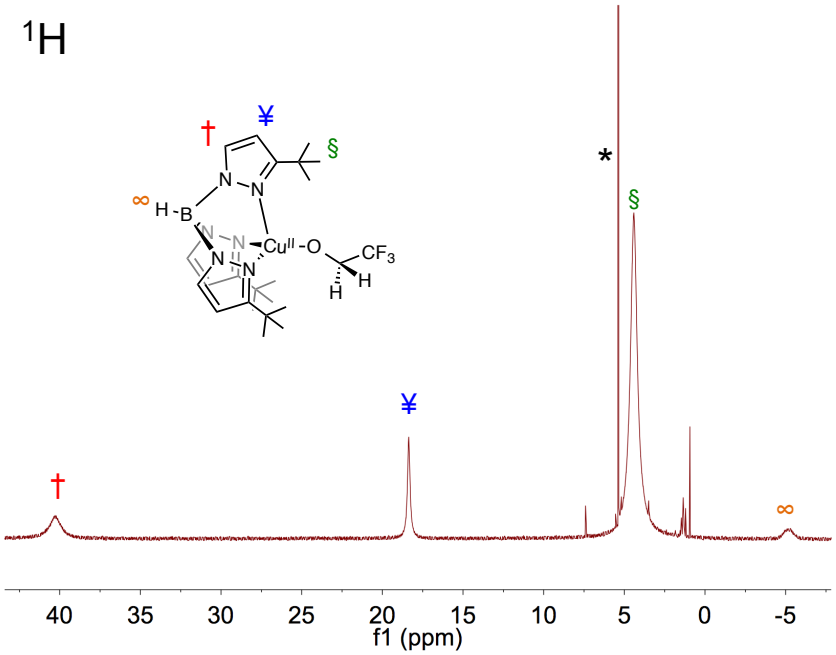

Figure 4.2. ^{1}H NMR spectrum of **(1)** in DCM-d_2. Residual solvent signal shown with *.

Table 4.3. ^{1}H NMR Resonances of related Tp$^{t\mathrm{Bu}}$Cu$^{\mathrm{II}}$-X and Tp$^{t\mathrm{BuMe}}$Cu$^{\mathrm{II}}$-X.[a,b]

Complex	*Pz-4-H*	*Pz-5-H*	*Pz-3-^{t}Bu*	B-H
Tp$^{t\mathrm{Bu}}$Cu$^{\mathrm{II}}$-Cl[c,9a]	49.3	24.1	4.8	-4.4
Tp$^{t\mathrm{Bu}}$Cu$^{\mathrm{II}}$-OTf[c,9a]	56.5	21.0	5.5	-5.4
(1)	40.5	18.4	4.4	-5.4
(3)	39.6	19.3	4.0	-4.6
	Pz-4-H	*Pz-5-CH$_3$*	*Pz-3-^{t}Bu*	B-H
Tp$^{t\mathrm{BuMe}}$Cu$^{\mathrm{II}}$-Cl[10b]	53.0	4.1	4.6	-5.1
Tp$^{t\mathrm{BuMe}}$Cu$^{\mathrm{II}}$-OTf	59.0	10.4	4.5	-6.0
(2)	43.3	2.0	4.3	-5.9

[a] Values at 25° C. NMR spectra in dichloromethane-d_2, with chemical shifts in ppm; [b] NMR assignments for pz-4-H and pz-5-H were made by comparison to Tp$^{t\mathrm{BuMe}}$Cu$^{\mathrm{II}}$ analogues. N.R. = not reported. [c] Complexes previously reported but without NMR characterization.

Although monomeric copper(II) alkoxide complexes like **(1)** and **(2)** have been frequently invoked as intermediates in copper/radical alcohol oxidation catalysis, there are very few well characterized, isolable examples present in the literature. Consistently, we found the preparation of these complexes to be deceptively sensitive. Treatment of either Tp$^{t\mathrm{Bu}}$Cu$^{\mathrm{II}}$-Cl or Tp$^{t\mathrm{Bu}}$Cu$^{\mathrm{II}}$-OTf with thallium or sodium alkoxide salts resulted in a substantial amount of copper displacement from the ligand to make Tp$^{t\mathrm{Bu}}$Tl or Tp$^{t\mathrm{Bu}}$Na,[12] respectively, and presumably mixed Cu$^{\mathrm{II}}$ salts.

Using the Tp$^{t\mathrm{Bu}}$Cu$^{\mathrm{II}}$-OTf/DBU/ROH protocol for non-fluorinated alcohols (ROH = EtOH, ^{i}PrOH, or BnOH) generated what we have tentatively assigned as the corresponding Tp$^{t\mathrm{Bu}}$Cu$^{\mathrm{II}}$-OR complexes (as suggested by ^{1}H NMR and visible color change). These were only transiently stable and could not be isolated. With the fluorinated alcohol 1,1,1-trifluoro-2-propanol (HOCH(CH$_3$)CF$_3$), the corresponding Tp$^{t\mathrm{Bu}}$Cu-OCH(CH$_3$)CF$_3$ complex **(3)**, could be prepared and fully characterized (see Experimental). This structure was slightly more tetrahedral (τ = 0.63) than **(1)** or **(2)**. In solution at room temperature (15.3 mM; toluene-d_8 or DCM-d_2/1% MeCN-d_3 (v/v)), **(3)** was unstable to decomposition on the timescale of most reactions of interest (~10 hours) and we chose to focus our studies primarily on **(1)** and **(2)**.

4.2.2. Spectroscopic studies of (1) and (2)

The X-band CW EPR spectra of both **(1)** and **(2)** in toluene glasses at 120 K displayed axial $g_{\|} > g_{\perp}$ signals similar to those observed for the structurally related Kitajima/Fujisawa examples.[11] For **(1)**, $g_{\|} = 2.43$, $|A^{Cu}_{\|}| = 39 \times 10^{-4}$ cm^{-1}, and $g_{\perp} = 2.07$ (Fig 4.3). **(2)** had a nearly identical spectrum with $g_{\|} = 2.43$, $|A^{Cu}_{\|}| = 41 \times 10^{-4}$ cm^{-1}, and $g_{\perp} = 2.07$. This contrasted the rhombic signals reported by Tolman for the more tetrahedral complexes (Table 4.1).[9a,d] The EPR spectrum of **(3)** was rhombic, consistent with its more tetrahedral geometry. The axial EPR signals of **(1)** and **(2)** were striking since, like the Kitojima/Fujisawa examples, both displayed $g_{\|}$ values that were unusually large and $|A^{Cu}_{\|}|$ values that were exceptionally small. Typically, 'normal' axial $g_{\|} > g_{\perp}$ Cu^{II} EPR spectra have much smaller $g_{\|}$ and much larger $|A^{Cu}_{\|}|$ (i.e. $[CuCl_4]^{2-}$ $g_{\|} = 2.221$, $|A^{Cu}_{\|}| = 164 \times 10^{-4}$ cm^{-1}).[13]

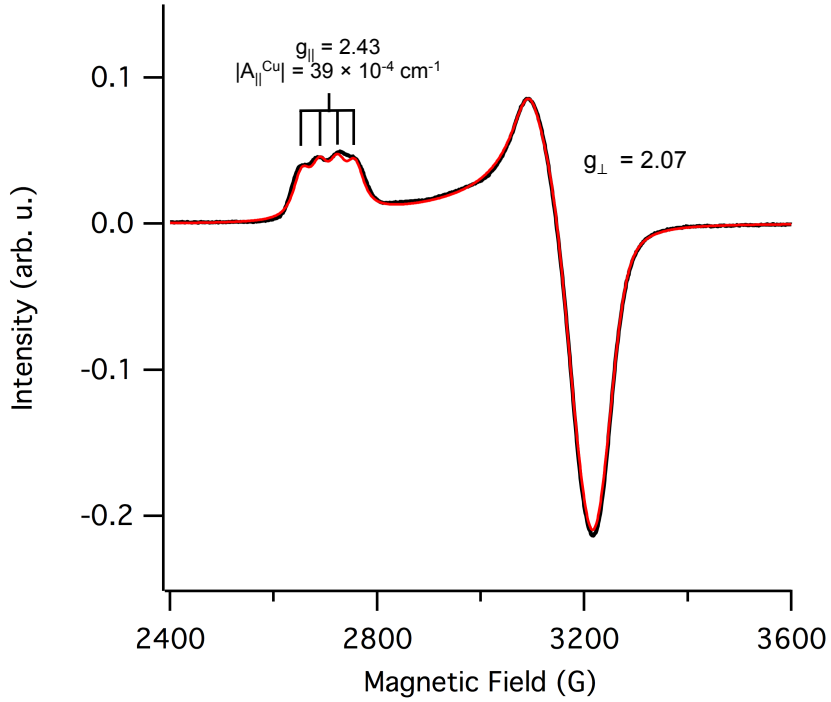

Figure 4.3. X-band EPR spectrum of (1) in a toluene glass at 120 K. Data is shown in black, simulation is shown in red.

The optical absorption spectra of **(1)** and **(2)** displayed charge transfer bands at 424 nm (3500 ± 350 M^{-1} cm^{-1}) and 423 nm (3300 ± 330 M^{-1} cm^{-1}), respectively. Less intense d-d transitions could also be observed at lower energy.

The structure, EPR spectra and optical features of **(1)** and **(2)** were found to be very similar to those reported for the extensively studied class of proteins referred to as 'Type 1 (T1) blue copper proteins.[14] Most T1 copper proteins have very similar trigonal monopyramidal type geometry with a copper center that is ligated by two histidine nitrogens and a cysteine thiolate in the basal plane. A neutral methionine sulfur binds in the axial plane with a notable longer bond distance. Like **(1)** and **(2)**, T1 copper proteins display a charge transfer band in the visible. This band has been attributed to a π to d_{x2-y2} transition from the cysteine thiolate to copper and usually occurs around 600 nm (Scheme 4.4).[14] It seems qualitatively consistent that a similar type of π to d_{x2-y2} transition in **(1)** or **(2)** occurs at higher energy since an alkoxide is less electron rich than a thiolate.

Scheme 4.4. LMCT from Cysteine Thiolate to Cu(II)

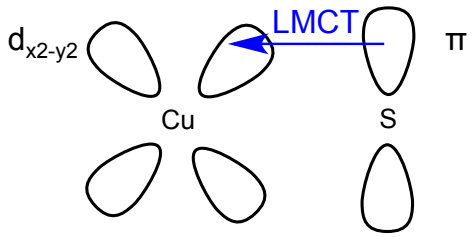

We found the spectroscopic similarities between the complexes reported here and T1 blue copper proteins interesting since it has been previously determined that in T1 blue copper proteins, there is a significant spin density from copper(II) delocalized onto the cysteine thiolate ligand. This spin delocalization gives rise to the small $|A^{Cu}_{||}|$ observed in the EPR spectra.[14] Since the EPR specta for **(1)** and **(2)** also display very small $|A^{Cu}_{||}|$, we were interested in the degree of spin delocalization onto the alkoxide. A large spin density on the alkoxide ligand may be relevant for invoking a copper(II) mediated α-C–H bond strength modulation.

To probe the degree of spin delocalization onto the alkoxide ligand, collaborators Ellen Hayes and Stefan Stoll performed ENDOR measurements on **(1)** and the OCD_2CF_3 isotopologue of **(1)**. The ENDOR spectrum of **(1)** shows coupling that disappears upon deuteration of the methylene alkoxide unit (Figure 4.4). This allowed Stoll and Hayes to assign this coupling to $|A^{\alpha\text{-C–}\underline{H}}|$ = 25 MHz, which corresponds to a total spin density of roughly 1.8%. As a point of reference, the analogous α-C–H coupling observed on the cysteinate ligand of the T1 Blue Copper enzyme plastocyanin has a 27 Hz or ~1.9% spin

density.[15] From this result, it was apparent there was substantial electronic communication between Cu(II) and the alkoxide ligand in this complex.

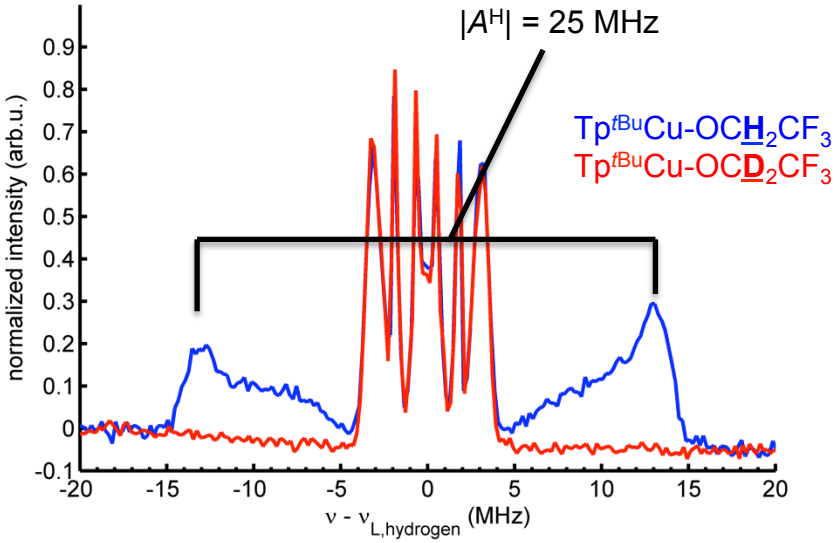

Figure 4.4. The overlayed ENDOR spectra of Tp^{tBu}Cu^{II}-OC$\underline{H}_2$CF$_3$ **(1)** (blue) and the deuterium labeled isotopologue Tp^{tBu}Cu^{II}-OC$\underline{D}_2$CF$_3$ (red).

4.2.3. Electrochemistry and Acid/Base Properties

Cyclic voltammograms of **(1)** (Tp^{tBu}Cu^{II}-OCH$_2$CF$_3$) or **(2)** (Tp^{tBuMe}Cu^{II}-OCH$_2$CF$_3$) in dichloromethane with 0.1 M [^{n}Bu$_4$][NPF$_6$] display irreversible cathodic peak potentials at -0.86 ± 0.01 V and -1.03 ± 0.01 V, respectively (both vs. Fc$^{+/0}$)(Figure 4.5). This data is consistent with previously reported electrochemical irreversibility reported by Tolman[9c] for similar Tp^{tBu}Cu complexes. The related Tp^{tBu}Cu^{II}-OCH(CH$_3$)CF$_3$ complex, **(3)**, displays an irreversible response at -0.84 ± 0.01 V. This is only slightly perturbed from the $E_{c,p}$ for **(1)**. **(1)** and **(3)** differ only in nature of the alkoxide ligand and suggests the electrochemical behavior observed here is primarily determined by the nature of the Tp ligand rather than by the –X ligand. It should be emphasized these comparisons are only qualitative because of the irreversible nature of the electrochemical waves.

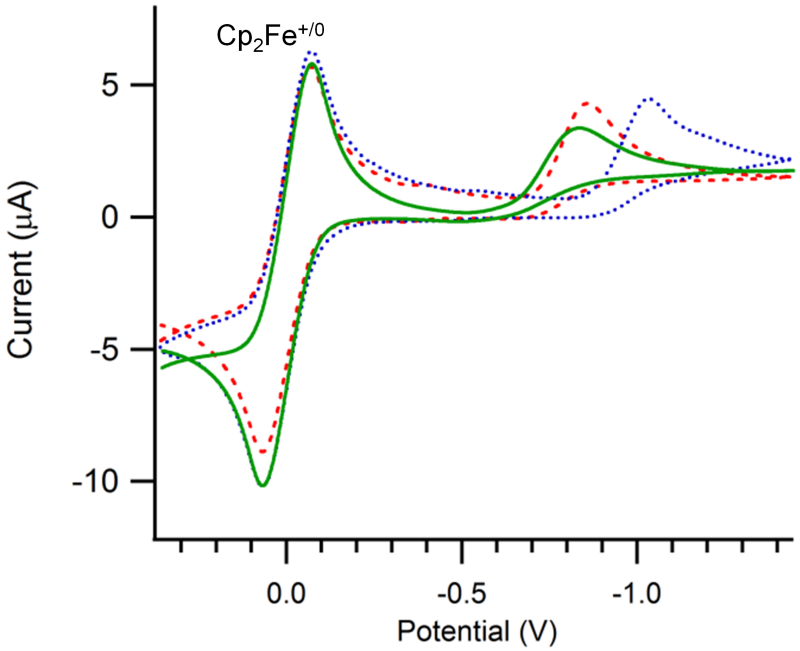

Figure 4.5. Cyclic voltammograms of 2.5 mM **(1)** (dashed red), **(2)** (dotted blue) and **(3)** (solid green) in dichloromethane at 100 mV s^{-1} under N_2 with 0.1 M [^{n}Bu$_4$N][PF_6] and a glassy carbon working electrode. The potential is referenced to the $Fc^{+/0}$ couple.

Treatment of either **(1)** or **(2)** (15.3 mM) with the weak acid, [DBUH$^+$][$^-$OTf] in DCM-d_2/1% MeCN-d_3 (v/v) (pK_a = 24.3 in MeCN)[16] does not result in proton transfer to the alkoxide ligand. Treatment of **(1)** with the stronger acid, 2,6-lutidinium triflate ([LutH$^+$][$^-$OTf]; pK_a = 14.1 in MeCN)[16] under the same conditions results in a ~20 ± 10% protonation and several minor unidentified organic products. These products slowly increase in concentration with time as determined by ^{1}H NMR. This *pseudo*-equilibrium measurement of K_{eq} ~ 1 implies that under these conditions, the pK_a of [Tp^{tBu}Cu^{II}···HOCH$_2$CF$_3$]$^+$ is very roughly equal to that of [LutH$^+$][$^-$OTf].

4.2.4. Reactions with H-Atom *Donors*

The addition of one equivalent of the potent hydrogen atom donor, TEMPO–H (2,2,6,6-tetramethylpiperdin-1-ol; O–H BDFE(toluene) = 65.2 kcal mol^{-1})[17] to a solution of **(1)** (Tp^{tBu}Cu^{II}-OCH$_2$CF$_3$) resulted in an immediate color change from orange to light pink (unless noted, all reactions are 15.3 mM in **(1)** in dichloromethane-d_2 with 1% MeCN-d_3 (v/v)). The ^{1}H NMR spectrum displayed signals for Tp^{tBu}Cu^{I}-MeCN-d_3 and TFE (2,2,2-trifluoroethanol). These products were determined to be quantitative based on

integration verses a fluorobenzene internal standard. The TFE signal was also observed and quantified using ^{19}F NMR spectroscopy. The disappearance of ^{1}H NMR signals for TEMPO–H indicate complete conversion to TEMPO (eq 4.1).

$$Tp^{tBu}Cu^{II}\text{-}OCH_2CF_3 + TEMPO\text{–}H + MeCN\text{-}d_3 \rightarrow Tp^{tBu}Cu^{I}\text{-}MeCN\text{-}d_3 + HOCH_2CF_3 + TEMPO \quad (4.1)$$

This reactions also proceeded rapidly and quantitatively in toluene-d_8. In the absence of a Lewis base like MeCN, dimerization of the copper(I) product occurs, $[Tp^{tBu}Cu^{I}]_2$ (eq 4.2). The ^{1}H NMR of these dimers at room temperature is complicated because of broken symmetry of the $Tp^{\S}$ ligands and peak broadening due to fluxional processes. [9c,10b,18] The ^{1}H NMR spectrum is dramatically simplified by using a DCM-d_2/1% MeCN-d_3 (v/v) solution as the added MeCN-d_3 binds the open coordination site of $Tp^{tBu}Cu^{I}$ preventing dimerization.

$$Tp^{tBu}Cu^{II}\text{-}OCH_2CF_3 + TEMPO\text{–}H \rightarrow \tfrac{1}{2}\,[Tp^{tBu}Cu^{I}]_2 + HOCH_2CF_3 + TEMPO \quad (4.2)$$

Similar reactivity is observed with the related hydroxylamine, ABNO–H (9-azabicyclo[3.3.1]nonane *N*-hydroxide; O–H BDFE(toluene) = 70.7 kcal mol^{-1}).[19] Like TEMPO–H, ABNO–H reacts within seconds in either toluene-d_8 or DMC-d_2/1% MeCN-d_3 (v/v) to generate the Cu(I) product, TFE and the corresponding hydroxylamine, ABNO (9-azabicyclo[3.3.1]nonane *N*-oxyl) (eq 4.3). The products of this reaction were detected and quantified with NMR and optical spectroscopies.

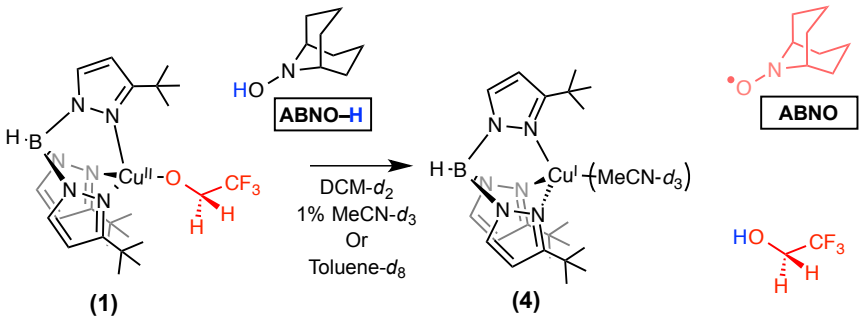

(4.3)

When the less potent hydrogen atom donor, $^{t}Bu_3ArO–H$ (2,4,6-tri-*tert*-butyl-phenol; O–H BDFE(toluene) = 76.7 kcal mol^{-1})[17] was added to **(1)**, the solution turned from orange to deep blue over the course of approximately 3 hours. Tp^{tBu}Cu^{I}-MeCN-d_3 and TFE were observed and quantified by ^{1}H NMR and ^{19}F NMR spectroscopies. $^{t}Bu_3ArO^{\bullet}$ (2,4,6-tri-*tert*-butyl-phenoxyl radical) was also produced and quantified from its optical spectrum using the reported optical extinction coefficient of 400 ± 10 M^{-1} cm^{-1} at 626 nm (eq 4.4).[20] This reaction also proceeded in toluene-d_8, yielding the same organic products but generating [Tp^{tBu}Cu^{I}]$_2$ rather than Tp^{tBu}Cu^{I}-MeCN-d_3.

$$Tp^{tBu}Cu^{II}\text{-}OCH_2CF_3 + {}^{t}Bu_3ArO–H + MeCN\text{-}d_3 \rightarrow Tp^{tBu}Cu^{I}\text{-}MeCN\text{-}d_3 + HOCH_2CF_3 + {}^{t}Bu_3ArO^{\bullet} \quad (4.4)$$

The analogous reaction occurs with the even poorer hydrogen atom donor, $^{t}Bu_2NPArO–H$ (2,6-di-*tert*-butyl-4-(4'-nitrophenyl)-phenol; O–H BDFE(toluene) = 77.5 kcal mol^{-1})[21] but requires 8 hours to reach completion (eq 4.5). This reaction proceeds quantitatively in DCM-d_2/1% MeCN-d_3 (v/v) but in toluene-d_8 the expected products are only observed in ~70% yield in addition to a variety of unidentifiable Tp^{tBu}Cu^{II}-OCH$_2$CF$_3$ derived side products. Approximately 30% of the $^{t}Bu_2NPArO–H$ remains at the end of the reaction.

$$Tp^{tBu}Cu^{II}\text{-}OCH_2CF_3 + {}^{t}BuNPArO–H + MeCN\text{-}d_3 \rightarrow Tp^{tBu}Cu^{I}\text{-}MeCN\text{-}d_3 + HOCH_2CF_3 + {}^{t}BuNPArO^{\bullet} \quad (4.5)$$

(1) reacts completely with the weak C-H bonds in 1,4-cyclohexadiene (1,4-CHD; first C-H BDFE(toluene) = 72.6 kcal mol^{-1})[19] but required over 2 weeks to reach completion even in the presence of 50 fold excess 1,4-CHD (eq 4.6). This reaction was not carried out in toluene-d_8.

$$Tp^{tBu}Cu^{II}\text{-}OCH_2CF_3 + 1,4\text{-}CHD + MeCN\text{-}d_3 \rightarrow Tp^{tBu}Cu^{I}\text{-}MeCN\text{-}d_3 + HOCH_2CF_3 + C_6H_6 \quad (4.6)$$

Treatment of **(1)** with 2,2,6,6-tetramethylpiperidine (N–H BDFE(toluene) = 84.2 ± 5 kcal mol^{-1})[19] resulted in no reaction in either DCM-d_2/1% MeCN-d_3 (v/v) or toluene-d_8.

The same reactions reported here for **(1)** were also observed for $Tp^{tBuMe}Cu^{II}$-OCH_2CF_3 **(2)** in DCM-d_2/1% MeCN-d_3,[22] but the reaction times were slightly longer relative to those of **(1)** (i.e. the reaction with $^tBu_3ArO$–H requires ~5 hours for **(2)** and ~3 hours for **(1)**). However in toluene-d_8, **(2)** only reacted quantitatively with the hydroxylamines, TEMPO–H and ABNO–H. With either $^tBu_3ArO$–H or $^tBu_2NPArO$–H in toluene-d_8, complete decomposition of **(2)** was observed over ~3 days yielding a small amount of $[Tp^{tBuMe}Cu^{I}]_2$, TFE, the corresponding phenoxyl radical (*ca*. 35 and 25%, respectively) and a number of unidentifiable side products. After **(2)** had completely decomposed, approximately 60% or 75% of the unreacted $^tBu_3ArO$–H or $^tBu_2NPArO$–H was detected by ^{1}H NMR, respectively.

Scheme 4.5. H-atom transfer reactions of Tp^{tBu}Cu^{II}-OCH$_2$CF$_3$ **(1)** with several substrates in DCM-d_2/1% MeCN-d_3 (v/v).

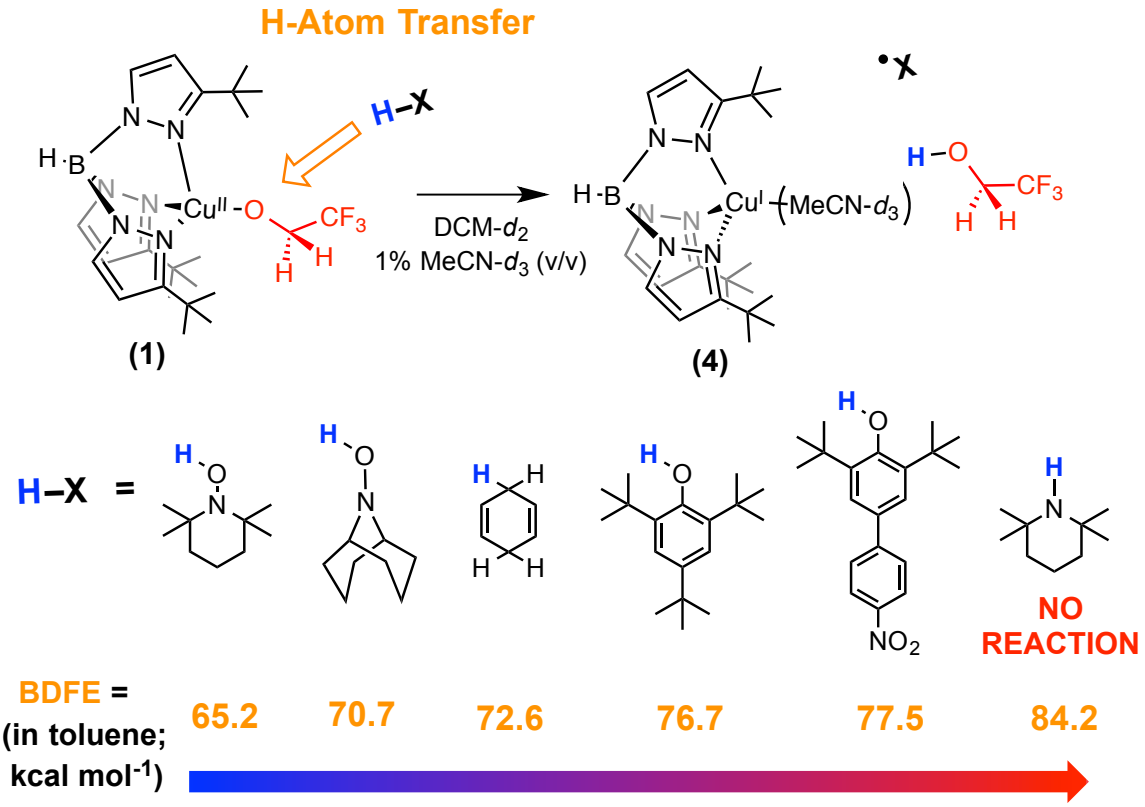

4.2.5. Reactions with H-Atom *Acceptors*

4.2.5.1. Reactions with ^{t}Bu$_3$ArO$^{\bullet}$

Treatment of Tp^{tBu}Cu^{II}-OCH$_2$CF$_3$ **(1)**, with one equivalent of ^{t}Bu$_3$ArO$^{\bullet}$ resulted in a solution color change from dark green (**(1)** is orange, ^{t}Bu$_3$ArO$^{\bullet}$ is blue) to light lime green over the course of ~10 hours. The ^{1}H NMR spectrum displayed the appearance of Tp^{tBu}Cu^{I}-MeCN-d_3 as well as an organic species that was identified as the 2-substituted dienon-ether (2,4-cyclohexadien-1-one,2,4,6-tri-*tert*-butyl-6-(2,2,2-trifluoroethoxide) or ^{t}Bu$_3$CHDO-TFE) in quantitative yield as determined by ^{1}H NMR (eq 4.7) (See Experimental). This reaction occurs in both DCM-d_2/1% MeCN-d_3 (v/v) and toluene-d_8.

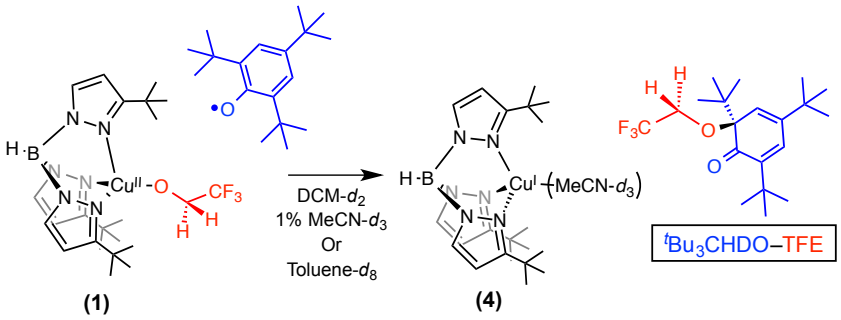

(4.7)

Kinetic analysis of this reaction in DCM-d_2/1% MeCN-d_3 (v/v) under *pseudo*-first order conditions showed a first order dependence on ^{t}Bu$_3$ArO$^\bullet$ but gave irreproducible second order rate constants that varied from 7.2×10^{-2} to 18.0×10^{-2} M^{-1} s^{-1} depending on the solvent batch used. These rate constants were generally consistent between runs when the same stock solvent was used but their values were not quantitatively useful since uncontrolled trace solvent impurities are likely responsible for the differences in rates.

From the extensive Cu/radical alcohol oxidation literature,[2,3] it would be expected that treating **(1)** with ^{t}Bu$_3$ArO$^\bullet$ would result in oxidation of the alkoxide ligand via a net HAT to ^{t}Bu$_3$ArO$^\bullet$ and ET to Cu^{II}. The predicted phenol and trifluoroacetaldehyde products are not observed. Fluorinated aldehydes are extremely electrophilic[23] and it would perhaps not be surprising if trifluoroacetaldehyde might react with ^{t}Bu$_3$ArO–H to yield the observed ^{t}Bu$_3$CHDO-TFE product. Trifluoroacetaldehyde is only commercially available as the hemiacetal or monohydrate making otherwise simple control experiments challenging.

In order to rule out the possibility that ^{t}Bu$_3$ArO–H and trifluoroacetaldehyde were generated as reactive intermediates *en route* to ^{t}Bu$_3$CHDO-TFE in this reaction, a series of experiments were preformed with the Tp$^{t\text{Bu}}$Cu^{II}-OC$\underline{D}_2$CF$_3$ isotopologue.

In a first experiment, kinetic measurements for the reaction of Tp$^{t\text{Bu}}$Cu^{II}-OC$\underline{D}_2$CF$_3$ with ^{t}Bu$_3$ArO$^\bullet$ were performed and compared to the analogous reaction with the proteo- isotopologue. This reaction displayed no kinetic isotope effect within experimental error, providing evidence against H(D) transfer in the rate determining step.

In a second experiment, half equivalents of both the H and D enriched complexes were combined and treated with a full equivalent of ^{t}Bu$_3$ArO$^\bullet$. A mechanism involving ^{t}Bu$_3$ArO–H and trifluoroacetaldehyde generation followed by a bimolecular

recombination to give $^{t}Bu_3$CHDO-TFE would result in statistical scrambling at the methylene unit of trifluoroethoxy substituent. No H/D scrambling is observed in the final product by ^{1}H NMR.

Finally, DFT free energy calculations (rM06/6-311+g(d,p), gas phase and toluene SCRF)[24] show that $^{t}Bu_3$CHDO-TFE is higher in energy than the sum of free energies of trifluoracetaldehyde and $^{t}Bu_3$ArO–H by 18.4 (gas phase) and 19.8 (toluene SCRF) kcal mol^{-1}.

From the result of these experiments and calculations, it is clear that $^{t}Bu_3$ArO–H and trifluoroacetaldehyde are not generated as intermediates in the reaction between **(1)** and $^{t}Bu_3$ArO$^{\bullet}$. The observed product, $^{t}Bu_3$CHDO-TFE is favored in this case because of a low kinetic barrier rather than being the most energetically stable species.

Scheme 4.6. Trifluoroacetaldehyde and $^{t}Bu_3$ArO–H are not Intermediates in the Reaction Between **(1)** and $^{t}Bu_3$ArO$^{\bullet}$.

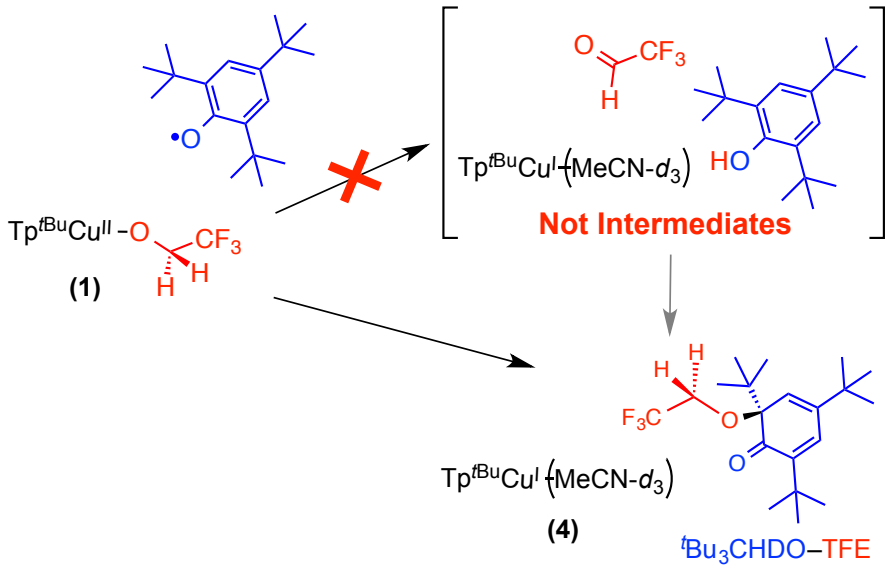

Treatment of **(1)** with the radical trap, 1,1-diphenylethylene[25] resulted in no reaction for days, suggesting against a dissociative radical pathway in this reaction.

Treatment of Tp^{tBuMe}Cu^{II}-OCH$_2$CF$_3$ **(2)**, with one equivalent of $^{t}Bu_3$ArO$^{\bullet}$ under identical conditions (toluene-d_8 or DCM-d_2/1% MeCN-d_3 (v/v)) results in no reaction after 24 hours. This was somewhat surprising since **(2)** reacted similarly to **(1)** with hydrogen atom donors under similar conditions.

4.2.5.2. Reactions with TEMPO

Treatment of **(1)** with one equivalent of TEMPO in DCM-d_2/1% MeCN-d_3 (v/v) resulted in a color change from red-orange to pale pink after 3 hours. The ^{1}H and ^{19}F NMR spectra indicated Tp$^{t\text{Bu}}$Cu$^{\text{I}}$-MeCN-d_3, had been generated as well as 0.5 equivalents of TFE and 0.25 equivalents of 2,2,2-trifluoroethyl trifluoroacetate[26] (eq 4.8). The absence of TEMPO derived ^{1}H NMR resonances and the pinkish hue of the completed reaction mixture suggested TEMPO was not consumed during the reaction. However, rigorous quantification of remaining TEMPO was not performed. The same organic products were observed when the reaction was carried out in toluene-d_8.

$$\text{Tp}^{t\text{Bu}}\text{Cu}^{\text{II}}\text{-OCH}_2\text{CF}_3 + \text{TEMPO} + \text{MeCN-}d_3 \rightarrow$$
$$\text{Tp}^{t\text{Bu}}\text{Cu}^{\text{I}}\text{-MeCN-}d_3 + \tfrac{1}{2}\,\text{HOCH}_2\text{CF}_3 + \tfrac{1}{4}\,\text{CF}_3\text{COOCH}_2\text{CF}_3 \qquad (4.8)$$

Likewise, the reaction between **(2)** and 1 equivalent of TEMPO in DCM-d_2/1% MeCN-d_3 (v/v) yielded Tp$^{t\text{BuMe}}$Cu$^{\text{I}}$-MeCN-d_3 and the same organic products but required ~6 hours to reach completion. No reaction was observed between **(2)** and TEMPO when carried out in toluene-d_8.

The kinetic traces of these reactions in both cases showed linear behavior. With **(1)** the reaction began immediately upon addition of TEMPO to the solution. With **(2)**, the linear trace was preceded by a 3 hour induction period. When a second equivalent of **(2)** was added to the completed reaction mixture, it was consumed in the same linear fashion but with no induction period (Figure 4.6). This type of behavior is suggestive of an autocatalytic process.[27]

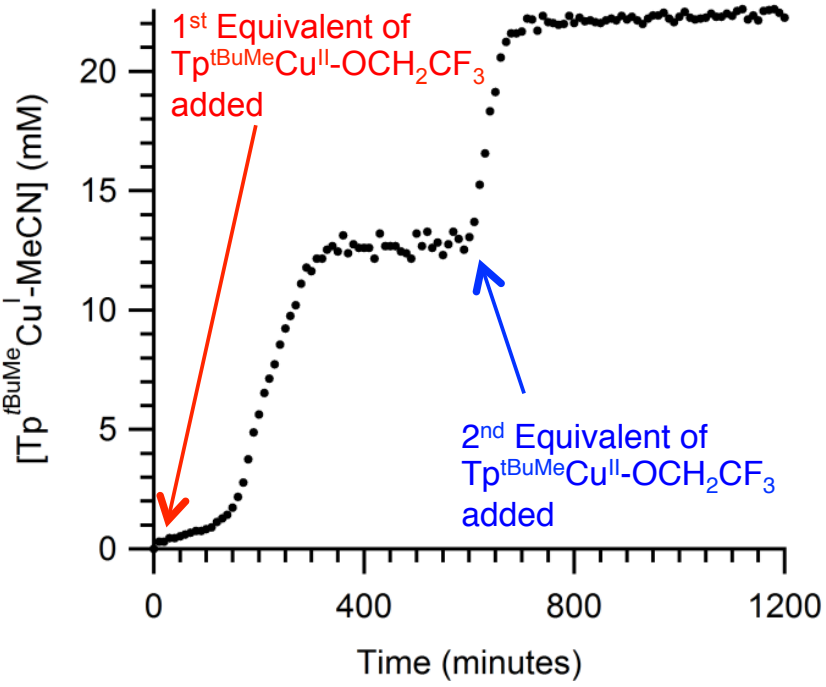

Figure 4.6. Kinetic trace for the TEMPO catalyzed disproportionation of $Tp^{tBuMe}Cu^{II}$-OCH_2CF_3 in DCM-d_2/1% MeCN-d_3 (v/v) to yield $Tp^{tBuMe}Cu^{I}$-MeCN-d_3, 0.5 eq TFE and 0.25 eq trifluoroethyl trifluoroacetate. The time course between 0 and 500 minutes shows the disproportionation reaction of 12 mM $Tp^{tBuMe}Cu^{II}$-OCH_2CF_3 catalyzed by 1 eq TEMPO as monitored by the appearance of $Tp^{tBuMe}Cu^{I}$-MeCN-d_3 by ^{1}H NMR. The second time course shows the same reaction upon addition of a second equivalent of $Tp^{tBuMe}Cu^{II}$-OCH_2CF_3.

Scheme 4.7. $Tp^{tBuMe}Cu^{II}$-OCH_2CF_3 **(2)** has solvent dependent reactivity with TEMPO.

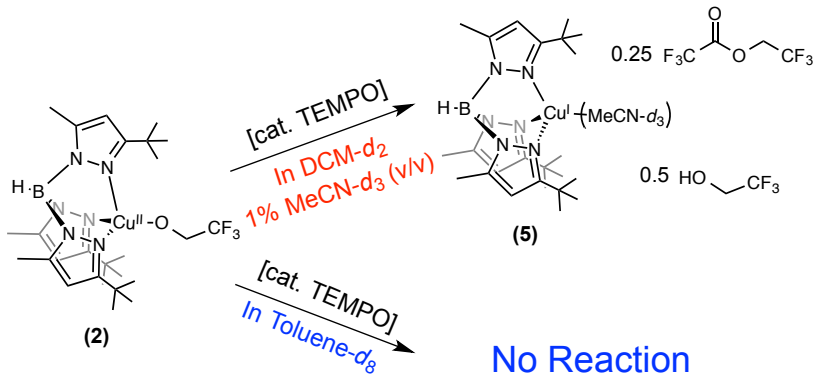

4.3. Discussion

4.3.1. Mechanistic Interpretations of H^+/e^- Transfer:

$Tp^{tBu}Cu^{II}$-OCH_2CF_3 **(1)** and $Tp^{tBuMe}Cu^{II}$-OCH_2CF_3 **(2)** react with X–H species by abstracting a net hydrogen atom ($H^\bullet$). In these reactions, the proton is transferred to the alkoxide ligand and the electron is transferred to Cu(II). Mechanistically, the transfer of H^+/e^- can be envisioned to proceed through a number of possible mechanisms. The most reasonable of these are (*i*) sequential electron transfer/proton transfer (ET/PT), (*ii*) sequential proton transfer/electron transfer (PT/ET), (*iii*) protolytic ligand exchange followed by radical dissociation, (*iv*) sequential radical dissociation/H-atom transfer or (*v*) concerted proton-electron transfer (CPET; defined here as ≡ HAT).

Sequential ET/PT and PT/ET mechanisms (mechanisms *i* and *ii*) are unlikely because of the high thermodynamic barrier for either initial electron transfer or initial proton transfer. Specifically, both **(1)** and **(2)** were found to be poor 1 electron oxidants from their irreversible cathodic peak potentials ($E_{p,c}$ = -0.86 ± 0.01 V for **(1)** and -1.03 ± 0.01 V for **(2)**; both in DCM vs $Fc^{+/0}$). The H-atom donors used here are very poor one electron reductants (i.e. $E^\circ(^t\text{Bu}_3\text{ArO–H})$ = +1.18 V,[17] E°(TEMPO–H) = +0.71 V,[17] $E_{p,a}(^t\text{Bu}_2\text{NPArO–H})$ = +0.975 V;[21] all in MeCN vs $Fc^{+/0}$). Despite the qualitative nature of these comparisons, it is clear that an initial electron transfer step is thermodynamically unfavorable in these systems.

Likewise, neither **(1)** or **(2)** are especially strong bases. This was indicated by the inability of $[DBUH^+][^-OTf]$ (pK_a = 24 in MeCN)[16] to protonate **(1)** or **(2)**. The *pseudo*-equilibrium measurements between **(1)** and $[LutH^+][^-OTf]$ (pK_a = 14.1 in MeCN)[16] suggest the basicity of **(1)** is roughly the same as 2,6-lutidine under these conditions. The H-atom donors used here are poor acids (i.e. $pK_a(^t\text{Bu}_3\text{ArO–H})$ = 28,[17] pK_a(TEMPO–H) = 41,[17] $pK_a(^t\text{Bu}_2\text{NPArO–H})$ = 24;[20] all in MeCN) so it is unlikely that these reaction occur via an initial proton transfer step.

A radical dissociation mechanism (mechanism *iii*) can be ruled out based on the absence of reactivity observed between **(1)** and the radical trap, 1,1-diphenylethylene.

A mechanism involving a protolytic ligand exchange followed by rapid radical dissociation (mechanism *iv*) is possible but seems unlikely. This is highlighted by the fact

that **(1)** is capable of reacting with the weak C–H bonds in 1,4-cyclohexadiene. 1,4-cyclohexadiene is neither acidic or nucleophilic and very unlikely to react through a protolytic exchange mechanism. Additionally, the net H• transfer reaction times scales well with the O–H bond strengths of the H-atom donors examined, as is predicted from a Marcus model for CPET.[28] Specifically, the O–H bond strength of TEMPO–H in toluene is only 65.2 kcal mol^{-1} [10] and its reaction with **(1)** is complete in ~1 second. The stronger bond in ^{t}Bu$_3$ArO–H (BDFE = 76.7 kcal mol^{-1} in toluene)[17] is also broken by **(1)** but requires 3 hours to reach completion. Finally, H• is removed from the even stronger O–H bond of ^{t}Bu$_2$NPArO–H (BDFE = 77.5 kcal mol^{-1} in toluene)[21] by **(1)** but requires ~8 hours. **(1)** reacts much slower with 1,4-cyclohexadiene (first C–H bond BDFE = 72.6 kcal mol^{-1} in toluene),[19] requiring ~2 weeks and 50 fold excess substrate to fully react. This is not unexpected since C–H bonds are known to react much slower than O–H or N–H bonds of the same strength.[28]

4.3.2. Thermodynamic Implications of H^+/e^- Transfer

4.3.2.1 '*Effective* BDFE' of ½ [Tp$^{t\mathrm{Bu}}$Cu$^{\mathrm{I}}$]$_2$ + TFE

Tp§Cu$^{\mathrm{II}}$-OCH$_2$CF$_3$ (Tp§Cu$^{\mathrm{II}}$-OCH$_2$CF$_3$ = **(1)** and **(2)**) reacts with X–H in toluene by net transfer of a hydrogen atom to yield TFE, X•, and [Tp§Cu$^{\mathrm{I}}$]$_2$. In toluene, **(1)** was capable of cleaving the relatively strong O–H bond in ^{t}Bu$_3$ArO–H (BDFE(toluene) = 76.7 kcal mol^{-1})[21]. **(2)** was a slightly weaker hydrogen atom acceptor in toluene, unable to cleanly react with ^{t}Bu$_3$ArO–H but able to remove a hydrogen atom from the weaker O–H bond in ABNO–H (BDFE(toluene) = 70.7 kcal mol^{-1})[19]. These benchmark reactions were quantitative and provide thermodynamic information about **(1)** and **(2)** regardless of the reaction mechanism.

For these reactions to occur, the X–H bond broken in ^{t}Bu$_3$ArO–H or ABNO–H must have homolytic bond dissociation free energies (BDFEs) that are smaller than the sum of the free energies required to (*i*) transfer a hydrogen atom to Tp§Cu$^{\mathrm{II}}$-OCH$_2$CF$_3$, (*ii*) dissociate HOCH$_2$CF$_3$ from Tp§Cu$^{\mathrm{I}}$, and (*iii*) to form ½ [Tp§Cu$^{\mathrm{I}}$]$_2$. It has been reported by Tolman and Parkin that [Tp$^{t\mathrm{Bu}}$Cu$^{\mathrm{I}}$]$_2$ and [Tp$^{t\mathrm{BuMe}}$Cu$^{\mathrm{I}}$]$_2$ dimers are stable to dissociation even at 90 °C in the absence of a Lewis base so the thermochemical contribution from their formations in these reactions is likely not negligible.[9c,10b]

The reported O–H BDFE of $^{t}Bu_3ArO$–H in toluene is 76.7 kcal mol^{-1} so it is clear the '*effective* BDFE' of ½ [Tp^{tBu}Cu^{I}]$_2$ + TFE is *at least* 76.7 kcal mol^{-1} (eq 4.9-4.11):

$$Tp^{tBu}Cu^{II}\text{-}OCH_2CF_3 + {}^{t}Bu_3ArO\text{–}H \rightarrow \tfrac{1}{2}\,[Tp^{tBu}Cu^{I}]_2 + HOCH_2CF_3 + {}^{t}Bu_3ArO^{\bullet} \quad (4.9)$$

$$\Delta G^{\circ} \leq 0 \text{ kcal mol}^{-1}\ ^{29}$$

$$^{t}Bu_3ArO^{\bullet} + {}^{\bullet}H \rightarrow {}^{t}Bu_3ArO\text{–}H \quad (4.10)$$

$$\Delta G^{\circ} = -76.7 \pm 0.5 \text{ kcal mol}^{-1}\ ^{17}$$

Summing equations (4.9) and (4.10):

$$Tp^{tBu}Cu^{II}\text{-}OCH_2CF_3 + {}^{\bullet}H \rightarrow \tfrac{1}{2}\,[Tp^{tBu}Cu^{I}]_2 + HOCH_2CF_3 \quad (4.11)$$

$$\Delta G^{\circ} \leq -76.7 \pm 0.5 \text{ kcal mol}^{-1}$$

Similarly, since 2,2,6,6-tetramethylpiperidine is unreactive with **(1)**, a high limit for this value can be set at 84.2 ± 5 kcal mol^{-1} (eq 4.12):

$$Tp^{tBu}Cu^{II}\text{-}OCH_2CF_3 + {}^{\bullet}H \rightarrow \tfrac{1}{2}\,[Tp^{tBu}Cu^{I}]_2 + HOCH_2CF_3 \quad (4.12)$$

$$-84.2 \pm 5 \text{ kcal mol}^{-1} \leq \Delta G^{\circ} \leq -76.7 \pm 0.5 \text{ kcal mol}^{-1}$$

An analogous assessment can be made for **(2)** using the reaction between **(2)** and ABNO–H as a thermodynamic benchmark. The O–H BDFE in ABNO–H in toluene is 70.7 kcal mol^{-1} [19] from which a low limit for the *effective* BDFE of ½ [Tp^{tBuMe}Cu^{I}]$_2$ + $HOCH_2CF_3$ of 70.7 kcal mol^{-1} is derived.

4.3.2. Assessment of the *Effective* Cu^{II}–O BDFE

With a high and low limit for the effective BDFE of ½ [Tp^{tBu}Cu^{I}]$_2$ + TFE, high and low limits for the *effective* homolytic Cu–O bond strength in Tp^{tBu}Cu^{II}-OCH_2CF_3 can be approximated using a simple Hess' Law approach in the following thermochemical cycle:

$$Tp^{tBu}Cu^{II}\text{-}OCH_2CF_3 + {}^{\bullet}H \rightarrow \tfrac{1}{2}\,[Tp^{tBu}Cu^{I}]_2 + HOCH_2CF_3 \qquad (4.12)$$

$$-84.2 \pm 5 \text{ kcal mol}^{-1} \leq \Delta G^{\circ} \leq -76.7 \pm 0.5 \text{ kcal mol}^{-1}$$

$$H\text{–}OCH_2CF_3 \rightarrow H^{\bullet} + {}^{\bullet}OCH_2CF_3 \qquad (4.13)$$

$$\Delta G^{\circ} = 101.3 \pm 3 \text{ kcal mol}^{-1}\ [19]$$

The sum of equation (4.12) and (4.13) gives a limit for the *effective* homolytic Cu^{II}–OR BDFE:

$$Tp^{tBu}Cu^{II}\text{–}OCH_2CF_3 \rightarrow \tfrac{1}{2}\,[Tp^{tBu}Cu^{I}]_2 + {}^{\bullet}OCH_2CF_3 \qquad (4.14)$$

$$17.1 \pm 6 \leq \Delta G^{\circ} \leq 24.6 \pm 3 \text{ kcal mol}^{-1}$$

Like the '*effective* O–H BDFE of $\tfrac{1}{2}\,[Tp^{tBu}Cu^{I}]_2 + HOCH_2CF_3$, the *effective* Cu–O BDFE reported here encompasses the free energy of homolytic bond Cu–O bond cleavage as well as the formation of the $[Tp^{tBu}Cu^{I}]_2$ dimer.

Again, the analogous thermochemical assessment can be performed for $Tp^{tBuMe}Cu^{II}\text{–}OCH_2CF_3$ **(2)** using the *effective* BDFE of $[Tp^{tBuMe}Cu^{I}]_2 + HOCH_2CF_3 \geq 70.7$ kcal mol^{-1} described in 4.3.1:

$$Tp^{tBuMe}Cu^{II}\text{–}OCH_2CF_3 \rightarrow \tfrac{1}{2}\,[Tp^{tBu}Cu_I]_2 + {}^{\bullet}OCH_2CF_3 \qquad (4.15)$$

$$\Delta G^{\circ} \leq 30.6 \pm 3 \text{ kcal mol}^{-1}$$

4.3.3 Calculating the Alkoxide Ligands *Effective* α-C–H BDFE

As previously described, copper(II) alkoxide intermediate have been invoked in a number of radical/copper mediated alcohol oxidation catalysts. It has been suggested that alkoxide oxidation involves the net transfer of a hydrogen atom (H^+/e^-) from the α-C–H alkoxide to an oxyl radical and an electron (e^-) to Cu(II). This net $2e^-/1H^+$ oxidation reaction has sometimes been described as a sequential HAT/ET because of large

experimental KIEs. It has also been suggested to proceed through a thermodynamically coupled and kinetically concerted process since typically the α-C–H bonds of a primary alcohol are much stronger than the O–H bonds formed by oxyl radical H-atom acceptors. Difficulty in preparing isolable Cu(II) alkoxide complexes with primary or secondary alkoxide ligands has previously precluded an experimentally derived thermochemical study of this step.

With the thermodynamic limits for **(1)** and **(2)** discussed, first experimental assessments of the thermochemistries of isoloable Cu(II) alkoxide species can be made. Taking the lower limit for '*effective* BDFE' of ½ $[Tp^{tBu}Cu^{I}]_2$ + $HOCH_2CF_3$ (converted to gas phase for comparison purposes)[30] a high limit for the free energy for the ET coupled α-C–H bond cleavage can be estimated. This calculation for **(1)** is shown here explicitly (eq 4.12, eq 4.15-4.17):

$$Tp^{tBu}Cu^{II}\text{-}OCH_2CF_3 + H^{\bullet} \rightarrow \tfrac{1}{2}\,[Tp^{tBu}Cu^{I}]_2 + H\text{–}OCH_2CF_3 \qquad (4.12)$$

$$\Delta G^{\circ}_{gas} \leq -71.9 \pm 3 \text{ kcal mol}^{-1}\ ^{30}$$

$$H\text{–}OCH_2CF_3 \rightarrow O{=}CH(CF_3) + H_2 \qquad (4.15)$$

$$\Delta G_{gas}^{\circ} = 17.5 \pm 3 \text{ kcal mol}^{-1}\ ^{30}$$

$$H_2 \rightarrow 2H^{\bullet} \qquad (4.16)$$

$$\Delta G_{gas}^{\circ} = 97.2 \pm 2 \text{ kcal mol}^{-1}\ ^{17}$$

The sum of equations (4.12), (4.15) and (4.16) give equation (4.17):

$$Tp^{tBu}Cu^{II}\text{-}OCH_2CF_3 \rightarrow \tfrac{1}{2}\,[Tp^{tBu}Cu^{I}]_2 + O{=}CH(CF_3) + H^{\bullet} \qquad (4.17)$$

$$\Delta G_{gas}^{\circ} \leq 42.8 \pm 5 \text{ kcal mol}^{-1}$$

The analogous calculation performed for **(2)** using the effective BDFE limit of ½ $[Tp^{tBuMe}Cu^{I}]_2$ + $HOCH_2CF_3$ converted to gas phase value of ≥ 66 ± 3 kcal mol^{-1} as a thermochemical benchmark yields:

$$Tp^{tBuMe}Cu^{II}–OCH_2CF_3 \rightarrow ½\ [Tp^{tBuMe}Cu^{I}]_2 + O{=}CH(CF_3) + H^{\bullet} \qquad (4.18)$$

$$\Delta G_{gas}° \leq 48.7 \pm 5 \text{ kcal mol}^{-1}$$

Even with the significant uncertainty associated with these gas phase estimate, it is readily apparent that if the effective α-C–H bond strengths of the trifluoroethoxide ligands are coupled to the one electron transfers to Cu^{II}, the C–H bonds in both **(1)** and **(2)** should be exceptionally weak. Thermodynamically, the envisioned reaction between **(1)** with either TEMPO or $^{t}Bu_3ArO^{\bullet}$ (gas phase O–H BDFEs of bonds formed are 62 ± 2 and 73 ± 2 kcal mol^{-1}, respectively)[19] to generate ½ $[Tp^{tBu}Cu^{I}]_2$ complex, trifluoroacetaldehyde and TEMPO–H or $^{t}Bu_3ArO$–H is downhill by roughly 20 or 30 kcal mol^{-1}, respectively, at least! Similarly, the analogous reactions between **(2)** and either TEMPO or $^{t}Bu_3ArO^{\bullet}$ is downhill by at least 13 or 24 kcal mol^{-1}, respectively.

Despite the highly favorable thermodynamics, these reactions do not occur. Notably, **(2)** is unreactive with either TEMPO or $^{t}Bu_3ArO^{\bullet}$ in toluene-d_8.

4.3.4. Implications for Copper/Radical Alcohol Oxidation

The structural, electronic and thermodynamic properties of **(1)** and **(2)** make them promising candidates for studying copper(II)-alkoxide oxidation with oxyl radicals: **I.** For both, the crystal structures show the α-C–H bond is sterically accessible to either TEMPO or $^{t}Bu_3ArO^{\bullet}$ radicals (Figure 4.7). Furthermore, both **(1)** and **(2)** are capable of reacting with bulky hydrogen atom donors through $H^{\bullet}$ transfer to the alkoxide oxygen – an even more sterically protected atom. **II**. EPR studies of **(1)** (taken to be similar to **(2)** based on other spectroscopic similarities) in collaboration with Stoll and Hayes have shown there is strong electronic communication between Cu(II) and α-C–H position of the bound 2,2,2-trifluoroethoxide ligand, and **III.** Thermodynamic analysis predicts the hypothetical reactions with TEMPO or $^{t}Bu_3ArO^{\bullet}$ to cooperatively dehydrogenate the alkoxide ligands with Cu^{II} is highly exoergic. Even with these seemingly favorable traits, **(2)** is unreactive

with both TEMPO and $^{t}Bu_3ArO^{\bullet}$. **(1)** is reactive with either TEMPO or $^{t}Bu_3ArO$ but these reactions follow different pathways.

The lack of reactivity between **(2)** and hydrogen atom acceptors demonstrate that *cleavage of the α-C–H bond of the trifluoroethoxide ligand is thermodynamically but not kinetically coupled to electron transfer to Cu(II) in this system*.

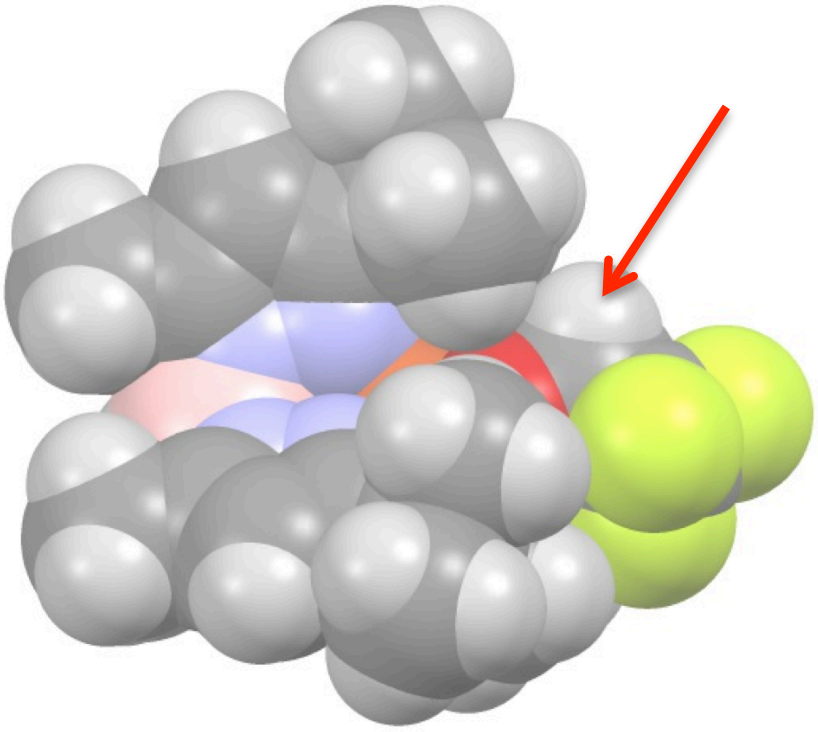

Figure 4.7. X-Ray Crystal Structure of $Tp^{tBuMe}Cu^{II}$-OCH_2CF_3 **(2)** depicting a space-filling model. The α-C–H position of interest is indicated by the red arrow.

Scheme 4.8. $Tp^{tBuMe}Cu^{II}$-OCH_2CF_3 **(2)** is Unreactive with $^tBu_3ArO^\bullet$ despite favorable thermodynamics.

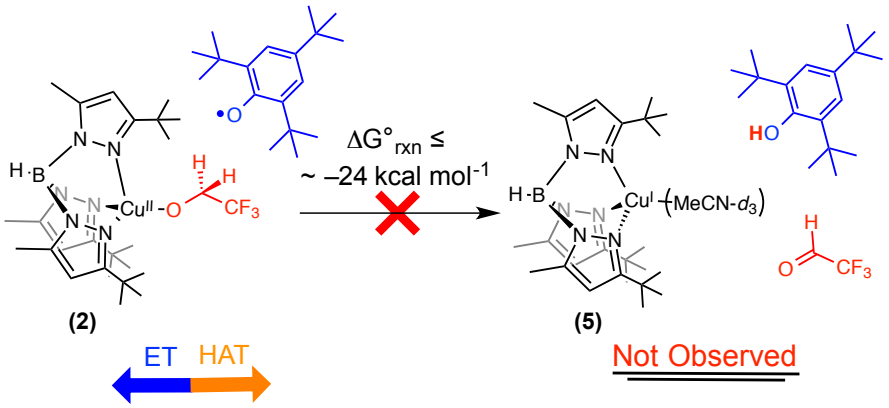

While there are clearly differences between this system and the biological and synthetic alcohol oxidation systems (i.e. geometry, non-fluorinated alcohols), some general conclusions can be made from this result. Most importantly, this result demonstrates unequivocally that *net driving force is not a primary predictor for alkoxide oxidation via a coupled HAT/ET mechanism*, if such a mechanism exists. This is clearly different from the case of most radical reactions, for which driving force is strongly related to reaction kinetics.[28,31] In light of this conclusion, it seems likely that the role of copper in copper/radical alcohol oxidations is not simply to act as a strong oxidant.

In 1979, Goddard and co-workers reported a theoretical study on the α-C–H bond strength of methoxide as a function of cation.[32] The findings of this study were that the α-C–H bond strengths (gas phase BDEs reported) are highly dependent on the nature of the alkoxide counter ion. With a proton counter ion, $HOCH_3$, the α-C–H bond strength was calculated to be 90.7 kcal mol^{-1}, which was weakened to 79.0 kcal mol^{-1} when replaced with K^+, $[K^+][^-OCH_3]$. When the cation was completely removed, $[^-OCH_3]$, the calculated α-C–H bond further weakened to 74.2 kcal mol^{-1}. These findings were explained by siting the additional electron population on the alkoxide oxygen as a resonance contributor to stabilize the methoxyl radical anion generated upon removal of $H^\bullet$ (Scheme 4.9; adapted from ref 32). This study has been previously referenced in support of a sequential HAT/ET mechanism in galactose oxidase.

Scheme 4.9. Resonance Forms of M^+ Methoxyl Radical Anion; adapted from Ref. 32.

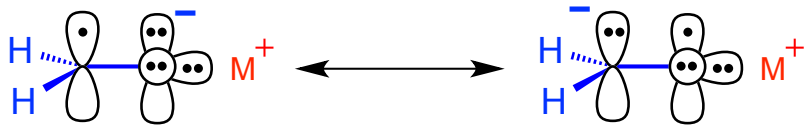

C-Centered Radical

O-Centered Radical

Stabilized With
More Ionic M–O Bond

From the trend reported by Goddard it seems likely that in copper/radical alcohol oxidations the modulation of the α-C–H bond strength is attributable not to the oxidation capability of Cu(II) but rather its cationic nature in relation to the alkoxide ligand. With a very oxidizing Cu(II) center, the α-C–H bond strength would in fact be expected to be *strengthened* by a more covalent Cu–O bond base on this trend, since the alkoxide oxygen has a smaller electron density. This is generally consistent with the mild reduction potentials measured for native galactose oxidase (150 mV vs NHE at pH 7.5)[33] The '*effective* BDFE' of the Cu–O bonds in the complexes reported here are very weak (≤ ~24-30 kcal mol^{-1}). This and the conclusions from ENDOR studies suggest the oxygen atom of the alkoxide ligand is very electron deficient. This would imply that the α-C–H bond of the alkoxide ligand is in fact *strengthened* in comparison to more ionic electron rich copper(II) alkoxide complexes.

This somewhat counterintuitive conclusion strongly suggests that the mechanism of copper/radical alcohol oxidation reactions does not involve a kinetically coupled HAT/ET step. The likely role of copper(II) in some cases may be modulate the alkoxide α-C–H by acting as an ionic counterion rather than as a strong oxidant. This supports a mechanism involving sequential rather than concerted HAT/ET that has sometimes been suggested for galactose oxidase.

A recent report by Stahl has shown this same conclusion cannot be drawn for copper/nitroxyl systems. In their report, the oxidation of radical probe substrates such as cyclobutanol and cyclopropyl carbinol were used to determine whether alcohol oxidation proceeded through a sequential radical transfer mechanism or a concerted two electron transfer.[3f] If a rate determining HAT was involved, radical ring opening would be

expected. Stahl reports no ring opening products are observed in their studies. Computational studies have shown a bimolecular reaction involving a HAT to TEMPO radical (Scheme 4.10A) has a kinetic barrier that is too high to corroborate kinetic data. The conclusion from this study, along with additional computational data and catalytic kinetic studies, was that copper/nitroxyl mediated alcohol oxidation involves the formation of an η^1-TEMPO-Cu(II)-alkoxide complex which is followed by a $H^+/2e^-$ transfer to the copper-TEMPO unit (scheme 4.10B). The thermochemical and reactivity studies reported here are in agreement with the computationally predicted high kinetic barrier for a bimolecular reaction as described in Scheme 4.10A.

Scheme 4.10. Adapted from Ref. 3f.

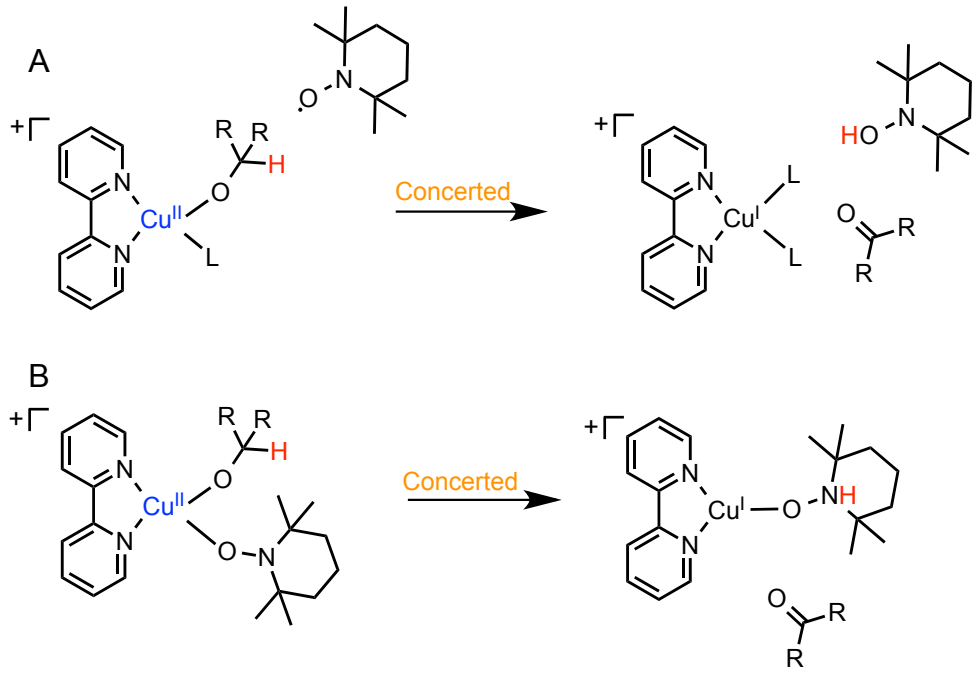

In the systems reported here, an η^1-TEMPO coordination mechanism is likely prohibited because of sterics but cannot be ruled out as a possible initiation step in the unusual autocatalytic reactions described for **(1)** and **(2)** in dichloromethane-d_2/1% MeCN-d_3 (v/v).

4.4. Conclusions

Copper/radical mediated alcohol oxidation reactions have been studied extensively from both biological and synthetic organic standpoints. The consensus intermediate involved in these reactions is a Cu(II) bound alkoxide ligand. The

mechanism by which the alkoxide ligand is oxidized has been an issue of long-standing interest in both fields. A variety of mechanisms have been proposed including (*i*) stepwise HAT from the α-C–H position to an oxyl radical followed by rapid ET to Cu(II), (*ii*) a concerted mechanism in which both HAT and ET occur in a single kinetic step,[2] and (*iii*) for copper/nitroxyl catalysis, the pre-coordination of TEMPO to Cu(II) followed by a concerted $H^+/2e^-$ transfer.[3f] Synthetic challenges involved in preparing isolable copper(II) alkoxide complexes as model complexes for this step have precluded a direct analysis of this reaction.

Model complexes **(1)** ($Tp^{tBu}Cu^{II}$-OCH_2CF_3) and **(2)** ($Tp^{tBuMe}Cu^{II}$-OCH_2CF_3) were prepared with the goal of studying this step directly. Reactivity studies and thermochemical analysis indicate alkoxide oxidation of **(1)** or **(2)** with $^tBu_3ArO^\bullet$ should be exoergic by ~30 kcal mol^{-1} or 24, respectively. With **(1)**, treatment with $^tBu_3ArO^\bullet$ results in a net $^\bullet OCH_2CF_3$ radical transfer from Cu(II) to generate an unusual dienone-ether complex. When the same reaction was attempted with **(2)**, no reaction was observed.

The results reported here clearly indicate that a concerted mechanism involving HAT to $^tBu_3ArO^\bullet$ and ET to Cu(II) is kinetically limited in this system. It is unclear whether this mechanism is viable in other systems with different coordination environments and substrates. Regardless, it can be generally concluded that net driving force is not a primary predictor for alkoxide oxidation via a kinetically coupled HAT/ET mechanism. This contrasts the common intuition regarding most radical reactions that often correlates thermodynamics and reaction kinetics.

4.5. Experimental

4.5.1. Materials:

Unless otherwise noted, all chemicals were purchased from Sigma-Aldrich and used without purification. Dichloromethane-d_2, acetonitrile-d_3, toluene-d_8 and 2,2,2-trifuoroethanol were purchased from Cambridge Isotope Labs. Dichloromethane-d_2, acetonitrile-d_3 were dried over CaH_2 and toluene-d_8 was dried over NaK and vacuum distilled. Acetonitrile was used as received from Burdick and Jackson (low water) and was stored in an argon pressurized stainless steel drum, plumbed directly into a glovebox.

Other solvents were purchased from Fischer and dried using a "Grubbs type" Seca Solvent System installed by GlassContour. TEMPO was purified by sublimation. TEMPO–H,[34] $^{t}Bu_3ArO^{\bullet}$,[20] $^{t}Bu_2NPArO$–H,[21] $^{t}Bu_2NPArO^{\bullet}$,[21] $Tp^{tBu}Cu^{II}$-Cl,[9d] $[Tp^{tBu}Cu^{I}]_2$,[9c] $Tp^{tBu}Cu^{I}$-MeCN,[9c] $Tp^{tBuMe}Cu^{II}$-Cl,[9b] $[Tp^{tBuMe}Cu^{I}]_2$,[10b] and $Tp^{tBuMe}Cu^{I}$-MeCN[35] were prepared using established literature protocols. All glassware was dried in an oven at 150 °C overnight and pumped into a nitrogen filled glovebox while hot. Celite was dried at 100 °C overnight under vacuum.

4.5.2. Instrumentation:

All ^{1}H (and ^{19}F) NMR spectra were obtained on Bruker 300 (282) and 500 (470) MHz instruments. The ^{1}H chemical shifts reported are referenced to TMS using the residual solvent peak and ^{19}F chemical shifts are referenced to a fluorobenzene internal standard. Unless otherwise noted, all reactions were preformed in a nitrogen filled glovebox. UV-visible absorption spectra were collected with a Hewlett-Packard 8453 diode array spectrometer equipped with a Unisoku USP-203 cryostat. EPR spectra were collected on a Bruker EMX CW X-band spectrometer. Cyclic voltammetry (CV) was performed using a CH Instruments 600D potentiostat. CHN elemetal analysis was performed by Atlantic Microlabs, Inc., Norcross, GA.

4.5.3. Representative reaction procedure:

In a typical NMR-scale reaction, a solution containing equimolar $Tp^{tBu}Cu^{II}$-OCH_2CF_3 and $^{t}Bu_3ArOH$ (15.3 mM in DCM-d_2/1% MeCN-d_3, C_6H_5F internal standard) were prepared in a nitrogen filled glovebox. The resulting reaction mixture was added to a J. Young NMR tube and covered in aluminum foil until the reaction had reached completion.

4.5.4. Syntheses:

hydro-*tris*(3-*tert*-butylpyrazol-1-yl)borate) copper(II) triflate, $Tp^{tBu}Cu^{II}$-OTf:

$Tp^{tBu}Cu^{II}$-OTf was prepared as previously described[9a] with minor modifications. To a 5ml toluene solution of $Tp^{tBu}Cu^{II}$-Cl (495 mg, 1.03 mmol) was added a 3 mL solution of AgOTf (264 mg, 1.03 mmol) with stirring. The reaction mixture rapidly changed colors from brown to deep purple and a thick precipitate of AgCl and $Tp^{tBu}Cu^{II}$-

OTf was formed. The solid mixture was collected by filtration, washed with toluene (3 × 5 ml) and dried under vacuum. Extraction with dichloromethane followed by filtration over Celite gave a deep purple solution, which upon removal of the solvent, yielded $Tp^{tBu}Cu^{II}$-OTf as a black solid (569 mg, 93 % yield). ^{1}H NMR (500 MHz, CD_2Cl_2) δ: 56.51 (broad, 3H), 20.98 (broad, 3H), 5.54 (broad, 27H), -5.38 (broad, 1H).

hydro-*tris*(3-*tert*-butyl-5-methyl-pyrazol-1-yl)borate) copper(II), $Tp^{tBuMe}Cu^{II}$-OTf:

To a 5ml toluene solution of $Tp^{tBuMe}Cu^{II}$-Cl (354 mg, 0.68 mmol) was added a 3 mL solution of AgOTf (175 mg, 0.68 mmol) with stirring. The reaction mixture rapidly changed colors from brown to deep purple. After 10 minutes, the resulting solution was filtered over Celite and the solvent removed in vacuo to yield $Tp^{tBuMe}Cu^{II}$-OTf as a black solid (411 mg, 95%). ^{1}H NMR (500 MHz, CD_2Cl_2) δ: 59.0 (broad, 3H), 10.42 (broad, 9H), 4.51 (broad, 27H), -5.97 (broad, 1H).

hydro-*tris*(3-*tert*-butylpyrazol-1-yl)borate) copper(II) 2,2,2-trifluoroethoxide, $Tp^{tBu}Cu^{II}$-OCH_2CF_3 (1):

A 2 mL dichloromethane solution containing DBU (39.1 mg, 0.26 mmoles) and 2,2,2-trifluoroethanol (77.0 mg, 0.79 mmoles) was added dropwise to a 15 mL stirring dichloromethane solution of $Tp^{tBu}Cu^{II}$-OTf (152 mg, 0.26 mmoles) upon which the reaction solution changed colors from deep purple to orange. After 10 minutes the solvent was removed in vacuo and the remaining solid was redissolved in a minimum amount of pentane and filtered. Large orange X-ray quality crystals grew upon standing at -30 °C (49.4 mg, 35%). ^{1}H NMR (500 MHz, CD_2Cl_2) δ: 40.55 (broad, 3H), 18.42 (broad, 3H), 4.36 (broad, 27H), -5.37 (broad, 1H). ^{19}F (470 MHz, CD_2Cl_2) δ: -65.9 (broad, 3F) UV/Vis: λ_{max} = 424 nm (3500 ± 350 M^{-1} cm^{-1}), λ_{max} = 886 nm (160 ± 16 M^{-1} cm^{-1}). Elemental Analysis – calculated: C, 50.79; H, 6.67; N, 15.45. Found: C, 51.03; H, 6.56; N, 15.65.

hydro-*tris*(3-*tert*-butylpyrazol-1-yl)borate) copper(II) 2,2,2-trifluoroethoxide-d_2, $Tp^{tBu}Cu^{II}$-OCD_2CF_3: $Tp^{tBu}Cu^{II}$-OCD_2CF_3 was prepared in the same manner as **(1)** but 2,2,2-trifluoroethanol-d_3 was used in place of proteo-2,2,2-trifluoroethanol.

hydro-*tris*(3-*tert*-butyl-5-methyl-pyrazol-1-yl)borate) copper(II) 2,2,2-trifluoroethoxide, $Tp^{tBuMe}Cu^{II}$-OCH_2CF_3 (2):

$Tp^{tBuMe}Cu^{II}$-OCH_2CF_3 was prepared as described for $Tp^{tBu}Cu^{II}$-OCH_2CF_3 (14% yield). ^{1}H NMR (500 MHz, CD_2Cl_2) δ: 43.3 (3H), 4.28 (27H), 1.98 (9H), -5.85 (1H). ^{19}F (470 MHz, CD_2Cl_2) δ: -66.52. UV/Vis: λ_{max} = 423 nm (3300 ± 330 M^{-1} cm^{-1}), λ_{max} = 902 nm (130 ± 13 M^{-1} cm^{-1}). Elemental Analysis – calculated: C, 53.29; H, 7.22; N, 14.34. Found: C, 53.34; H, 7.38; N, 14.34.

hydro-*tris*(3-*tert*-butylpyrazol-1-yl)borate) copper(II) 1,1,1-trifluoro-2-propoxide, $Tp^{tBu}Cu^{II}$-$OCH(CH_3)CF_3$ (3):

$Tp^{tBuMe}Cu^{II}$-$OCH(CH_3)CF_3$ was prepared as described for $Tp^{tBu}Cu^{II}$-OCH_2CF_3 (61% yield). ^{1}H NMR (500 MHz, CD_2Cl_2) δ: 39.60 (broad, 3H), 19.34 (broad, 3H), 4.30 (27H), -4.59 (1H). ^{19}F (470 MHz, CD_2Cl_2) δ: -65.52 (3H, broad). UV/Vis: λ_{max} = 432 nm (3900 ± 390 M^{-1} cm^{-1}), λ_{max} = 869 nm (130 ± 13 M^{-1} cm^{-1}). Elemental Analysis – calculated: C, 51.66; H, 6.87; N, 15.06. Found: C, 51.72; H, 6.77; N, 15.27.

Azabicyclo[3.3.1]nonane *N*-hydroxide, ABNO–H:

In an argon filled 'wet box', $Na_2S_2O_4$ (300 mg, 1.72 mmol) in ~3 mL of water was added to a ~5 mL 1:1 acetone/water solution of ABNO (150 mg, 1.07 mmol) with stirring. After 30 minutes, acetone was removed under vacuum leaving water and an insoluble white precipitate. The white precipitate was extracted with pentane (3 × 5 mL) and filtered. Pentane was removed under vacuum leaving a white solid. Repeated dissolution in ether and removal of solvent under vacuum served to remove any residual water remaining from the reaction (122 mg; 81% yield). The ^{1}H NMR spectrum was consistent with ABNO–H prepared via another synthetic route previously reported.[36]

4.5.5. Characterization of ^{t}Bu$_3$CHD-TFE

Attempts to purify ^{t}Bu$_3$CHD-TFE from the reaction mixture were unsuccessful. This was largely due to the very small scales these reactions were performed on. Characterization was obtained on products generated *in situ*. All spectroscopic data is consistent with the proposed structure. ^{1}H NMR of ^{t}Bu$_3$CHDO-TFE (300 MHz, DCM-d_2, 1% MeCN-d_3 (v/v), fluorobenzene int. std.): δ 6.80 (d, $^4J_{HH}$ = 2.4 Hz, 1H), 5.91 (d, $^4J_{HH}$ = 2.4 Hz, 1H), 3.66 (dq, $^2J_{HH}$ = 11.4 Hz, $^3J_{HF}$ = 9.0 Hz, 1H), 3.37 (dq, $^2J_{HH}$ = 11.4 Hz, $^3J_{HF}$ = 9.0Hz), 1.22 (s, 9H), 1.16 (s, 9H), 0.93 (s, 9H). ^{19}F NMR (282 MHz, DCM-d_2, 1%

MeCN-d_3 (v/v), fluorobenzene int. std.): δ −73.95 (t, $^3J_{HF}$ = 9.0 Hz, 3F). GC/MS (E.I.) predicted *m/z*: 360; observed *m/z* 304. Molecular ion not observed. *m/z* 304 corresponds to ^{t}Bu$_3$CHD-TFE minus isobutylene. IR (KBr) 1670 cm^{-1}.

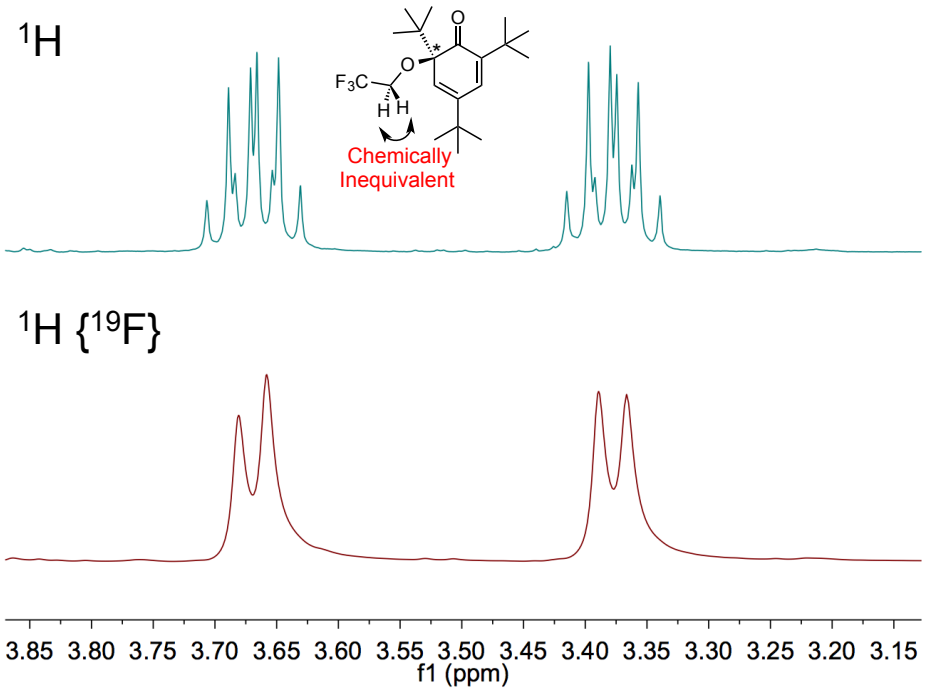

Figure 4.8. ^{1}H and ^{1}H {^{19}F} NMR spectra of ^{t}Bu$_3$CHD-TFE expanded to show the chemically inequivalent trifluoroethylene signals.

4.5.6. Pseudo-First Order Kinetic Measurements for Tp^{tBu}Cu^{II}-OCH$_2$CF$_3$ plus ^{t}Bu$_3$ArO$^\bullet$ in DCM/1% MeCN (v/v).

$$Tp^{tBu}Cu^{II}\text{-}OCH_3CF_3 + {}^tBu_3ArO^\bullet \rightarrow Tp^{tBu}Cu^{I}\text{-}MeCN\text{-}d_3 + {}^tBu_3CHDO\text{-}TFE$$

In each measurement, a cuvette equipped with a gas tight septum was filled with a known concentration of ^{t}Bu$_3$ArO$^\bullet$ (8.9 – 88.6 mM) in DCM/MeCN 1% (v/v). Tp^{tBu}Cu^{II}-OCH$_2$CF$_3$ was injected into the cuvette from a gastight syringe (to give a final concentration of 0.5 mM) immediately prior to starting kinetic measurements. The kinetics were monitored by UV/Vis spectroscopy. The large excess of ^{t}Bu$_3$ArO$^\bullet$ saturated most of the signal from Tp^{tBu}Cu^{II}-OCH$_2$CF$_3$ but monitoring the optical change between 400 and 500 nm proved sufficient for tracking reaction progress. Data were fit by SPECFIT/32^{TM} global analysis program to a simple first order model. The second order

rates calculated were generally reproducible when the same solvent batch was used for measurements but were irreproducible between stock solvents or even when the same stock solvent was used on different days.

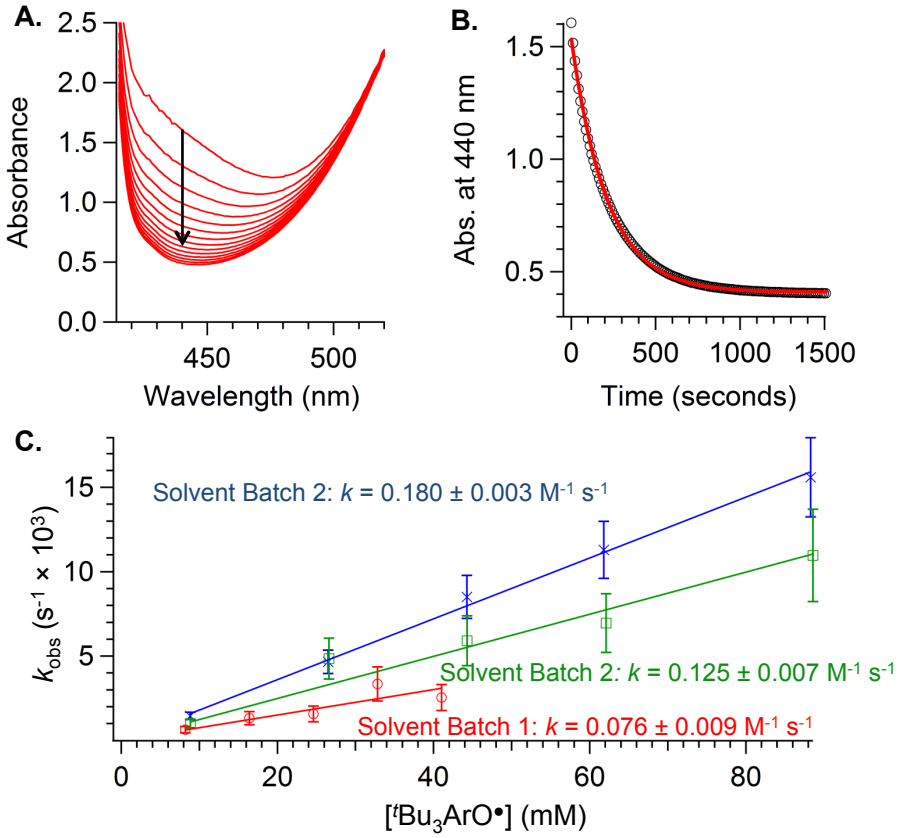

Figure 4.9. (A) Selected optical spectra of the reaction between Tp$^{t\text{Bu}}$Cu$^{\text{II}}$-OCH$_2$CF$_3$ (0.5 mM) with ^{t}Bu$_3$ArO (26.5 mM). (B) Kinetic trace of the same reaction monitored at 440 nm. The raw data is indicated by black circles (○) and the solid red line represents the single exponential fit. (C) The pseudo-first order plot of the reaction between Tp$^{t\text{Bu}}$Cu$^{\text{II}}$-OCH$_2$CF$_3$ and ^{t}Bu$_3$ArO$^\bullet$ collected with three different solvent batches under similar conditions.

4.5.6. Kinetic Isotope Experiments with $Tp^{tBu}Cu^{II}$-$OCH(D)_2CF_3$ and $^tBu_3ArO^\bullet$

$$Tp^{tBu}Cu^{II}\text{-}OCH(D)_3CF_3 + {}^tBu_3ArO^\bullet \rightarrow Tp^{tBu}Cu^{I}\text{-}MeCN\text{-}d_3 + {}^tBu_3CHDO\text{-}TFE$$

The kinetic trace for these reactions was obtained by preparing a 15.3 mM DCM-d_2/1%MeCN-d_3 (v/v) solution of either $Tp^{tBu}Cu^{II}$-OCH_2CF_3 or $Tp^{tBu}Cu^{II}$-OCD_2CF_3 with one eq TEMPO in a J. Young NMR tube in a nitrogen filled glovebox. Shortly after mixing (*ca.* 5 minutes), ^{1}H NMR spectra were collected at 5 minute intervals until the reaction had reached completion. Only 1 scan per spectrum was collected in order to ensure complete T1 relaxation was reached between scans. Reaction progress was monitored by integration of the $Tp^{tBu}Cu^{I}$-MeCN-d_3 pyrazole peak at δ 5.95 ppm vs. a fluorobenzene internal standard. The same experiment was performed with the $Tp^{tBu}Cu^{II}$-OCD_2CF_3 isotopologue and is also shown. Within the error of the experiment (± ~10 %), no kinetic isotope effect is observed.

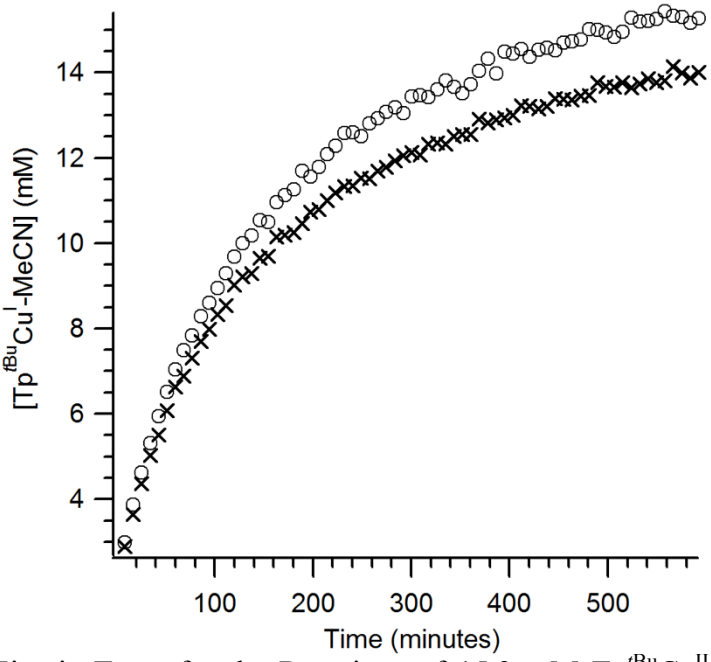

Figure 4.10. Kinetic Trace for the Reactions of 15.3 mM $Tp^{tBu}Cu^{II}$-OCH_2CF_3 (o) and $Tp^{tBu}Cu^{II}$-OCD_2CF_3 (×) with 1 eq $^tBu_3ArO^\bullet$ in DCM-d_2/1% MeCN-d_3 (v/v).

4.5.7. Crystallographic Characterization of (3).

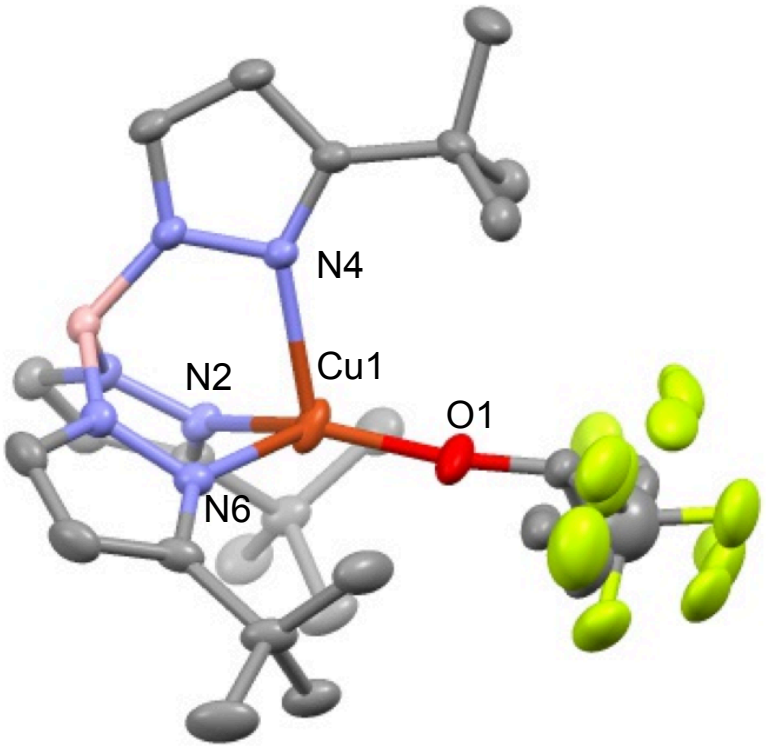

Figure 4.11. ORTEP drawing of $Tp^{tBu}Cu^{II}$-$OCH(CH_3)CF_3$. Hydrogen atoms are omitted for clarity. One pentane molecule co-crystallizes with $Tp^{tBu}Cu^{II}$-$OCH(CH_3)CF_3$ but is not shown here. The $OCH(CH_3)CF_3$ ligand is disordered over 4 positions.

Table 4.4. Select bond lengths (Å) and angles (deg) of $Tp^{tBu}Cu^{II}$-$OCH(CF_3)CH_3$ **(3)**.

Primary Metal Coordination Sphere			
N2-Cu1	1.9733(16)	N6-Cu1	2.0640(16)
N4-Cu1	2.1740(15)	O1-Cu	1.7923(17)
N2-Cu1-O1	137.53(8)	N2-Cu1-N6	91.68(7)
N4-Cu1-O1	110.91(7)	N2-Cu1-N4	91.64(6)
N6-Cu1-O6	121.47(9))	N6-Cu1-N4	92.24(6)

4.5.7. Decomposition Studies of (3)

$Tp^{tBu}Cu^{II}$-$OCH(CH_3)CF_3$ → $Tp^{tBu}Cu^{I}$-MeCN-d_3 + 0.5 $HOCH(CH_3)CF_3$ + ???

Decomposition of $Tp^{tBu}Cu^{II}$-$OCH(CH_3)CF_3$ occurred overnight in either DCM-d_2/1% MeCN-d_3 (v/v) or toluene-d_8. When 1 equivalent TEMPO was added to $Tp^{tBu}Cu^{II}$-$OCH(CH_3)CF_3$, the same decomposition products were observed but the reaction only required ~5 hours to reach completion. We were able to identify $Tp^{tBu}Cu^{I}$-MeCN-d_3 and 0.5 equivalents of TFE as products but were unable to determine the identity of the final product. We could determine it was diasterotopic from the ^{19}F NMR spectrum and comparison to the decomposition of an enantiopure $Tp^{tBu}Cu^{II}$-$OCH(CH_3)CF_3$ (*R*). Because stereochemistry is preserved, the decomposition most likely does not involve homolytic cleavage of the α-C–H bond

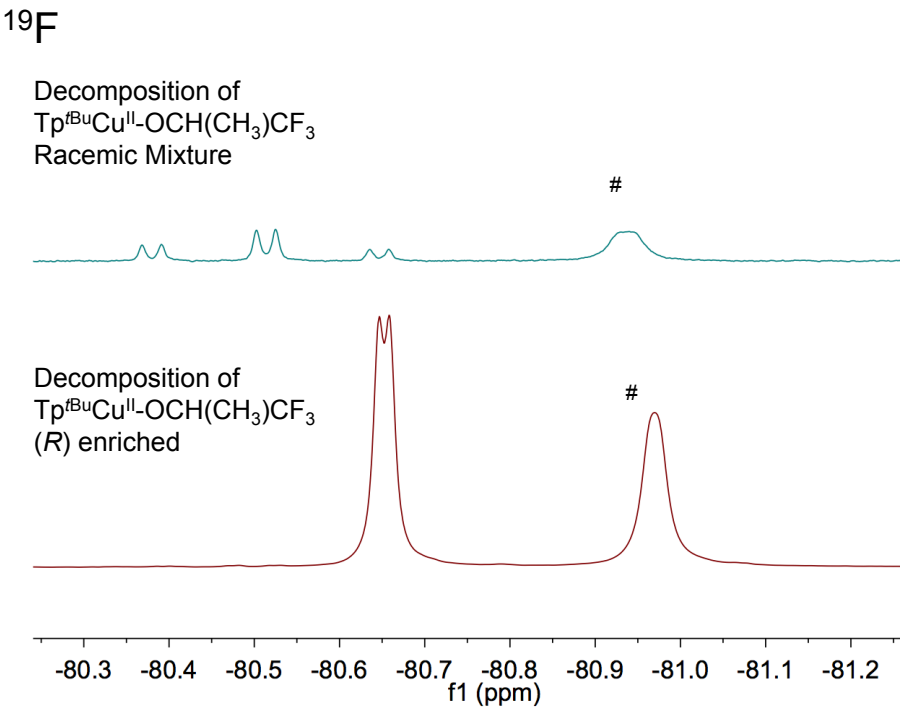

Figure 4.12. ^{19}F NMR spectra (282 MHz top; 470 MHz bottom) of the decomposition reaction of 15.3 mM or racemic $Tp^{tBu}Cu^{II}$-$OCH(CH_3)CF_3$ (top) or (R) enriched $Tp^{tBu}Cu^{II}$-$OCH(CH_3)CF_3$ (bottom) in DCM-d_2/1% MeCN-d_3 (v/v). Trifluoroisopropanol is shown by #.

4.5.8. Thermochemical Conversions

4.5.8.1. Background

The interconversion between gas phase bond dissociation enthalpy (BDE) and bond dissociation free energy (BDFE) of X–H bonds can be achieved by using equation 4.17, using $S°(H^{\bullet}) = 27.42$ cal K^{-1} mol^{-1}.[17]

$$BDFE_g(X–H) = BDE_g(X–H) – TS°(H^{\bullet}) – T\{S°(X^{\bullet}) – S°(X–H)\} \quad (4.17)$$

Typically for small molecules, $S°(X^{\bullet}) \cong S°(X–H)$ because they are generally very similar in size and structure. With this simplification, the relationship between $BDFE_g$ and BDE_g at 298K is simplified to equation 4.18.[17]

$$BDFE_g(X–H) = [BDE_g(X–H) – 8.2 \text{ kcal mol}^{-1}] \pm 0.5 \text{ kcal mol}^{-1} \quad (4.18)$$

The interconversion between X–H gas phase BDFEs and solution BDFEs of can be achieved by accounting for the free energy of solvation of $H^{\bullet}$ and the difference in free energy of solvation of XH and $X^{\bullet}$ (equation 4.19).[17]

$$BDFE_{solv} = BDFE_g + \Delta G°_{solv}(H^{\bullet}) + [\Delta G°_{solv}(X^{\bullet}) – \Delta G°_{solv}(XH)] \quad (4.19)$$

$\Delta G°_{solv}(H^{\bullet})$ in toluene is 4.77 kcal mol^{-1} (calculated from the solubility of $H^{\bullet}$ [assumed to be the same as H_2[17]] at STP (equation 4.20)).[17,37]

$$\Delta G°_{solv}(H^{\bullet}) = -RT\ln(K_{sol}) \quad (4.20)$$

In aprotic solvents like toluene, the $[\Delta G°_{solv}(X^{\bullet}) – \Delta G°_{solv}(XH)]$ term is taken as the free energy of the XH–solvent hydrogen bond. This can be calculated using empirically determined H-bonding acidity (α_2^H) and basicity parameters (β_2^H) described by Abraham (equation 4.21).[38]

$$\Delta G°_{solv} = -10.02\alpha_2^H\beta_2^H - 1.492 \quad (4.21)$$

The β_2^H parameter in toluene is 0.14.[28b] Values for α_2^H have been extensively tabulated by Abraham.[38]

A more complete description of these conversions and the use of Abraham's model of interconverting solution BDFE values can be found in references 28b.

4.5.8.2. Calculating the toluene BDFE of the first C–H bond of 1,4-cyclohexadiene:

The reported gas phase BDFE of the first C–H bond in 1,4-cyclohexadiene is 67.8 kcal mol^{-1}.[17]

The first C–H BDFE in toluene can be calculated using the reported gas phase BDFE of 67.8 kcal mol^{-1}. Using this value in equation 4.19 with the previously described $\Delta G°_{tol}(H^{\bullet}) = 4.77$ and assuming $\alpha_2^H \cong 0$,[17] the C–H $BDFE_{tol}$ is calculated to be 72.6 ± 3 kcal mol^{-1}.

4.5.8.3. Calculating the toluene BDFE of the N–H bond in 2,2,6,6-tetramethylpiperidine, TMP-H:

The gas phase BDE of TMP–H is 87.6 kcal mol^{-1}.[4] This value can be converted to a gas phase BDFE using equation 4.18: N–H $BDFE_g$ = 79.4 ± 2 kcal mol^{-1}.
Using equation 4.19 with the previously described $\Delta G°_{tol}(H^{\bullet}) = 4.77$ and the reported α_2^H value of secondary amines of 0,[38] the N–H $BDFE_{tol}$ is calculated to be 84.2 ± 3 kcal mol^{-1}.

4.5.8.4. Calculating the toluene BDFE of the O–H bond in 2,2,2-trifluoroethanol, TFE.

The gas phase BDE of CF_3CH_2O–H is 107.0 kcal mol^{-1}. This value is converted to a gas phase BDFE using equation 4.18: O–H $BDFE_g$ = 98.8 ± 2 kcal mol^{-1}.[3]
Using this value in equation 4.19 with the previously described $\Delta G°_{tol}(H^{\bullet}) = 4.77$, toluene $\beta_2^H = 0.14$, and reported $\alpha_2^H = 0.567$ for TFE,[38] the $BDFE_{tol}$ value is calculated: O–H $BDFE_{tol}$ = 101.3 ± 3 kcal mol^{-1}.

4.5.8.5. Calculating the toluene BDFE of the O–H bond in H_2O.

The reported gas phase BDFE of HO–H is 111.0 kcal mol^{-1}.[17] This value can be converted to a toluene phase BDFE using equation 4.19 with $\Delta G°_{tol}(H^{\bullet}) = 4.77$, toluene $\beta_2^H = 0.14$, and reported $\alpha_2^H = 0.353$[38] for H_2O: HO–H $BDFE_{toluene}$ = 113.8 ± 3 kcal mol^{-1}.

4.5.8.6. Calculating the gas phase $\Delta G°_{dehydrog}$ of 2,22-trifluoroethanol.

The $\Delta H_{g,dehydrog}$ can be calculated from the standard heats of formation of 2,2,2-trifluoroethanol (-211.3 kcal mol^{-1})[39] and trifluoroacetaldehyde (-185.8 kcal mol^{-1}; calculated).[39]

$CF_3CH_2OH \rightarrow 2C + 1.5\ F_2 + 0.5\ O_2 + 1.5\ H_2$ $\Delta H° = 211.3$ kcal mol^{-1}

$2C(s) + 1.5\ F_2 + 0.5\ O_2 + 0.5\ H_2 \rightarrow O=C(H)CF_3$ $\Delta H° = -185.8$ kcal mol^{-1}

$CF_3CH_2OH \rightarrow O=C(H)CF_3 + H_2$ $\Delta H°_{dehydrog} = 25.5$ kcal mol^{-1}

The enthalpy of dehydrogenation, $\Delta H°_{dehydrog}$= can be converted to a free energy of formation at 298K from the standard molar entropies of H_2 ($S°_{gas} = 31.2$ cal mol^{-1} K^{-1}),[40] ethanol ($S°_{gas} = 67.3$ cal mol^{-1} K^{-1})[40] and acetaldehyde ($S°_{gas} = 63.0$ cal mol^{-1} K^{-1})[40] (taken to be the same as for 2,2,2-trifluoroethanol and trifluoroacetaldehyde).

$$\{S°_{gas}(H_2) + S°_{gas}(\text{acetaldehyde})\} - S°_{gas}(\text{ethanol}) = 26.9 \text{ cal mol}^{-1} \text{ K}^{-1}$$

Thus, at 298 K, $\Delta G°_{gas,dehydrog}$(2,2,2-trifluoroethanol) = 17.5 ± 3 kcal mol^{-1}

4.5.8.7. Calculating the gas phase BDFE of TEMPO–H

The gas phase BDE of TEMPO–H is 70 ± 1 kcal mol^{-1}. This value is converted to a gas phase BDFE using equation (4.18): O–H $BDFE_g$ = 62 ± 2 kcal mol^{-1}.[4]

4.5.8.8. Calculating the gas phase BDFE of ^{t}Bu$_3$ArO–H

The gas phase BDE of ^{t}Bu$_3$ArO–H is 81 ± 1 kcal mol^{-1}. This value is converted to a gas phase BDFE using equation (4.18): O–H $BDFE_g$ = 73 ± 2 kcal mol^{-1}.[4]

4.5.8.9. Calculating the gas phase effective BDFE of ½ [Tp§Cu^{I}]$_2$ + HOCH$_2$CF$_3$

The low limits for the effective O–H BDFE of ½ [Tp$^{t\text{Bu}}$Cu^{I}]$_2$ + $HOCH_2CF_3$ and ½ [Tp$^{t\text{BuMe}}$Cu^{I}]$_2$ + $HOCH_2CF_3$ in toluene are 76.7 and 70.7 kcal mol^{-1}, respectively. Using equation (4.19) and assuming the solvation free energy differences of ½ [Tp§Cu^{I}]$_2$ + $HOCH_2CF_3$ and Tp§Cu^{II}-OCH_2CF_3 are small, these values can be converted to 71.9 ± 3 and 66.0 ± 3 kcal mol^{-1} for ½ [Tp$^{t\text{Bu}}$Cu^{I}]$_2$ + $HOCH_2CF_3$ and ½ [Tp$^{t\text{BuMe}}$Cu^{I}]$_2$ + $HOCH_2CF_3$, respectively.

Other quoted BDFE values in toluene (taken to be the same as in benzene) are found in reference 17.

Table. 4.5. Crystallographic collection and refinement data

	(1)	**(2)**	**(3)•Pentane**
Empirical formula	$C_{23}H_{36}BCuF_3N_6O$	$C_{26}H_{42}BCuF_3N_6O$	$C_{29}H_{50}BCuF_3N_6O$
Formula weight	543.93	586.01	630.10
Temperature (K)	110(2)	110(2)	110(2) K
Wavelength (Å)	0.71073	0.71073	0.71073 Å
Crystal description	orange block	orange prism	Orange plate
Crystal system	Monoclinic	Monoclinic	Monoclinic
Space group	P 2_1/n	P 2_1/c	P 2_1/n
Unit cell dimensions			
a (Å)	9.6749(12)	9.6817(16)	10.2492(13)
b (Å)	16.817(2)	34.735(6)	20.261(3)
c (Å)	16.646(2)	9.6425(16)	15.796(2)
α(deg)	90	90	90
β(deg)	96.881(6)	115.495(10)	90.045(6)
γ(deg)	90	90	90
Volume ($Å^3$)	2688.9(6)	2926.9(8)	3280.3(7)
Z	4	4	4
Density (calculated) (Mg/m^3)	1.344	1.330	1.276
Absorption coefficient (mm^{-1})	0.860	0.795	0.714
F(000)	1140	1236	1340
Crystal size (mm^3)	0.30x0.30x0.10	0.07x0.05x0.03	0.21x0.20x0.17
θ range for data collection	1.73 to 28.48°.	2.33 to 25.45°.	1.63 to 34.22°.
Index ranges	-12<=h<=12 -22<=k<=22, -22<=l<=22	-11<=h<=11, -41<=k<=41, -11<=l<=11	-16<=h<=16, -32<=k<=31, -24<=l<=24
Reflections collected	91453	68260	149335
Independent reflections	6739	5391	13476
R_{int}	0.0314	0.1214	0.0447
Completeness to θ = 25.00°	99.6 %	99.9 %	99.4 %
Max/min. transmission	0.9190/0.7825	0.9765/0.9465	0.8882/0.8645
Refinement method	Full-matrix least-squares on F^2		
Data / restraints / parameters	6739/0/325	5391/0/355	13476/322/530
Goodness-of-fit on F^2	1.036	1.008	1.033
Final R	0.0276	0.0435	0.0639
R_w	0.0701	0.0742	0.1514
Largest diff. peak and hole ($e/Å^{-3}$)	0.661/-0.292	0.377/-0.403	1.752/3.380

Notes for Chapter 4

---

(1) Dany Capitao had significant contributions to the work described in this Chapter.

(2) (a) Whittaker, J. W. *Chem. Rev.* **2003**, 103, 2347. (b) Lyons, C. T.; Stack, D. P. *Coord. Chem. Rev.* **2013**, 257, 528. (c) Jazdzewski, B. A.; Tolman, W. B. *Coord. Chem. Rev.* **2000**, 200, 633. (d) Himo, Fahmi, Eriksson, L. A.; Maseras, F.; Siegbahn, P. E. M. *J. Am. Chem. Soc.* **2000**, 122, 8031. (e) Whittaker, J. W. *Arch. Biochem. Biophys.* **2005**, 433, 227. (f) Pratt, R. C.; Stack, T. D. P. *Inorg. Chem.* **2005**, 44, 2367. Solomon, E. I.; Heppner, D. E.; Johnston, E. M.; Ginsbach, J. W.; Cirera, J.; Qayyum, M.; Kieber-Emmons, M. T.; Kjaergaard, C. H.; Hadt, R. G.; Li, T. *Chem. Rev.* **2014**, 114, 3659. (g) Wachter, R. M.; Branchaud, B. P. *J. Am. Chem. Soc.* **1996**, 118, 2782. (h) Turner, B. E.; Branchaud, B. P. *Bioorg. Med. Chem. Lett.* **1999**, 9, 3341. (i) Whittaker, M. M.; Whittaker, J. W. *Biochemistry*, **2001**, 40, 7140.

(3) (a) Sheldon, R. A.; Arends, I. W. C. E. *Adv. Synth. Catal.* **2004**, 346, 1051. (b) Cao, Q.; Dornan, L. M.; Rogan L.; Hughes, N. L.; Muldoon, M. L. *Chem. Commun.* **2014**, 50, 4524. (c) Ryland, B. L.; Stahl, S. S. *Angew. Chem., Int. Ed.* **2014**, DOI:10.1002/anie.201403110. (d) Hoover, J. M.; Ryland, B. L.; Stahl, S. S. *J. Am. Chem. Soc.* **2013**, 135, 2357. (e) Hoover, J. M.; Ryland, B. L.; Stahl, S. S. *Adv. Catal.* **2013**, 3, 2599. (f) Ryland, B. L.; McCann, S. D.; Brunold, T. C.; Stahl, S. S. *J. Am. Chem. Soc.* **2014** DOI:10.1021/ja50701371.

(4) Luo, Y. –R. *Comprehensive Handbook of Chemical Bond Energies*; CRC Press: Boca Raton, Fl, 2007.

(5) Gephart III, R. T.; McMullin, C. L.; Sapiezynkski, N. G.; Jang, E. S.; Aguila, M. J. R.; Cundari, T. R.; Warren, T. H. *J. Am. Chem. Soc.* **2012**, 134, 17350.

(6) (a) Jeffries, P. M.; Wilson, S. R.; Girolami, G. S. *Inorg. Chem.* **1992**, 31, 4503. (b) Subhash, C. G.; Kramer, K. S.; Chiang, M. Y.; Buhro, W. E. *Polyhedron* **1990**, 9, 611. (c) Chi, Y.; Hsu, P. F.; Liu, C. S.; Ching, W. L.; Chou, T. Y.; Carty, A. J.; Peng, S. M.; Lee, G. H.; Chuang, S. H. *J. Mater. Chem.* **2002**, 12, 3541.

(7) Tubbs, K. J.; Fuller, A. L.; Bennett, B.; Arif, A. M.; Berreau, L. M. *Inorg. Chem.* **2003**, 42, 4790.

(8) Vela, J.; Stoian, S.; Flaschenreim, C. J.; Münck, E.; Holland, P. L. *J. Am. Chem. Soc.* **2004**, 126, 4522.

(9) (a) Tolman, W. B. *Inorg. Chem.* **1991**, 30, 4877. (b) Carrier, S. M.; Ruggiero, C. E.; Tolman, W. B. *J. Am. Chem. Soc.* **1992**, 114, 4407. (c) Carrier, S. M.; Ruggiero, C. E.; Houser, R. P.; Tolman, W. B. *Inorg. Chem.* **1993**, 32, 4889. (d) Ruggiero, C. E.; Carrier, S. M.; Antholine, W. E.; Whittaker, J. M.; Cramer, C. J.; Tolman, W. B. *J. Am. Chem. Soc.* **1993**, 115, 11285.

(10) (a) Han, R.; Looney, A.; McNeill, K; Parkin, G.; Rheingold, A. L. ; Haggerty, B. S. *J. Inorg. Biochem.* **1993**, 49, 105. (b) Yoon, K.; Parkin, G. *Polyhedron* **1995**, 14, 811.

(11) (a) Kitajima, N.; Fujisawa, K.; Tanaka, M.; Moro-oka, T. *J. Am. Chem. Soc.* **1992**, 114, 9232. (b) Kitajima, N.; Ktayama, T.; Fujisawa, K.; Iwata, Y.; Moro-oka, Y. *J. Am. Chem. Soc.* **1993**, 115, 7872. (c) Qui, D.; Kilpatrick, L.; Kitajima, N.; Spiro, T. G. *J. Am. Chem. Soc.* **1994**, 116, 2585. (d) Fujisawa, K.; Iwata, Y.; Kitajima, N.; Higashimura, H.; Kubota, M.; Miyashitu, Y.; Yamada, Y.; Okamoto, K.; Moro-oka, Y. *Chem. Lett.* **1993**, 28, 739. (e) Fujisawa, K.; Kobayashi, T.; Fujita, K.; Kitajima, N.; Moro-oka, Y.; Miyashita, Y.; Yamada, Y.; Okamoto, K. *Bull. Chem. Soc. Jpn.* **2000**, 73. 1797. (f) Chen, P.; Fujisawa, K.; Solomon, E. I. *J. Am. Chem. Soc.* **2000**, 122, 10177.

(12) Trofimenko, S.; Calabrese, J. C.; Thompson, J. S. *Inorg. Chem.* **1987**, 26, 1507.

(13) Holm, R. H.; Kennepohl, P.; Solomon, E. I. *Chem. Rev.* **1996**, 96, 2239.

(14) Solomon, E. I.; Szilagyi, R. K.; George, S. D.; Basumallick, L. *Chem. Rev.* **2004**, 104, 419.

(15) Roberts, J. E.; Cline, J. F.; Lum, V.; Freeman, H.; Gray, H. B.; Peisach, J.; Reinhammar, B.; Hoffman, B. M. *J. Am. Chem. Soc.* **1984**, 106, 5324.

(16) Kaljurand, I.; Kütt, A.; Sooväli, L.; Rodima, T.; Mäemets, V.; Leito, I.; Koppel, I. A. *J. Org. Chem.* **2005**, 70, 1019.

(17) Warren, J. J.; Tronic, T. T.; Mayer, J. M. *Chem. Rev.* **2010**, 110, 6961.

(18) The ^{1}H NMR signals for $[Tp^{tBuMe}Cu^{I}]_2$ are not broadened at room temperature but its spectrum is still simplified by the addition of MeCN-d_3.

(19) Gas phase BDEs and BDFEs reported in references 4 and 17 were converted to toluene or gas phase BDFEs. See Experimental for a full description.

(20) Manner, V. W.; Markle, T. F.; Freudenthal, J. H.; Roth, J. P.; Mayer, J. M. *Chem. Commun.* **2008**, 256.

(21) Porter, T. R.; Kaminsky, W.; Mayer, J. M. *J. Org. Chem.* **2014** DOI:10.1021/jo501531a

(22) The same reactions performed with **(1)** were also performed with **(2)** with the exception of the reaction with 1,4-cyclohexadiene or the reaction with $^{t}Bu_2NPArO$–H in DCM-d_2/1% MeCN-d_3 (v/v).

(23) Siegemund, G.; Schwertfeger, W.; Feiring, A.; Smart, B.; Behr, F.; Vogel, H.; Mekusick, B. *Ullmann's Encyclopedia of Industrial Chemistry: Fluorine Compounds, Organic*; Wiley-VCH Verlag GmbH & Co. KGaA. Weinheim, Germany: 2000.

(24) (a) Calculations carried out by Zhaosheng "Bill" Qian (b) Zhao, Y.; Truhlar, D. G. *Acc. Chem. Res.* **2008**, 41, 157.

(25) Korth, H. G.; Chateauneuf, J.; Lusztyk, J.; Ingold, K. U. *J. Org. Chem.* **1991**, 56, 2405.

(26) (a) Trifluoroethyl trifluoroacetate was identified by GC/MS and comparison to an independently prepared sample. (b) Grieco, P. A.; Parker, D. T. *J. Org. Chem.* **1988**, 53, 3325.

(27) Frenklach, M.; Clary, D. *Ind. Eng. Chem. Fundam.* **1983**, 22, 433.

(28) (a) Mayer, J. M. *Acc. Chem. Res.* **2011**, 44, 36. (b) Warren, J. J.; Mayer, J. M. *Proc. Natl. Acad. Sci.* **2010**, 107, 5282. (c) Mayer, J. M *J. Phys. Chem. Lett.* **2011**, 2, 1481.

(29) This reaction was carried out at 15.3 mM and is entropically more favorable than if it were preformed at 1 M standard state since 2 reagents react to generate 2.5 products. Describing the free energy of this reaction as $\Delta G°$ assumes the same reaction would occur at 1 M concentrations.

(30) See Experimental for gas phase thermochemical conversions.

(31) (a) Lin, C. Y.; Coote, M. L.; Gennaro, A.; Matyjaszewski, K. *J. Am. Chem. Soc.* **2008**, 130, 12762. (b) Lin, C. Y.; Marque, S. R. A.; Matyjaszewski, K.; Coote, M. L. *Macromolecules* **2011**, 44, 7568. (c) Braunecker, W. A.; Matyjaszewski, K. *Prog.*

Polym. Sci. **2007**, 32, 93. (d) Marque, S.; Mercier, C. L.; Tordo, P.; Fischer, H. *Macromolecules* **2000**, 33, 4403. (e) Moad, G.; Rizzardo, E. *Macromolecules*, **1995** 28, 8722. (f) Hodgson, J. L.; Lin, C. Y.; Coote, M. L.; Marque, S. R. A.; Matyjaszewski, K. *Macromolecules* **2010**, 43, 3728. (g) Skene, W. G.; Belt, S. T.; Connolly, T. J.; Hahn, P.; Scaiano, J. C. *Macromolecules* 1998, 31, 9103.

(32) Steigerwald, M. L.; Goddard III, W. A.; Evans, D. A. *J. Am. Chem. Soc.* **1979**, 101, 1994.

(33) Wright, C.; Sykes, A. G. *J. Inorg. Biochem.* **2001**, 85, 237.

(34) Mader, E. A.; Davidson, E. R.; Mayer, J. M. *J. Am. Chem. Soc.* **2007**, 129, 5153.

(35) Muñoz-Molina, J. M. A.; Sameera, W. M. C.; Álvarez, E.; Maseras, F.; Belderrain, T. S. R.; Pérez, P. J. *Inorg. Chem.* **2011**, 50, 2458.

(36) Nelsen, S. F.; Kessel, C. R.; Brien, D. J. *J. Am. Chem. Soc.* **1980**, 102, 702.

(37) Brunner, E. J. *J. Chem. Eng. Data* **1985**, 30, 269.

(38) (a) Abraham, M. H.; Grellier, P. L.; Prior, D. V.; Duce, P. P. *J. Chem. Soc. Perkin Trans. II* **1989**, 699. (b) Abraham, M. H.; Frellier, P. L.; Prior, D. V.; Morris, J. J.; Taylor, P. T. *J. Chem. Soc. Perkin Trans. II* **1990**, 521.

(39) Bartmess, J. E.; Leibman, J. *Struct. Chem.* **2013**, 24, 2035.

(40) *CRC Handbook of Chemistry and Physics, 95th ed*; CRC Press: Boca Raton, Fl, 2014.

Chapter 5:
Sterically Directed Nitronate Complexes of 2,6-Di-*tert*-Butyl-4-Nitrophenoxide with Cu(II) and Zn(II) and Their H-Atom Transfer Reactivity

5.1 Introduction

Chemical reactions between copper(II) and phenols or phenol derivatives are widespread throughout chemistry and biology and are critical in a variety of processes. For example, in biology the enzyme tyrosinase uses a di-copper containing active site to oxidize tyrosine to dopaquinone in the first biosynthetic step of the production of the pigment, melanin.[1] Defects in this process result in the pigment deficiency disorder known as albinism. In chemistry, copper catalysts have been developed for the production of BINOL (1,1'-*bis*-2,2'-napthol) and BINOL derivatives from napthol for their use as ligands in asymmetric catalysis.[2]

One of the features that makes copper and phenols so well suited for one another in many of these reactions is their ability to form a copper(II) phenoxide intermediate.[2b] Formation of this intermediate results in activation of the phenoxide ligand through radical delocalization onto the 2, 4, and 6 positions of the ring (Scheme 5.1). This allows for radical-radical coupling reactions or O_2 addition to take place at these positions. Because of the importance of this motif in organic and enzymatic catalysis, the reactivity of copper with phenols has been well studied from a fundamental standpoint. There are many examples of copper(II) phenoxide complexes that have been reported and their reactivities have been well studied.[3]

Scheme 5.1. Resonance forms of Copper(II) Phenoxide

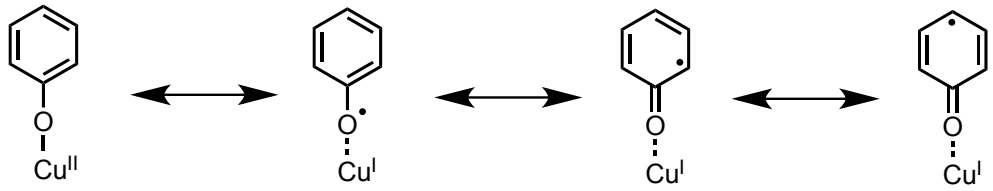

We report here an example of a Cu(II) complex ligated by the bulky tridentate Tp^{tBu} ligand (Tp^{tBu} = hydro-*tris*(3-*tert*-butyl-pyrazol-1-yl)borate) that binds 2,6-di-*tert*-butyl-4-nitro-phenoxide ($O_2N^tBu_2C_6H_2O^-$) *through the nitro group* (nitronate) *rather than the phenoxide oxygen* ($Tp^{tBu}Cu^{II}$- $O_2N^tBu_2C_6H_2O$; **(1)**). The nitronato $-O_2N=R$ unit binds κ^2 to the $Tp^{tBu}Cu^{II}$ unit, with the ligand better described as a nitronato-quinone rather than

a phenoxide (Scheme 5.2.). The same $[Tp^{tBu}Cu^{II}]^+$ complex binds the unsubstituted 4-nitrophenoxide through the phenolic oxygen. This indicates the unusual nitronate binding mode observed with the 2,6-di-substituted phenoxide is the result of steric clash between the Tp^{tBu} ligand and the *tert*-butyl groups of the phenol. This same pattern was also observed for the $[Tp^{tBu}Zn^{II}]^+$ analogues except the nitronate ligand binds κ^1 in this case.

Scheme 5.2. Resonance forms of 2,6-di-*tert*-butylphenoxide

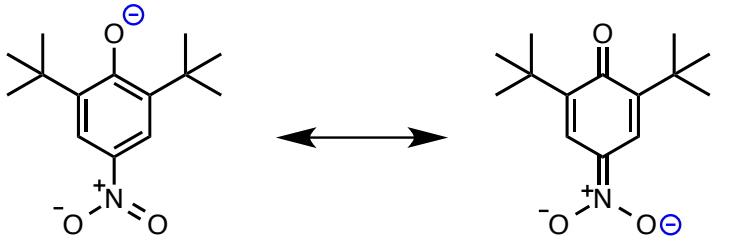

A variety of ransition metal-nitronate complexes have previously been reported for several different metals.[4] These examples have been limited to nitronate ligands derived from α-deprotonated primary and secondary aliphatic nitro compounds (Scheme 5.3). With only one exception, these bind to metals in a κ^2 fashion.[4a,5] To our knowledge, the examples reported here are the first cases of transition metal complexes with nitronate ligands derived from an aromatic nitro compound.

Scheme 5.3. α-Deprotonation of primary or secondary aliphatic nitro compound

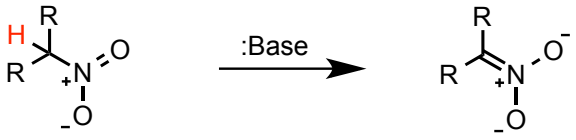

While this binding motif is different than what is typically found in copper mediated catalytic reactions involving phenols, we found the nitronate bound ligand was still activated for radical reactivity. **(1)** was found to be a competent hydrogen atom acceptor, capable of removing a hydrogen atom from the hydroxylamine, TEMPO–H (2,2,6,6-tetramethylpiperidin-1-ol).

The results described here serve to demonstrate an unusual sterically enforced transition metal-ligand binding motif as well as to highlight a new copper-phenol interaction that differs from what is generally observed in biological and chemical catalysis.

5.2. Results

5.2.1. Sythesis and Characterization

5.2.1.1. $Tp^{tBu}Cu^{II}$-$O_2N^tBu_2C_6H_2O$ (1)

Treatment of the previously described $Tp^{tBu}Cu^{II}$-OCH_2CF_3[6] with one equivalent of 2,6-di-*tert*-butyl-4-nitro-phenol ($O_2N^tBu_2C_6H_2OH$) in toluene-d_8 results in a rapid color change from red-orange to dark blue-green. The ^1H NMR spectrum of this reaction displays new paramagnetically shifted resonances, the disappearance of free $O_2N^tBu_2C_6H_2OH$ and the appearance of free 2,2,2-trifluoroethanol providing evidence a protolytic ligand exchange reaction. When performed on a larger scale in benzene, removal of the solvent and 2,2,2-trifluoroethanol in *vacuo* and crystallization from pentane at –30 °C yielded large green crystals of $Tp^{tBu}Cu^{II}$-$O_2N^tBu_2C_6H_2O$ **(1)**. (eq 5.1)

$$Tp^{tBu}Cu^{II}\text{-}OCH_2CF_3 + O_2N^tBu_2C_6H_2OH \rightarrow$$

$$Tp^{tBu}Cu^{II}\text{-}O_2N^tBu_2C_6H_2O + HOCH_2CF_3 \qquad (5.1)$$

The X-ray crystal structure of **(1)** indicates that indeed eq 5.1 involves protolytic displacement of the 2,2,2-trifluoroethoxide ligand by the phenoxide, however surprisingly $O_2N^tBu_2C_6H_2O^-$ anion does not bind through the phenolic oxygen. Instead, the phenolate moiety binds κ^2 through the nitronate oxygen ligands in an unusual nitronato-quinone resonance form.

The corresponding structure shows a nearly perfect square monopyramidal geometry in which two of the Tp^{tBu} ligand pyrazole nitrogens bind to Cu(II) in the same square plane with the nitronato oxygens. The third Tp^{tBu} pyrazole nitrogen binds axially with a notable longer Cu–N bond distance (Figure 5.1; Table 5.1).

The bond lengths of the $O_2N^tBu_2C_6H_2OH$ derived ligand clearly shows the dearomatization of the benzene ring (Table 5.1). The C23–C24 and C27–C26 bond distances are quite contracted (avg. bond length = 1.3575(6) Å) while lengthening is observed for C24–C25 and C25–C26 (avg. bond length = 1.481(7) Å) and C22–C23 and C22–C27 (avg. bond length = 1.427(6) Å). The C25–O1 bond length of 1.236(7) is consistent with a quinone-like carbonyl bond[7] while the C22–N7 bond of 1.333(6) Å is similar to the C=N bond lengths reported for a related copper(II) *bis*(2-propyl-κ^2-nitronate) complex of 1.34(4) and 1.35(4) Å.[8]

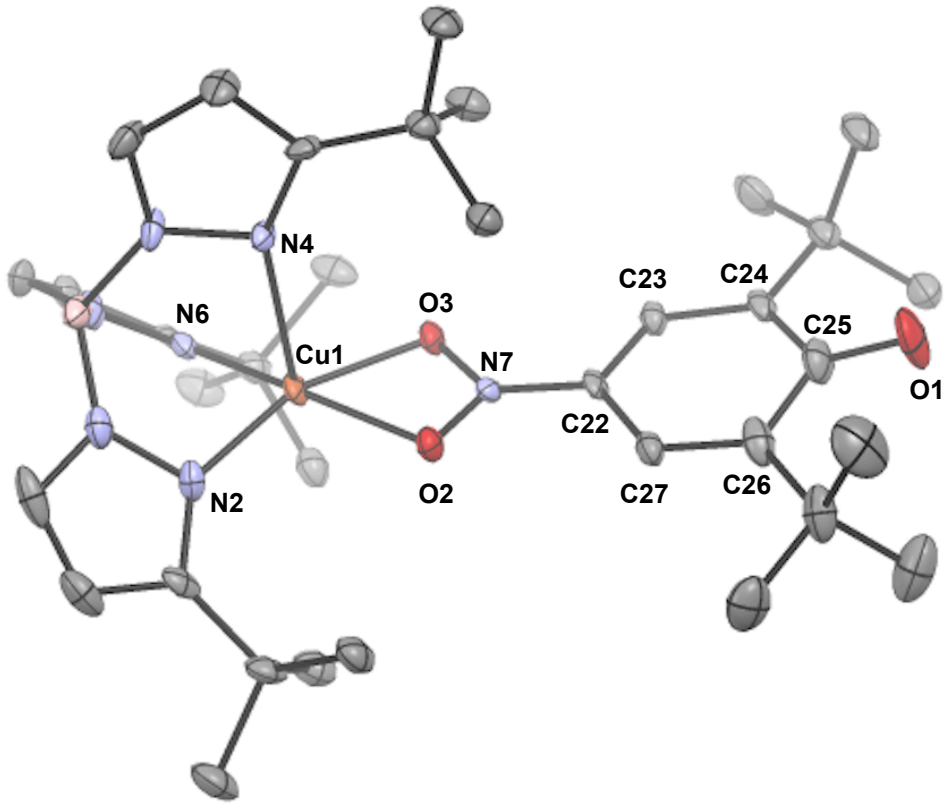

Figure 5.1. ORTEP of $Tp^{tBu}Cu^{II}$-$O_2N^tBu_2C_6H_2O$ **(1)** showing 50% probability thermal ellipsoids and select atom labels. Hydrogen atoms are omitted for clarity.

Table 5.1. Select bond lengths (Å) and angles (deg) of $Tp^{tBu}Cu^{II}$-$O_2N^tBu_2C_6H_2O$ **(1).**

Primary Metal Coordination Sphere			
N2-Cu1	1.9854(4)	O2-Cu1	1.989(3)
N4-Cu1	2.333(4)	O3-Cu1	2.019(3)
N6-Cu1	1.979(4)		
N2-Cu1-N4	94.39(17)	N4-Cu1-O2	100.92(14)
N2-Cu1-N6	92.01(17)	N4-Cu1-O3	97.69(14)
N2-Cu1-O2	97.81(16)	N6-Cu1-O2	163.57(15)
N2-Cu1-O3	161.08(15)	N6-Cu1-O3	102.16(15)
N4-Cu1-N6	91.38(15)	O2-Cu1-O3	65.65(14)
Nitronate Ligand			
O2-N7	1.307(5)	C24-C25	1.486(7)
O3-N7	1.293(5)	C25-C26	1.476(8)
N7-C22	1.333(6)	C26-C27	1.355(7)
C22-C23	1.420(7)	C27-C22	1.434(7)
C23-C24	1.360(6)	C25-O1	1.236(7)

The nitronate N7 atom forms bonds to O2 and O3 with bond lengths of 1.307(5) and 1.293(5) Å, respectively. These chelating oxygens, O2 and O3, likewise bind Cu1 with similar, but statistically different bond lengths of 1.989(3) and 2.019(3), respectively.

The X-band EPR spectrum[9] of **(1)** at 120 K in a toluene glass displays what appears to be an axial $g_{\|} > g_{\perp}$ signal. However, the splitting from $|A^{Cu}|$ shows irregularity at high fields so it is likely this signal is better described as rhombic rather than axial. The complete simulation of this spectrum has proved challenging but some tentative and incomplete assignments can be made: $g_z = 2.32$ ($|A_z^{Cu}| = 128$ G), $g_x = 2.07$. Hyperfine splitting can be observed on g_z arises from coupling to the pyrazole nitrogens ($|A_x^N = 12$ G) like has previously been reported by Tolman[10] for the structurally related[11] $Tp^{tBu}Cu^{II}$-κ^2-OAc. This complex has a similar splitting pattern but was assigned as axial rather than rhombic. The $|A_{\|}^{Cu}|$ reported by Tolman was slightly larger than the value of $|A_z^{Cu}|$ reported here (142 G vs 128). Similarly, the hyperfine splitting from the pyrazole nitrogens is slightly larger in $Tp^{tBu}Cu^{II}$- κ^2-OAc with $|A_{\perp}^{N}| = 14$ G. These results seem consistent with a greater spin delocalization onto the nitronate ligand in **(1)** than the acetate ligand resulting in a slightly reduced spin density on Cu^{II} and the Tp^{tBu} ligand.

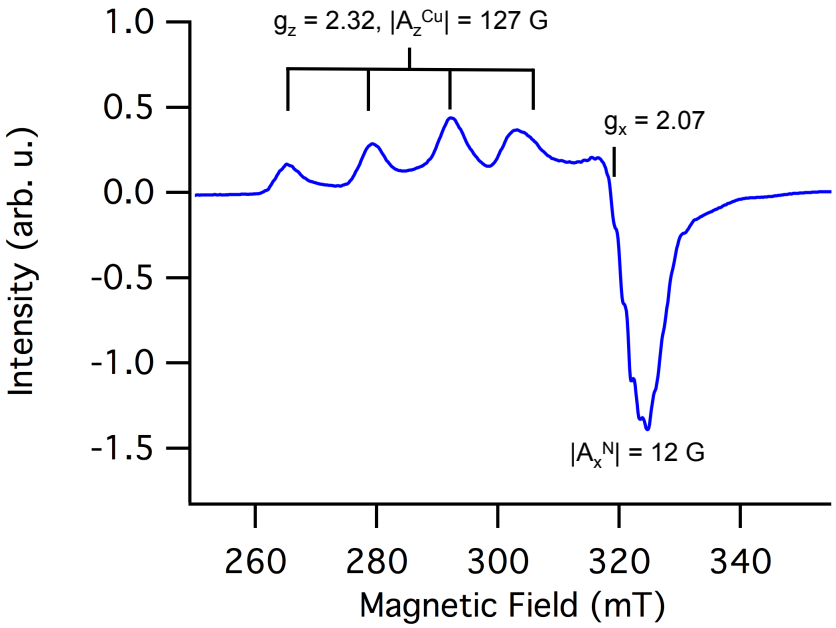

Figure 5.2. X-Band EPR spectrum of **(1)** at 120 K in a toluene glass.[9]

5.2.1.2. $Tp^{tBu}Zn^{II}O_2N^tBu_2C_6H_2O$ (2)

The addition of one equivalent of DBU (1,8-diazabicycloundec-7-ene) to a dichloromethane solution of equimolar $Tp^{tBu}Zn^{II}$-OTf and 2,6-di-*tert*-butyl-4-nitrophenol ($O_2N^tBu_2C_6H_2OH$) results in the colorless solution turning light yellow. Removal of the solvent followed by recrystallization from pentane at –30 °C results in the formation of large yellow crystals of $Tp^{tBu}Zn^{II}$-$O_2N^tBu_2C_6H_2O$ **(2)**, the Zn(II) analogue of **(1)**.

The X-ray structure of **(2)** displays a distorted tetrahedral Zn(II) center with 3 Zn–N bonds to the Tp^{tBu} ligand. In the fourth position, the $O_2N^tBu_2C_6H_2O^-$ derived ligand is bound in a similar nitronato-quinone form however unlike in **(1)**, this ligand binds to the metal center through only one of the nitronate oxygens.

The bond lengths of the nitronato-quinone ligand are similar to those observed in **(1)** with the exception that the Zn(II) bound nitronate oxygen has a substantially longer bond length than the unbound oxygen (N7–O2 = 1.3314(13) vs 1.2660(14) Å, respectively) (Figure 5.3., Table 5.2).

The distorted geometry about Zn(II) is notable since it deviates quite substantially from tetrahedral. A quantitative assessment of this distortion can be made using the pyramidalizion normalization parameter, τ. ($\tau = [\Sigma(L_{basal}\text{-}M\text{-}L_{basal}) - \Sigma(L_{basal}\text{-}M\text{-}L_{axial})]/90$; $\tau = 0$ for a perfect tetrahedral and $\tau = 1$ for perfect trigonal monopyramidal).[12] The τ value of **(2)** is 0.69 and is therefore better described as having trigonal monopyramidal geometry. This contrasts the much more tetrahedral structures reported by Parkin and others for related $Tp^{tBu}Zn^{II}$–X complexes which typically range from 0.3 to 0.4.[13]

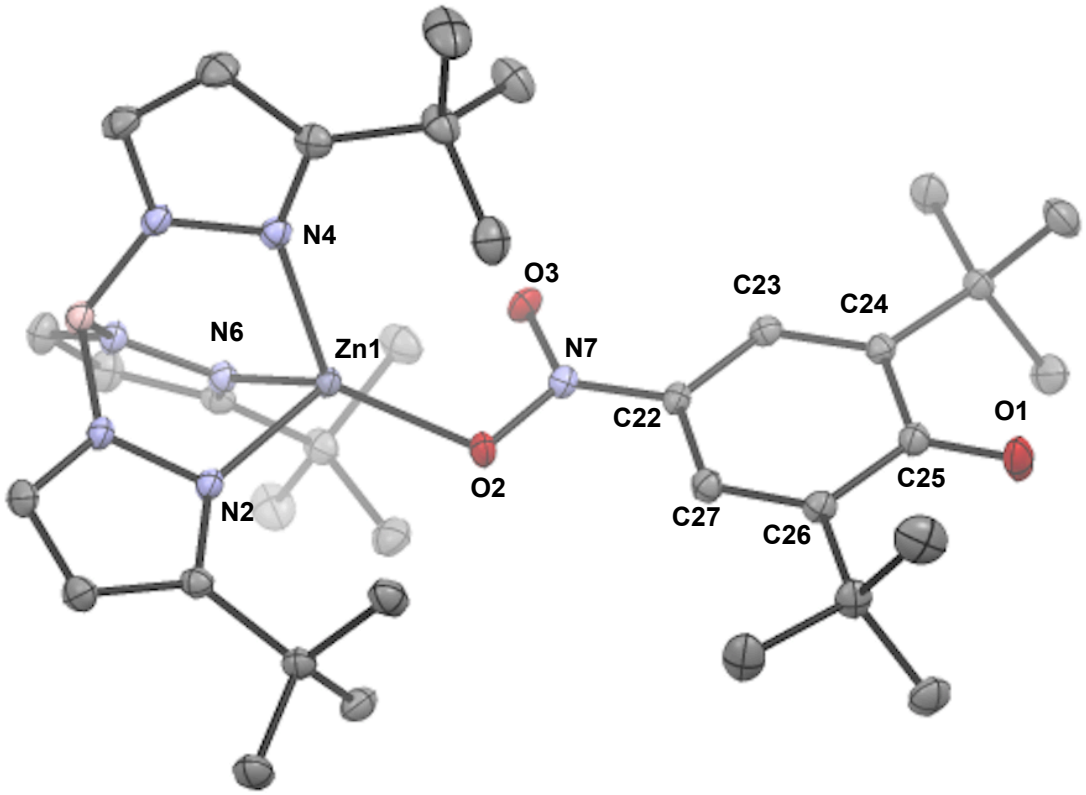

Figure 5.3. ORTEP of $Tp^{tBu}Zn^{II}$-$O_2N^tBu_2C_6H_2O$ **(2)** showing 50% probability thermal ellipsoids and select atom labels. Hydrogen atoms are omitted for clarity.

Table 5.2. Select bond lengths (Å) and angles (deg) of $Tp^{tBu}Zn^{II}$-$O_2N^tBu_2C_6H_2O$ **(2).**

Primary Metal Coordination Sphere			
N2-Zn1	2.0298(11)	O2-Zn1	1.9356(9)
N4-Zn1	2.0516(10)	O3···Zn1	2.6488(9)
N6-Zn1	2.0755(10)		
N2-Zn1-N4	100.82(4)	N4-Zn1-N6	91.87(4)
N2-Zn1-N6	92.52(4)	N4-Zn1-O2	121.55(4)
N2-Zn1-O2	131.50(4)	N6-Zn1-O2	107.34(4)
O2-Zn1-O3	116.28(10)		
Nitronate Ligand			
O2-N7	1.3314(13)	C24-C25	1.4854(17)
O3-N7	1.2660(14)	C25-C26	1.4900(17)
N7-C22	1.3441(16)	C26-C27	1.3549(17)
C22-C23	1.4270(17)	C27-C22	1.4287(17)
C23-C24	1.3505(18)	C25-O1	1.2338(16)

5.2.1.3. $Tp^{tBu}Cu^{II}$-$OArNO_2$ (3)

Analogous to the synthesis of **(1)**, the addition of one equivalent of 4-nitrophenol ($HOArNO_2$) to $Tp^{tBu}Cu^{II}$-OCH_2CF_3 in toluene results in a rapid color change from orange-red to green-brown. After removing the solvent in *vacuo*, the dark colored solids were redissolved in diethyl ether and large brown and green dichroic crystals of $Tp^{tBu}Cu^{II}$-$OArNO_2$ **(3)** were grown from slow evaporation.

The X-ray structure of **(3)** shows a distorted tetrahedral geometry about copper (τ = 0.62) with 4-nitro-phenoxide bound to the metal center through the phenoxide oxygen (Figure 5.4, Table 5.3).

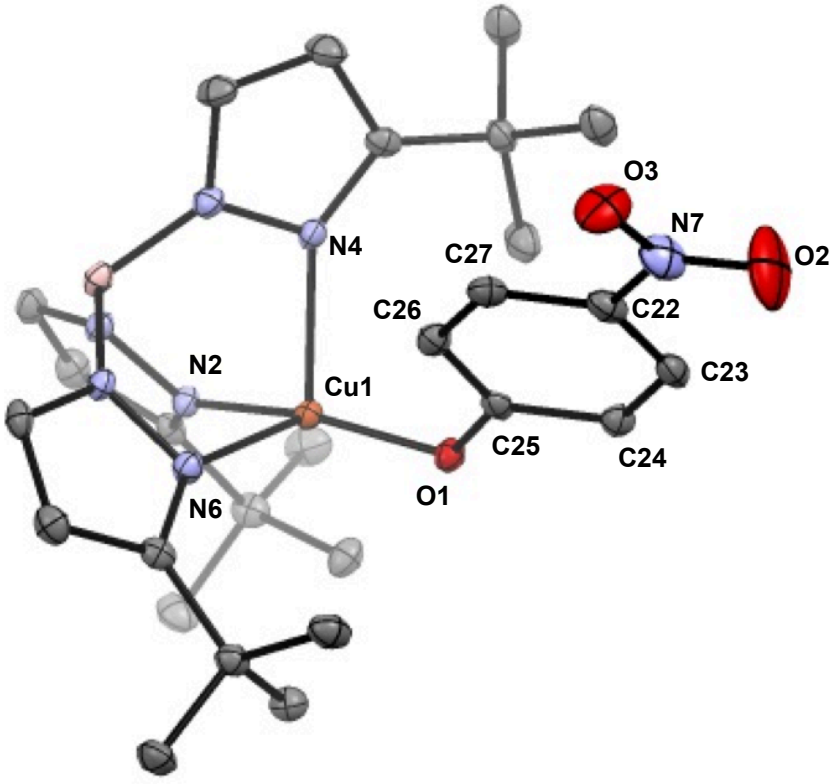

Figure 5.4. ORTEP of $Tp^{tBu}Cu^{II}$-$OArNO_2$ **(3)** showing 50% probability thermal ellipsoids and select atom labels. Hydrogen atoms are omitted for clarity.

Table 5.3. Select bond lengths (Å) and angles (deg) of $Tp^{tBu}Cu^{II}$-$OArNO_2$ **(3).**

Primary Metal Coordination Sphere			
N2-Cu1	1.9362(17)	N6-Cu1	2.0472(16)
N4-Cu1	2.0771(16)	O1-Cu1	1.8547(14)
N2-Cu1-N4	87.76(7)	N4-Cu1-N6	106.86(7)
N2-Cu1-N6	89.44(7)	N4-Cu1-O1	102.61(6)
N2-Cu1-O1	159.86(7)	N6-Cu1-O1	103.66(6)
Phenoxide Ligand			
O2-N7	1.232(3)	C24-C25	1.410(3)
O3-N7	1.221(3)	C25-C26	1.406(3)
N7-C22	1.449(3)	C26-C27	1.371(3)
C22-C23	1.390(3)	C27-C22	1.392(3)
C23-C24	1.379(3)	C25-O1	1.324(3)

The X-band EPR spectrum[9] of **(3)** in toluene at 120K has a rhombic signal that could be well modeled with simulation (Figure 5.5). This type of rhombic signal is similar to what has been observed for structurally related $Tp^{tBu}Cu^{II}$-X complexes previously reported by Tolman.[14]

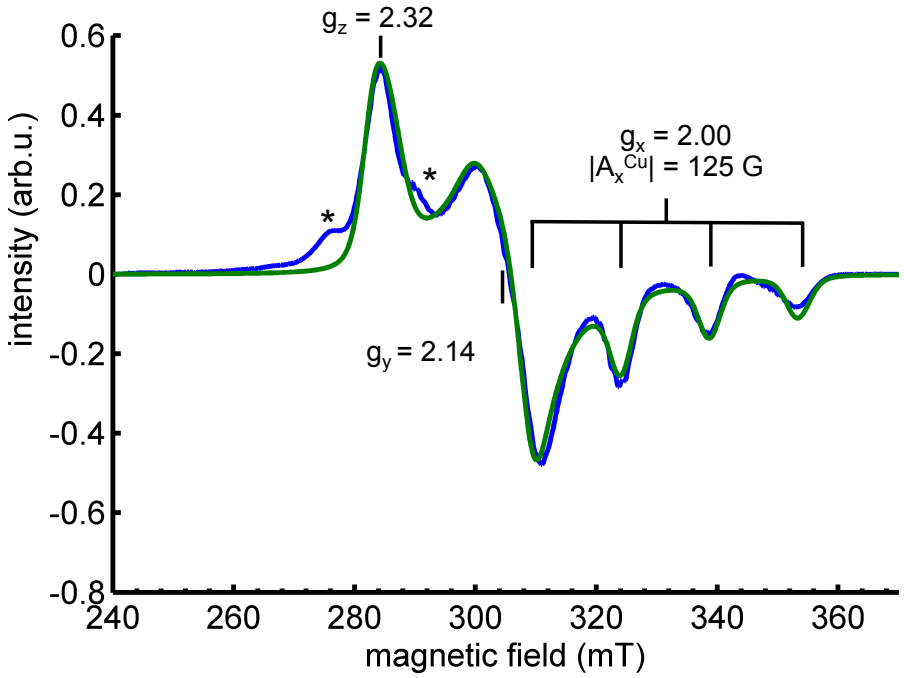

Figure 5.5. X-Band EPR spectrum of **(3)** in a toluene glass at 120 K. The asterisks (*) indicate the presence of a minor impurity. Data shown in blue, sim. shown in green.[9]

5.2.1. Non-reactivity between ½ [Tp^{tBu}Cu^{I}]$_2$ and isolable radicals

Treatment of 14 mM of the previously reported [Tp^{tBu}Cu^{I}]$_2$[15] with 28 mM of 2,4,6-tri-tert-butylphenoxyl radical (^{t}Bu$_3$ArO$^{\bullet}$)[16] in benzene(-d_6) resulted in no reaction by UV/Vis and ^{1}H NMR spectroscopies (eq 5.2). The 4-phenyl-inserted ^{t}Bu$_2$NPArO$^{\bullet}$[17] radical also was unreactive with [Tp^{tBu}Cu^{I}]$_2$ under the same conditions (eq 5.3). This is consistent with the results discussed in Chapter 4 where Tp^{tBu}Cu^{II}-OCH$_2$CF$_3$ reacts with either 2,4,6-tri-*tert*-butylphenol (^{t}Bu$_3$ArO–H) or 2,6-di-*tert*-buty-4-(4'-nitrophenyl)phenol (^{t}Bu$_2$NPArO–H) to yield ½ [Tp^{tBu}Cu^{I}]$_2$, HOCH$_2$CF$_3$ and the corresponding phenoxyl radical.

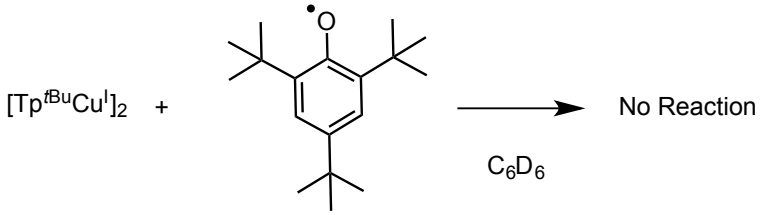

(5.2)

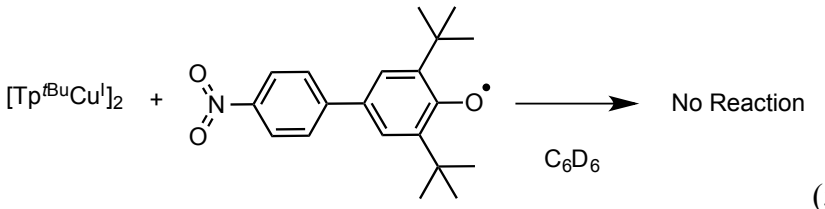

(5.3)

To determine if the lack of a Cu–O bond formation was the result of steric crowding, attempts to prepare [Tp^{tBu}Zn^{II}]$^{+}$ with an O-coordinated ^{t}Bu$_3$ArO^{-} ligand (2,4,6-tri-*tert*-butyl-phenoxide) starting from the Tp^{tBu}Zn^{II}-OTf precursor were made by treatment with one equivalent of ^{t}Bu$_3$ArO–H and DBU. Upon workup, only Tp^{tBu}Zn^{II}-OTf was recovered.[18a] Similar attempts with Tp^{tBu}Zn^{II}-Cl and lithiated ^{t}Bu$_3$ArO^{-} were also unsuccessful.[18b]

5.3. Reactivity

5.3.1. Electrochemical Measurements

The cyclic voltammogram (CV) of **(1)** in dichloromethane with 0.1 M [^{n}Bu$_4$N][PF$_6$] shows irreversible electrochemical responses at both oxidizing and reducing potentials (Fig 5.6). The peak cathodic current, $E_{c,a}$, occurs at –0.84 ± 0.01 V *vs* $Fc^{+/0}$. This was similar to the irreversible $E_{c,a}$ values for related Tp$^{t\text{Bu}}$Cu^{II}-X complexes reported in Chapter 4 (–0.860 for X = $^{-}$OCH$_2$CF$_3$ and –0.840 for X = $^{-}$OCH(CH$_3$)CF$_3$).

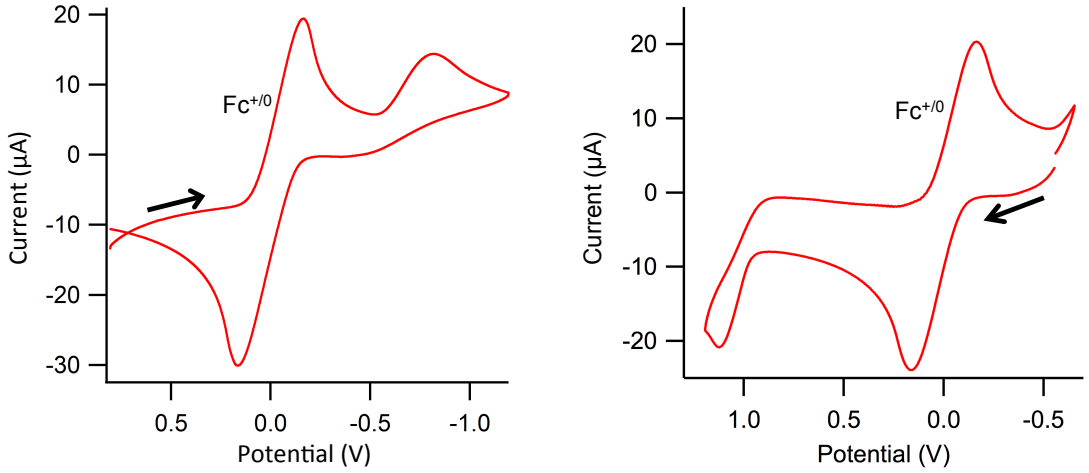

Figure 5.6. Cyclic Voltammogram of **(1)** in dichloromethane with 0.1 mM [^{n}Bu$_4$N][PF$_6$] with scan rate of 100 mV s^{-1}. The voltammogram on the left shows sweeping to negative potentials and the voltammogram on the right shows sweeping to positive potentials. Electrochemical setup consisted of a glassy carbon working electrode and platinum auxiliary electrode. Potential is referenced to the ferrocene/ferrocenium internal standard. $E_{a,p}$ = 1.10 ± 0.05 V vs. $Fc^{+/0}$.

5.3.2. Reactivity with H-Atom Transfer Reagents

The addition of one equivalent of the hydrogen atom donor 2,2,6,6-tetramethylpiperidin-1-ol, TEMPO–H, to 12 mM **(1)** in benzene(-d_6) results in a color change from green-brown to light pink over the course of approximately one hour. ^{1}H NMR spectra show quantitative formation of 2,6-di-*tert*-butyl-4-nitrophenol ($O_2N^{t}Bu_2C_6H_2O$–H) and [Tp$^{t\text{Bu}}$Cu^{I}]$_2$. The optical spectrum of the same reaction displays a small absorption indicative of TEMPO radical at 460 nm. Based on the reported molar extinction coefficient of 11.1 M^{-1} cm^{-1} at 460 nm,[19] the formation of TEMPO is quantitative. The balanced reaction is therefore as described by equation 5.4.

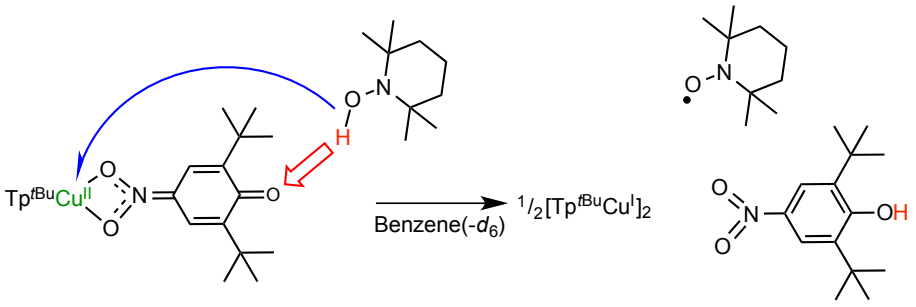

(5.4)

Treating 2.5 mM $[Tp^{tBu}Cu^{I}]_2$ and 5 mM $O_2N^tBu_2C_6H_2O$–H with 5 mM of the strong hydrogen atom acceptor, $^tBu_3ArO^\bullet$ in benzene results in a color change from blue ($^tBu_3ArO^\bullet$) to green-brown over one hour. The optical trace of this reaction (Figure 5.7) displays clean isosbestic points and shows **(1)** is generated in approximately 60% yield as indicated from the spectral overlay of the independently measured spectrum of a known concentration of **(1)**. Notably, all $^tBu_3ArO^\bullet$ is consumed during this reaction.

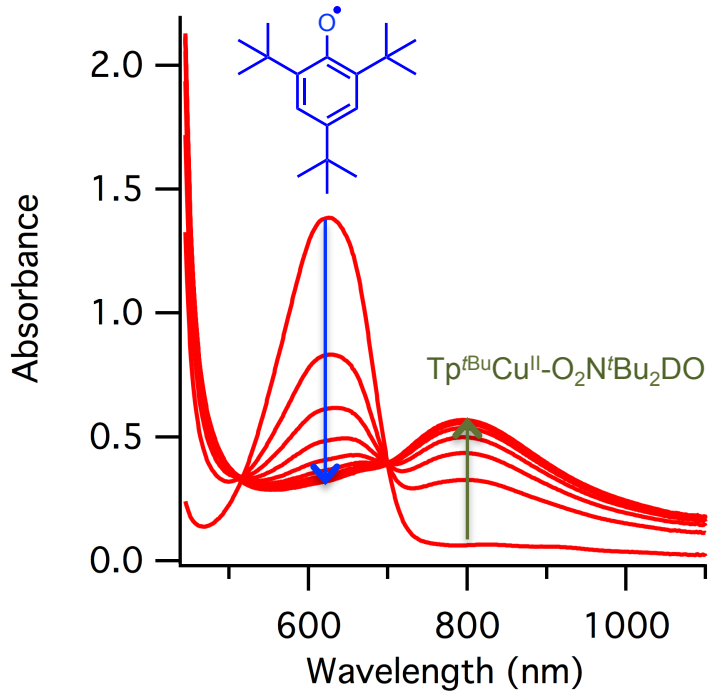

Figure 5.7. Stack of optical traces of the reaction between 2.5 mM $[Tp^{tBu}Cu^{I}]_2$, 5 mM $O_2N^tBu_2C_6H_2O$–H and 5 mM $^tBu_3ArO^\bullet$ in benzene over the course of 1 hour. The blue arrow shows the disappearance of $^tBu_3ArO^\bullet$ with time while the green arrow shows the appearance of $Tp^{tBu}Cu^{II}$-$O_2N^tBu_2C_6H_2O$ **(1)**.

The ^{1}H NMR spectrum of the same reaction (scaled up to 6 mM [Tp^{tBu}Cu^{I}]$_2$) and 12 mM ^{t}Bu$_3$ArO$^\bullet$ and 12 mM O$_2$N^{t}Bu$_2$C$_6$H$_2$O–H) carried out in benzene-d_6 likewise shows the appearance of **(1)** (~50%) as well as peaks for ^{t}Bu$_3$ArO–H (~80%) and remaining O$_2$N^{t}Bu$_2$C$_6$H$_2$O–H (~40%). The stoichiometry of this reaction is not clear since the amount of ^{t}Bu$_3$ArO–H is substantially larger than the amount of **(1)** generated. Because of this ambiguity, we are hesitant to conclude a great deal from this result other than simply the combination of reagents yields **(1)** in reasonable yield and a hydrogen atom transfer from ½ [Tp^{tBu}Cu^{I}]$_2$ + O$_2$N^{t}Bu$_2$C$_6$H$_2$O–H to ^{t}Bu$_3$ArO$^\bullet$ may be involved in some capacity.

5.4. Discussion

5.4.1. Sterically Directed Phenolate/Nitronate Linkage

The κ^2-nitronate complex, Tp^{tBu}CuO$_2$N^{t}Bu$_2$C$_6$H$_2$O **(1)** is readily formed in moderate yield by protolytic exchange of the phenol with Tp^{tBu}Cu^{II}-OCH$_2$CF$_3$. In contrast, the same reaction with the less bulky 4-nitrophenol gives the O-bond phenoxide complex, **(3)**. This is further contrasted by the reactivity of Tp^{tBu}Cu^{II}-OCH$_2$CF$_3$ described in Chapter 4 in which, treatment of Tp^{tBu}Cu^{II}-OCH$_2$CF$_3$ with the bulky 2,4,6-tri-*tert*-buty-phenol (^{t}Bu$_3$ArO–H) or 2,6-di-*tert*-butyl-4-(4'-nitrophenyl)phenol (^{t}Bu$_2$NPArO–H) results in a hydrogen atom transfer, generating ½ [Tp^{tBu}Cu^{I}]$_2$, HOCH$_2$CF$_3$ and the corresponding phenoxyl radical.

The similar Tp^{tBu}Zn^{II} system shows a related binding pattern, forming a nitronate complex with O$_2$N^{t}Bu$_2$C$_6$H$_2$OH, although a κ^1 analogue, **(2).** To our knowledge, this is only the second κ^1-transition metal-nitronate complex ever reported.[4a,5] In a very similar previously reported system, [Tp^{tBuMe}Zn^{II}]$^+$ (Tp^{tBuMe} = hydro-*tris*(3-*tert*-butyl-5-methyl-pyrazol-1-yl)borate), like [Tp^{tBu}Cu^{II}]$^+$, binds 4-nitro-phenoxide through the phenolic oxygen.[20]

These results indicate that the preference for the nitronate coordination in compounds **(1)** and **(2)** is most likely the result of the large steric clash between Tp^{tBu} *tert*-butyl groups and the *tert*-butyl groups of O$_2$N^{t}Bu$_2$C$_6$H$_2$O–H that prevents binding through the phenolic oxygen. The unreactive nature of ^{t}Bu$_3$ArO$^\bullet$ radical with ½[Tp^{tBu}Cu^{I}]$_2$ and the inability to independently prepare [Tp^{tBu}Zn^{II}]$^+$ with an O

coordinated $^{t}Bu_3ArO^-$ ligand provides additional support that the binding motif observed in **(1)** and **(2)** is primarily a steric effect.

Similar hydro-*tris*(pyrazolyl)borate (Tp) copper(II) complexes with bulky phenoxide ligands have been reported. Fujisawa[3i] reported that with the slightly less sterically hindered ligand on copper, $Tp^{iPriPr}Cu$- (Tp^{iPriPr} = hydro-*tris*(3,5-di-*iso*-propyl-pyrazol-1-yl)borate) with the 2,6-di-substituted phenoxides such as 2,6-di-methyl-phenoxide (Me_2ArO^-) and 2,6-di-*tert*-butyl-phenoxide ($^{t}Bu_2ArO^-$) could be prepared. These complexes were not crystallographically characterized however it was assumed the phenolate ligands were bound through the phenolic oxygen. The report of the $^{t}Bu_2ArO^-$ bound complex is particularly interesting since the Tp^{tBu} ligand reported here is only slightly bulkier than Tp^{iPriPr} yet does not appear to allow coordination of the structurally related $^{t}Bu_3ArO^-$.

A similar example of a structurally characterized metal complex with a bulky Tp ligand and a bulky phenoxide is the Tp^{PhMe} (hydro-*tris*(3-phenyl-5-methyl-pyrazol-1-yl)borate) nickel(II) complex with a 2,6-di-*iso*-propyl phenoxide ($^{i}Pr_2ArO^-$) bound reported by Jensen and co-workers.[21] Both the Tp^{PhMe} ligand and $^{i}Pr_2ArO^-$ are less sterically demanding than Tp^{tBu} and $^{t}Bu_3ArO^-$ but the space-filling model of the nickel complex suggests that even these components are only barely spatially compatible (Figure 5.8).

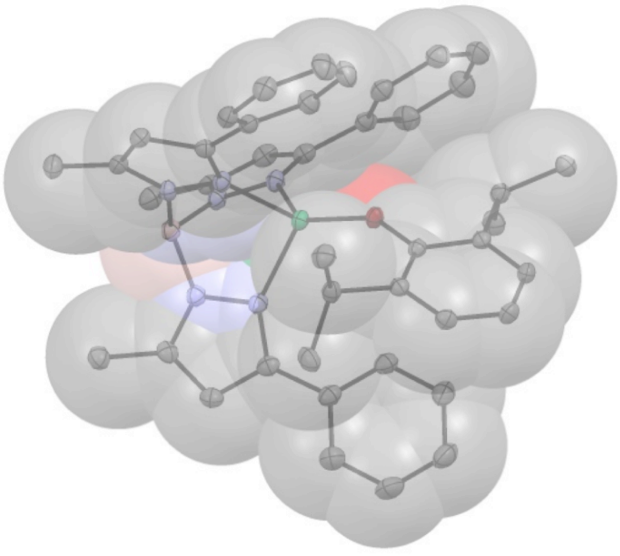

Figure 5.8. The ORTEP of $Tp^{PhMe}Ni^{II}$-O$^{i}Pr_2Ar$ with the space-filling diagram overlay (cif data taken from ref 22).

5.4.2. H-Atom Transfer Reactivity and Thermochemistry

Treatment of **(1)** with the hydrogen atom donor TEMPO–H results in a net H^+/e^- transfer event that produces $O_2N^tBu_2C_6H_2O$–H, ½ $[Tp^{tBu}Cu^I]_2$, and TEMPO in quantitative yield. Regardless of mechanism, the well-defined stoichiometry of this reaction provides thermochemical information about this system. Because this reaction proceeds quantitatively and therefore must be exoergic by at least 0 kcal mol^{-1}, a low limit for the 'effective bond dissociation free energy (BDFE)'[22] of $[Tp^{tBu}Cu^I]_2$ + $O_2N^tBu_2C_6H_2O$–H can be calculated from the known O–H bond strength of TEMPO–H (eq 5.5–5.7).

$$Tp^{tBu}Cu^{II}\text{-}O_2N^tBu_2C_6H_2O + TEMPO\text{–}H \rightarrow$$

$$\tfrac{1}{2}\,[Tp^{tBu}Cu^I]_2 + O_2N^tBu_2C_6H_2O\text{–}H + TEMPO \qquad (5.5)$$

$$\Delta G^\circ \leq 0 \text{ kcal mol}^{-1}\ ^{22}$$

$$TEMPO + H^\bullet \rightarrow TEMPO\text{–}H \qquad (5.6)$$

$$\Delta G^\circ = -65.2 \text{ kcal mol}^{-1}\ ^{23}$$

Summing (eq 5.5) and (eq 5.6) gives:

$$Tp^{tBu}Cu^{II}\text{-}O_2N^tBu_2C_6H_2O + H^\bullet \rightarrow \tfrac{1}{2}\,[Tp^{tBu}Cu^I]_2 + O_2N^tBu_2C_6H_2O\text{–}H \qquad (5.7)$$

$$\Delta G^\circ \leq -65.2 \text{ kcal mol}^{-1}$$

Since the O–H bond strength of $O_2N^tBu_2C_6H_2O$–H is known, this 'effective BDFE' limit can be used to extrapolate a limit for homolytically cleaving the Cu^{II}–κ^2-O_2N=R chelating bond and forming ½ $[Tp^{tBu}Cu^I]_2$ can in turn be calculated:

$$Tp^{tBu}Cu^{II}\text{-}O_2N^tBu_2C_6H_2O + H^\bullet \rightarrow \tfrac{1}{2}\,[Tp^{tBu}Cu^I]_2 + O_2N^tBu_2C_6H_2O\text{–}H \qquad (5.7)$$

$$\Delta G^\circ \leq -65.2 \text{ kcal mol-1}$$

$$O_2N^tBu_2C_6H_2O\text{–}H \rightarrow O_2N^tBu_2C_6H_2O^\bullet + {}^\bullet H \qquad (5.8)$$

$$\Delta G^\circ = 80.2 \text{ kcal mol}^{-1}\ ^{17,24}$$

Summing (eq 5.7) and (eq 5.8) gives:

$$Tp^{tBu}Cu^{II}\text{-}O_2N^tBu_2C_6H_2O \rightarrow \tfrac{1}{2}\,[Tp^{tBu}Cu^{I}] + O_2N^tBu_2C_6H_2O^{\bullet} \qquad (5.9)$$

$$\Delta G^\circ \leq 15 \text{ kcal mol}^{-1}$$

It is important to note that this value encompasses both the free energy cost of homolytically cleaving the copper(II)-nitronate chelate as well as the free energy gained from the formation of the $[Tp^{tBu}Cu^{I}]_2$ dimer. This dimer has been reported to be stable with respect to dissociation even at 362 K so it is likely dimer formation has a substantial free energy contribution in equation 5.9.[15]

The mechanism by which H^+/e^- is transferred from TEMPO–H to **(1)** could proceed through several possible pathways. It is unlikely this reaction proceeds through a stepwise ET/PT mechanism since **(1)** is a very weak oxidant ($E_{c,p}$ = –0.84 ± 0.01 V vs $Fc^{+/0}$ in dichloromethane) and TEMPO–H is a very poor reductant ($E°$ of +0.71 V vs $Fc^{+/0}$ in acetonitrile).[23] This comparison is clearly not quantitative but even considering large errors, it is qualitatively apparent electron transfer from TEMPO–H to **(1)** is energetically very unfavorable.

Similarly, TEMPO–H is a very weak acid (pK_a = 41 in MeCN)[23] and is unlikely to protonate the nitronato-quinone ligand since even the fully dissociated $O_2N^tBu_2C_6H_2O^-$ is very weakly basic in comparison ($O_2N^tBu_2C_6H_2O$–H pK_a = 19 in MeCN).[25]

Other mechanistic possibilities include a concerted proton-electron transfer (CPET), a protolytic ligand exchange followed by TEMPO dissociation, or through a rate determining ligand dissociation event. These cannot be distinguished with the data currently available.

5.4.3. Extended Nitronato-Quinone Discussion

Attempts to prepare a nitonate complex derived from the 4-phenyl inserted phenol 2,6-di-*tert*-butyl-4-(4'-nitrophenyl)phenoxide ($^tBu_2$NPArO–H) in the same manner **(1)** was prepared were unsuccessful. Instead of generating the extended nitronate-quinone complex, treatment of $Tp^{tBu}Cu^{II}\text{-}OCH_2CF_3$ with $^tBu_2$NPArO–H results in the formation of $HOCH_2CF_3$, ½ $[Tp^{tBu}Cu^{I}]_2$ and phenoxyl radical.

The formation of an extended quinone complex should be sterically allowed since the bulk surrounding the nitro group in $^{t}Bu_2NPArO–H$ is even less crowded than in $O_2N^{t}Bu_2C_6H_2O–H$. This difference in reactivity then must be a thermodynamic effect.

The phenolic bond strength (bond dissociation free energy; BDFE) in $^{t}Bu_2NPArO–H$ is only 2.6 kcal weaker than that in $O_2N^{t}Bu_2C_6H_2O–H$.[17,24] This corresponds to a difference in equilibrium constant of ~80. If the copper-nitronate bond strengths paralleled these, it would be expected that at least a small portion of the extended nitronato-quinone would form since the equilibrium for formation of **(1)** lies completely on the side of nitronato-quinone formation (K_{eq} for formation >> 1). The fact that an extended nitronato-quinone complex is not detected implies the phenolic bond strengths of the two nitro-phenols do not parallel the bond strength of their copper-nitronato-quinone bond strengths. This is likely due to the difference in thermochemical costs of dearomatizing a single aromatic ring *vs* two aromatic rings.

5.5. Conclusions

Reported here is an example of a system in which the steric bulk surrounding $[Tp^{tBu}Cu^{II}]^+$ and $[Tp^{tBu}Zn^{II}]^+$ dictates the binding mode of $O_2N^{t}Bu_2C_6H_2O^-$. Because of the steric presence at the 2,6 positions of this phenolate, binding through the nitronato functionality is observed. With the 2,6-unsubstituted 4-nitrophenolate, this different does not occur and binding through the phenolate oxygen to $[Tp^{tBu}Cu^{II}]^+$ is observed. The difference in binding is likely due primarily to the steric differences of the phenolates.

$Tp^{tBu}Cu^{II}$-$O_2N^{t}Bu_2C_6H_2O$ **(1)** reacts with the hydrogen atom donor TEMPO–H by transfer of one proton and one electron (H^+/e^-). Regardless of mechanism, this result provides thermochemical information about this system. From thermochemical analysis, a limit for the 'effective BDFE' of **(1)** was calculated to be -65.2 kcal mol^{-1}. This value encompasses the hydrogen atom affinity of **(1)**, the dissociation of the phenol from $Tp^{tBu}Cu^{I}$ and the $Tp^{tBu}Cu^{I}$ dimerization event to generate ½ $[Tp^{tBu}Cu^{I}]_2$. Further analysis led to an 'effective BDFE' of the copper(II)-nitronate bond in **(1)** of <~15 kcal mol^{-1}. Similarly, this value encompasses both the thermochemical contributions from homolytic bond dissociation as well as from the formation of ½ $[Tp^{tBu}Cu^{I}]_2$.

The mechanism by which TEMPO–H transfers H^+/e^- to **(1)** is not fully understood. We conclude it is unlikely this reaction occurs through stepwise PT/ET or

ET/PT events based on the thermochemical arguments presented but additional data is required for further mechanistic elucidation.

Chemical interactions between copper(II) and phenols has been extensively studied for their relevance to biological and chemical catalysis. The findings reported here serve to highlight a new and unusual sterically directed ligation mode of a bulky nitrophenol to copper that is dramatically different from what is typically observed in other systems.

5.6. Experimental

5.6.1. Materials

Unless otherwise noted, all reactions were carried out in a nitrogen filled glovebox. All materials were purchased from Sigma-Aldrich and used without purification. Benzene-d_6 and toluene-d_8 were purchased from Cambridge Isotope Labs and dried over NaK prior to being vacuum distilled. Dichloromethane-d_2 was also purchased from Cambridge Isotope Labs and dried over CaH_2 prior to being vacuum distilled.

Other solvents were purchased from Fischer and dried using a "Grubbs type" Seca Solvent System installed by Glass-Contour. $Tp^{tBu}K$,[27] $Tp^{tBu}Cu^{II}$-OCH_2CF_3,[6] $[Tp^{tBu}Cu^{I}]_2$,[15] ^{t}Bu_2-NO_2-ArO–H,[28] ^{t}$Bu_3$$ArO^{\bullet}$,[16] ^{t}$Bu_2$$NPArO^{\bullet}$,[17] and TEMPO–H[29] were prepared following published synthetic protocols. All glassware was dried in an oven at 150 °C overnight and pumped into a nitrogen filled glovebox while still hot.

5.6.2. Instrumentation

All ^{1}H NMR spectra were collected on Bruker 300 and 500 MHz instruments. ^{1}H chemical shifts were referenced to TMS using the residual solvent peak. UV-visible absorption spectra were collected with a Hewlett-Packard 8453 diode array spectrometer and are reported as λ_{max} in nm (ε in M^{-1} cm^{-1}). EPR spectra were collected on a Bruker EMX X-band spectrometer. Cyclic voltammetry (CV) was performed using a CH instrument 600D potentiostat. CHN elemental analysis was performed by Atlantic Microlabs, Inc., Norcross, GA.

5.6.3. Syntheses

5.6.3.1. hydro-*tris*(3-*tert*-butylpyrazol-1-yl)borate) copper(II) 3,5-bis(*tert*-butyl)-4-benzenone-κ^2-nitronate, Tp^{tBu}Cu^{II}-O$_2$N^{t}Bu$_2$C$_6$H$_2$O (1): To a ~5 mL solution of Tp^{tBu}Cu^{II}-OCH$_2$CF$_3$ (58.7 mg, 0.11 mmoles) in benzene was added ^{t}Bu$_2$-NO$_2$-ArOH (27.1 mg, 0.11 mmoles) with stirring. The solution quickly changed in color from orange to blue-green. Removal of the solvent in vacuo gave dark green solid. Crystallization from pentane at –30 °C yielded 50 mg of large X-ray quality crystals (66 %). ^{1}H NMR (500 MHz, benzene-d_6) δ: 2.8 (broad, 27H), 1.0 (s, 18H); UV/Vis (toluene): 830 nm (180 ± 20); Anal. Calcd. For $C_{35}H_{54}BCuN_7O_3$: C, 60.47; H, 7.83; N, 14.01. Found: C, 60.74; H, 7.89; N, 14.16.

5.6.3.2. hydro-*tris*(3-*tert*-butylpyrazol-1-yl)borate) zinc(II) chloride, Tp^{tBu}Zn^{II}-Cl: The preparation of Tp^{tBu}Zn^{II}-Cl was achieved with modifications to previously reported methods.[29] To a 10 ml THF solution of Tp^{tBu}K (233.8 mg, 0.51 mmoles) was added anhydrous zinc(II) chloride (76.3 mg, 0.56 mmol) with stirring. After 30 minutes the solvent was removed in vacuo, the white solid redissolved in dichloromethane, and the suspension filtered over Celite to yield crude Tp^{tBu}Zn^{II}-Cl as a colorless solid. Recrystallization from pentane at –30 °C yielded colorless crystals (161.7 mg, 66%). The ^{1}H NMR signals of these crystals were in good agreement those previously reported.

5.6.3.3. hydro-*tris*(3-*tert*-butylpyrazol-1-yl)borate) zinc(II) triflate, Tp^{tBu}Zn^{II}-OTf: To a toluene solution of 5 mL Tp^{tBu}Zn^{II}Cl (327.6 mg, 0.68 mmol) was added AgOTf (174.5 mg, 0.68 mmol) with stirring. A chalky gray-red precipitate formed over 1 hour and was collected by filtration on a Celite plug. Extraction with dichloromethane yielded a colorless solution, which upon removal of the solvent, gave Tp^{tBu}Zn^{II}-OTf as a white solid (366.5 mg, 91%). ^{1}H NMR (500 MHz, CD_2Cl_2): 7.62 (d, $^3J_{HH}$ = 2.3 Hz, 3H), 6.12 (d, $^3J_{HH}$ = 2.3 Hz, 3H), 1.37 (s, 27H). Tp^{tBu}Zn^{II}-OTf was also characterized by X-ray crystallography from recrystallization from pentane and co-crystallized with a disordered pentane molecule. The elemental analysis was found to be slightly high in C and H which is likely a result of residual co-crystallized pentane. Anal. Calcd. For $C_{22}H_{34}BF_3N_6O_3SZn$: C, 44.35; H, 5.75; N, 14.11. Found: C, 44.84; H, 5.91; N, 14.13.

5.6.3.4. hydro-*tris*(3-*tert*-butylpyrazol-1-yl)borate) zinc(II) 3,5-bis(*tert*-butyl)-4-benzenone-κ^1-nitronate, Tp^{tBu}Zn^{II}-O$_2$N^{t}Bu$_2$C$_6$H$_2$O (2): To a ~5 mL dichloromethane solution of Tp^{tBu}Zn^{II}-OTf (101.3 mg, 0.17 mmoles) was added dropwise a ~2 mL dichloromethane solution of DBU (25.9 mg, 0.17 mmoles) and 2,6-di-*tert*-butyl-4-nitro phenol (42.7 mg, 0.17 mmoles) with stirring. Upon addition, the solution turned from colorless to yellow. After 10 minutes the solvent was removed in vacuo and the remaining solid was redissolved in a minimum amount of pentane and filtered. Large yellow X-ray quality crystals grew upon standing at -30 °C (73.1 mg, 62%). ^{1}H NMR (500 MHz, CD_2Cl_2) δ: 7.74 (s, 2H), 7.61 (d, $^3J_{HH}$ = 2.3 Hz, 3H), 6.12 (d, $^3J_{HH}$ = 2.3 Hz, 3H), 1.33 (s, 27H), 1.31 (s, 18H). Anal. Calcd. For $C_{35}H_{54}BN_7O_3Zn$: C, 60.31; H, 7.81; N, 14.07. Found: C, 60.42; H, 7.59; N, 14.20.

5.6.3.5. hydro-*tris*(3-*tert*-butypyrazol-1-yl)borate) copper(II) 4-nitro-phenolate (3): To a ~5 mL dichloromethane solution of Tp^{tBu}Cu^{II}-OCH$_2$CF$_3$ (62.2 mg, 0.114 mmoles) was added a ~2 mL dichloromethane solution of 4-nitro-phenol (15.9 mg, 0.114 mmoles). Upon addition, the solution turned from orange to brown-green. After the solvent was removed in vacuo, the resulting solids were redissolved in diethyl ether, filtered over Celite and crystallized by slow evaporation yielding green/brown dichroic crystals of **(3)** (65.5 mg, 98%). ^{1}H NMR (300 MHz, CD_2Cl_2) δ: 7.6 (broad, 27H). UV/Vis (toluene): 583 (430 ± 43), 667 (400 ± 40), 830 (130 ± 13). Anal. Calcd. For $C_{27}H_{38}BCuN_7O_3$: C, 55.63; H, 6.57; N, 16.82. Found: C, 55.44; H, 6.56; N, 16.85.

5.6.3.6. hydro-*tris*(3-*tert*-butypyrazol-1-yl)borate) copper(II)-κ^2-acetate, Tp^{tBu}Cu^{II}-κ^2-OAc: Tp^{tBu}Cu^{II}-κ^2-OAc was prepared following the procedure reported by Tolman.[10] X-ray quality crystals were grown from pentane at -30 °C.

Table 5.4. Crystallographic collection and refinement data

	(1)	**(2)**	**(3)**
Empirical formula	$C_{35}H_{54}BCuN_7O_3$	$C_{35}H_{54}BN_7O_3Zn$	$C_{27}H_{38}BCuN_7O_3$
Formula weight	695.20	697.03	582.99
Temperature (K)	100(2)	100(2)	100(2)
Wavelength (Å)	0.71073	0.71073	0.71073
Crystal description	green prism	yellow prism	dichroic brown-green needle
Crystal system	Monoclinic	Monoclinic	Monoclinic
Space group	P 2_1	P 2_1/c	C c
Unit cell dimensions			
a (Å)	11.3921(4)	13.5042(10)	19.8577(9)
b (Å)	10.0553(4)	14.5848(12)	8.0385(3)
c (Å)	16.8141(7)	19.8333(16)	18.2723(9)
α(deg)	90	90	90
β(deg)	98.477(2)	94.113(2)	102.001(4)
γ(deg)	90	90	90
Volume ($Å^3$)	1905.03(13)	3800.0(5)	2853.0(2)
Z	2	4	4
Density (calculated) (Mg/m^3)	1.212	1.218	1.357
Absorption coefficient (mm^{-1})	0.615	0.688	0.807
F(000)	742	1488	1228
Crystal size (mm^3)	0.18 x 0.10 x 0.05	0.15 x 0.15 x 0.10	0.10 x 0.03 x 0.03
θ range for data collection	2.33 to 28.34°.	2.09 to 28.47°.	2.10 to 28.38°.
Index ranges	-15<=h<=15, -12<=k<=13, -22<=l<=22	-18<=h<=18, -19<=k<=19, -26<=l<=26	-26<=h<=26, -10<=k<=10, -24<=l<=24
Reflections collected	51079	9503	41198
Independent reflections	9047	4313	7126
R_{int}	0.0723	0.0442	0.0543
Completeness to θ = 25.00°	97.7 %	100.0 %	100.0 %
Max/min. transmission	0.9699/0.8974	0.9344/0.9038	0.9762/0.9237
Refinement method	Full-matrix least-squares on F^2		
Data / restraints / parameters	9047/115/439	9503/0/439	7126/2/361
Goodness-of-fit on F^2	1.080	1.037	1.044
Final R	0.0738	0.0274	0.0304
R_w	0.1592	0.0651	0.0615
Largest diff. peak and hole ($e/Å^{-3}$)	1.731/-1.010	0.362/-0.233	0.272/-0.346

Table 5.4. (*cont*). Crystallographic collection and refinement data

	$Tp^{tBu}Zn^{II}$-OTf	$Tp^{tBu}Cu^{II}$-κ²-OAc
Empirical formula	$C_{27}H_{46}BF_3N_6O_3SZn$	$C_{23}H_{37}BCuN_6O_2$
Formula weight	667.94	503.94
Temperature (K)	100(2) K	100(2) K
Wavelength (Å)	0.71073 Å	0.71073 Å
Crystal description	colorless prism	green prism
Crystal system	Monoclinic	Orthorhombic
Space group	P 21/n	P n m a
Unit cell dimensions		
a (Å)	10.4203(10)	15.964(3)
b (Å)	20.5076(19)	15.477(3)
c (Å)	15.4032(15)	10.284(2)
α(deg)	90	90
β(deg)	91.771(5)	90
γ(deg)	90	90
Volume ($Å^3$)	3290.0(5)	2540.9(8)
Z	4	4
Density (calculated) (Mg/m^3)	1.348	1.317
Absorption coefficient (mm^{-1})	0.864	0.891
F(000)	1408	1068
Crystal size (mm^3)	0.30x0.20x0.05	0.29 x 0.25 x 0.10
θ range for data collection	1.99 to 25.35°.	2.36 to 28.49°.
Index ranges	-12<=h<=12, -24<=k<=24, -18<=l<=18	-21<=h<=21, -20<=k<=20, -13<=l<=13
Reflections collected	93541	83201
Independent reflections	5986	3313
R_{int}	0.1165	0.0407
Completeness to θ = 25.00°	99.1 %	100.0 %
Max/min. transmission	0.9581/0.7816	0.9162 and 0.7823
Refinement method	Full-matrix least-squares on F^2	
Data / restraints / parameters	5986/11/380	3313/0/172
Goodness-of-fit on F^2	1.140	1.048
Final R	0.0690	0.0232
R_w	0.1576	0.0649
Largest diff. peak and hole ($e/Å^{-3}$)	1.104/-1.019	0.362/-0.233

5.7.1. ORTEP of $Tp^{tBu}Zn^{II}$-OTf and Select Bond Lengths and Angles

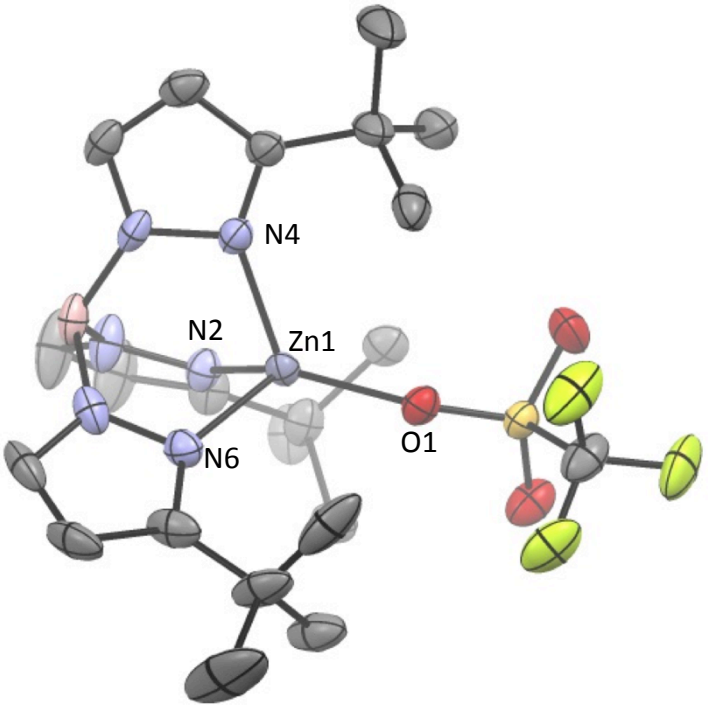

Figure 5.9. ORTEP of $Tp^{tBu}Zn^{II}$-OTf with select atom labels showing 50% probability ellipsoids. Hydrogen atoms and the co-crystallized pentane molecule are omitted for clarity. $\tau = 0.40$.

Table 5.5 Select bond lengths (Å) and angles (deg) of $Tp^{tBu}Zn^{II}$-OTf**.**

Primary Metal Coordination Sphere			
N2-Zn1	2.010(4)	N6-Zn1	2.018(4)
N4-Zn1	2.024(4)	O1-Zn1	1.938(4)
N2-Zn1-N4	97.04(18)	N4-Zn1-N6	95.26(18)
N2-Zn1-N6	94.78(18)	N4-Zn1-O1	119.82(17)
N2-Zn1-O2	126.31(17)	N6-Zn1-O1	116.87(17)

5.7.2. ORTEP of $Tp^{tBu}Cu^{II}$-κ^2-OAc

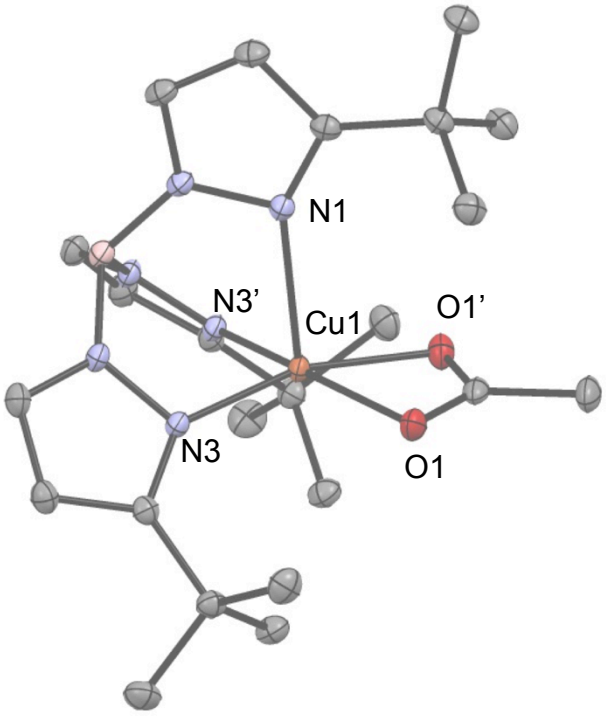

Figure 5.10. ORTEP of $Tp^{tBu}Cu^{II}$-κ^2-OAc with select atom labels showing 50% probability ellipsoids. Hydrogen atoms are omitted for clarity.

Table 5.6. Select bond lengths (Å) and angles (deg) of $Tp^{tBu}Cu^{II}$-κ^2-OAc

Primary Metal Coordination Sphere			
N1-Cu1	2.3580(15)	N3'-Cu1	1.9957(10)
N1'-Cu1	2.3580(15)	O1-Cu	2.0251(9)
N3-Cu1	1.9957(10)	O1'-Cu	2.0251(9)
N1-Cu-N3	92.75(4)	N1-Cu1-O1'	98.72(4)
N2-Zn1-N6	94.78(18)	N3-Cu1-N3'	91.94(6)
N1-Cu-N3'	92.75(4)	O1-Cu-O1'	64.81(5)
N1-Cu1-O1	98.72(4)		

Notes for Chapter 5

---

(1) (a) Solomon, E. I.; Heppner, D. E.; Johnston, E. M.; Ginsbach, J. W.; Cirera, J.; Qayyum, M.; Kieber-Emmons, M. T.; Kjaergaard, C. H.; Hadt, R. G.; Li, T. *Chem. Rev.* **2014**, 114, 3659. (b) Solomon, E. I.; Sundaram, U. M.; Machonkin, T. E. *Chem. Rev.* **1996**, 96, 2563.

(2) (a) Allen, S. E.; Walvoord, R. R.; Padilla-Salinas, R.; Kozlowski, M. C. *Chem. Rev.* **2013**, 113, 6234. (b) Wendlandt, A. E.; Suess, A. M.; Stahl, S. S. *Angew. Chem. Int. Ed.* **2011**, 50, 11062.

(3) (a) Somdatta, G.; Cirera, J.; Vance, M. A.; Ono, T.; Fujisawa, K.; Solomon, E. I. *J. Am. Chem. Soc.* **2008**, 130, 16262. (b) Jazdzewski, B.; Holland, P. L.; Pink, M.; Young Jr.; V. G.; Spencer, D. J. E.; Tolman, W. B. *Inorg. Chem.* **2001**, 40, 6097. (c) Jazdzewski, B.; Tolman, W. B. *Coord. Chem. Rev.* **2000**, 200-202, 633. (d) Bullock, J. I.; Hobson, R. J.; Povey, D. C. *J. Chem. Soc. Dalton Trans.* **1974**, 2037. (e) Calderazzo, F.; Marchetti, F.; Dell'Amico, G.; Pelizzi, G.; Colligiani, A. *J. Chem. Soc. Dalton Trans.* **1980**, 1419. (f) Kwik, W.–L. *J. Coord. Chem.* **1988**, 19, 279. (g) Whittaker, M.; Chuang, Y.; Whittaker, J. *J. Am. Chem. Soc.* **1993**, 15, 10029. (h) Ji, B.; Zhou, Z.; Ding, K.; Li, Y. *Polyhedron* **1998**, 17, 4327. Lyon, C. T.; Stack, T. D. P. *Coord. Chem. Rev.* **2014** ASAP. (i) Fujisawa, K.; Iwata, Y.; Kitajima, N.; Higashimura, H.; Kubota, M.; Miyashi, Y.; Yamada, Y.; Okamoto, K.–I.; Moro-oka, Y. *Chem. Lett.* **1999**, 28, 739.

(4) (a) Zhang, X.; Emge, T. J.; Ghosh, R.; Krogh-Jespersen, Goldman, A. S. *Organometallics*, **2006**, 25, 1303. (b) Camus, A.; Marsich, N.; Nardin, G.; Randaccio, L. *J. Chem. Soc. Dalton Trans.* **1975**, 2560. (c) Marsich, N.; Camus, A.; *J. Inorg. Nucl. Chem.* **1977**, 39, 275. (c) Cook, J. A.; Drew, M. G. B.; Rice, D. A. *J. Chem. Soc. Dalton Trans.* **1975** 1973. (d) Diel, B N.; Hope, H. *Inorg. Chem.* **1986**, 25, 4448. (e) Ito, H.; Ito, T. *Chem. Lett.* **1985**, 1251. (e) Kovács, T.; Speier, G.; Réglier, M.; Giorgi, M.; Vértes, A.; Vankó, G. *Chem. Commun.* **2000**, 469. (f) Balogh-Hergovich, É.; Speier, G.; Huttner, G.; Zsolnai, L. *Inorg. Chem.* **1998**, 37, 6535. (g) Kubota, M.; Yamamoto, A. *Bull. Chem. Soc. Jpn.* **1978**, 51, 2909. (h) Yamamoto, T.; Kubota, M.; Miyashita, A.; Yamamoto, A. *Bull. Chem. Soc. Jpn.*

1978, 51, 1835. (i) Miller, J. A.; Nelson, J. A. *Organometallics* **1991**, 10, 2958. (j) Lee, J. P.; Keller, C. L.; Werlein, A. A.; Janzen, D. E.; Van Derveer, D. G.; Grant, G. L. *Organometallics* **2012**, 31, 6505.

(5) Goldman and co-workers reported that treatment of an iridium pincer complex with a κ^2 bound nitromethanate with CO results in displacement of one of the bound nitromethanate oxygens and the formation of a κ^1 nitromethanate complex (ref. 4a).

(6) These results are presented in detail in Chapter 4.

(7) Lü, J. –M.; Rosokha, S. V.; Neretin, I. S.; Kochi, J. K. *J. Am. Chem. Soc.* **2006**, 128, 16708.

(8) Simonsen, O. *Acta Cryst.* **1973**, B29, 2600.

(9) Ellen Hayes contributed greatly to EPR data collection, simulation and interpretation.

(10) Tolman, W. B. *Inorg. Chem.* **1991**, 30, 4877.

(11) $Tp^{tBu}Cu^{II}$-κ^2-OAc was prepared as described by Tolman (ref 10), crystallized from pentane at –30 °C and structurally characterized by X-ray crystallography. See experimental for additional details.

(12) Vela, J.; Stoian, S.; Flaschenreim, C. J.; Münck, E.; Holland, P. L. *J. Am. Chem. Soc.* **2004**, 126, 4522.

(13) (a) Yoon, K.; Parkin, G. *J. Am. Chem. Soc.* **1991**, 113, 8414. (b) Han, R.; Looney, A.; McNeill, K.; Parkin, G.; Rheingold, A. L.; Haggerty, B. S. *J. Inorg. Biochem.* **1993**, 49, 105. (c) Hambly, T. W.; Lynch, M. J.; Zvargulis, E. S. *J. Chem. Soc. Dalton Trans.* **1996**, 4283.

(14) Ruggiero, C. E.; Carrier, S. M.; Antholine, W. E.; Whittaker, J.; Cramer, C J.; Tolman, W. B. *J. Am. Chem. Soc.* **1993**, 115, 11285.

(15) Carrier, S. M.; Ruggiero, C. E.; Houser, R. P.; Tolman, W. B. *Inorg. Chem.* **1993**, 32, 4889.

(16) Manner, V. W.; Markle, T. F.; Freudenthal, J. H.; Roth, J. P.; Mayer, J. M. *Chem. Commun.* **2008**, 256.

(17) Porter, T. R.; Kaminsky, W.; Mayer, J. M. *J. Org. Chem.* **2014**, Accepted. (and Chapter 3 in this Thesis.

(18) (a) Attempts to prepare $Tp^{tBu}Zn^{II}$-OAr^tBu_3 in an analogous method to how **(2)** was prepared were performed (see Experimental). After the addition of DBU and $^tBu_3ArO$–H to a solution of $Tp^{tBu}Zn^{II}$-OTf, the solution was stirred for ~ 1 hour. After one hour, the solvent was removed in vacuo, the resulting solids taken up in pentane, filtered over Celite, and crystallized at –30 °C. The resulting white crystals were determined to be $Tp^{tBu}Zn^{II}$-OTf by ^{1}H NMR. (b) Lithiated $^tBu_3ArO^-$ ($LiOAr^tBu_3$) was prepared *in situ* by the addition of one equivalent of lithium *bis*(trimethylsilyl)amide (LiHMDS) in THF. Addition of this solution to a THF solution containing one equivalent of $Tp^{tBu}Zn^{II}$-Cl was carried out with stirring. After 1 hour, the solvent was removed in *vacuo*, the solids taken up in toluene, filtered over Celite and crystallized at –30 °C. The resulting crystals were determined to be the $LiOAr^tBu_3$•THF by ^{1}H NMR and preliminary X-ray crystallography. $LiOAr^tBu_3$•THF: ^{1}H NMR (500 MHz, CD_2Cl_2) δ: 7.07 (s, 2H), 3.39 (m, 2H), 1.64 (m, 2H), 1.44 (s, 18H), 1.24 (s, 9H).

(19) (a) Molar extinction coefficient reported in dichloromethane and taken to be the same in benzene. (b) Wu, A.; Mader, E. A.; Datta, A.; Hrovat, D. A.; Mayer, J. M. *J. Am. Chem. Soc.* **2009**, 131, 11985.

(20) Kumar, M.; Papish, E. T.; Zeller, M.; Hunter, A. D. *Dalton Trans.* **2011**, 40, 7517.

(21) Deb, T.; Rohde, G. T.; Young, V. G., Jr.; Jensen, M. P. *Inorg. Chem.* **2012**, 51, 7257.

(22) This reaction was carried out at 12 mM and is entropically more favorable than if it were preformed at 1 M standard state since 2 reagents react to generate 2.5 products. Describing the free energy of this reaction as $\Delta G°$ assumes the same reaction would occur at 1 M concentrations.

(23) Warren, J. J.; Tronic, T. T.; Mayer, J. M. *Chem. Rev.* **2010**, 110, 6961.

(24) Brigati, G.; Lucarini, M.; Mugnaini, V.; Pedulli, G. F. *J. Org. Chem.* **2002**, 67, 4828.

(25) Parker, V. D. *J. Am. Chem. Soc.* **1992**, 114, 7458.

(26) Trofimenko, S.; Calabrese, J. C.; Thompson, J. S. *Inorg. Chem.* **1987**, 26, 1507.

(27) Cross, G. G.; Fischer, A.; Henderson, G. N. *Can. J. Chem.* **1984**, 62, 2803.

(28) Mader, E. A.; Davidson, E. R.; Mayer, J. M. *J. Am. Chem. Soc.* **2007**, 129, 5153.

(29) Gorrell, I. B.; Looney, A.; Parkin, G. *J. Chem. Soc. Chem. Commun.* **1990**, 220.

Chapter 6:
High Kinetic Barrier for Ketone Reduction or Alkoxide Oxidation by Titanocenes and H-Atom Transfer Reagents.

6.1. Introduction

Copper/radical alcohol oxidation catalysts are well known in both chemistry and in biology.[1] In these systems, the net $2H^+/2e^-$ oxididation of an alcohol to a ketone or an aldehyde is accomplished using the oxidizing equivalents from Cu(II) and an oxyl radical. In biological systems this radical is derived from a modified tyrosine. In preparative scale organic synthesis the oxyl radical is typically a nitroxyl radical. While the mechanisms for these reactions sometimes differ depending on the specific system, one suggested mechanism involves the formation of a copper(II) alkoxide complex followed by a one electron transfer (ET) to copper(II) coupled to a hydrogen atom transfer (HAT) to an external radical (Scheme 6.1).[1a,l]

Scheme 6.1. One Suggested Mechanism for Copper/Radical Alcohol Oxidation.

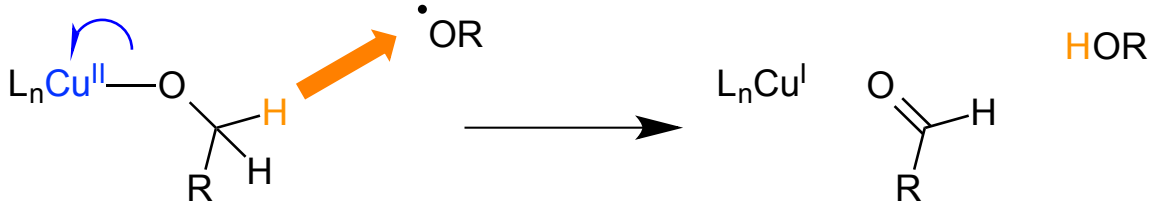

Experimental evidence for this type of reaction is currently limited and in fact most data suggests this mechanism is not operative in the systems carefully studied. This is highlighted in chapter 4 and in a recent report by Stahl and co-workers.[1b] While these reports offer convincing evidence against a coupled ET/HAT mechanism in some cases, these conclusions cannot necessarily be generalized to all copper(II)/radical alcohol oxidation systems since their mechanisms are already known to differ depending on subtle perturbations to the reaction conditions and ligands used.[1b]

A systematic study of copper/radical alcohol oxidation with different alkoxide substrates and supporting ligands would be valuable however this is generally not feasible due to the synthetic challenges of isolating copper(II) alkoxide complexes (see Chapter 4).

While copper/radical catalysis involves alkoxide oxidation, the same general type of coupled ET/HAT reaction mechanism could be envisioned to proceed in the reverse direction to generate a metal alkoxide from a ketone with the use of a reducing metal complex and a hydrogen atom donor (scheme 6.2). Studying the reaction from the opposite direction could potentially offer synthetic advantages over copper systems while still providing insight regarding the mechanism of cooperative metal/radical alcohol oxidations.

Scheme 6.2. Reverse and Forward Reaction of Cu(II)/Radical Alkoxide Oxidation

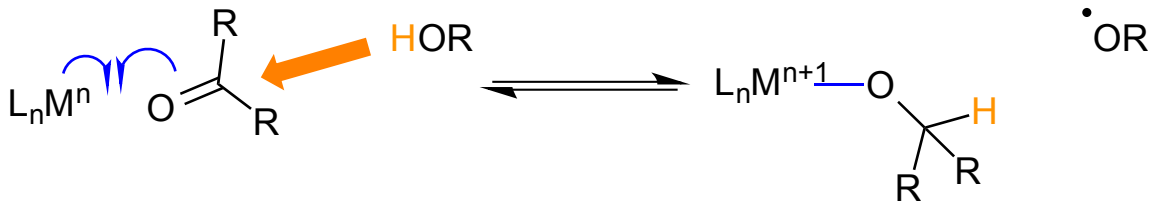

Reported here are attempts to reduce ketones with the combination of the reducing organometallic transition metal complex $[Cp_2Ti^{III}Cl]_2$ (titanocene chloride dimer) and the different hydrogen atom donors TEMPO–H (2,2,6,6-tetramethylpiperidin-1-ol), $^tBu_3ArO$–H (2,4,6-di-*tert*-butyl-phenol) and 1,2-diphenylhydrazine. When combined with TEMPO–H, $[Cp_2Ti^{III}Cl]_2$ reacts by cleaving the N–OH bond in TEMPOH to generate $[Cp_2Ti^{IV}Cl]_2$-μ-O and TEMP–H (2,2,6,6-tetramethylpiperidine). With $^tBu_3ArO$–H or 1,2-diphenylhydrazine no reaction is observed between ½ $[Cp_2Ti^{III}Cl]_2$ and a variety of ketones over the course of days.

To determine whether this reaction could proceed in the opposite direction, $Cp_2Ti^{IV}Cl(OR)$ complexes were prepared via a new reaction protocol. These complexes were likewise unreactive with the hydrogen atom acceptor $^tBu_3ArO^{\bullet}$ (2,4,6-tri-*tert*-butyl-phenoxyl radical) indicating alkoxide oxidation or ketone reduction in this system is necessarily limited kinetically rather than thermodynamically for these envisioned reactions. The implications of these results are discussed.

The previously reported method for preparing $Cp_2Ti^{IV}Cl(OR)$ relied on treatment of $Cp_2Ti^{IV}Cl_2$ with ROH and a base.[2] This method is effective but often results in over substitution to generate $Cp_2Ti^{IV}(OR)_2$. Also discussed in this report is the development of a new protocol for rapidly preparing $Cp_2Ti^{IV}Cl(OR)$ via the alcoholysis of

$Cp_2Ti^{IV}(Cl)OAr^tBu_3$ (titanocene chloride 2,4,6-tri-*tert*-butyl-phenoxide) with ROH. This preparation was found to be modular and highly useful for generating $Cp_2Ti^{IV}Cl(OR)$ *in situ* with a large number of R groups very rapidy on small scales.

6.2. Results

6.2.1. Screening Reagent Compatibility

$[Cp_2Ti^{III}Cl]_2$ and related species have been extensively studied and are known to be highly reactive in certain cases.[3] $[Cp_2Ti^{III}Cl]_2$ is known to be a strong halide abstractor capable of breaking alkyl halide bonds to generate $Cp_2Ti^{IV}Cl(X)$ and organic radicals.[4] It is also known to facilitate pinacol coupling reactions of aromatic aldehydes (scheme 6.3).[5] As such, to make any conclusions about the reactivity of

Scheme 6.3. Benzaldehyde Pinacol Coupling Reaction by $Cp_2Ti^{III}Cl$

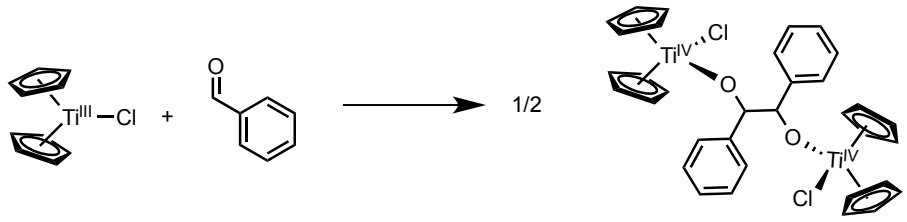

$Cp_2Ti^{III}Cl$ with the combination of ketones and H-atom donors it was critical to establish any combination of only two reagents would not react in the absence of the third. To screen the fidelity of these reagents, control experiments were performed to determine reagent compatibility. Notably, $[Cp_2Ti^{III}Cl]_2$ reacts with TEMPO–H to yield TEMP–H and the known[6] μ-O dimer, $[Cp_2Ti^{IV}Cl]_2$-μ-O as determined by ^{1}H NMR and X-ray crystallography (Scheme 6.4, Figure 6.1). Also of note was that treatment of ½ $[Cp_2Ti^{III}Cl]_2$ with an excess of any ketone attempted resulted in the formation of the titanocene-ketone adduct as was evident from the color change from green to red and the broadening of the ketone signals by ^{1}H NMR. This indicated that in solution, $[Cp_2Ti^{III}Cl]_2$ was dissociated with the ketone strongly interacting and poised to react with a hydrogen atom acceptor. Both $^tBu_3ArO$–H and 1,2-diphenyhydrazine were found to be independently compatible with both $[Cp_2Ti^{III}Cl]_2$ and ketones implying the combination

of these reagents with ½ $[Cp_2Ti^{III}Cl]_2$ and different ketones would not undergo undesirable side reactions.

Scheme 6.4. Reaction between ½ $[Cp_2Ti^{III}Cl]_2$ (shown as monomer) with TEMPO–H

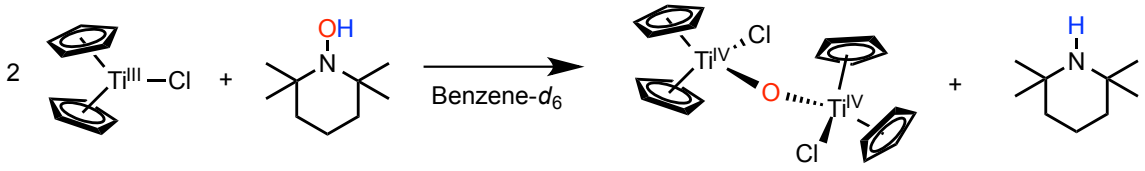

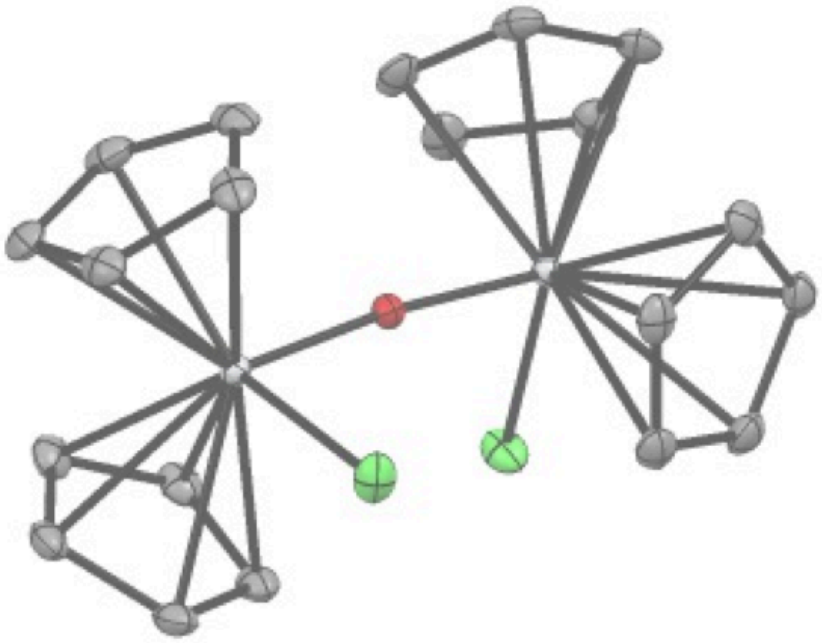

Figure 6.1. ORTEP of $[Cp_2Ti^{IV}Cl]_2$-μ-O showing 50% probablility thermal ellipsoids. Hydrogen atoms are omitted for clarity.

Aldehydes were found to be relatively stable over short time periods (*ca.* 6 hours) however decomposition was observed over longer times. Aldehydes were also found to be reactive with 1,2-diphenylhydrazine generating a variety of unidentifiable products as

determined by ^{1}H NMR. Due to the instability of aldehydes in comparison to ketones, we chose to focus primarily on ketones.

6.2.2. Attempted Reactions with ½ [$Cp_2Ti^{III}Cl]_2$, ketones and H-atom donors.

In several NMR tubes, 19.5 mM of [$Cp_2Ti^{III}Cl]_2$ was combined with 390 mM (20 eq) of various ketones (Scheme 6.5; [$Cp_2Ti^{III}Cl]_2$ shown as monomer) and 39 mM of the H-atom donor $^{t}Bu_3ArOH$ (O–H BDFE in benzene = 76.6 kcal mol^{-1})[7] in benzene-d_6. Addition of any of all ketones to [$Cp_2Ti^{III}Cl]_2$ resulted in a color change from green to red as observed in the control reaction however no other reaction was observed over the course of days. Likewise, perform the same experiment in neat acetone-d_6 also resulted in no reaction.

Scheme 6.5. Ketone Reduction Reactions Attempted with $^{t}Bu_3ArO$–H in Benzene-d_6

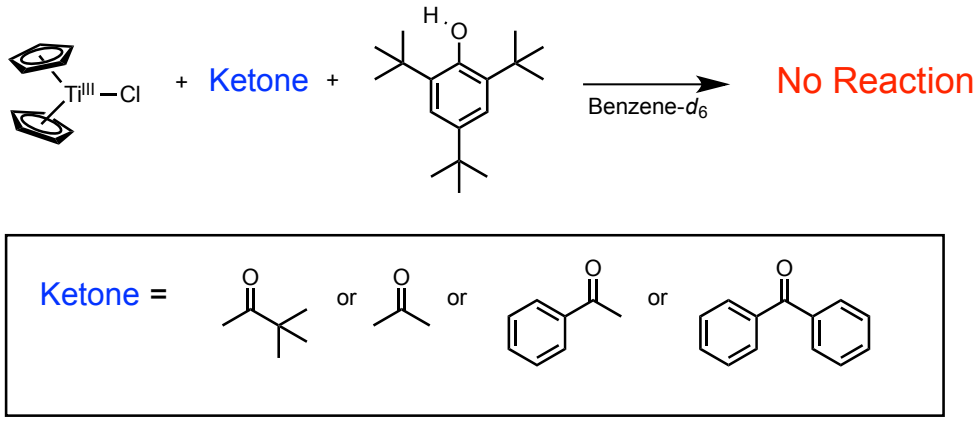

Similarly, treatment of a benzene-d_6 solution containing 39 mM [$Cp_2Ti^{III}Cl]_2$ and 80 mM pinacalone with 39 mM of the strong H-atom donor 1,2-diphenylhydrazine (first N–H BDFE = 64.3 kcal mol^{-1})[8] resulted in no reaction over days.

6.2.3. Preparation of $Cp_2Ti^{IV}Cl(OAr^{t}Bu_3)$ (1)

Treatment of ½ [$Cp_2Ti^{III}Cl]_2$ with one equivalent of the isolable radical $^{t}Bu_3ArO^{\bullet}$ in benzene-d_6 resulted in the immediate color change from green-blue ([$Cp_2Ti^{III}Cl]_2$ is green $^{t}Bu_3ArO^{\bullet}$ is blue) to dark maroon. The ^{1}H NMR spectrum displayed a single resonance for the Cp rings as well as three new *tert*-butyl signals and two aromatic doublets. This NMR pattern is consistent with the formation of a diamagnetic $Cp_2Ti^{IV}Cl(OAr^{t}Bu_3)$ complex, **(1),** in which the hindered rotation about the Ti-O bond gives rise to distinct *tert*-butyl and *meta*-H signals from the phenoxide ligand. This reaction was scalable and found to be quantitative by ^{1}H NMR. Unfortunately, multiple

attempts to obtain x-ray quality crystals were unsuccessful. A related Cp_2Ti^{IV}-TEMPO complex was reported by Waymouth and prepared in a similar fashion.[9]

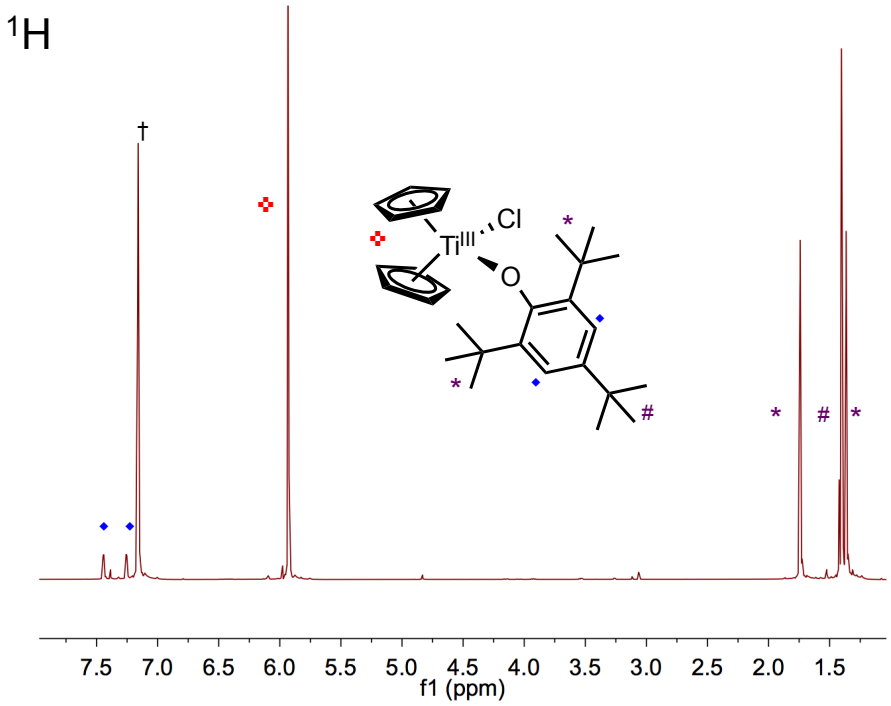

Figure 6.2. ^{1}H NMR spectrum of $Cp_2Ti^{IV}Cl(OAr^tBu_3)$ **(1)** in benzene-d_6. Resonances are assigned and the residual solvent signal is shown by †.

In attempts to detect possible Ti–O bond homolysis, a 40 mM solution of $Cp_2Ti^{IV}Cl(OAr^tBu_3)$ in benzene-d_6 was heated to 70 °C in the presence of 10 equivalents of CCl_4. Cp_2Ti^{III}-X is known to abstract a Cl atom from CCl_4[8c,10] so if bond homolysis of of the Ti–O bond occurred, the reaction solution would be expected to contain some amount of $Cp_2Ti^{IV}Cl_2$. After 24 hours of heating, no reaction was observed by ^{1}H NMR indicating homolysis was not occurring at this temperature.

Monitoring $Cp_2Ti^{IV}Cl(OAr^tBu_3)$ by ^{1}H NMR at elevated temperatures resulted in peak broadening but no coalescence even at temperatures as high as 70 °C (figure 6.3).

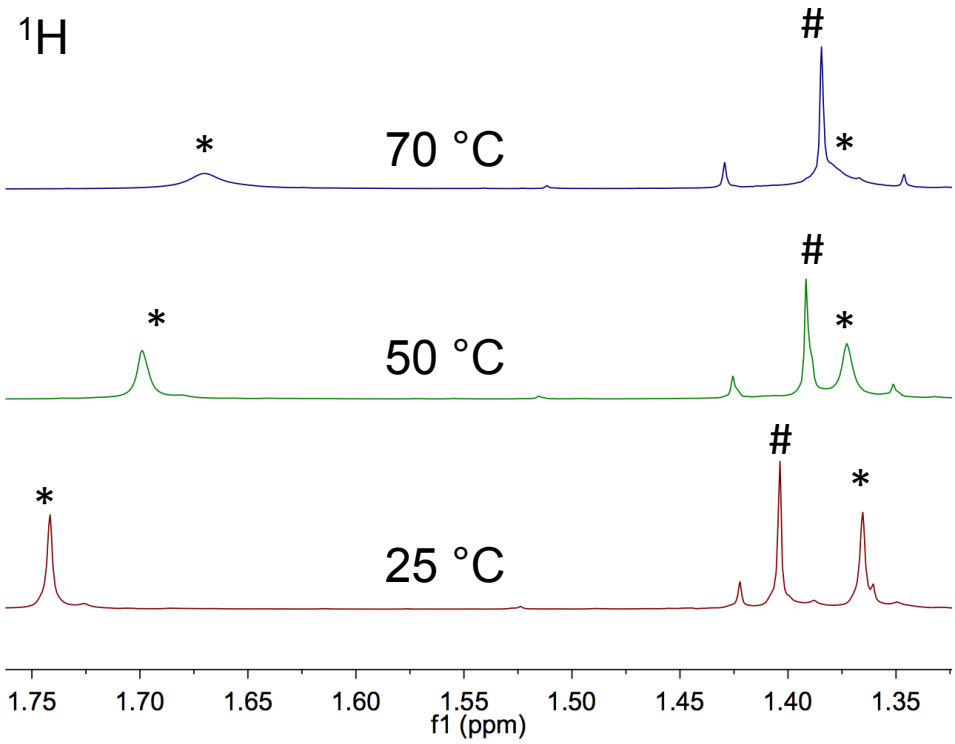

Figure 6.3. Variable temperature ^{1}H NMR spectra of $Cp_2Ti^{IV}Cl(OAr^{t}Bu_3)$ in C_6D_6 expanded to show the *tert*-butyl region. The *ortho-tert*-butyl signals are labeled with * and the *para-tert*-butyl signal with #. Other peaks correspond to trace impurities present in the sample.

Treatment of $Cp_2Ti^{IV}Cl(OAr^{t}Bu_3)$ with ROH results in the quantitative alcoholysis to generate $Cp_2Ti^{IV}Cl(OR)$ and $^{t}Bu_3ArOH$ after roughly 90 minutes. This protocol was found to be highly versatile and proceed cleanly with all alcohols attempted (Table 6.1). This procedure was used to prepare all of the $Cp_2Ti^{IV}Cl(OR)$ complexes discussed in the following section. Notably, attempts to hydrolyze the reported and related $Cp_2Ti^{IV}Cl(\eta^1\text{-TEMPO})$[9] complex with different alcohols was not successful.

Table 6.1. $Cp_2Ti^{IV}Cl(OR)$ Complexes Prepared via alcoholysis of $Cp_2Ti^{IV}Cl(OAr^tBu_3)$

Entry	ROH	Product ($Cp_2Ti^{IV}Cl(OR)$)
1		**(2)**
2	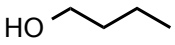	**(3)**
3	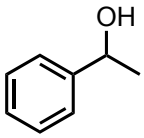	**(4)**[11]
4	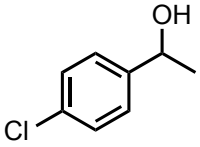	**(5)**
5	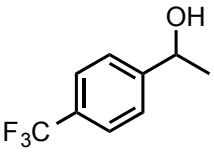	**(6)**
6	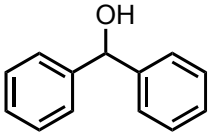	**(7)**[12]
7	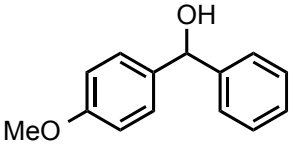	**(8)**
8	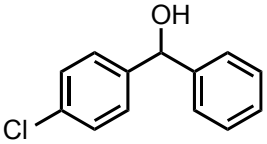	**(9)**
9	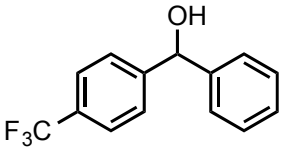	**(10)**
10	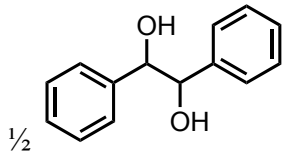	**(11)** **[Ti^{IV}–ORRO–Ti^{IV} dimer]**
11	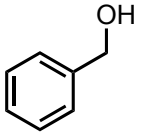	**(12)**[11]

6.2.3. Attempted Reactions between $Cp_2Ti^{IV}Cl(OR)$

In an NMR tube, a 39 mM solution of $Cp_2Ti^{IV}Cl(OR)$ with various OR (entries 1-9 in Table 1) was combined with two equivalents of $^tBu_3ArO^\bullet$. No reactions were observed after days.

With the benzyloxide derivative (entry 11 in table 6.1), this complex reacted with two equivalents of $^tBu_3ArO^\bullet$ overnight however multiple products were observed including a very small amount of benzaldehyde (Figure 6.4). This initially seemed promising however a series of control experiments indicated benzadehyde was independently reactive with $Cp_2Ti^{III}(Cl)$ (as has previously been reported),[5] $Cp_2Ti^{IV}Cl(OBn)$ **(12)** and $Cp_2Ti^{IV}Cl(OAr^tBu_3)$ **(1)**. Reacting benzaldehyde with $Cp_2Ti^{IV}Cl(OBn)$ or $Cp_2Ti^{IV}Cl(OAr^tBu_3)$ and gave a variety of unidentifiable products but these products were different than the unidentifiable products observed when $^tBu_3ArO^\bullet$ was reacted with $Cp_2Ti^{IV}Cl(OBn)$.

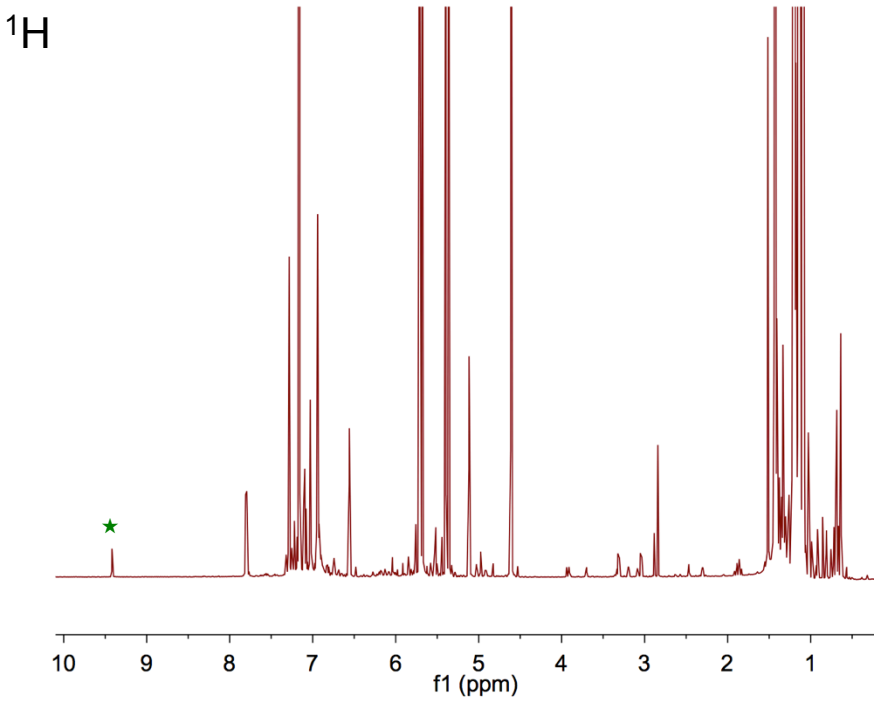

Figure 6.4. ^1H NMR spectrum of the reaction mixture containing $Cp_2Ti^{IV}Cl(OBn)$ and 2 eq of $^tBu_3ArO^\bullet$ in benzene-d_6 after 24 hours. Trace benzaldehyde is shown by ★.

6.3. Discussion

6.3.1. Neither Ketone Reduction or Alkoxide Oxidation is Observed

In the envisioned reaction scheme between ½ $[Cp_2Ti^{III}Cl]_2$, ketones and $^tBu_3ArO$–H, an hydrogen atom would be transferred from $^tBu_3ArO$–H to the carbonyl carbon of the ketone while a bond would form between ½ $[Cp_2Ti^{III}Cl]_2$ and the carbonyl oxygen (Scheme 6.2). This reaction does not occur over days in benzene with any of the ketones attempted.

In the opposite reaction, a hydrogen atom would be transferred from the α-C–H group of a titanium(IV) bound alkoxide ligand to an external radical, $^tBu_3ArO^{\bullet}$, while a homolytic bond cleavage between titanium(IV) and the alkoxide oxygen. This reaction is the microscopic reverse of the reduction reaction but this reaction is also not observed.

Regardless of the specific thermochemical parameters for this system, it is necessary that one of these reactions be thermodynamically favorable. Since no reaction is observed in either direction, it can be concluded that this envisioned ET/HAT type mechanism must be kinetically limited in this system. This is in agreement with the conclusions reported in Chapter 4 and by Stahl and co-workers[1b] which suggest a mechanism such as this is not operating in related copper/radical alcohol oxidation systems.

6.3.2. $Cp_2Ti^{IV}Cl(OAr^tBu_3)$

The combination of persistent radicals with reducing metals or other chemical reagents has seen an increase in attention recently. Hayton and co-workers have investigated the coordination chemistry and reactivity of TEMPO radical in combination with Lewis acids as a way of enhancing the H-atom affinity of the radical.[14] This approach has proven quite successful as it was found the combinations of TEMPO with either $AlBr_3$ or $FeBr_3$ could facilitate the oxidation of benzylic or secondary aliphatic alcohols to aldehydes or ketones and dihydroanthracene to anthracene.[14a] The thermochemical enhancements provided by these Lewis acids are clearly evident from these reaction since the α-C–H bond dissociation enthalpy of a secondary alcohol is roughly 93 kcal mol^{-1} while the bond BDE of the O–H bond in TEMPO–H alone is only ~71 kcal mol^{-1}.[15]

A more relevant example of radical-metal reactivity is in the reports of Waymouth and co-workers who have explored the use of $Cp_2Ti^{IV}Cl(\eta^1$-TEMPO) as a catalyst for living radical polymerization.[9] This complex was prepared in much the same fashion as described here for $Cp_2Ti^{IV}Cl(OAr^tBu_3)$ in which one equivalent of TEMPO was added to ½ $[Cp_2Ti^{III}Cl]_2$. Heating $Cp_2Ti^{IV}Cl(\eta^1$-TEMPO) to 60 °C resulted in a reversible bond homolysis as determined by trapping experiments with CCl_4[9c] and an upper limit for the homolytic bond strength of Ti^{IV}-O has been determined to be 25 kcal mol^{-1}.[9b]

The $Cp_2Ti^{IV}Cl(OAr^tBu_3)$ complex reported here is highly reminiscent of the $Cp_2Ti^{IV}Cl(\eta^1$-TEMPO) complex reported by Waymouth. In this system however, thermolysis of the Ti^{IV}–OAr^tBu_3 bond is not observed when heated to 70 °C as determined by the lack of reactivity with excess CCl_4.[9c,10] The stronger Ti–O bond in $Cp_2Ti^{IV}Cl(OAr^tBu_3)$ can be crudely rationalized by examining the difference in O–H bond strengths between the parent phenol $^tBu_3ArO$–H and TEMPO–H as a rough measure of the relative oxyl radical stability. The bond dissociation free energy (BDFE) of $^tBu_3ArO$–H in benzene is reported to be 76.7 kcal mol^{-1} while the TEMPO–H O–H bond is only 65.2 kcal mol^{-1}.[7] The steric clash between the *ortho-tert*-butyl signals of the phenolate ligand are expected to destabilize the Ti^{IV}–O bond relative to the less bulky TEMPO ligand however because homolysis of the Ti^{IV}-OAr^tBu_3 bond is not observed, this effect must not be substantial with respect to the difference in Ti^{IV}–O bonds between the two species.

The preparation of $Cp_2Ti^{IV}Cl(OR)$ complexes has been previously reported and achieved by treatment of $Cp_2Ti^{IV}Cl_2$ with one equivalent of ROH and base.[2] These protocols are established and proven but were deemed unsatisfactory for our needs since these procedures frequently involve over substitution and require workup and purification steps. In attempts to bypass these issues, the development of a new methodology for preparing $Cp_2Ti^{IV}Cl(OR)$ *in situ* was developed. The addition of one equivalent of ROH to $Cp_2Ti^{IV}Cl(OAr^tBu_3)$ resulted in complete alcoholysis of the phenoxide to generate previously unreported[16] $Cp_2Ti^{IV}Cl(OR)$ complexes in quantitative yield. Using this protocol, a large number of $Cp_2Ti^{IV}Cl(OR)$ complexes could be prepared rapidly on an NMR scale (~0.05 mmoles) and screened for their reactivity with hydrogen atom acceptors.

While treatment of $Cp_2Ti^{IV}Cl(OAr^tBu_3)$ with all alcohols (ROH) attempted (Table 1) resulted in the complete alcoholysis to generate $Cp_2Ti^{IV}Cl(OR)$, treatment of $Cp_2Ti^{IV}Cl(\eta^1$-TEMPO) resulted in no reaction. This difference in reactivity may be the result of steric differences between $TEMPO^-$ and $^tBu_3ArO^-$.

6.4. Conclusions

Alcohol oxidations mediated by copper and oxyl radicals are well known in both chemistry and biology.[1] The catalytic mechanisms by which operate can differ depending on the specific system but it has been proposed that in some cases these may involve a hydrogen atom transfer from the α-C–H position of a copper(II) alkoxide that is coupled to a one electron oxidation by copper. Synthetic challenges of preparing isolable copper(II) alkoxide complexes limit the scope of possible model systems to examine this process easily.

Reported here are our attempts to study the microscopic reverse of this reaction using a reducing organometetallic complex, $[Cp_2Ti^{III}Cl]_2$ in combination with different ketones and hydrogen atom donors. In all cases, no reaction was observed in benzene-d_6 over days.

Likewise, treatment of $Cp_2Ti^{IV}(Cl)OR$ with hydrogen atom acceptors resulted in no reaction under the same conditions. Because no reaction was observed in either direction, it can be concluded that a HAT/ET process is necessarily limited by a high kinetic barrier rather than a thermodynamic barrier in this system.

Treatment of ½ $[Cp_2Ti^{III}Cl]_2$ with one equivalent of $^tBu_3ArO^\bullet$ results in the immediate formation of $Cp_2Ti^{IV}Cl(OAr^tBu_3)$ as was apparent from the color change to dark maroon and by ^{1}H NMR. This complex was stable to Ti^{IV}–O bond homolysis up to 70 °C but was found to be a useful precursor for preparing $Cp_2Ti^{IV}Cl(OR)$ *in situ* via alcoholysis by the corresponding ROH.

6.5. Experimental

6.5.1. General considerations

Unless otherwise noted, all reactions were carried out in a nitrogen filled glovebox. All chemicals were purchased from Sigma-Aldrich and used as received. Benzene-d_6 was purchased from Cabridge Isotope Labs and dried over NaK for 24 hours

prior to being vacuum distilled and degassed. $[Cp_2Ti^{III}Cl]_2$,[17] TEMPO–H[18] and $^tBu_3ArO^{\bullet}$[19] were prepared according to established literature protocols. All NMR spectra were collected on Bruker 300 or 500 MHz spectrometers and referenced to TMS with the residual benzene-d_5 solvent peak.

6.5.2. Synthesis of $Cp_2Ti^{IV}Cl(OAr^tBu_3)$ (1)

To a ~10 mL THF solution of $[Cp_2Ti^{III}Cl]_2$ (34.8 mg, 0.08 mmoles) was added $^tBu_3ArO^{\bullet}$ (42.6 mg, 0.16 mmoles) in a 5 mL THF solution. Immediately upon addition, the color changed from green to dark maroon. After stirring for 30 minutes, the solvent was removed under vacuum yielding dark maroon solids. ^{1}H NMR (500 MHz, C_6D_6) δ: 7.44 (d, $^4J_{HH}$ = 2.7 Hz, 1H), 7.25 (d, $^4J_{HH}$ = 2.7 Hz, 1H), 5.93 (s, 10H), 1.74 (s, 9H), 1.40 (s, 9H), 1.37 (s, 9H). The ^{1}H NMR spectrum was consistent with the proposed structure. No additional characterization was acquired.

6.5.3. Representative Procedure for preparing $Cp_2Ti^{IV}Cl(OR)$

To an NMR tube containing $Cp_2Ti^{IV}Cl(O^tBu_3ArO)$ (20.3 mg, 0.043 mmoles) in 300 μL of C_6D_6 was added 1-butanol (3.1 mg, 0.043 mmoles) in 300 μL of C_6D_6. After ~12 hours the ^{1}H NMR spectrum displayed new signals for $Cp_2Ti^{IV}Cl(O^nBu)$ and $^tBu_3ArO$–H. $Cp_2Ti^{IV}Cl(OnBu)$ **(3)**: ^{1}H NMR (500 MHz, C_6D_6) δ: 5.90 (s, 10H), 4.28 (t $^3J_{HH}$ = 6.1 Hz, 2H), 1.5-1.2 (m 4H), 0.93 (t, $^3J_{HH}$ = 7.3 Hz). $Cp_2Ti^{IV}Cl(OR)$ was not isolated in any case but their ^{1}H NMR spectra were consistent with the proposed structure.

6.5.4. ^{1}H NMR characterization of $Cp_2Ti^{IV}Cl(OR)$

(2) ^{1}H NMR (500 MHz, C_6D_6) δ: 5.88 (s, 10H), 4.53-4.47 (m, 1H), 1.04 (d, $^3J_{HH}$ = 6.0 Hz) **(4)** ^{1}H NMR (500 MHz, C_6D_6) δ: 7.25 – 7.05 (m, 5H), 5.95 (s, 5H) 5.82 (q $^3J_{HH}$ = 6.3 Hz 1H), 1.28 (d, $^3J_{HH}$ = 6.3, 3H) **(5)** ^{1}H NMR (500 MHz, C_6D_6) δ: 7.19 (d, $^3J_{HH}$ = 8.4 Hz, 2H), 6.90 (d, $^3J_{HH}$ = 8.4 Hz), 5.9 (s, 5H), 5.79 (s, 5H), 5.28 (q, $^3J_{HH}$ = 6.2 Hz, 1H), 1.29 (d, $^3J_{HH}$ = 6.2 Hz, 3H) **(6)** ^{1}H NMR (500 MHz, C_6D_6) δ: 7.43 (d, $^3J_{HH}$ = 8.0 Hz, 2H), 7.02 (d, $^3J_{HH}$ = 8.0Hz, 2H), 5.91 (s, 5H), 5.79 (s, 5H), 5.31 (q, $^3J_{HH}$ = 6.3 Hz, 1H), 1.28 (d, $^3J_{HH}$ = 6.3Hz, 3H). **(7)** ^{1}H NMR (500 MHz, C_6D_6) δ: 7.33 (d, $^3J_{HH}$ = 7.7 Hz, 4H), 7.19 (t, $^3J_{HH}$ = 7.7 Hz, 4H), 7.06 (t, J = 7.3 Hz, 2H), 6.35 (s, 1H), 5.87 (s, 10H). **(8)** ^{1}H NMR (500 MHz, C_6D_6) δ: 7.4-7.0 (m, 9H), 5.90 (s, 5H), 5.89 (s, 5H), 6.35 (s, 1H), 3.30 (s, 3H). **(9)** ^{1}H NMR (500 MHz, C_6D_6) δ: 7.25-7.05 (m, 9H), 6.19 (s, 1H), 5.85 (s, 5H), 5.83 (s, 5H). **(10)** ^{1}H NMR (500 MHz, C_6D_6) δ: 7.4-7.05 (m, 9H), 6.21 (s, 1H), 5.85 (s, 5H), 5.83

(s, 5H). **(11)** ^{1}H NMR (500 MHz, C_6D_6) δ: 7.4-7.0 (m, 10H), 6.43 (s, 2H), 5.92 (s, 10H), 5.91 (s, 10H). **(12)** ^{1}H NMR (500 MHz, C_6D_6) δ: 7.4-7.1 (m, 5H), 5.90 (s, 10H), 5.34 (s, 2H).

Notes for Chapter 6

---

(1) (a) Whittaker, J. W. *Chem. Rev.* **2003**, 103, 2347. (b) Ryland, B. L.; McCann, S. D.; Brunold, T. C.; Stahl, S. S. *J. Am. Chem. Soc.* **2014**, ASAP (August 2014). (c) Lyons, C. T.; Stack, T. D. P. *Coord. Chem. Rev.* **2013**, 257, 528. (d) Jazdzewski, B. A.; Tolman, W. B. *Coord. Chem. Rev.* **2000**, 200, 633. (e) Himo, F.; Eriksson, L. A.; Maseras, F.; Siegbahn, P. E. M. *J. Am. Chem. Soc.* **2000**, 122, 8031. (f) Whittaker, J. W. *Arch. Biochem. Biophys.* **2005**, 44, 2367. (g) Pratt, R. C.; Stack, T. D. P. *Inorg. Chem.* **2005**, 433, 227. (h) Semmelack, M. F.; Schmid, C. R.; Cortés, D. A.; Chou, C. S. *J. Am. Chem. Soc.* **1984**, 106, 3374. (i) Gamez, P.; Arends, I. W. C. E; Sheldton, R. A.; Reedijk, J. *Adv. Synth. Catal.* **2004**, 346, 805. (j) Kumpulainen, E. T. T.; Koskinen, A. M. P. *Chem. Eur. J.* **2009**, 15, 10901. (k) Hoover, J. M.; Stahl. S. S. *J. Am. Chem. Soc.* **2011**, 133, 16901. (l) Hoover, J. M.; Ryland, B. L.; Stahl, S. S. *J. Am. Chem. Soc.* **2013**, 135, 2357.

(2) Köcher, S.; Walfort, B.; Rheinwald, G.; Rüffer, T.; Lang, H. *J. Organomet. Chem.* **2008**, 693, 3213.

(3) Wilkinson, G.; Stone, F. G. *Titanium: Comprehensive Organometallic Chemistry*; Pergamon Press: New York, NY, 1982.

(4) Spencer, R. P.; Schwartz, J. *Tetrahedron* **2000**, 56, 2103.

(5) (a) Enemærke, R. J.; Larsen, J.; Hjøllund, G. H.; Skrydstrup, T.; Daasbjerg, K. *Organometallics*, **2005**, 24, 1252. (b) Barden, M. C.; Schwartz, J. *J. Am. Chem. Soc.* **1996**, 118, 5484. (c) Gansäuer, A. *Chem. Commun.* **1997**, 457.

(6) (a) Fachinetti, G.; Floriani, C.; Chiesi-Villa, A.; Guastini, C. *J. Am. Chem. Soc.* **1979**, 101, 1767. (b) Le Page, Y.; McCowan, J. D.; Hunter, B. K.; Heyding, R. D. *J. Organomet. Chem.* **1980**, 193, 201.

(7) Warren, J. J.; Tronic, T. T.; Mayer, J. M. *Chem. Rev.* **2010**, 110, 6961.

(8) Porter, T. R.; Mayer, J. M. *Chem. Sci.* **2014**, 5, 372.

(9) (a) Mahanthappa, M. K.; Huang, K.–W.; Cole, A. P.; Waymouth, R. M. *Chem. Commun.* **2002**, 502. (b) Huang, K. –W.; Han, J. H.; Cole, A. P.; Musgrove, C. B.; Waymouth, R. M. *J. Am. Chem. Soc.* **2005**, 127, 3807. (c) Huang, K. –W.; Waymouth, R. M. *J. Am. Chem. Soc.* **2002**, 124, 8200.

(10) Bruce, A. E.; Bruce, M. R. M.; Tyler, D. R. *J. Am. Chem. Soc.* **1984**, 106, 6660.

(11) Sandström, J. *Dynamic NMR Spectroscopy*; Academic Press: New York, NY, 1982.

(12) Wu, S.; Yaokun, Z. *Gaodeng Xuexiao Huaxue Xuebao* **1983**, 4, 127.

(13) Lui, Z.; Wu, S.; Zhang, Y. *Hecheng Huaxue* **1996**, 4, 190.

(14) (a) Scepaniak, J. J.; Wright, A. M.; Lewis, R. A.; Wu, G.; Hayton, T. W. *J. Am. Chem. Soc.* 2012, 134, 19350. (b) Wright, A. M.; Page, J. S.; Scepaniak, J. J.; Wu, G.; Hayton, T. W. *Eur. J. Inorg. Biochem.* 2013, 3817.

(15) (a) Luo, Y.–R. Comprehensive Handbook of Chemical Bond Energies; CRC Press: Boca Raton, Fl, 2007. (b) Bond strengths given as BDEs rather than BDFEs for comparison purposes since alcohol α-C–H bond strengths are only reported as BDEs.

(16) Complexes 4, 12, and 7 have been previously reported in references 11, 11 and 12 respectfully.

(17) Coutts, R. S. P.; Wailes, P. C. *J. Organomet. Chem.* **1973**, 47, 375.

(18) Mader, E. A.; Davidson, E. R.; Mayer, J. M. *J. Am. Chem. Soc.* **2007**, 129, 5153.

(19) Manner, V. W.; Markle, T. F.; Freudenthal, J. H.; Roth, J. P.; Mayer, J. M. *Chem. Commun.* **2008**, 256.

Chapter 7:
Selective Aliphatic and Aromatic Nitro Reductions by Colloidal Photo-Reduced TiO_2 Nanoparticles at Low pH

7.1 Introduction

Titanium dioxide (TiO_2) bulk and nanomaterial semiconductors have been studied extensively from a fundamental perspective and for their use in technological applications.[1] These materials have found widespread use in areas such as self-cleaning paints,[2] wastewater remediation,[2] organic photo-oxidation and photo-reduction reactions,[3] and recently in the Mayer Laboratory as models for studying proton-coupled electron transfer (PCET) in metal oxide semiconductors.[4] Previous studies in our laboratory have shown that photo-reduced amorphous oleate capped TiO_2 nanoparticles were potent H^+/e^- donors, capable of rapidly transferring a net hydrogen atom ($H^\bullet \equiv H^+/e^-$) to either TEMPO (2,2,6,6-tetramethypiperdinyl) or $^tBu_3ArO^\bullet$ (2,4,6-tri-*tert*-butyl-phenoxyl) radicals in toluene.[4]

Recently, Bahnemann and co-workers described the reduction of a variety of reagents with photo-charged anatase TiO_2 nanoparticles suspended in water at low pHs.[5] Included in these reports was the facile reduction of dinitrogen to ammonia as well as the reduction of nitrate to ammonia, copper(II) to copper(0) and dioxygen to water. These reactions piqued our interest since most of these processes involved the transfer of multiple electrons and multiple protons yet occurred on stopped-flow time scales.

Previous work in the Mayer laboratory by D. Gary, B. Horst and J. Peper has been unable to reproduce the reduction of dinitrogen, but it was found that particles prepared and photo-reduced as described by Bahnemann were capable of reducing 4-MeO-TEMPO (2,2,6,6-tetramethyl-4-methoxypiperidinyl) to 4-MeO-TEMPO–H (2,2,6,6-tetramethyl-4-methoxypiperidin-1-ol) as well as dimethylsulfoxide (DMSO) to dimethysulfide (DMS) (Scheme 7.1).[6] Mechanistic studies of these reactions are ongoing.

Scheme 7.1. e^-:TiO_2 Reactions Previously Discovered in the Mayer Lab.

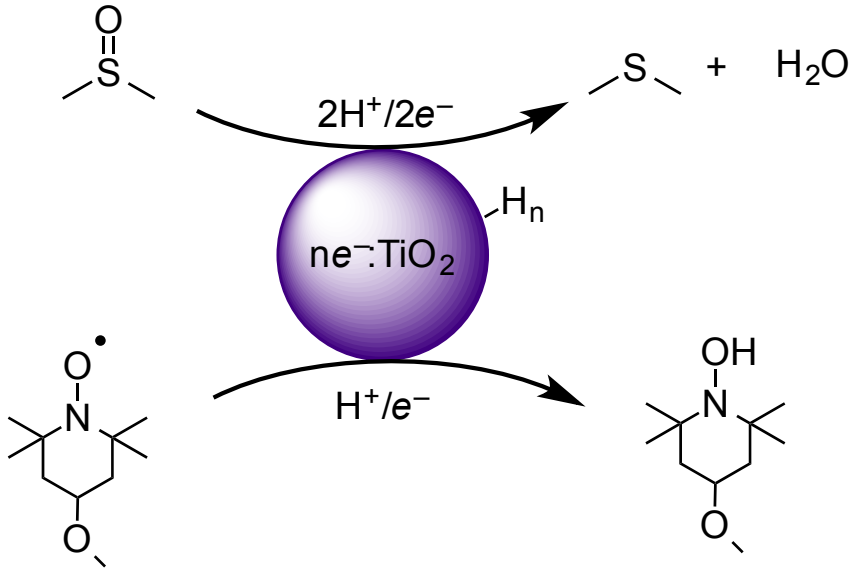

In attempts to expand the substrate scope of possible proton-coupled reduction reactions, photo-charged TiO_2 nanoparticles were prepared using the procedure described by Bahnemann and were screened for their reactivities with a series of reducible organic substrates. We found these materials were highly active for the stoichiometric reduction of nitro functionalities (both aliphatic and aromatic) and pyridine-*N*-oxide, but showed no reactivity with other reducible organic substrates such as benzyl or phenyl bromide, acetone, 2-phenyl-2-propanol, or ^{t}BuN=N^{t}Bu (di-*tert*-butyldiazene). While the photo-catalytic reductions of aromatic and aliphatic nitro functional groups with TiO_2 have been previously reported,[7] this was to our knowledge the first example in which the electron stoichiometry was well defined and the reaction products were generated in quantitative yield with exclusive formation of aniline or amine (both protonated at pH 2.4). The details of these studies will be described here and the mechanistic possibilities discussed.

7.2. Results

7.2.1. Photo-Charging and Anaerobic Charge Loss of TiO_2 Nanoparticles

Photo-irradiation of titanium dioxide nanoparticles with UV light (> ~3.2 eV) results in the excitation of a valence band (VB) electron (e^-) into the conduction band (CB) and leaves a hole (h^+) in the valence band. This hole can be rapidly quenched in the presence of a hole scavenger such as methanol or ethanol near the surface of the particle. In the absence of O_2 or other reducible substrates, the electron remains trapped in the

particle, e^-:TiO_2 (scheme 7.2).[4c] This process can occur several times, resulting in multiple reducing equivalents confined in the same particle.[5] From the high resolution scanning electron microscopy (HRSEM) to estimate particle size and titrations with benzoquinone to count reducing equivalents, Bahnaman estimates the particles used in their studies have an average of 6-9 electrons per nanoparticle.[5]

Scheme 7.2. Photocharging of TiO_2 Nanoparticles.

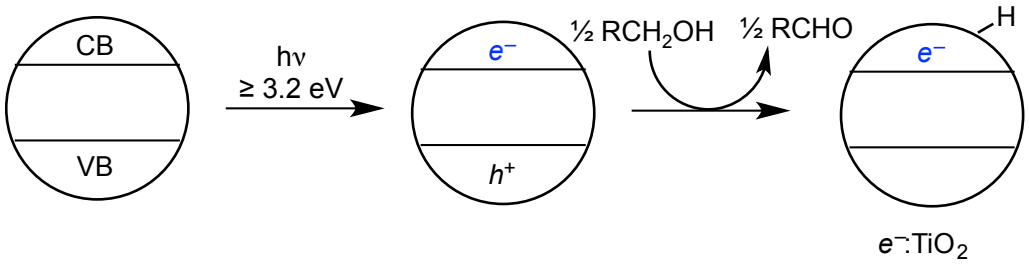

Following Bahnaman's procedures with minor modifications, a 5 mL D_2O solution containing 1% methanol-d_4 (v/v) and 25 mg of TiO_2 nanoparticles were added to a cuvette fitted with a Kontes adaptor and was sparged with argon for 30 minutes. Once sparging was complete, the colorless solution was irradiated under UV light with stirring. After *ca.* 6 hours, the solution turned dark purple, displaying a broad absorption across the visible spectrum indicating photocharging had occurred. Over the course of 18 hours after charging, this absorption intensity faded by nearly half under anaerobic conditions (Figure 7.1).

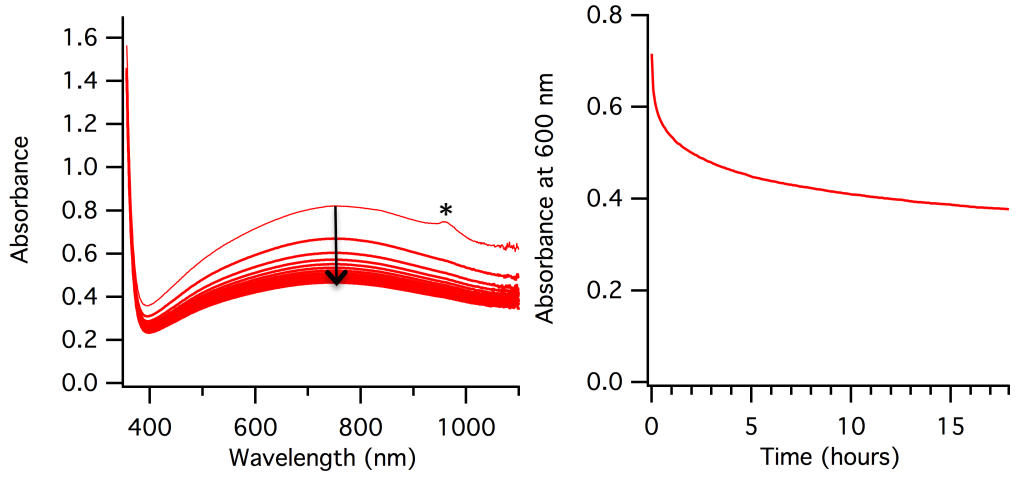

Figure 7.1 Anaerobic bleaching of e^-:TiO_2 is observed immediately after photolysis is complete. The spectral decay over 18 hours is shown on the left and the single wavelength trace at 600 nm is shown on the right. The asterisk (*) indicates an unknown absorbance feature observed at early time points.

To determine whether this absorption bleach was the result of some anaerobic un-charging event or from electron relaxation into trapped states[8] lacking optical signatures, NMR titrations were performed at two different times after charging. The absorption spectrum of charged particles taken quickly after charging showed an absorption of 0.496 at 600 nm. The addition of excess 4-MeO-TEMPO with an ethanol-d_1 internal standard to an aliquot of these freshly charged particles displayed the formation of 1.6 mM 4-MeO-TEMPO–H by ^{1}H NMR integrations. After 24 hours, the optical spectrum of the same solution of charged particles was collected and showed an absorption of 0.414 at 600 nm, corresponding to a 16% decrease in intensity. The same 4-MeO-TEMPO titration procedure was carried out with these particles and showed the generation of 1.35 mM 4-MeO-TEMPO-H (table 7.1).

Table 7.1. Particle Titration Data at Two Different Times After Photolysis

Quench Delay	Abs. At 600 nm	[4-MeO-TEMPO–H] (mM)	ε (M^{-1} cm^{-1})[a]
ca. 20 minutes	0.496	1.60 ± 0.08	310 ± 15
ca. 24 hours	0.414	1.35 ± 0.07	307 ± 15

[a]The ε of charged TiO_2 particles is known to be pH dependent. The pH of these solutions was not measured so this value is reported simply for comparison purposes

The difference in 4-MeO-TEMPO-H generated between these reactions is proportional to the difference in absorption at 600 nm indicating the fading color is not due to electron relaxation into spectroscopically silent states but rather is likely due to unknown anaerobic processes. This absorbance bleach was observed multiple times under rigorously O_2 free conditions such that we are confident this was not a result of un-charging from trace air leakage into the cuvette.

7.2.2. NMR Method to Determine e^-/TiO_2 Molar Extinction Coefficient at pH 2.4

Understanding how the absorption intensity of charged nanoparticles are related to the number of reducing equivalents they contain is important for monitoring stoichiometric reactions optically. The molar extinction coefficient (ε) of charged TiO_2 nanoparticles in water has been reported by several groups but these values are in poor agreement and range from 470 to 1200 M^{-1} cm^{-1}.[5,7c,9] Work performed by J. Peper has

found that TiO_2 nanoparticles independently prepared using the Bahnemann procedure have substantially lower ε values in the range of 170 ± 100 M^{-1} cm^{-1} at low pH values.[6] At higher pH (*ca.* pH 12), Peper found this number was much larger in the range of roughly 1200 M^{-1} cm^{-1}.[6]

While the variability of ε with pH was problematic for correlating reducing equivalents with absorption, it perhaps clarifies the discrepancy between values reported in the literature. Understanding specifically how solvent pH and molar extinction coefficient are related would be valuable for using these particles as stoichiometric reductants.

The molar extinction coefficients reported in the literature and by Peper were measured by optical titrations using a chemical oxidant (i.e. benzoquinone or 4-MeO-TEMPO).[5,6] These experiments show that absorbance is linearly related with electron concentration indicating each electron has effectively the same optical absorbance whether it is contained in a nanoparticles by itself or with several other electrons. Titrations performed in this way have proven useful but tedious to collect. To streamline this process, a protocol for rapidly collecting electron concentration data using a combination of optical absorption spectroscopy and NMR was designed.

Three different batches of TiO_2 nanoparticles were dissolved in 18 MΩ water at a concentration of 5 g L^{-1}. The pH values of these solutions were measured and were found to be pH 2.4 (± 0.02) in all cases. Particles from the same three batches were dissolved in D_2O (25 mg in 5 mL) with 1% methanol-d_4 (v/v), degassed and photolyzed for 2 hours. After charging, the particles were allowed to 'rest' overnight in a nitrogen filled glovebox so that anaerobic un-charging events could effectively reached completion. The optical spectrum of each of these samples was recorded and aliquots of each were quenched with a slight excess of 4-MeO-TEMPO in methanol-d_4 containing an ethanol-d_1 internal standard. This procedure was repeated two additional times with each of the same partially charged solutions to investigate whether longer charge times had a measureable effect. This data is summarized in table 7.2.

Table 7.2. Titration Data for e^-:TiO_2 solutions with pre-charge pH values of 2.4.

Batch	Charge Time (hours)	Absorbance	[e^-] (mM)	ε (M^{-1} cm^{-1})
1	2	0.406	2.2	180
2	2	0.282	2.2	130
3	2	0.378	2.0	190
1	4	0.591	3.2	190
2	4	0.632	3.8	170
3	4	0.790	3.6	220
1	6	0.646	3.0	~~290~~*
2	6	0.687	4.2	170
3	6	0.553	3.7	150
				Average ε = 175 ± 27 M^{-1} cm^{-1}

*This outlier data point was omitted for average calculation.

The molar extinction coefficients calculated for all three batches of particles and charge times were found to be generally reproducible with a consensus value of 175 ± 27 M^{-1} cm^{-1}. This was in good agreement with the value previously measured by Peper of 170 ± 100 M^{-1} cm^{-1} and served to confirm the accuracy of both titration methods. Titration measurements using this procedure were only carried out with particles with pre-charge solution pHs of 2.4, but this protocol could prove very useful for quickly determining molar extinction coefficients of particles at different pHs.

7.2.3. Screening Reactivity with Reducible Organic Reagents

Gary, Horst and Peper have found that photocharged TiO_2 nanoparticles in water are capable of reducing dimethylsulfoxide (DMSO) to dimethylsulfide (DMS) with an approximate bimolecular rate constant of 0.2 M^{-1} s^{-1}.[6] This reaction was of interest from a mechanistic standpoint since the reduction of DMSO is biased to proceed through 2 electron pathways and reduced TiO_2 is generally thought to react only through single electron transfer pathways.[1-3,7c] Mechanistic investigations of this reaction are ongoing.

In attempts to expand the scope of stoichiometric reduction reactions, a series of reducible organic reagents were screened for their reactivity with photo-reduced TiO_2

nanoparticles. A 5 mL D_2O solution containing 1% methanol-d_4 (v/v) and 25 mg of TiO_2 nanoparticles was sparged and photolyzed for 6 hours. After charging, the particles were allowed to 'rest' overnight in the glovebox. After 24 hours, aliquots of charged particles were treated with an excess of reducible organic reagent (including 4-MeO-TEMPO as a titration reference) in a known volume of methanol-d_4 containing ethanol-d_1 as an internal standard. The reaction products were determined by ^{1}H NMR (Appendix 7). The results of these experiments are summarized in Table 7.2.

Table 7.3. Organic Reduction Reactions Screened for Reactivity with e^-:TiO_2

Reagent	Product	[Product] (mM)[a]	Relative Yield
	Series 1		
4-MeO-TEMPO	4-MeO-TEMPO–H	0.59	6
4-nitrotoluene	4-aminotoluene*	0.10	1
	Series 2		
4-MeO-TEMPO	4-MeO-TEMPO–H	0.28	6
2-nitropropane	2-aminopropane	0.05	1.1
Pyridine-*N*-oxide	pyridine	0.15	3.2
acetone	NR	N/A	N/A
2-phenyl-propanol	NR	N/A	N/A
di-*tert*-butyldiazene	NR	N/A	N/A
phenylbromide	NR	N/A	N/A
benzylbromide	NR	N/A	N/A

[a]Error associated with product concentrations taken to be ± 5%. NR = No Reaction.

**Caution. 4-Aminotoluene is toxic and should be handled with care*

Reductions of aromatic and aliphatic nitro substituents to the corresponding aniline or amine and the reduction of pyridine-*N*-oxide to pyridine occurred nearly instantaneously. This was evident from the disappearance of the purple color of e^-:TiO_2 upon mixing. None of the other organic substrates showed evidence of reactivity after 24 hours as determined by ^{1}H NMR and the persistent purple color of the solutions.

The concentration of 4-MeO-TEMPO-H generated served as a titration for the number of electrons contained in each aliquot of photo-reduced particles. The reduction of 4-MeO-TEMPO to 4-MeO-TEMPO–H is a $1H^+/1e^-$ process so the overall stoichiometry with the reducing equivalents in an aliquot of charged particles is 1:1.

The reduction of pyridine-*N*-oxide to pyridine and water is a $2H^+/2e^-$ process requiring two reducing equivalents from e^-:TiO_2. Similarly, the reduction of an aromatic or aliphatic nitro group to an aniline or amine is a $6H^+/6e^-$ process. It would therefore be expected that equivalent aliquots of photo-charged TiO_2 nanoparticles would react with TEMPO, pyridine-*N*-oxide, and R-NO_2 yielding their respective reduced species in a ratio of 6:3:1. Within the error of the NMR measurements, this is the ratio observed experimentally. This means that every reducing equivalent from e^-:TiO_2 is consumed and used exclusively to reduce the respective organic reagent. It is especially interesting to note that in the $6H^+/6e^-$ reduction of R-NO_2, no partially reduced nitrone[7a] intermediates are observed by ^{1}H NMR. This is true even though the reaction was carried out in the presence of ~3 fold excess R-NO_2 and suggests the rate determining step for this reaction occurs between e^-:TiO_2 and R-NO_2.

Methanol-d_4 was used as a co-solvent for organic reagent additions because of solubility issues. Addition of the same organic reagents to e^-:TiO_2 in the absence of methanol resulted in the same reactivity pattern as determined from the solution color bleach but the products were not quantified. In the next section, we assume the same reactivity is operative in the absence of methanol-d_4 as a co-solvent.

7.3. Mechanistic Discussion of Aliphatic and Aromatic Nitro Reduction

The reduction of aromatic and aliphatic nitro groups to the corresponding anilines and amines are multi-proton multi-electron processes and could in principle occur through a variety of mechanisms. These could involve a series of one-electron, one-proton reductions – either sequential or concerted – or through concerted multi-electron proton transfer events or some combination of both. It has previously been suggested that under photocatalytic conditions, the reduction of nitrobenzene to aniline involves the formation of a nitrosobenzene intermediate that is subsequently reduced by $1H^+/1e^-$ to nitrosylbenzene radical (scheme 7.3).[7a] EPR studies have detected this intermediate.[7e]

The mechanism by which nitrobenzene is reduced to nitrosobenzene is unknown. This reaction is frequently described schematically as a $2H^+/2e^-$ reduction[7a,e] but not discussed explicitly. To assess the possible mechanisms for this reaction, it is useful to examine the thermodynamic parameters of the reagents involved.

Scheme 7.3. Previously Suggested Pathway for Nitrobenzene Reduction

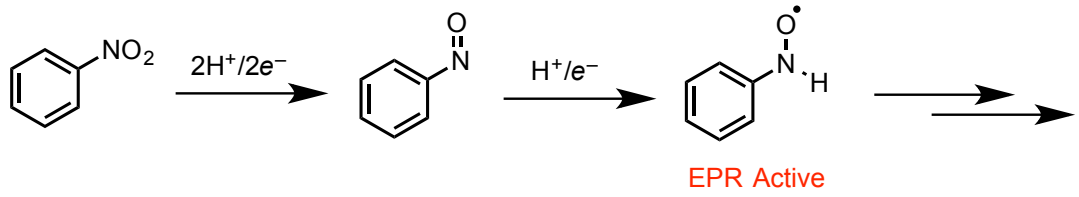

7.3.1. Thermochemical Assessment of $1H^+/1e^-$ Reduction of Nitrobenzene

Previous work by J. Peper has shown that TiO_2 nanoparticles in pH 2.4 solutions can be partially charged by the chemical reductant chromium(II) allowing for an approximation of the reduction potential of e^-:TiO_2 of $E_{pH2.4} = -0.40 \pm 0.05$ V vs NHE. Assuming this potential corresponds to the *proton coupled reduction*, it can be converted to an 'effective bond dissociation free energy' (BDFE) of roughly 51.6 ± 1.0 kcal mol^{-1} by approximating a pH dependence of 1.37 kcal mol^{-1} per pH unit (equivalently 0.059 mV/pH unit) and using equation 7.1. This is shown schematically in eq 7.2.

$$BDFE(XH) = 23.06[E_{pH2.4}(X^{\bullet}/XH)] + 1.37(pH2.4) + 57.6 \text{ kcal mol}^{-1} \qquad (7.1)$$

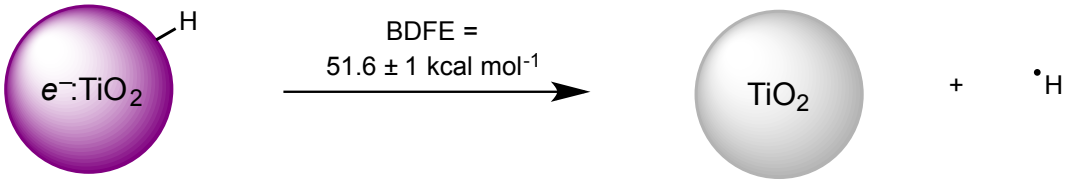

(7.2)

The aqueous reduction potentials for a series of nitro-containing organic molecules have been reported.[11] These potentials show 59 mV/pH unit dependences from

pH 0 until the pH is equal to the pK_a of the protonated nitro radical anion. The reported reduction potential of nitrobenzene is E_{pH7} = –0.486 ± 0.05 V vs. NHE at pH 7 and its corresponding protonated radical anion (NBH) has a pK_a of 3.2.[11] Assuming the onset of Nernstian behavior (0.059 mV/pH) occurs at pH = pK_a, the reduction potential can be converted to $E_{pH2.4}$ = –0.440 ± 0.05 V or $E°$ = –0.300 ± 0.05 V vs. NHE via eqs 7.3 and 7.4, respectively.

$$E_{pH2.4} = E_{pH7} - 0.059(pH2.4 - pK_a(NBH))^{10} \quad (7.3)$$

$$E° = E_{pH7} - 0.059(pH0 - pK_a(NBH))^{10} \quad (7.4)$$

$E°$ can be further converted[10] to give an O–H bond dissociation free energy for protonated and reduced nitrobenzene of ~50.7 ± 1 kcal mol^{-1} (eq 7.5).

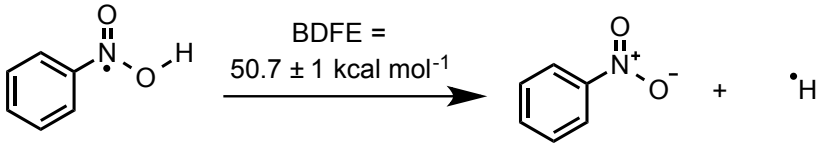

(7.5)

Comparing the reduction potentials of e^-:TiO_2 nanoparticles and nitrobenzene at pH 2.4 indicates that transferring a net H^+/e^- from e^-:TiO_2 to nitrobenzene is essentially thermoneutral ($\Delta E_{pH2.4}$ ≅ 0.03 V). From this comparison, it is clearly possible the reduction of nitrobenzene to aniline could involve a rate determining H^+/e^- transfer as opposed to a concerted $nH^+/2e^-$ transfer event. While the studies reported here were limited to nitrotoluene, it is likely its thermochemistry is roughly the same as that of nitrobenzene from which the same conclusions can be drawn.

7.3.2. Thermochemical Assessment of $1H^+/1e^-$ Reduction of 2-Nitropropane

The one-electron reduction potentials of aromatic and aliphatic nitro containing organic compounds at pH 7 were shown to be empirically related to the EPR hyperfine coupling constant a^{NO2}_{-} of their radical anion in water at pH 7 (eq 7.6).[11]

$$E_{pH7} = 0.315 - 0.054(a^{NO2}_{-}) \quad (7.6)$$

The reported a^{NO2}_{-} value for 2-nitropropane (2NP) radical anion at pH 7 was reported to be 25.3 G[12] which gives $E_{pH7} = -1.05 \pm 0.10$ V vs NHE from eq 7.6. The pK_a of reduced and protonated 2NP (2NPH) is unknown but can be conservatively estimated to have an acidity equal to the reported pK_a of 4.4[13] for reduced and protonated nitromethane. Using eq 7.7 or 7.8 gives $E_{pH2.4} = -0.93 \pm 0.10$ V or $E° = -0.80 \pm 0.10$ V vs. NHE. This corresponds to a reduced and protonated species with an O–H BDFE of 39.2 ± 2.5 kcal mol^{-1} (7.9).

$$E_{pH2.4} = E_{pH7} - 0.059(pH2.4 - pK_a(2NPH))^{10} \quad (7.7)$$

$$E° = E_{pH7} - 0.059(pH0 - pK_a(2NPH))^{10} \quad (7.8)$$

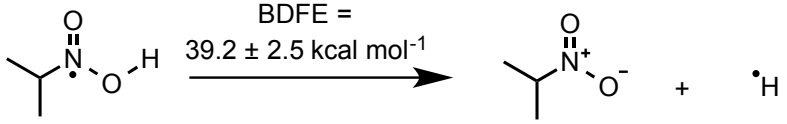

(7.9)

This means that at pH 2.4 a rate determining H^+/e^- reduction of 2NP by e^-:TiO_2 would be endoergic by 0.53 ± 0.15 V or 12.2 ± 3 kcal mol^{-1}. If this reaction proceeded with zero activation energy ($\Delta G^‡ = \Delta\Delta G°$), the rate constant would be between ~40 M^{-1} s^{-1} and 10×10^5 M^{-1} s^{-1} at room temperature. In order to rule out this mechanism, kinetic studies would be required to determine whether the observed activation barrier, $\Delta G^‡_{obs}$ is lower than $\Delta\Delta G°$ for H^+/e^- transfer from e^-:TiO_2 to 2-nitropropane.

While we cannot eliminate a rate determining concerted $nH^+/2e^-$ mechanism as a possibility, it seems reasonable based on the thermochemical analysis presented here that the reduction of 2-nitropropane proceeds through a rate determining H^+/e^- transfer.

7.3.3. Thermochemical Assessment of $1H^+/1e^-$ Reduction of Pyridine-*N*-Oxide

The one electron reduction potentials of pyridine-*N*-oxide have been previously reported at both pH 7 (E = –1.16 V vs NHE) and at pH 3.5 (E = –1.04 V vs NHE).[14] These values indicate the reduction of pyridine-*N*-oxide is proton dependent and suggest the reduced and protonated product has a pK_a between 7 and 3.5 since the potentials vary less than 0.059 V per pH unit. Assuming that ideal Nernstian behavior (0.059 mV/pH unit) is observed between pH 3.5 and pH 0.7 (pK_a pyr-OH^+ = 0.7) [15] gives $E_{pH2.4}$ = –0.97 ± 0.05 and $E°$ = –0.87 ± 0.05 V vs NHE from eqs 7.10 and 7.11. Converting this value to a bond strength gives an N–O BDFE of ~37.4 ± 2 kcal mol^{-1} (eq 7.12). Within error, this value is the same as the O–H BDFE predicted for reduced and protonated 2-nitropropane.

$$E_{pH2.4} = E_{pH3.5} - 0.059(\text{pH } 2.4 - \text{pH } 3.5)^{10} \tag{7.10}$$

$$E° = E_{pH3.5} - 0.059(\text{pH } 0.7 - \text{pH } 3.5)^{10} \tag{7.11}$$

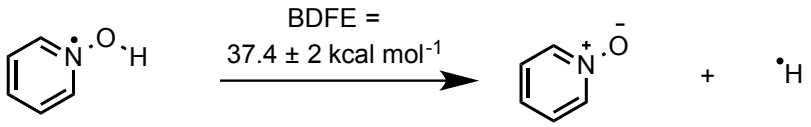

(7.12)

Because the thermodynamics for $1H^+/1e^-$ reduction of pyridine-*N*-oxide by e^- :TiO_2 at pH 2.4 are the same as for the reduction of 2-nitropropane with e^-:TiO_2, the same mechanistic ambiguity exists. It seems reasonable that this reaction could involve a rate determining H^+/e^- transfer but a concerted $nH^+/2e^-$ mechanism cannot be ruled out as a possibility.

7.3.4. Thermochemical Assessment of Non-Reactivity with Acetone

Photocharged TiO_2 nanoparticles at pH 2.4 are very strong net H^+/e^- reductants with $E_{pH2.4}$ = –0.40 ± 0.05 V vs NHE. At pH 2.4, the thermodynamic potential of the $H^+/½H_2$ couple is –0.142 V vs NHE. This implies that the formation of ½ H_2 from one reducing equivalent in e^-:TiO_2/H^+ is downhill by ~0.26 V or ~6 kcal mol^{-1} (eq 7.13 – 7.15). This has been corroborated experimentally by J. Peper who reported hydrogen gas evolution when platinum mesh was added to a solution of charged particles.[6]

$$e^-:TiO_2/H^+ \rightarrow TiO_2 + H^+ + e^- \qquad E_{pH2.4} = -0.40 \pm 0.05 \text{ V} \qquad (7.13)$$

$$H^+ + e^- \rightarrow ½\ H_2 \qquad E_{pH2.4} = 0.142 \text{ V} \qquad (7.14)$$

Summing eq 7.13 and 7.14:

$$e^-:TiO_2/H^+ \rightarrow ½\ H_2 \qquad E_{pH2.4} = -0.26 \pm 0.05 \text{ V} \qquad (7.15)$$

The significance of this is result is that e^-:TiO_2 is a *stronger reductant than dihydrogen* and is thermochemically competent to reduce any substrate that can be reduced by H_2. Since hydrogenation of ketones is always thermodynamically downhill,[16] the net conversion of acetone to isopropanol with $2H^+/2e^-$ equivalents from photocharged TiO_2 nanoparticles *should* occur but does not. Clearly, in this case e^-:TiO_2 does not behave as a multi-electron multi-proton reductant.

The reported gas phase bond dissociation enthalpy (BDE) for the O–H bond in isopropyl radical is 30.1 ± 2 kcal mol^{-1}.[17] With several assumptions, this can be converted to a BDFE in water with a value of 23.8 ± 4 kcal mol^{-1} or –1.47 ± 0.20 V vs NHE (eq 7.16)(see appendix 7). Assuming a 0.059 V/pH unit dependence on this redox process, an $E_{pH2.4}$ for this reduction can be calculated: $E_{pH2.4}$ = –1.61 ± 0.20 V vs NHE.

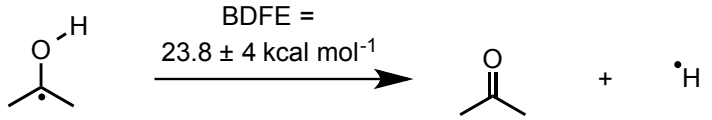

(7.16)

Using these approximations, the reduction of acetone by e^-:TiO_2/H^+ at pH 2.4 is endoergic by 1.2 ± 0.2 V or 27.8 ± 5 kcal mol^{-1}. At the most conservatively low limit, a barrierless reaction would proceed at a maximum rate of ~10^{-4} M^{-1} s^{-1}. At the high limit, the rate would be at most ~5 × 10^{-12} M^{-1} s^{-1}. The lack of reactivity observed between e^-:TiO_2 and acetone is in general agreement with the high thermodynamic barrier for sequential H^+/e^- transfer determined in this system.

7.3.5. Oxygen Atom Transfer Mechanism

From the thermochemical analysis presented here, it seems reasonable that the reduction of nitro functional groups and pyridine-*N*-oxide could proceed through a rate determining H^+/e^- transfer event rather than a concerted $nH^+/2e^-$ transfer.[18] With acetone, the thermochemical barrier for H^+/e^- transfer is much higher which is consistent with its unreactive nature with e^-:TiO_2.

While the correlation between H^+/e^- transfer thermochemistry is consistent with the reactivity discussed, it should be noted that the same correlation can be made when comparing the X=O bond strengths between the substrates involved. The trend in X=O bond strengths (gas phase BDEs) ranging from weakest to strongest is as follows: pyridine-*N*-oxide < DMSO < nitrotoluene < 2-nitropropanol << acetone.[18] This also parallels the reactivity patterns observed. As such, we cannot eliminate the possibility of a rate determining O-atom transfer in these reactions.

7.4. Conclusions

Photocharged colloidal TiO_2 nanoparticles suspended in acidic aqueous solutions have been found to be highly selective chemical reagents for the reduction of nitro-aliphatics and aromatics to amines and anilines, respectively and pyridine-N-oxide to pyridine. Under the same conditions, other reducible organic substrates are unreactive for at least 24 hours. The reductions of nitro-containing organic compounds with TiO_2 are well established under photocatalytic conditions, however this is the first case to our knowledge of an example where the reaction stoichiometry is well defined. In the examples presented here, every reducing equivalent generated during photolysis can be accounted for in the reduced products observed by ^{1}H NMR. These reductions yield

anilines and amines exclusively as $6H^+/6e^-$ reduced products suggesting the rate determining step for these reactions occurs early in the overall reaction.

The operative mechanism (or mechanisms) for these reduction reactions is not well understood but it is likely that H^+/e^- transfer is involved in the rate-determining step from thermochemical analysis.

The hydrogenation of acetone by photocharged TiO_2 nanoparticles is thermochemically favorable but does not occur after 24 hours. The thermodynamic barrier for sequential H^+/e^- transfer is much higher for acetone than for the nitro or N-oxide compounds, which may explain why it does not react and the other compounds do.

The reactivity experiments and thermochemical analysis presented here are self-consistent with photo-reduced TiO_2 nanoparticles being strong H^+/e^- donors and kinetically limited multi-electron, multi-proton reductants but a rate determining O-atom transfer cannot be excluded as a possibility. Kinetic measurements and an expanded substrate scope would be required to further elucidate this mechanism.

7.5. Experimental

7.5.1. General Considerations

Unless otherwise note, all chemicals were purchased from Sigma-Aldrich and used without purification. D_2O, methanol-d_4 and ethanol-d_1 were purchased from Cambridge Isotope labs. TiO_2 nanoparticles were prepared according to literature procedures.[5] NMR experiments were carried out in an argon filled 'wet box.'

7.5.2. Equipment

**Caution. 4-Aminotoluene is toxic and should be handled with care*

Optical measurements were carried out using a Hewlett-Packard 8453 diode array spectrometer. NMR spectra were collected on Bruker 500 MHz instruments and referenced to TMS using the residual solvent peak. Photolysis was carried out with a 500 W Hg/Xe lamp.

7.5.3. Representative Organic Reduction Reaction Protocol

In an argon filled 'wet box,' 600 μL aliquots of photocharged TiO_2 nanoparticles in D_2O/1% methanol-d_4 (v/v) were added to separate NMR tubes. To each was added an excess of a different organic substrate dissolved in 100 μL of methanol-d_4 containing a

known concentration of ethanol-d_1. NMR spectra were collected on a 500 MHz instrument with 45 second delay times to ensure complete T1 relaxation. Integration of the corresponding product peaks against ethanol-d_1 gave product concentrations. Concentrations were volume corrected to reflect the volume of the aliquot of e^-:TiO_2 solution prior to methanol-d_4 addition.

The organic reagents were added to the particles in methanol-d_4 instead of D_2O because of solubility issues with some of the reagents. The same reactions were carried out with the addition of neat organic reagent to solutions of nanoparticles and the same reactivity pattern was observed from color bleaching. The products of these reactions were not determine but assumed to be the same as when methanol-d_4 was used as a co-solvent. Thermochemical discussions rely on this assumption.

Notes for Chapter 7

(1) Kamat, P. V. *J. Phys. Chem. Lett.* **2001**, 2, 839.

(2) Fujishima, A.; Zhang, X.; Tryk, D. *Surf. Sci. Rep.* **2008**, 63, 515.

(3) Fox, M. A.; Dulay, M. T. *Chem. Rev.* **1993**, 93, 341.

(4) Schrauben, J. N.; Hayoun, R.; Valdez, C. N.; Braten, B. M.; Fridley, L.; Mayer, J. M. *Science* **2012**, 336, 1298.

(5) Mohamed, H. H.; Mendive, C. B.; Dillert, R.; Bahnemann, D. W. *J. Phys. Chem. A.* **2011**, 115, 2139.

(6) Unpublished data.

(7) (a) Ferry, J. L.; Glaze, W. H. *Langmuir* **1998**, 14, 3551. (b) Shiraishi, Y.; Hirai, T. *J. Photochem. Photobiol. C.* **2008**, 9, 157. (c) Hendersen, A. *Surf. Sci. Rep.* **2011**, 66, 185 (d) Makorova, O. V.; Rajh, T.; Thurnauer, M. C.; Martin, A.; Kemme, P. A.; Cropek, D. *Energy and Environ. Sci.* **2000**, 3, 479. (e) Flores, S. O.; Rios-Bernij, O.; Valenzuela, M. A.; Cordóva, I.; Gómez, R.; Gutiérrez, R. *Top. Catal.* **2007**, 44, 507. (f) Cropek, D.; Kemme, P. A.; Makarova, O. V.; Chen, L. X.; Rajh, T. *J. Phys. Chem. C.* **2008**, 112, 8311.

(8) Nunzi, F.; Mosconi, E.; Storchi, L.; Ronca, E.; Selloni, A.; Grätzel, M.; De Angelis, F. *Energy Environ. Sci.* **2013**, 6, 1221.

(9) Safrany, A. *J. Phys. Chem. B.* **2000**, 104, 5848.

(10) Warren, J. J.; Tronic, T. T.; Mayer, J. M. *Chem. Rev.* **2010**, 110, 6961.

(11) Meisel, D.; Neta, P. *J. Am. Chem. Soc.* **1975**, 97, 5198.

(12) Eiben, K.; Fessenden, R. W. *J. Phys. Chem.* **1968**, 72, 3387.

(13) Asmus, K. –D.; Taub, I. A. *J. Phys. Chem.* **1968**, 72, 3382.

(14) (a) Leach, S. C.; Weaver, R. D.; Kinoshita, K.; Lee, W. W. *J. Electroanal. Chem.* **1981**, 129, 213. (b) Reported values are given referenced to SCE and converted to NHE.

(15) (a) The pK_a of protonated pyridine-*N*-oxide is 0.7 ± 0.02 (ref 15b) so Nernstian behavior is expected between pH 3.5 and 0.7 (b) Klofutar, C.; Paljk, Š.; Kremser, D. *Spectrochimica Acta* **1973**, 22A, 139.

(16) (a) Rogers, D. W. *Heats of Hydrogenation: Experimental and Computational Hydrogen Thermochemistry of Organic Compounds*; World Scientific: Washington DC, 2006. (b) This assumes ΔS is small relative to ΔH_{rxn}.

(17) Pyridine-*N*-oxide could react through either a concerted H^+/e^- transfer or through a stepwise H^+/e^- reduction since the pK_a of protonated pyridine-*N*-oxide is 0.7. The mechanism is likely dependent on the pH of the solution.

(18) Luo, Y. –R. *Comprehensive Handbook of Chemical Bond Energies*; CRC Press: Boca Raton, Fl, 2007.

A.7.1. Representative ^{1}H NMR Spectra of Organic Reduction Reactions

e^-:TiO_2/H^+ + 4-MeO-TEMPO → TiO_2 + 4-MeO-TEMPO–H

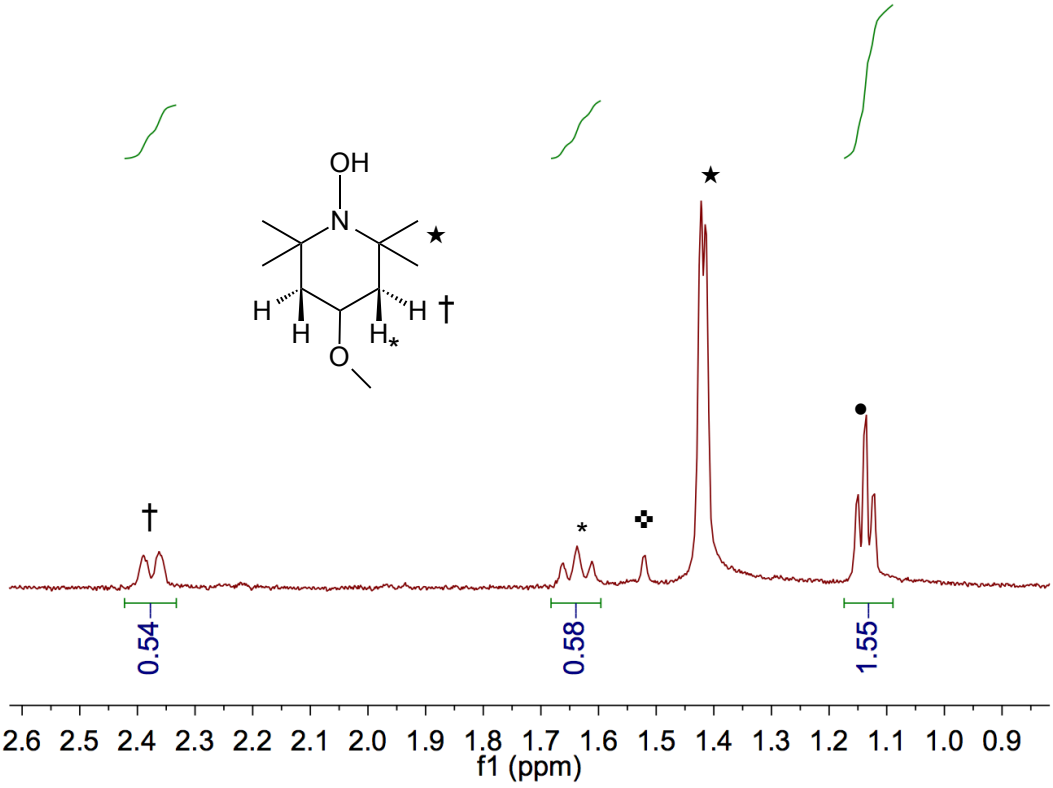

Figure A.7.1. ^{1}H NMR Spectrum of the completed reaction between e^-:TiO_2/H^+ and 4-MeO-TEMPO in 85% D_2O/15% methanol-d_4 showing the formation of 4-MeO-TEMPO–H. The resonance marked with • is a signal from the ethanol-d_1 internal standard and the signal marked with ✣ is a minor impurity believed to originate from acid induced disproportionation of 4-MeO-TEMPO.

6 e^-:TiO_2/H^+ + 2-nitropropane → 6 TiO_2 + 2-aminopropane

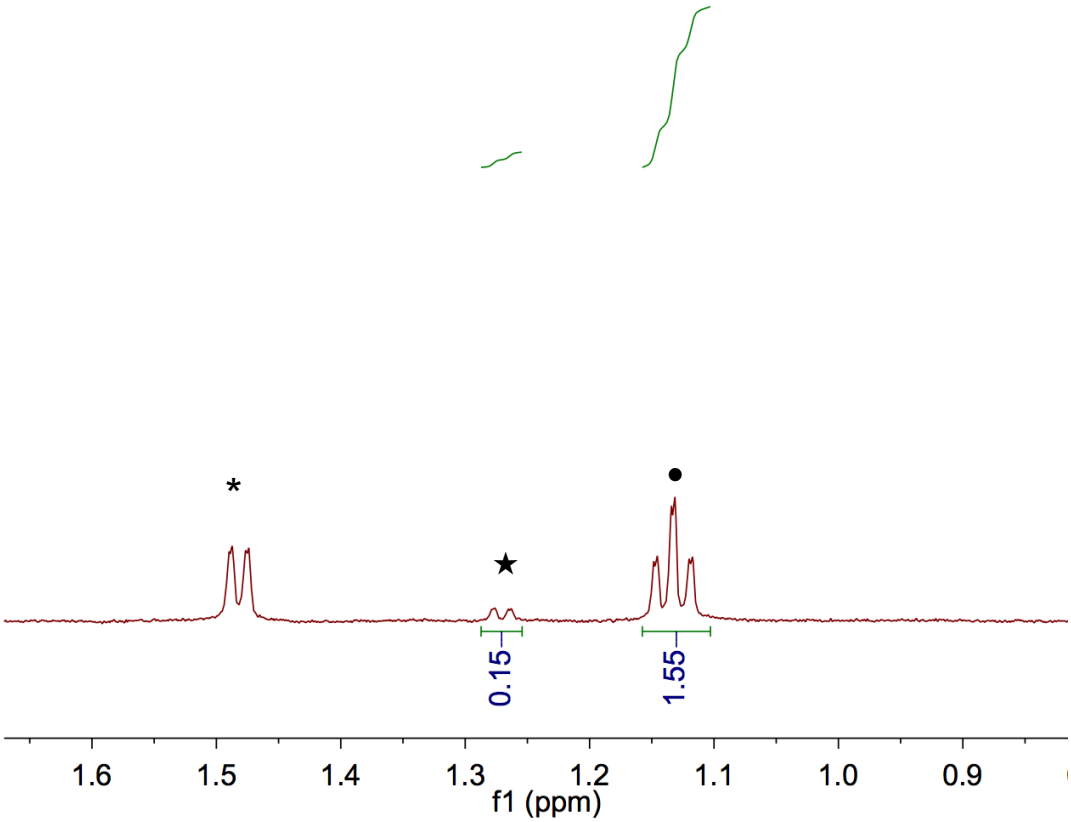

Figure A.7.1. ^{1}H NMR Spectrum of the completed reaction between e^-:TiO_2/H^+ and 4-MeO-TEMPO in 85% D_2O/15% methanol-d_4 showing the formation of 2-aminopropane (★). The resonance marked with • is a signal from the ethanol-d_1 internal standard and the signal marked with * is unreacted 2-nitropropane.

A.7.2. Converting the Gas Phase BDE of the O–H bond in Isopropyl Radical to a BDFE in pH 7 Water.

A.7.2.1. Converting From BDE_{gas} to $BDFE_{gas}$

Gas phase X–H bond dissociation enthalpies (BDEs) are related to gas phase bond dissociation free energies (BDFEs) by eq A7.1 when it is assumed $S°(X–H) \cong S°(X^{\bullet})$. $S°(H^{\bullet}) = 27.42$ cal mol^{-1} K^{-1} so at 298 K $TS°(H^{\bullet}) = 8.12$ kcal mol^{-1}. And equation A7.1 can be simplified to eq 7.2.[1]

$$BDFE_{gas} = BDE_{gas} - TS°(H^{\bullet}) \quad \text{(A7.1)}$$

$$BDFEgas = BDEgas - 8.12 \text{ kcal mol}^{-1} \quad \text{(A7.2)}$$

The reported[2] gas phase BDE of the O–H bond in isopropyl radical is 30.1 ± 2 kcal mol^{-1} so its gas phase BDFE is 22 ± 2 kcal mol^{-1} from eq A7.2.

A7.2.2. Converting from $BDFE_{gas}$ to $BDFE_{H2O}$

Gas phase X–H BDFEs are related to solution phase BDFEs by equation A7.3.[1]

$$BDFE_{solv}(X–H) = BDFE_{gas}(X–H) + \Delta G°_{solv}(H^{\bullet}) + \Delta G°_{solv}(X) - \Delta G°_{solv}(X–H) \quad \text{(A7.3)}$$

It is assumed that $\Delta G°_{solv}(H^{\bullet}) = \Delta G°_{solv}(H_2)$.[1] The value of $\Delta G°_{solv}(H_2)$ in water is 2.3 kcal mol^{-1}.[3] The values for $\Delta G°solv(X) - \Delta G°solv(X–H)$ can be estimated by using empirical hydrogen bonding parameters α_2^H and β_2^H as described by eq 7.4.[1]

$$\Delta G_{solv}°(X^{\bullet}) - \Delta G_{solv}°(X–H) = -10.02\alpha_2^H(solv)\beta_2^H(X^{\bullet}) + 10.02\alpha_2^H(X–H)\beta_2^H(solv) \quad \text{(A7.4)}$$

The reported α_2^H and β_2^H terms for water are 0.353[4] and 0.38,[5] respectively. The α_2^H term for isopropyl radical is not known but can be approximated to be the same as

that of isopropanol that has an α_2^H value of 0.324.[4] The β_2^H value for acetone is reported to be 0.50.[5]

With these values, the BDFE for the O–H bond in isopropyl radical is calculated to be 23.8 ± 4 kcal mol^{-1}.

A more thorough description of this type of conversion can be found in ref. 5.

A7.3. References for Chapter 7 Appendix

(1) (a) Warren, J. J.; Mayer, J. M. *Proc. Natl. Acad. Sci.* **2010**, 107, 5282. (b) Warren, J. M.; Tronic, T. T.; Mayer, J. M. *Chem. Rev.* **2010**, 110, 6961.

(2) Luo, Y. –R. *Comprehensive Handbook of Chemical Bond Energies*; CRC Press: Boca Raton, Fl, 2007.

(3) Roduner, E. *Radiat. Phys. Chem.* **2005**, 72, 201.

(4) Abraham, M. H.; Grellier, P. L.; Prior, D. V.; Duce, P. P. *J. Chem. Soc. Perkin Trans. II* **1989**, 699.

(5) Abraham, M. H.; Grellier, P. L. Prior, D. V.; Morris, J. J.; Taylor, P. J. *J. Chem. Soc. Perkin Trans. II* **1990**, 521.

Thesis Soundtrack
(Arranged Chronologically)

1. Oasis – Don't Look Back in Anger
2. Andrew Jackson Jihad – People II: The Reckoning
3. The Strokes – Someday
4. Fugazi – Strangelight
5. Man Man – Van Helsing Boom Box
6. Man Man – Feathers
7. Pavement – Billie
8. Tom Waits – The Black Rider
9. Ween – Birthday Boy
10. Ween – Oh My Dear (Falling in Love)
11. Pavement – Zürich is Stained
12. The Dead Milkmen – Dean's Dream
13. Pavement – Range Life
14. Tom Waits – Come on up to the House
15. Andrew Jackson Jihad – American Tune
16. Frank Black & the Catholics – Chip Away Boy
17. The Dead Milkmen – Brat in the Frat
18. Pavement – Box Elder
19. The Beatles – Rocky Raccoon
20. Ween – Doctor Rock
21. Pixies – Dig for Fire
22. Carly Rae Jepsen – Call me Maybe
23. Bob Dylan – You're a Big Girl Now
24. Bob Dylan – Shelter from the Storm
25. Pixies – Havalina
26. Wilson Phillips – Hold On
27. David Bowie – Oh! You Pretty Things
28. Guantanamo Baywatch – Diana
29. Pavement – Father to a Sister of Though
30. Pavement – We are Underused
31. Way Yes – Important
32. Jay Reatard – Nightmares
33. Beck – Gamma Ray
34. Jay Reatard – Gamma Ray
35. The Arcade Fire – Wake Up
36. Grandaddy – A.M. 180
37. The Clash – Police & Thieves
38. The Clash – Lose This Skin
39. Bruce Springsteen – Thunder Road
40. The Specials – You're Wondering Now

Vita

Thomas Porter was born and raised in Spokane, WA. He graduated *magna cum laude* from Washington State University in 2009 with a B.S. in Chemistry and a minor in Mathematics. In 2009, he moved to Seattle, WA to attend graduate school at the University of Washington. After graduating with a Ph.D. in Inorganic Chemistry from the Laboratory of James Mayer, Thomas will move to Paris, France to pursue post-doctoral studies in heterogeneous electrocatalysis at Université Paris Diderot under the supervision of Cyrille Costentin.